Università Politecnica delle Marche
Scuola di Dottorato di Ricerca in Ingegneria Civile, Edile e Architettura
Curriculum in Integrated Facility Engineering and Resilient Environments
XXXVI cycle (2020-2023)

Analysis of the reliability of the VECD approach for conventional and innovative asphalt mixtures

Ph.D. Dissertation of:
Sara Spadoni

Advisor:
Prof. Francesco Canestrari

Curriculum supervisor:
Prof. Francesco Fatone

Università Politecnica delle Marche
Scuola di Dottorato di Ricerca in Ingegneria Civile, Edile e Architettura
Curriculum in Integrated Facility Engineering and Resilient Environments
XXXVI cycle (2020-2023)

Analysis of the reliability of the VECD approach for conventional and innovative asphalt mixtures

Ph.D. Dissertation of:
Sara Spadoni

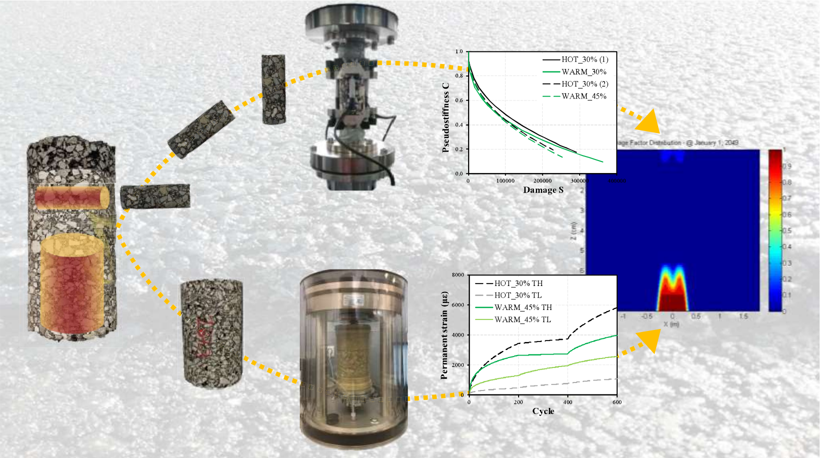

Advisor: **Prof. Francesco Canestrari**

Curriculum supervisor: **Prof. Francesco Fatone**

Università Politecnica delle Marche
Dipartimento di Ingegneria Civile, Edile e Architettura
Via Brecce Bianche — 60131 - Ancona, Italy

Acknowledgements

I would like to express my deepest gratitude to my tutor Professor Canestrari, whose support, knowledge and constant enthusiasm have been fundamental for my professional and personal growth during this journey.
I am also grateful to Professor Graziani, Professor Ferrotti, Professor Cardone and Technician Pierluigi for enriching my academic experience and for providing a stimulating and serene work environment.
Special thanks also to Professor Jaskuła and his research group for making me feel part of their family during the months abroad, and to Professor Kim for the precious time dedicated to us.
Sincere gratitude to Lorenzo, who taught me everything from the very first months of my PhD, as well as to all my colleagues met during years: Elena, Carlo, Simona, Vittoria, Simone, Eugenio, Valentina, Sara and Andrea.
I extend my heartfelt thanks to my family who always believed in my abilities, and to Pierluigi for his unconditional love, essential presence and unwavering encouragement.

30th April, 2024

Abstract

In Europe, heavy-transport demand has increased in the last decades, as a result of the growth of the global economy. In this scenario, road infrastructures, especially motorways, play a crucial role, since the pavement must ensure a proper level of service and safety for the users. Nowadays the research is mainly focused on the development and study of high-performance and sustainable materials. However, there is lack of reliable pavement design tools that allow to fully take into account the improved material properties or non-standard materials, since the most common design methods are either based on elastic theory or mechanistic-empirical approaches which require in-field observations in the long-term. To this regard, the Asphalt Mixture Performance-Related Specification (AM-PRS) developed in U.S. could represent a valid alternative, since they allow the determination and use of intrinsic material properties through the application of solid mechanical theories. The AM-PRS provides the mechanical-based fatigue and rutting characterization through the ViscoElastic Continuum Damage approach and the viscoplastic shift model, respectively. The aim of this PhD research work is to analyze the reliability of such approach for Italian (and European) conventional and innovative asphalt mixtures destined to motorway pavements. Therefore, the performance of dense-graded hot mix asphalt (HMA) with compound made of recycled plastic added through the dry method, and warm mix asphalt (WMA) with 30% or 45% of RAP were studied in comparison with the reference HMA with SBS modified bitumen. Three typical Polish asphalt mixtures with neat or SBS modified bitumen were also investigated. Regarding mixtures for wearing course, the performance of an open-graded (OG) WMA with 25% of RAP was compared to the one of the reference OG HMA with 15%. A stone mastix asphalt (SMA) mixture, commonly used in Poland, was included in the research as well. The results showed that the VECD approach is reliable for all the dense-graded mixtures for binder and base course, and it is capable of capturing the variation in performance associated with the mixture composition (i.e., virgin or recycled aggregate, type and amount of bitumen). However, the reliability of the failure criterion for OG may need further studies, since the low stiffness is identified as a rubbery behavior. Moreover, the suitability of stress sweep rutting tests for SMA may need to be evaluated. As a final challenge, the applicability of the VECD approach to Cold Recycled Materials (CRMs) was investigated by adopting a 2-stages procedure for pavement performance simulations. The results are encouraging and showed that CRMs could be used as replacements for both the aggregate base course and the lowest asphalt concrete course, enhancing the pavement performance and sustainability.

Sommario

In Europa, la domanda di pavimentazioni in grado di soddisfare il traffico pesante è aumentata negli ultimi decenni, a seguito della crescita dell'economia globale. In questo scenario, le infrastrutture stradali, in particolare le autostrade, giocano un ruolo cruciale, poiché la pavimentazione deve garantire un adeguato livello di servizio e di sicurezza agli utenti. La ricerca si è concentrata sullo sviluppo e sullo studio di materiali ad alte prestazioni e sostenibili. Tuttavia, mancano strumenti di progettazione della pavimentazione affidabili che consentano di tenere pienamente conto delle proprietà superiori dei materiali o dei materiali non convenzionali. Infatti, i metodi di progettazione più comuni sono basati sulla teoria elastica con l'utilizzo di formule empiriche, o sono empirico-meccanici che richiedono osservazioni a lungo termine per la calibrazione. A questo proposito, le Asphalt Mixture Performance-Related Specifications (AM-PRS) sviluppate negli Stati Uniti potrebbero rappresentare una valida alternativa, poiché prevedono la determinazione e l'utilizzo delle proprietà intrinseche dei materiali tramite l'applicazione di teorie meccaniche. Le AM-PRS forniscono la caratterizzazione meccanica a fatica attraverso l'approccio del ViscoElastic Continuum Damage e all'ormaiamento attraverso un modello viscoplastico chiamato shift model. Lo scopo del presente lavoro di dottorato è quello di analizzare l'affidabilità di tale approccio per conglomerati bituminosi convenzionali ed innovativi italiani (ed europei) destinati alle pavimentazioni autostradali. Sono state quindi studiate le prestazioni di conglomerati bituminosi chiuso a caldo (Hot Mix Asphalt, HMA) con compound di plastica riciclata aggiunti con il metodo dry, e di miscele tiepide (Warm Mix Asphalt, WMA) con il 30% o il 45% di RAP rispetto al conglomerato a caldo di riferimento con bitume modificato con SBS. Inoltre, sono state analizzati anche tre tipici conglomerati bituminosi impiegati in Polonia con bitume non modificato o modificato con SBS. Per quanto riguarda i conglomerati bituminosi per strati di usura, la prestazione di un WMA aperto (Open-Graded, OG) con il 25% di RAP è stata confrontata con quella dell'OG HMA di riferimento con il 15%. Alla ricerca è stato aggiunto uno Stone Mastix Asphalt (SMA) impiegato in Polonia. I risultati hanno mostrato che l'approccio VECD è affidabile per tutti i conglomerati chiusi per strati di collegamento e di base, ed è in grado di cogliere le differenze nelle prestazioni dovute alla composizione della miscela (aggregato vergine o riciclato, tipo e quantità di bitume). Tuttavia, l'affidabilità del criterio di rottura per OG potrebbe richiedere ulteriori studi, poiché la bassa rigidezza è identificata come un comportamento gommoso. Inoltre, potrebbe essere necessario valutare l'idoneità delle prove di ormaiamento di tipo stress sweep per lo SMA. Come obiettivo finale, è stata studiata l'applicabilità dell'approccio VECD ai materiali riciclati a freddo (CRM), adottando una procedura a 2 fasi per le simulazioni delle prestazioni della pavimentazione. I risultati sono promettenti e hanno mostrato che i CRM potrebbero essere utilizzati sia in sostituzione dello strato di base non legato sia in sostituzione dello strato di conglomerato più profondo migliorando le prestazioni e la sostenibilità della pavimentazione.

Table of Contents

List of Figures

List of Tables

List of Standard Specifications

AASHTO M 320:2023. Standard specifications for performance-graded asphalt binder.

AASHTO M 332:2023. Standard specification for performance-graded asphalt binder using Multiple Stress Creep Recovery (MSCR) test.

AASHTO PP 99:2023. Standard practice for preparation of small cylindrical performance test specimens using the Superpave Gyratory Compactor (SGC) or field cores.

AASHTO R 83:2022. Standard practice for preparation of cylindrical performance test specimens using the Superpave Gyratory Compactor (SGC).

AASHTO R 84:2017. Standard practice for developing dynamic modulus master curves for asphalt mixtures using the Asphalt Mixture Performance Tester (AMPT).

AASHTO T 166:2022. Standard method of test for bulk specific gravity (Gmb) of compacted asphalt mixtures using saturated surface-dry specimens.

AASHTO T 312:2019. Standard method of test for preparing and determining the density of asphalt mixture specimens by means of the Superpave Gyratory Compactor.

AASHTO T 321:2022. Standard method of test for determining the fatigue life of compacted asphalt mixtures subjected to repeated flexural bending.

AASHTO T 331:2023. Standard method of test for bulk specific gravity (Gmb) and density of compacted asphalt mixtures using automatic vacuum sealing method.

AASHTO T 378:2017. Standard method of test for determining the dynamic modulus and flow number for asphalt mixtures using the Asphalt Mixture Performance Tester (AMPT).

AASHTO T 400:2023. Standard method of test for determining the damage characteristic curve and failure criterion using the Asphalt Mixture Performance Tester (AMPT) cyclic fatigue test.

AASHTO T 411:2023. Standard method of test for determining the damage characteristic curve and failure criterion using small specimens in the Asphalt Mixture Performance Tester (AMPT) cyclic fatigue test.

AASHTO TP 132:2023. Standard method of test for determining the dynamic modulus for asphalt mixtures using small specimens in the Asphalt Mixture Performance Tester (AMPT).

AASHTO TP 134: 2019. Standard method of test for Stress Sweep Rutting (SSR) test using Asphalt Mixture Performance Tester (AMPT).

AASHTO TP 134: 2023. Standard method of test for Stress Sweep Rutting (SSR) test using Asphalt Mixture Performance Tester (AMPT).

AASHTO:2004. Chapter 6: HMA Rehabilitation of Existing Pavements - Guide for Mechanistic-Empirical Design of New and Rehabilitated Pavement Structures, Part 3. NCHRP Project 137A Final Report. National Cooperative Highway Research Program, Transportation Research Board, and American Association of State Highway and Transportation Officials, Washington, DC.

ASTM D4402-06:2012. Standard test method for viscosity determination of asphalt at elevated temperatures using a rotational viscometer.

EN 12593:2015. Bitumen and bituminous binders – Determination of Fraass breaking point.

EN 12607-1:2014. Bitumen and bituminous binders – Determination of the resistance to hardening under influence of heat and air – Part 1: RTFOT method.

EN 12697-1:2020. Bituminous mixtures – Test methods – Part 1: Soluble binder content.

EN 12697-24:2018. Bituminous mixtures – Test methods – Part 26: Resistance to fatigue.

EN 12697-26:2018+A1:2022. Bituminous mixtures – Test methods – Part 26: Stiffness.

EN 12697-31:2019. Bituminous mixtures – Test methods – Part 31: Specimen preparation by gyratory compactor.

EN 12697-5:2018. Bituminous mixtures – Test methods – Part 5: Determination of the maximum density.

EN 12697-6:2020. Bituminous mixtures – Test methods – Part 6: Determination of bulk density of bituminous specimens.

EN 12697-8:2018. Bituminous mixtures – Test methods – Part 8: Determination of void characteristics of bituminous specimens.

EN 13043:2002. Aggregates for bituminous mixtures and surface treatments for roads, airfields and other trafficked areas.

EN 13302:2018. Bitumen and bituminous binders – Determination of dynamic viscosity of bituminous binder using a rotating spindle apparatus.

EN 13398:2017. Bitumen and bituminous binders – Determination of elastic recovery of modified bitumen.

EN 13589:2018. Bitumen and bituminous binders – Determination of tensile properties of modified bitumen by force ductility method.

EN 13703:2003. Bitumen and bituminous binders – Determination of deformation energy.

EN 13808:2013. Bitumen and bituminous binders – Framework for specifying cationic bituminous emulsions.

EN 14023:2010. Bitumen and bituminous binders – Specification framework for polymer modified bitumens.

EN 1426:2015. Bitumen and bituminous binders – Determination of needle penetration.

EN 1427:2015. Bitumen and bituminous binders – Determination of softening point – Ring and Ball method.

EN 197-1:2011. Cements – Part 1: Composition, specifications and conformity criteria for common cements.

EN12591:2009. Bitumen and bituminous binders – Specifications for paving grade bitumens.

Mechanistic-Empirical Pavement Design Guide:2008. American Association of State Highway and Transportation Officials, Washington, DC.

NTC:2022. Norme Tecniche per le Costruzioni – Capitolato Speciale: Pavimentazione *(in Italian).*

List of Abbreviations

2S2P1D	2 Springs, 2 Parabolic elements, 1 Dashpot
AADTT	Annual Average Daily Truck Traffic
ABC	Aggregate Base Course
AC	Asphalt Concrete
AM-PRS	Asphalt Mixture Performance-Related Specifications
AV	Air Void content
CA	Christensen-Anderson
CAM	Christensen-Anderson-Marasteanu
CRM	Cold Recycled Material
CS	Cracked Subbase
DG	Dense-Graded
DGAC	Dense-Graded Asphalt Course
DMR	Dynamic Modulus Ratio
EATA	European Asphalt Technology Association
EN	European Standard
ESAL	Equivalent Standard Axle Load
EVA	Ethylene Vinyl Acetate
FDE	Fractional Derivative Element
FEM	Finite Element Method
FFE	Fourier finite element
FHWA	Federal Highway Administration
FWD	Falling Weight Deflectometer
HiMA	Highly Modified Asphalt
HWD	Heavy Weight Deflectometer
IS	Intact Subbase
ITFT	Indirect Tensile Fatigue Test
ITSM	Indirect Tensile Stiffness Modulus

JMF	Job Mix Formula
KTKNPiP	Katalog Typowych Konstrukcji Nawierzchni Podatnych i Polsztywnych
LEM	Limited Element Method
LVE	Linear-ViscoElastic
MEPDG	Mechanical-Empirical Pavement Design
NCSU	Nort Carolina State University
NMAS	Nominal Maximum Aggregate Size
OG	Open-Graded
OGFC	Open Graded Friction Course
PG	Performance Grade
PID	Proportional Integral and Derivative gain
PmB	Polymer modified Bitumen
RAP	Reclaimed Asphalt Pavement
RSI	Rutting Strain Index
SBS	Styrene-Butadiene-Styrene
SMA	Stone Mastix Asphalt
SPT	Simple Performance Tester
SSD	Saturated Surface Dry
t-TSP	Time-Temperature Superposition Principle
t-TSSP	Time-Temperature-Stress Superposition Principle
UnivPM	Università Politecnica delle Marche
VMA	Voids in the Mineral Aggregate
WMA	Warm Mix Asphalt

Chapter 1. Introduction

In Europe, heavy-transport demand has increased in the last decades, as a result of the growth of the global economy. In this scenario, road infrastructures, especially motorways and expressways, play a crucial role, since the pavement must ensure a proper level of service and safety to the users. In particular, fatigue cracking represents the most common distress since it occurs due to extensive cyclic application of load and/or variations in temperature. Fatigue cracking can begin at the bottom of asphalt concrete (i.e., bottom-up cracking) and propagate upwards due to bending stresses at the bottom of the layer, or on the surface (i.e., top-down cracking) and propagate downwards due to complex mechanisms (Canestrari & Ingrassia, 2020; B. S. Underwood, 2006). Fatigue damage causes a pattern of cracked square areas in the direction of the traffic, and the deterioration becomes faster due to the water penetration into the pavement structure, reducing the functionality of the pavement.

Research is focused on two main aspects, which must be simultaneously considered: improvement of the material properties, and reliable pavement design tools that allow to fully take into account the improved material properties or non-standard materials.

Researchers are studying and developing new materials which could improve the performance of the pavement against the most common distresses, i.e., fatigue cracking and rutting, and thermal cracking in those areas subjected to low temperature. Moreover, such materials must promote the always more important sustainability and circular economy, since the construction sector is responsible for the consumption of non-renewable resources, production of waste and emissions. Specifically, the conventional asphalt mixtures employ virgin aggregates and bitumen, which derives from the extraction of petroleum. To fulfill these deficiencies, the research has been focused on the use of RAP, which comes from the milling of old pavement, as replacement of virgin aggregate, as well as on replacing part of the bitumen with the so-called “bio-binder”, i.e., renewable materials. To enhance the asphalt mixtures performance, ad-hoc polymers have been developed, such as the mostly used SBS, which allow a strongly higher rutting and fatigue performance, or the innovative compounds made from plastics, even recycled. Finally, to reduce the emissions at the asphalt plant due to asphalt production, warm mix asphalt technologies have been optimized, allowing a reduction of the production temperature up to 40 °C, and better working conditions, and the use of cold recycled materials is gaining attention, too.

However, the improved and not-conventional resulting materials properties cannot be usually taken into account when the performance of such materials is investigated within the pavement structure. In fact, in Europe the pavement design is commonly elastic based, whereas the actual behavior is viscoelastic. The calculated stress and strain are then used to predict the service life adopting empirical equations. A more advanced method is the mechanistic-empirical pavement design (MEPD), in which the materials are considered with their viscoelastic behavior. Yet, the model requires to be calibrated with long-term in-field observations which strictly depend on the construction site (i.e., climatic and traffic conditions).

A possible solution is the application of Asphalt Mixture Performance-Related Specifications (AM-PRS), which include ViscoElastic Continuum Damage approach for fatigue characterization and viscoplastic shift model for rutting characterization. Differently from any other approach, such AM-PRS are entirely mechanistic-based. Performance-related specifications are defined as "quality assurance specifications that describe the desired levels of key materials and construction quality characteristics that have been found to correlate with fundamental engineering properties that predict performance" (Y. R. Kim, 2018). The research group in North Carolina State University, guided by Dr. Youngsoo Richard Kim, has been developing and continuously optimizing PRS for asphalt mixtures for two decades under the sponsorship of FHWA.

The main strength of this approach is the determination of fundamental fatigue and rutting properties of the material, which are independent of the testing conditions, and to predict the long-term performance of the pavement (unlike the conventional empirical fatigue tests, whose results are valid only under the specific boundary and loading conditions considered). Even though in U.S. the AM-PRS are well-known and routinely applied by road agencies laboratories, in Europe few applications can be found.

The aim of this PhD thesis is to assess the reliability of the AM-PRS for conventional and innovative asphalt mixtures for Italian motorways. Then, the same approach is applied to typical Polish asphalt mixtures in order to enlarge the database with European mixtures. Finally, the preliminary work regarding the applicability of the S-VECD approach on Cold Recycled Mixtures is carried out, since the S-VECD approach has never been applied before on such materials.

The PhD dissertation is divided into the following chapters:

- *Chapter 2* describes the testing methods and the analysis of the experimental data in accordance with the reference AASHTOs. The main functions of FlexPAVE^{TM} software program are specified, with a focus on the output results. Each chapter from 3 to 7 deals with different materials investigated through the VECD approach and viscoplastic shift model.
- *Chapter 3* regards the S-VECD characterization of asphalt mixtures containing polymeric compounds added with the dry method. The reference dense-graded and open-graded hot mix asphalts, compared with many mixtures along the PhD dissertation, are included in this chapter.
- *Chapter 4* regards the S-VECD characterization and application of the viscoplastic shift model of four typical Polish asphalt mixtures.
- *Chapter 5* regards the S-VECD characterization of field cores made of warm mix asphalt containing 30% of RAP (the same of the reference hot mix asphalt), extracted after six years of service.
- *Chapter 6* regards the S-VECD characterization and application of the viscoplastic shift model on warm mix asphalt for both wearing and base courses with higher than the usual RAP content.

- *Chapter 7* regards the evaluation of the applicability of the S-VECD approach to characterize the fatigue behavior of Cold Recycled Materials.
- *Chapter 8* reports the main findings of this thesis and some recommendations for future research.

Chapter 2.
The Asphalt Mixture Performance-Related Specifications for the mechanical characterization and pavement design of flexible pavements

2.1 Introduction

The fatigue characterization is conventionally carried out in laboratory through the application of repeated cycling bending stresses on cylindrical or prismatic specimens at few temperatures and/or frequencies and the correlation of the results to observations in the field. Analogously, the rutting characterization is performed by means triaxial cyclic compression test or wheel tracker test at few temperatures and/or frequencies, from whose results the service life can be predicted. However, the applicability of such methods for performance prediction is severely degraded when conditions change beyond those used to develop the initial correlation. Furthermore, the combined elements of material and structure within the test method complicate the assessment of true material behavior (B. S. Underwood, 2006).

The research group in North Carolina State University, guided by Dr. Youngsoo Richard Kim, has been developing AM-PRS for two decades, which are actually under constant optimization, under the sponsorship of FHWA.

The aim of such work is to identify the proper laboratory tests on asphalt mixtures that can be carried out in a short time, and a solid theoretical analysis capable of determining fundamental properties of the material that can be used for pavement performance prediction under several traffic and climatic conditions. Moreover, such methods are user-friendly, even for users who are not interested in the heavy theoretical background behind the output and for practitioners (e.g., road agencies) for whom test results can be overwhelming. That's why the FHWA provides Excel spreadsheets, called FlexMAT$^{\text{TM}}$, i.e., Excel-based material-level analysis programs, to elaborate the data with only few simple clicks (Y. R. Kim, 2018). The AMP-RS are currently used to evaluate fatigue and rutting performance, whereas thermal cracking performance is under development. The characterization in terms of viscoelastic properties is required for the fatigue analysis. The fatigue cracking performance is based on the simplified viscoelastic continuum damage (S-VECD) model. The rutting characterization is based on the viscoplastic shift model using the data obtained from Stress Sweep Rutting (SSR) tests.

In summary, dynamic modulus tests and cyclic fatigue tests to characterize the S-VECD model for fatigue cracking, plus SSR tests to characterize the shift model for rutting would take from three to five days to complete using an AMPT (Y. R. Kim, 2018). The subsequent analysis is very fast due to provided Excel spreadsheets.

In the last stage, the parameters obtained from the analysis of the laboratory tests results, are used as input in ad-hoc developed software, called FlexPAVE™ (formerly known as the LVECD program), to run pavement performance simulations to predict the behavior of the material at the structural level. FlexPAVE™ is a fast Fourier transform-based three-dimensional viscoelastic finite element analysis tool that can simulate moving loads and actual climatic conditions considering hourly and daily temperature variations in a year.

The following sections describe the up-to-date methods and analysis of the AM-PRS, then adopted to characterize many asphalt mixtures. It should be underlined that the aim of the PhD thesis is to assess the reliability of such approach to European (mostly Italian) asphalt mixtures, analyzing the obtained results compared with the conventional parameters and with the well-known behavior of the mixtures, without going into details of the mechanical theory (which may require years of study to be fully understood). For these reasons, the descriptions of the methods are practical, specifying the execution of laboratory tests, and the main concepts of the huge theories for the analysis are recalled, accompanied by the proper references for the in-depth study.

2.2 Production of the specimens

The geometries of the test specimens are reported in Table 2.1. The conventional large specimens have a diameter of 100-mm, and height of 150-mm for dynamic modulus and rutting tests, and height of 130-mm for fatigue tests. The small specimen geometry has been added to the conventional large specimens for dynamic modulus and fatigue tests, if the mixture is dense-graded and with a NMAS up to 19.0 mm. Small specimens have a diameter of 38-mm and height of 110-mm for both the tests. The small specimen geometry improves the efficiency of laboratory specimen fabrication, by allowing the extraction of multiple test specimens per gyratory-compacted sample, and furthermore enables the testing of as-built pavement courses (Castorena et al., 2017; Lee et al., 2017).

Table 2.1. Production of the specimens: geometry of the test specimens.

Geometry	Dynamic modulus test *(D x H, mm)*	Fatigue test *(D x H, mm)*	Rutting test *(D x H, mm)*
Large	100 x 150	100 x 130	100 x 150
Small	38 x 110	38 x 110	-

The production of the specimens follows AASHTO PP 99 (2023) and AASHTO R 83 (2022) for small and large cylindrical specimens, respectively. The specimens can be laboratory-produced and extracted from the pavement (i.e., field cores).

For both laboratory and field specimens, the AV must be determined with the density calculated with the saturated surface dry (SSD) method (AASHTO T 166, 2022; EN 12697-6, 2020) for specimens with close surface or using automatic vacuum sealing method/sealed specimens in case of open surface (AASHTO T 331, 2021; EN 12697-6, 2020).

2.2.1 Laboratory specimens

Laboratory specimens are extracted from gyratory samples (AASHTO T 312, 2019; EN 12697-31, 2019). Gyratory samples are compacted at a target AV content and fixed geometry. The height is 180 mm, and the diameter is 150 mm.
AASHTO PP 99 (2023) proposes two methods for estimating the mass of required asphalt mixture, i.e., method A and B. In this PhD work, the following procedure was followed, which differs for few details from Method A. The target AV of the gyratory sample is based on the target AV of the test specimens. Specifically, the mass of asphalt mixture required to produce the test specimen (large or small), can be determined through repeat trial samples. Once known the maximum specific gravity of the mixture, the volume of the compacted gyratory samples and the target AV of the test specimens, the first tentative target mass of the gyratory sample corresponds to the AV of the test specimens + 3% (from experience or knowing the compactability of the mixture from previous studies). Three trial gyratory samples are compacted using this target mass and the other two at the target AV +2%. After one day of cooling, test specimens are cored and cut from each gyratory sample, and the AV of them is determined through saturated surface method for DG mixtures or automatic vacuum sealing for OG mixtures. The gyratory sample masses are plotted against the AV of the test specimens, obtaining a graph like the one shown in Figure 2.1. The data are fitted with a linear relationship, from which the mass of the gyratory sample corresponding to the target AV of the test specimens can be extrapolated.

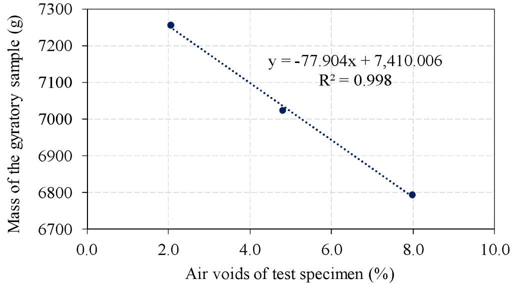

Figure 2.1. Production of laboratory specimens: example of relationship between mass of gyratory sample and AV of test specimens.

The mixture is heated at its compaction temperature, and the calculated mass of mixture is transferred into the mould (with diameter of 150 mm), which is heated at the same compaction of the mixture for at least 30 minutes, with a transfer funnel (e.g., a slump cone). In order to minimize air voids variation and ensure homogeneity of the mixture, the materials must be manually mixed before putting it into the mould. The mould must be filled in 2-3 equal lifts, and after each of them, the walls of the mould must be scraped with a long spatula. The spatula must be also inserted in the center of the mixture about 10 times, without damaging aggregates. The gyratory samples are compacted fixing the height of 180 mm and extracted from the mould.

After one day of cooling, the AV of the gyratory specimens can be determined in order to check the specimen density.

One large specimen can be vertically extracted from each gyratory sample, first coring in the center and then sawing both ends removing the same amount of material from each end (Figure 2.2a).

Conversely, four small specimens can be vertically extracted from each gyratory sample. The locations where the cores will be taken must be marked on the gyratory sample (even with a template, Figure 2.2c), within its 100-mm diameter center. Then, 35-mm thick materials must be sawed from each end (Figure 2.2b, Figure 2.3).

For both the geometry, extracting the specimens from the inner part of the gyratory sample aims to minimize the effects of the radial air void gradient (Lee et al., 2017), since higher AV content is in the most superficial volume of the sample.

Finally, the dimensional tolerance given by the reference AASHTOs regarding the average diameter and its standard deviations, height, end flatness and end perpendicularity must be checked. If such dimensional tolerances are not met, the specimen must be rejected.

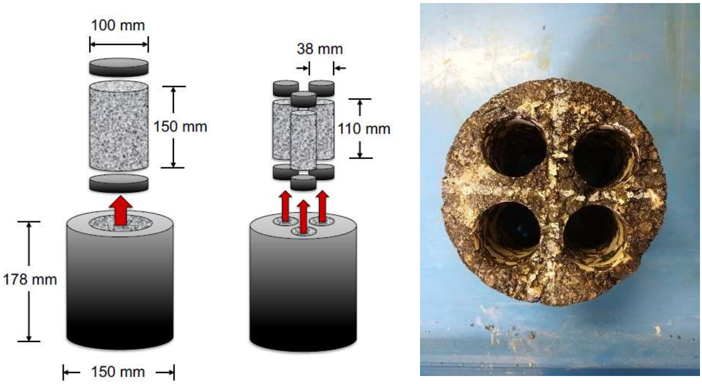

(a) **(b)** **(c)**

Figure 2.2. Production of laboratory specimens: extracted (a) small and (b) specimens coring small specimens from a gyratory sample (Lee et al., 2017), and (c) marked gyratory sample after extraction of small specimens.

Figure 2.3. Production of laboratory specimens: stages to core and cut small specimens.

2.2.2 Field cores

Large specimens must be vertically extracted from cores with the same (i.e., 100 mm) or higher diameter of the test specimen. Field cores must be cut at the interfaces between the courses, and the same amount of material must be sawed from each course end to obtain the test specimen.

For small specimens, the field cores must have a minimum diameter of 150-mm. The direction of the traffic must be marked on the surface before coring. If the traffic direction is not marked on the field core, the most probable direction of traffic can be evaluated and selected. Small specimens are cored horizontally from within the DG asphalt mixture courses of pavement that are at least 50 mm thick. Specimens must be cored perpendicularly to the traffic direction. The ends of the core are then trimmed to create a specimen with a recommended height of 110 mm (Figure 2.4).

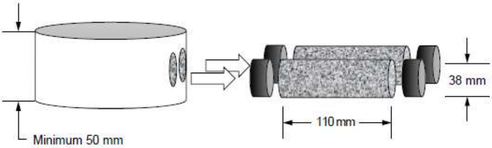

Figure 2.4. Production of field specimens: scheme of test specimens horizontally cored from the field course (AASHTO PP 99, 2023).

The dimensional tolerance given by the reference AASHTOs regarding the average diameter and its standard deviations, height, end flatness and end perpendicularity must be checked. If such dimensional tolerances are not met, the specimen must be rejected.

2.3 Determination of the viscoelastic properties through dynamic modulus tests

2.3.1 Description of the test

Dynamic modulus tests are conducted following AASHTO R 84 (2017) and AASHTO T 378 (2017) for large specimens, and AASHTO TP 132 (2023) for small specimens by means of an Asphalt Mixture Performance Tester (AMPT, Figure 2.5). In both the tests, asphalt specimens are subjected to frequency-sweep in axial compression loading, testing at various temperatures and frequencies. The suggested frequencies by the reference AASHTOs are 10 Hz, 1 Hz, 0.1 Hz, plus 0.01 Hz at the highest temperature for the large specimens. However, more frequencies can be tested between 20 Hz and 0.01 Hz, checking the reliability of the first frequency results. The testing temperatures are 4 °C and 20 °C and an additional temperature (the highest) based on the PG of the binder and the specimen geometry. For small specimens, the highest temperature is 35 °C and 40 °C for PG 58-XX and softer and for PG 64-XX and stiffer, respectively. For large specimens, the highest temperature is 35

°C, 40 °C and 45 °C, for PG with high temperature equal of lower than 58, between 64 and 70, equal or higher than 76.
At least three or two specimens for small and large geometry, respectively, with the target AV content ±0.5% should be tested. For the measurement of axial deformations during the tests, three vertical LVDTs are mounted on the middle part of the specimen 120° apart from each other. First, gauge points must be glued to the specimens, in order to set a gauge length of 70 mm ± 1 mm, measured in the center of the specimen. The gauge point fixing jig shown in Figure 2.6a can be used, and small specimen adapters are provided (Figure 2.6b).
After the specimen is conditioned at the test temperature (90 minutes or 4 hours for small and large specimens, respectively), the specimen is assembled with platens in the following order from bottom to top: bottom loading platen, test specimen centered with the bottom platen, top loading platen centered with the bottom platen with the steel ball on it. The so called "X-men" are mounted on the gauge points and three LVDTs are installed on them. The set-up of the specimen inside the climatic chamber of the AMPT in shown in Figure 2.7. The deformation-measuring system (i.e., LVDTs, stroke of the actuator) must be within its operating range and the top loading platen must be free to rotate during loading. The amplitude of the sinusoidal load is varied to maintain average strain levels of 75÷125 με for the large specimens, and 50÷75 με for small specimens. The norm of the dynamic modulus |*E**| and phase angle δ of each test specimen are measured, beginning to test at the lowest temperature and highest frequency. The software usually applies 10 cycles of conditioning followed by 10 cycles of the actual test.

Figure 2.5. AMPT Pro in the Transport and Road Research Laboratory in UnivPM (Italy).

(a) **(b)**

Figure 2.6. Dynamic modulus test: gauge point fixing jig for (a) large and (b) small specimens.

The data quality statistic requirements (Table 2.2) must be met in order to accept the test results. Some of the most common problems which causes not acceptable test results are reported in Table 2.3, and the reference AASHTOs provide even more problems with the corresponding solutions.

Table 2.2. Dynamic modulus test: data quality statistic requirements.

Data Quality Statistics	Limit
Deformation drift	In direction of applied load up 100% in the direction opposite of the applied load
Peak-to-peak strain	75÷125 με (large specimens), 50÷75 με (small specimens)
Load standard error	10%
Deformation standard error	10%
Deformation uniformity	30%
Phase uniformity	3°

Table 2.3. Dynamic modulus test: most common problem for low quality data.

Problem	Source
Non-sinusoidal stress	Poor PID tuning
Positive deformation drift	Gauge points are moving apart
Loss of contact between specimen and AMPT	Too low contact stress (especially at high temperatures)
Poor data quality (high deformation uniformity)	Unparallel specimen ends
Eccentric loading causing poor data quality (high deformation uniformity and/or phase angle)	Off-centered specimen against platen
High deformation uniformity	Poor LVDT placement

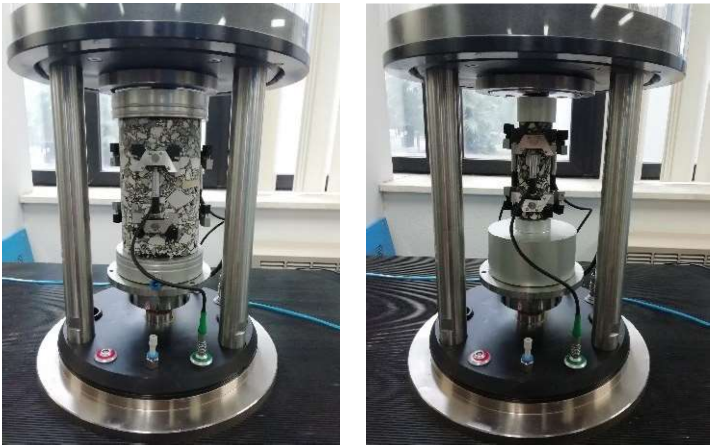
(a) **(b)**

Figure 2.7. Dynamic modulus test: set-up of (a) large and (b) small specimen.

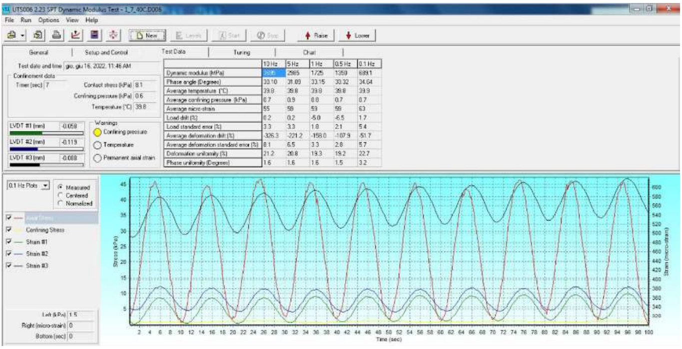

UTS006 2.23 SPT Dynamic Modulus Test - 1_7_40C.D006

Test date and time: gio, giu 16, 2022, 11:46 AM

Confinement data

Timer (sec): 7

Contact stress (kPa): 8.1

Confining pressure (kPa): 0.6

Temperature (°C): 39.8

LVDT #1 (mm): -0.058

LVDT #2 (mm): -0.119

LVDT #3 (mm): -0.088

● Confining pressure
○ Temperature
○ Permanent axial strain

	10 Hz	5 Hz	1 Hz	0.5 Hz	0.1 Hz
Dynamic modulus (MPa)	[illegible]	2985	1725	1350	689.1
Phase angle (Degrees)	30.10	31.09	33.15	33.32	34.64
Average temperature (°C)	39.8	39.8	39.8	39.8	39.9
Average confining pressure (kPa)	0.7	0.9	0.8	0.7	0.7
Average micro-strain	55	59	59	59	63
Load drift (%)	0.2	0.2	-5.0	-6.5	1.7
Load standard error (%)	3.3	3.3	1.8	2.1	5.4
Average deformation drift (%)	-326.3	-221.2	-158.0	-107.9	-51.7
Average deformation standard error (%)	8.1	6.5	3.3	2.8	5.7
Deformation uniformity (%)	21.2	20.8	19.3	19.2	22.7
Phase uniformity (Degrees)	1.6	1.6	1.6	1.5	3.2

Left (kPa): 1.5

Right (micro-strain): 0

Bottom (sec): 0

Figure 2.8. Dynamic modulus test: example of output from AMPT's software.

The experimental results from specimens of the same mixture must satisfy the *Single-Operator Precision (Repeatability)*, expressed by the coefficient of variation of the dynamic modulus $s_r\%$ (Equation (2.1.1)) and the standard deviation of the phase angle $s_r(°)$ (Equation (2.1.2)), which were found to be functions of the dynamic modulus of the mixture and the NMAS.

$$s_r\% = \left[29.8 \cdot e^{0.022 \cdot NMAS}\right] \cdot |E^*|^{-\left[0.189 \cdot e^{0.012 \cdot NMAS}\right]} \tag{2.1.1}$$

$$s_r(°) = \left[4.67 \cdot e^{0.022 \cdot NMAS}\right] \cdot |E^*|^{-0.23} \tag{2.1.2}$$

where E^* is the average dynamic modulus of the tested specimens.

Moreover, the maximum difference in percentage from the average E^* value and the maximum difference in degree from the average δ value for each specimen are limited. AASHTO T 378 (2017) provides tables for the limit of such repeatability parameters.

The *Multilaboratory Precision (Reproducibility)* is expressed by the coefficient of variation of the dynamic modulus $s_R\%$ (Equation (2.2.1)) and the standard deviation of the phase angle $s_R(°)$ (Equation (2.2.2)). It is used to check the reproducibility of the results on the same material tested by two different operators in two different laboratories. A table for the limit of such repeatability parameters is given by AASHTO T 378 (2017).

$$s_R\% = 223.81 \cdot |E^*|^{-0.312} \tag{2.2.1}$$
$$s_R(°) = 31.4 \cdot |E^*|^{-0.346} \tag{2.2.2}$$

The mastercurves of the storage modulus E_1 ($E_1 = |E^*| \cdot cos\ \delta$) and shift factors a_T are simultaneously determined through a nonlinear optimization scheme. The model is fitted on E_1 since its calculation is necessary for the subsequent analysis of the fatigue test results. The mastercurves of E_1 and a_T are determined by minimizing the error between the experimental data and results from the 2S2P1D model applied for the storage modulus. Equation (2.3) presents the 2S2P1D model by Olard & Di Benedetto (2003), which expresses the linear viscoelastic behavior of a mixture by a combination of two springs (2S), two parabolic elements (2P), and one dashpot (1D).

$$E_1(i\omega\tau) = E_{1,0} + \frac{E_{1,\infty} - E_{1,0}}{1+\xi(i\omega\tau)^{-k}+(i\omega\tau)^{-h}+(i\omega\beta\tau)^{-1}} \tag{2.3}$$

where $E_{1,0}$ and $E_{1,\infty}$ are the storage modulus values for pulsation $\omega = 2\pi \cdot frequency$ (rad/s) $\omega \to 0$ and $\omega \to \infty$, respectively, and describe the behavior of the springs; k and h describe the behavior of the parabolic elements; ξ is a proportional constant between the parabolic elements; and β is linked to the Newtonian viscosity of the dashpot.

The time-temperature shift factors a_T are calculated as follows (Equation (2.4)):

$$log(a_T) = a_1 \cdot T^2 + a_2 \cdot T + a_3 \tag{2.4}$$

where a_1, a_2 and a_3 are fitting coefficients, and T is the testing temperature.

2.3.2 The 2S2P1D model

The development and step-by step improvements which led to the 2S2P1D model are described in Olard & Di Benedetto (2003), and in this section the main aspects are reported with an additional focus on the meaning of the model.

The first fundamental concept is that any combination of springs and linear dashpot constitutes an analogical linear viscoelastic model. The spring represents the elastic element, and the dashpot represents the Newtonian viscous element, as shown in Figure 2.9a. The well-known simple Maxwell and Kelvin-Voigt models are a combination of these two

elements in parallel (viscoelastic liquid) and in series (viscoelastic solid), respectively (Figure 2.9b), and they are the base of more complex associations. Models with *n* Maxwell models in parallel or *n* Kelvin-Voigt models in series, with the possibility to add one spring and one dashpot in parallel/series (Figure 2.9c), are called generalized Maxwell and generalized Kelvin Voigt models, respectively. Such models can efficiently describe the behavior of bituminous materials (bitumen or mixture) as *n* increases (at least *n* = 8).
Models with a finite number of *n* element are defined "with discrete spectrum", whereas models with infinite number of *n* are defined "with continuous spectrum" and they are always appropriate to describe the bituminous behavior.
The different models that have a continuous spectrum can be classified in two categories: analytical and analogical ("advanced"). For the analytical models, mathematical formulations are used to fit experimental data. Some examples are the CA (Christensen-Anderson, (Christensen & Anderson, 1992)) and the generalized CAM (Christensen-Anderson-Marasteanu, (Zeng et al., 2002)) models. Conversely, the "advanced" analogical models with continuous spectrum (i.e. can be represented by an infinite number of Kelvin-Voigt elements in series or Maxwell elements in parallel) have a physical meaning and representation. For this reason, analogical models are usually considered as more pertinent than the models in which empirical mathematical formulas are used to fit experimental data (Olard & Di Benedetto, 2003).

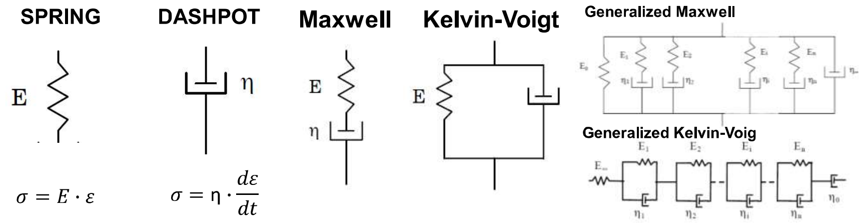

(a) **(b)** **(c)**

Figure 2.9. Dynamic modulus test: (a) spring and dashpot representation and constitutive equations, (b) Maxwell and Kelvin Voigt models, (c) generalized Maxwell and Kelvin Voigt models.

The parabolic element
The 2S2P1D model belongs to the "advanced" analogical models, since the spring, dashpot and parabolic elements, which have a physical meaning and representation, are used.
However, differently form springs and dashpot whose behavior and formulations are simple and easy to understand (Figure 2.9a), the parabolic element is a more complex element and less intuitive one. The parabolic element is also called Fractional Derivative Element (FDE), and it is an analogical model (Olard & Di Benedetto, 2003).
Huet (1963) first introduced the mathematical element "α^{th} fractional derivative of a function $f(t)$" of the time t as (Equation 2.5.1) (Ouis, 2003):

$$\frac{d^\alpha}{dt^\alpha} f(t) = \frac{1}{\Gamma(1-\alpha)} \frac{d}{dt} \int_0^t \frac{f(\tau)}{(t-\tau)^\alpha} d\tau \tag{2.5.1}$$

where $0 < \alpha < 1, \Gamma$ is the gamma function $\Gamma(n) = \int_0^\infty t^{n-1} e^{-t} dt \;\; (n > 0)$

It should be noted that a differentiation of an order α^{th}, in which α has a (positive) non-integer value, has no physical and mathematical meaning. Nevertheless, it is allowed to define an arbitrarily operator for certain signals (Pronk, 2003).

Equation (2.5.1) becomes Equation (2.5.2), since the fractional derivative is only allowed and defined for sinusoidal signals, implicating that the load/stress signal is a sinusoidal signal (Pronk, 2003).

$$\sigma = \eta \cdot \tau^{\alpha-1} \frac{d^{\alpha}\varepsilon(t)}{dt^{\alpha}} \; with\, 0 < \alpha < 1 \tag{2.5.2}$$

where η is the Newtonian viscosity, τ that is the characteristic time (or relaxation time) with varies only with temperature that accounts for the Time-Temperature Superposition Principle (t-TSP), t is time and ε is the deformation.

The characteristic time τ is defined as (Equation (2.5.3)):

$$\tau(T) = a_T(T) \cdot \tau_0 \tag{2.5.3}$$

where $a_T(T)$ is the shift factor at the temperature T (Equation (2.4)) and τ_0 is $\tau(T_{ref})$ determined at the reference temperature T_{ref}.

Replacing the sinusoidal signal $\sigma = \sigma_0 \cdot e^{i\omega t}$ in Equation (2.5.2), Equation (2.5.4) is obtained (Pronk, 2003):

$$\sigma = \eta \cdot \tau^{\alpha-1}(i\omega)^{\alpha}\varepsilon = \frac{\eta}{\tau}(i\omega\tau)^{\alpha}\varepsilon \leftrightarrow \sigma = \frac{\eta}{\tau}(\omega\tau)^{\alpha} \cdot e^{+i\frac{\pi}{2}\alpha} \cdot \varepsilon \tag{2.5.4}$$

Reporting the words of Pronk, "the *beauty* of Equation (2.5.4) is that it describes the response of a rheological element changing from a linear spring ($\alpha = 0$) with modulus $E^* = \frac{\eta}{\tau}$ and argument $\varphi = 0$ to a linear dashpot ($\alpha = 1$) with a modulus of $E^* = (\omega\tau)\frac{\eta}{\tau}$ and argument $\delta = +\frac{\pi}{2}$ ". For $0 < \alpha < 1$, the modulus is $E^* = \frac{\eta}{\tau}(\omega\tau)^{\alpha}$ and the argument is $\delta = +\frac{\pi}{2}\alpha$. This concept is graphically explained in Figure 2.9a. Even the creep stiffness, resulting in a parabolic function (Equation (2.5.5)), is intermediate between elastic and viscous behavior (i.e., parabolic). Consequently, the stiffness dynamic modulus is expressed by Equation (2.5.6).

$$J(t) = a\left(\frac{t}{\tau}\right)^{\alpha} \tag{2.5.5}$$

$$E^*(i\omega\tau) = \frac{\eta(i\omega\tau)^{\alpha}}{\tau} \tag{2.5.6}$$

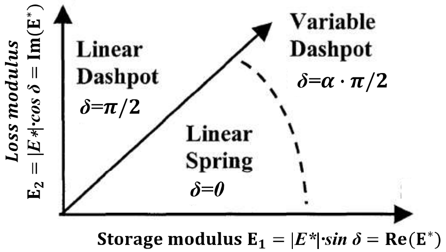

Figure 2.10. Dynamic modulus test: the response of the parabolic element (Pronk, 2003).

Huet model (1963)
The first "advance" analogical model was the Huet model (Huet, 1963), propose for binders, composed by a spring and two parabolic elements in series. It has a continuous spectrum. The physical representation with the constitutive equations of the elements and the corresponding equilibrium and compatibility equations, is shown in Figure 2.11.

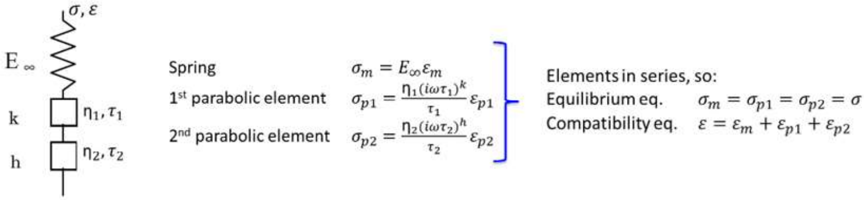

Figure 2.11. Dynamic modulus test: Huet model and formulations.

Replacing the constitutive equations of the elements in the compatibility equation, considering the equivalency given by the equilibrium equation (Figure 2.11), it can be obtained Equation (2.6.1). From this latter one, Equation (2.6.2) can be easily deduced.

$$\varepsilon = \frac{\sigma}{E_\infty} + \frac{\sigma\tau_1}{\eta_1 (i\omega\tau_1)^k} + \frac{\sigma\tau_2}{\eta_2 (i\omega\tau_2)^h} = \left[\frac{1}{E_\infty} + \frac{\tau_1}{\eta_1 (i\omega\tau_1)^k} + \frac{\tau_2}{\eta_2 (i\omega\tau_2)^h}\right]\sigma = \\ = \left[\frac{1}{E_\infty}\left(1 + \frac{\tau_1 E_\infty}{\eta_1 (i\omega\tau_1)^k} + \frac{\tau_2 E_\infty}{\eta_2 (i\omega\tau_2)^h}\right)\right]\sigma \tag{2.6.1}$$

$$\sigma = \varepsilon\left[\frac{1}{E_\infty}\left(1 + \frac{\tau_1 E_\infty}{\eta_1 (i\omega\tau_1)^k} + \frac{\tau_2 E_\infty}{\eta_2 (i\omega\tau_2)^h}\right)\right]^{-1} = \varepsilon\left[\frac{E_\infty}{1 + \frac{E_\infty \cdot \tau_1}{\eta_1 \cdot (i\omega\tau_1)^k} + \frac{E_\infty \cdot \tau_2}{\eta_2 \cdot (i\omega\tau_2)^h}}\right] \tag{2.6.2}$$

where $\eta_1 = \frac{E_\infty \tau_1}{\xi_1}$ and $\eta_2 = \frac{E_\infty \tau_2}{\xi_2}$, with τ that is the characteristic time, and ξ_1, ξ_2 that are model constants (Pronk, 2003, 2005).

It is worth assuming that the material has the same characteristic time $\tau_1 = \tau_2 = \tau$, and put $\xi_1 = 1, \xi_2 = \xi$ (dimensionless constant) (Pronk, 2003, 2005). Consequently, the formulation of Huet model is expressed by Equation (2.6.3), and the dynamic modulus is expressed by the familiar Equation (2.6.4).

$$\sigma = \varepsilon \left[\frac{E_\infty}{1+\xi(i\omega\tau)^{-k}+(i\omega\tau)^{-h}}\right] \tag{2.6.3}$$

$$E^*(\omega) = \frac{E_\infty}{1+\xi(i\omega\tau)^{-k}+(i\omega\tau)^{-h}} \tag{2.6.4}$$

where E_∞ is the limit of dynamic modulus (glassy modulus) when $\omega\tau \rightarrow \infty$. In Cole-Cole diagrams (i.e., loss modulus $E_2 = |E^*|\cdot \sin\delta$ vs. storage modulus $E_1 = |E^*|\cdot \cos\delta$), h and k are the slope of the tangent $\Delta E_2/\Delta E_1$ when $\omega\tau \rightarrow 0$ and when $\omega\tau \rightarrow \infty$, respectively.

It was experimentally found that $1 > h > k > 0$ for binders and asphalt mixtures, since the bituminous materials are more viscous at low temperatures (higher E_2) and more elastic at high temperatures (higher E_1).

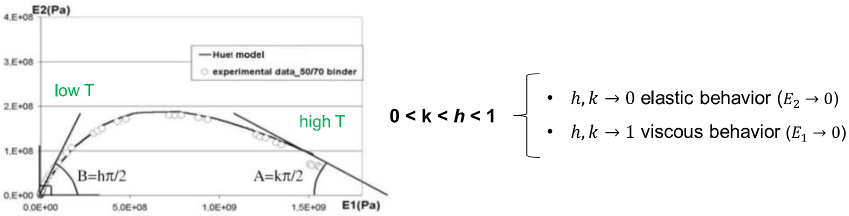

$0 < k < h < 1$

- $h, k \rightarrow 0$ elastic behavior ($E_2 \rightarrow 0$)
- $h, k \rightarrow 1$ viscous behavior ($E_1 \rightarrow 0$)

Figure 2.12. Dynamic modulus test: meaning of *h* and *k* of the parabolic elements in Huet model.

Huet-Sayegh model

The Huet-Sayegh model was developed based on the Huet model to characterize the asphalt mixture. A spring in parallel was added by Sayegh, in order to model the stiffness at very low frequencies due to the aggregate skeleton. It has a continuous spectrum. The physical representation with the constitutive equations of the elements and the corresponding equilibrium and compatibility equations, is shown in Figure 2.13.

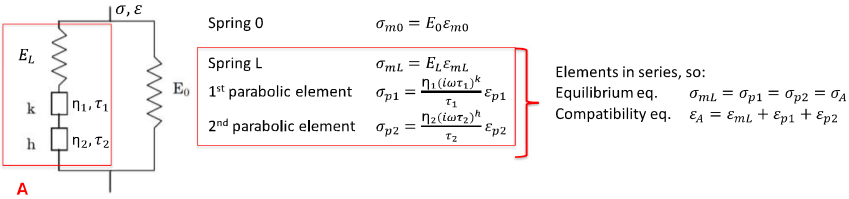

Spring 0 $\sigma_{m0} = E_0\varepsilon_{m0}$

Spring L $\sigma_{mL} = E_L\varepsilon_{mL}$

1st parabolic element $\sigma_{p1} = \frac{\eta_1(i\omega\tau_1)^k}{\tau_1}\varepsilon_{p1}$

2nd parabolic element $\sigma_{p2} = \frac{\eta_2(i\omega\tau_2)^h}{\tau_2}\varepsilon_{p2}$

Elements in series, so:

Equilibrium eq. $\sigma_{mL} = \sigma_{p1} = \sigma_{p2} = \sigma_A$

Compatibility eq. $\varepsilon_A = \varepsilon_{mL} + \varepsilon_{p1} + \varepsilon_{p2}$

Figure 2.13. Dynamic modulus test: Huet model and formulations (part A).

Analogously to the calculations for Huet model, replacing the constitutive equations of the three elements in series (1 spring plus 2 dashpots, called "A part") in the compatibility equation and considering the equivalency given by the equilibrium equation (Figure 2.13), it can be obtained Equation (2.7.1). From this latter one, Equation (2.7.2) can be easily deduced.

$$\begin{aligned}\varepsilon_A &= \frac{\sigma_A}{E_L} + \frac{\sigma_A \tau_1}{\eta_1 (i\omega\tau_1)^k} + \frac{\sigma_A \tau_2}{\eta_2 (i\omega\tau_2)^h} = \left[\frac{1}{E_L} + \frac{\tau_1}{\eta_1 (i\omega\tau_1)^k} + \frac{\tau_2}{\eta_2 (i\omega\tau_2)^h}\right] \sigma_A = \\ &= \left[\frac{1}{E_L}\left(1 + \frac{\tau_1 E_L}{\eta_1 (i\omega\tau_1)^k} + \frac{\tau_2 E_L}{\eta_2 (i\omega\tau_2)^h}\right)\right] \sigma_A\end{aligned} \tag{2.7.1}$$

$$\sigma_A = \varepsilon_A \left[\frac{1}{E_L}\left(1 + \frac{\tau_1 E_L}{\eta_1 (i\omega\tau_1)^k} + \frac{\tau_2 E_L}{\eta_2 (i\omega\tau_2)^h}\right)\right]^{-1} = \varepsilon_A \left[\frac{E_L}{1+\frac{E_L \cdot \tau_1}{\eta_1 \cdot (i\omega\tau_1)^k}+\frac{E_L \cdot \tau_2}{\eta_2 \cdot (i\omega\tau_2)^h}}\right] \tag{2.7.2}$$

Then Equation (2.7.2) is used into the equilibrium equation (Figure 2.14), as explicated in Equation (2.7.3). In this latter, the compatibility equation (Figure 2.14) is used to finally obtain Equation (2.7.4).

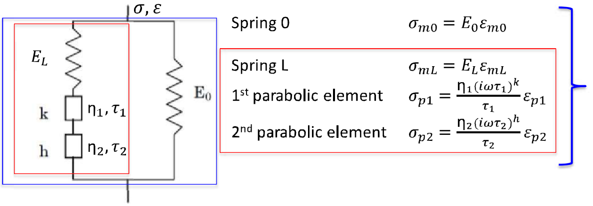

Figure 2.14. Dynamic modulus test: Huet model and formulations (part B).

$$\sigma = \sigma_A + \sigma_{m0} = \varepsilon_A \left[\frac{E_L}{1+\frac{E_L \cdot \tau_1}{\eta_1 \cdot (i\omega\tau_1)^k}+\frac{E_L \cdot \tau_2}{\eta_2 \cdot (i\omega\tau_2)^h}}\right] + E_0 \varepsilon_{m0} \tag{2.7.3}$$

$$\sigma = \varepsilon \left[\frac{E_L}{1+\frac{E_L \cdot \tau_1}{\eta_1 \cdot (i\omega\tau_1)^k}+\frac{E_L \cdot \tau_2}{\eta_2 \cdot (i\omega\tau_2)^h}} + E_0\right] \tag{2.7.4}$$

As for Huet model, it is worth assuming $\tau_1 = \tau_2 = \tau$, and put $\xi_1 = 1, \xi_2 = \xi$ (dimensionless constant into the definition of the Newtonian viscosity η_1, η_2). Moreover, in order that the response when $\omega\tau \to \infty$ is E_∞ as in Huet model, $E_L = E_\infty - E_0$. Consequently, the formulation of Huet-Sayegh model is expressed by Equation (2.7.5) and the dynamic modulus is expressed by the familiar Equation (2.7.6).

$$\sigma = \varepsilon \left[E_0 + \frac{E_\infty - E_0}{1+\xi (i\omega\tau)^{-k} + (i\omega\tau)^{-h}}\right] \tag{2.7.5}$$

$$E^*(\omega) = E_0 + \frac{E_\infty - E_0}{1+\xi (i\omega\tau)^{-k} + (i\omega\tau)^{-h}} \tag{2.7.6}$$

where E_∞ is the limit of dynamic modulus (glassy modulus) when $\omega\tau \to \infty$, and E_0 is the limit of dynamic modulus (equilibrium modulus due to the aggregate skeleton, absent in Huet model) when $\omega\tau \to 0$. The meaning of h and k are the same as in Huet model.

However, it was found out that Huet-Sayegh model (as Huet model) is not suitable for binders at very low frequencies, where the response is equivalent to a parabolic element instead of a linear dashpot, as shown in Figure 2.15. In this figure, the slope has *1:h* value, whereas the experimental data follows a *1:1* value.

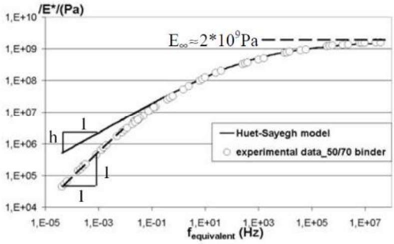

Figure 2.15. Dynamic modulus test: comparison between experimental data and Huet-Sayegh model (focus on the slope at low frequencies) (Olard & Di Benedetto, 2003).

2S2P1D model

To avoid the drawbacks regarding the behavior at low frequencies (Figure 2.15), Olard & Di Benedetto proposed a generalized Huet-Sayegh model, named 2S2P1D, adding a linear dashpot in series with the two parabolic elements and the spring of stiffness $E_\infty - E_0$. This model has a continuous spectrum, and it is suitable for both binders and mixtures. In particular for binders, for which $E_0 = 0$, the model is equivalent to a linear dashpot at very low frequencies.

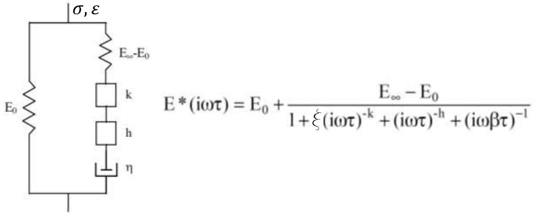

$$E^*(i\omega\tau) = E_0 + \frac{E_\infty - E_0}{1+\xi(i\omega\tau)^{-k} + (i\omega\tau)^{-h} + (i\omega\beta\tau)^{-1}}$$

Figure 2.16. Dynamic modulus test: 2S2P1D model, representation and formulation.

The mathematical steps are the same for Heut and Huet-Sayegh models, adding the expression of the dashpot $(i\beta\omega\tau)^{-1}$ deriving from the Equation (2.5.6), where η=$(E_\infty - E_0)\beta\tau$ with β dimensionless constant. When $\omega\tau \rightarrow 0$, $E^*(\omega) \rightarrow E_0 + i\omega(E_\infty - E_0)\beta\tau$. So, for β → ∞, 2S2P1D model is equivalent to Huet-Sayegh model. The model is based on only 7 constants $(\xi, k, h, E_\infty, E_0, \beta, \tau_0)$, plus the constant needed for the determination of the characteristic time τ_0. For binders, $E_0 = 0$. Figure 2.17 finally resume the physical meaning of all such parameter in Cole-Cola diagram.

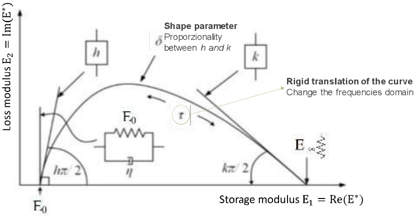

Figure 2.17. Dynamic modulus test: meaning of the parameter of 2S2P1D model in Cole-Cole.

2.4 The ViscoElastic Continuum Damage approach to characterize the fatigue behavior

2.4.1 Description of the test

The S-VECD model is a material model that describes changes in the constitutive relationship as fatigue damage grows and characterizes the fundamental material properties that are independent of temperature, mode of loading (i.e., control strain, control stress, and monotonic loading), and loading amplitude (Chehab et al., 2003; Daniel et al., 2002; Y. R. Kim & Little, 1990; Y. D. Wang et al., 2018). The S-VECD model has been developed based on the experimental data obtained from cyclic fatigue test carried out with the AMPT.

Cyclic fatigue tests are conducted using small specimens for dense-graded mixtures with NMAS equal or lower than 19 mm in accordance with AASHTO T 411 (2023) and on large specimens in accordance with AASHTO T 400 (2023) for mixtures with NMAS up to 25 mm, by means of the AMPT.

The specimen must be carefully prepared for fatigue tests, paying particular attention to each stage in order to obtain a valid test, especially for the small specimen geometry. First gauge points must be glued to the specimen, as for dynamic modulus tests (Figure 2.6) in order to set a gauge length of 70 mm ± 1 mm approximately 120° apart, measured in the center of the specimen. Then, the ends of the specimens must be cleaned with a towel slightly moist with acetone. The end plates, too, must be cleaned with towel and acetone. An epoxy that ensures high tensile resistance is used to glue the specimen to the end plates. AASHTO T 411 suggests the use of Devcon 10240 Plastic Steel 5 Minute Putty, which has been successfully used in this PhD work for small specimens. AASHTO T 400 suggests the use of Devcon 10110 for large specimens, whereas the epoxy Fischer 390 S was successfully used in this PhD work. Once the epoxy is properly mixed, it is spread on the end specimens and on the end plates filling the grooves (Figure 2.18a). The bottom plate is placed in the ad-hoc gluing jig and the end plate is placed on the top thanks to a magnet. The specimen is placed on the bottom plate and the top plate is lowered (Figure 2.18b-c).

The specimen must be centered and positioned perpendicularly, since any eccentricity in loading leads to a wrong crack propagation in the specimen (since not only tensile stresses are applied but also compression ones), so an invalid test. Indeed, this is the most crucial step in the preparation of the specimen. For the time the glue gets hard, the specimen cannot be moved. After this time, the specimen is conditioned at the test temperature. Then, the specimen is inserted into the AMPT, and the lower loading plate is tighten. The actuator is brough into position and applies a seating load of 0.01 kN. The top loading plate is loosely attached to the AMPT. The maximum gap between the loading plate and the AMPT must be checked and, if present, shims must be placed (Figure 2.19). Bolts are tightened, turning 1/3 of a complete turn one bolt and then the other, so that any tensile stress is applied. The specimen is now secure to the AMPT. The command load to 0.0 kN is set. Three LVDTs are mounted on the X-men on the gauge points, and the stroke of each LVDT is adjusted to be centered within the operating range. The final set-up of large and small specimens is shown in Figure 2.20a-b, respectively. The testing chamber is closed and, after the testing temperature is newly reached and stabilized, the test can start.

Figure 2.18. Cyclic fatigue test: glue spread on the end specimens and on the end platens, (a) large and (b) small specimens into the gluing jig.

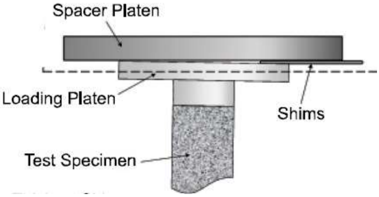

Figure 2.19. Cyclic fatigue test: positioning of the shims.

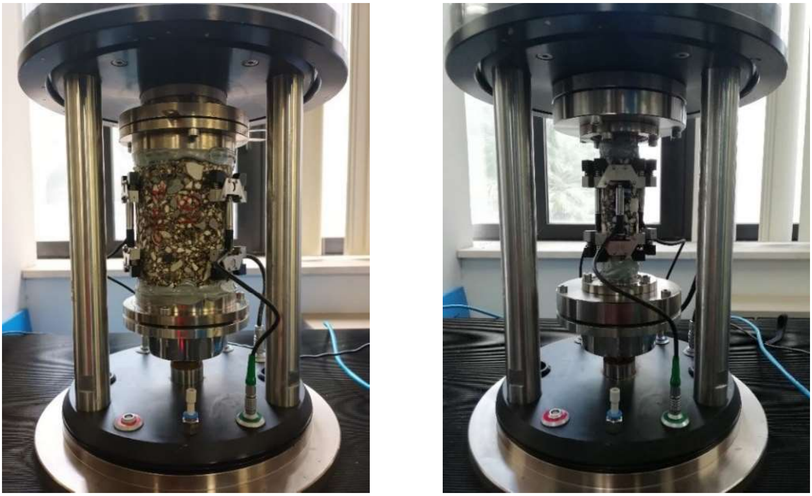

Figure 2.20. Cyclic fatigue test: set-up of (a) large and (b) small specimens in the AMPT.

The test temperature for highly modified bitumen shall be 18 °C. For all the other mixtures, the reference ASSHTOs provide the test temperature based on the PG binder grade (Figure 2.21), which should not be higher than 21 °C. Specifically, Figure 2.21a is used for PG binder grades developed using AASHTO M 320 (2023), or PG grades designated as "S" in AASHTO M 332 (2023). Figure 2.21b is used for PG grades designated as "H", "V", or "E", in AASHTO M 332 (2023). If the mixture is produced with recycled material, the PG grade of the virgin binder should be used.

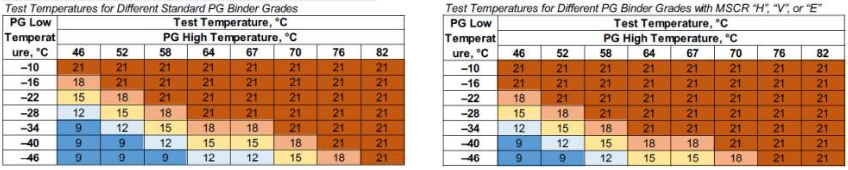

Test Temperatures for Different Standard PG Binder Grades

PG Low Temperature, °C	Test Temperature, °C							
	PG High Temperature, °C							
	46	52	58	64	67	70	76	82
–10	21	21	21	21	21	21	21	21
–16	18	21	21	21	21	21	21	21
–22	15	18	21	21	21	21	21	21
–28	12	15	18	21	21	21	21	21
–34	9	12	15	18	18	21	21	21
–40	9	9	12	15	15	18	21	21
–46	9	9	9	12	12	15	18	21

(a)

Test Temperatures for Different PG Binder Grades with MSCR "H", "V", or "E"

PG Low Temperature, °C	Test Temperature, °C							
	PG High Temperature, °C							
	46	52	58	64	67	70	76	82
–10	21	21	21	21	21	21	21	21
–16	21	21	21	21	21	21	21	21
–22	18	21	21	21	21	21	21	21
–28	15	18	21	21	21	21	21	21
–34	12	15	18	21	21	21	21	21
–40	9	12	15	18	18	21	21	21
–46	9	9	12	15	15	18	21	21

(b)

Figure 2.21. Cyclic fatigue test: test temperature.

Prior to fatigue testing, a dynamic modulus fingerprint test is performed to analyze the specimen-to-specimen variability and calibrate the strain level needed for the fatigue tests. The fingerprint test consists in applying 55 cycles of a sinusoidal tension-compression axial load adjusted to achieve a target peak-to-peak on-specimen strain amplitude between 50 με to 75 με at the target test temperature of the fatigue and at the frequency of 10 Hz. The data quality statistics requirements for fingerprint test are indicated in Table 2.4. If such requirements are not met, the specimen must be discarded.

Table 2.4. Cyclic fatigue test: data quality statistic requirements for fingerprint test.

Indicator	Limit
Standard error of the applied stress	10%
Average standard error of the measured strains	10%
Uniformity coefficient of the measured strains	35%
Uniformity coefficient of the phase angle measurements	3°

The ratio of the fingerprint modulus value $|E^*|_{fingerprint}$ to the reference modulus value that is derived from the mastercurve $|E^*|_{LVE}$ is referred to as the dynamic modulus ratio (*DMR,* Equation (2.8)), and its value should be within the range of 0.85 to 1.15 for each specimen to limit specimen-to-specimen variability.

$$DMR = \frac{|E^*|_{fingerprint}}{|E^*|_{LVE}} \tag{2.8}$$

After a rest period of five minutes, direct tension cyclic fatigue tests are conducted at the frequency of 10 Hz in actuator displacement control mode of loading. The peak-to-peak on-specimen amplitude of the sinusoidal strain is selected based on the materials in order to obtain a test duration between 2000 and 80000 cycles. The input peak-to-peak microstrain value depends on the type of mixture and on its stiffness. A table is provided by the reference

AASHTOs, indicating the strain level and the range within it can vary to obtain tests of different duration. However, such values have not been demonstrated proper for the mixtures investigated in this PhD work. For this reason, Appendix B reports all the adopted input strains of all the valid tests. Specifically, the fatigue tests are performed by maintaining a constant amplitude of the actuator displacement (i.e., constant crosshead mode). Compared to strain-controlled tests, crosshead-controlled tests are easier to run and reduce the risk of damaging the equipment if improperly performed (B. S. Underwood et al., 2010). The applied sinusoidal axial load is adjusted to keep the actuator displacement amplitude constant throughout the test. Even though the on-specimen strain remains tensile, both tensile and compressive stresses are applied on the specimen due to viscous effects. The actual on-specimen strain is lower than the actuator strain level due to inevitable machine compliance issues (Chehab et al., 2003). During the test, the software shows the trend of dynamic modulus and phase angle (Figure 2.22a), as well as the increasing trend of the strain recorded by the LVDTs (Figure 2.22b). The test is automatically stopped by the software when the machine is no longer able to apply a well-shaped sinusoidal load.

At the end of the test, a so-called "middle failure" must be obtained, i.e., the specimen failure in which the macrocrack develops within the range of all axial deformation sensors (Figure 2.23a). If end-failure (Figure 2.23b) occurs, i.e. the specimen failure outside the range of one or more axial deformation sensors, the test must be discarded. The failure surface should be in the binder, without broken aggregate.

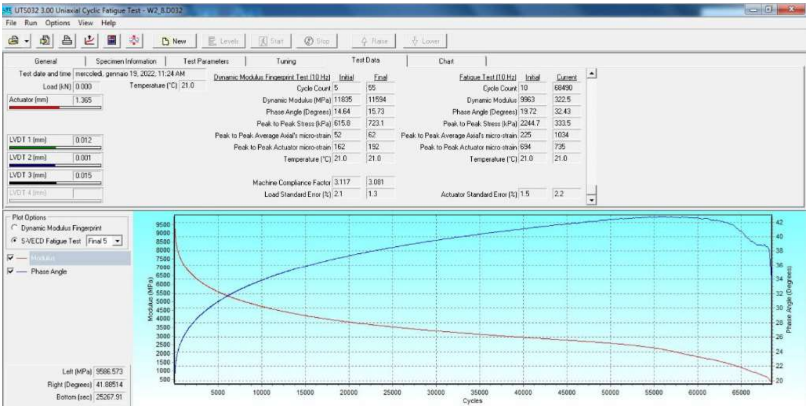

Test date and time: mercoledì, gennaio 19, 2022, 11:24 AM
Load (kN): 0.000
Temperature (°C): 21.0
Actuator (mm): 1.365
LVDT 1 (mm): 0.012
LVDT 2 (mm): 0.001
LVDT 3 (mm): 0.015
LVDT 4 (mm):

Dynamic Modulus Fingerprint Test (10 Hz)	Initial	Final
Cycle Count	5	55
Dynamic Modulus (MPa)	11835	11594
Phase Angle (Degrees)	14.64	15.73
Peak to Peak Stress (kPa)	615.8	723.1
Peak to Peak Average Axial's micro-strain	52	62
Peak to Peak Actuator micro-strain	162	192
Temperature (°C)	21.0	21.0
Machine Compliance Factor	3.117	3.081
Load Standard Error (%)	2.1	1.3

Fatigue Test (10 Hz)	Initial	Current
Cycle Count	10	68490
Dynamic Modulus	9963	322.5
Phase Angle (Degrees)	19.72	32.43
Peak to Peak Stress (kPa)	2244.7	333.5
Peak to Peak Average Axial's micro-strain	225	1034
Peak to Peak Actuator micro-strain	694	735
Temperature (°C)	21.0	21.0
Actuator Standard Error (%)	1.5	2.2

● S-VECD Fatigue Test: Final 5
Left (MPa): 9586.573
Right (Degrees): 41.88514
Bottom (sec): 25267.91

(a)

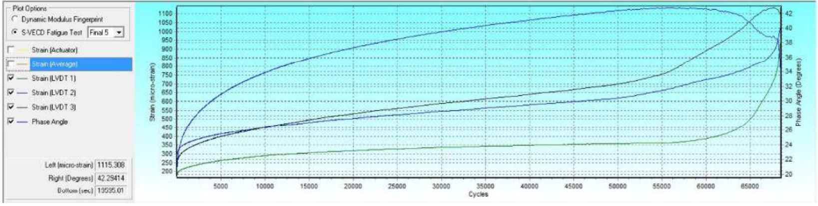

● S-VECD Fatigue Test: Final 5
Left (micro-strain): 1115.308
Right (Degrees): 42.29414
Bottom (sec): 13595.01

(b)

Figure 2.22. Cyclic fatigue test: output examples from AMPT's software.

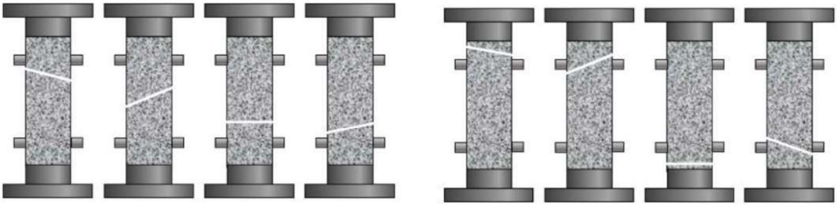

Figure 2.23. Cyclic fatigue test: examples of (a) middle and (b) end failures (AASHTO T 411, 2023).

2.4.2 The S-VECD model

The Simplified-ViscoElastic Continuum Damage (S-VECD) model is an approach that allows the fatigue performance of a mixture to be characterized based on the results of dynamic modulus tests and uniaxial cyclic fatigue tests (B. Underwood et al., 2012).
VECD theory is built on three fundamental concepts: the elastic–viscoelastic correspondence principle, continuum damage mechanics, and the time-temperature superposition principle with growing damage.

The elastic-viscoelastic correspondence principle
The response of an elastic material is only dependent on the current input. Conversely, linear viscoelastic (LVE) materials exhibit time- and temperature-dependent behavior. It means that the current response is dependent on the input history (i.e., the sum of the current input and all past input. Constitutive relationships for LVE materials are typically expressed in the convolution integral form, as shown in Equations (2.9) and (2.10):

$$\sigma = \int_0^t E(t-\tau)\frac{d\varepsilon}{d\tau}d\tau \tag{2.9}$$
$$\varepsilon = \int_0^t D(t-\tau)\frac{d\sigma}{d\tau}d\tau \tag{2.10}$$

where $E(t)$ and $D(t)$ are the relaxation modulus and creep compliance, respectively (τ term is the integration variable).

The elastic–viscoelastic correspondence principle is based on the pseudo-strain concept, which allows to reduce the viscoelastic behavior of the material into the corresponding elastic behavior (Schapery, 1984, 1987).
In short, this principle states that viscoelastic problems can be solved with elastic solutions when physical strains are replaced by pseudo strains (B. S. Underwood, 2006):

$$\varepsilon^R = \frac{1}{E_R}\int_0^t E(t-\tau)\frac{d\varepsilon}{d\tau}d\tau \tag{2.11}$$

where E_R is a particular reference modulus, typically taken as one.

Using pseudo strain in place of physical strain, the constitutive relationship presented in Equation (2.9) can be rewritten as:

$$\sigma = E_R \varepsilon^R \tag{2.12}$$

The viscoelastic solution of a problem can be obtained from an elastic solution of the same problem by working in a Laplace transformed domain with the substitution of E and ν with Carson transformed E and ν. Indeed, pseudo strains are simply the linear viscoelastic stress response to a particular strain input. The most important effect of pseudo strains is seen when plotting with stress, because any time effects are removed from the resulting graph.

In a cyclic fatigue test, the total dissipated energy is the sum of the dissipated energy due to viscous damping and the dissipated energy due to damage growth. When pseudostrain are considered, the dissipated energy due to viscous damping is deleted, and the area of the hysteresis loop includes only the dissipated energy due to damage growth. An example of hysteresis loops is reported in Figure 2.24. As a consequence of the introduction of the pseudostrain, the pseudostiffness C^R is defined as (Equation (2.13)):

$$C^R = \sigma / \varepsilon^R \tag{2.13}$$

During cyclic loading, the pseudostiffness (i.e., the slope of the loop) decreases and the enclosed area of the hysteresis loop increases due only to the actual damage in the material.

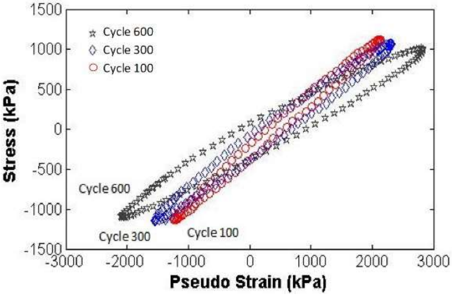

Figure 2.24. Cyclic fatigue test: hysteresis loops using pseudostrain (R. Y. Kim et al., 2022).

Continuum damage mechanics

Continuum damage mechanics considers a damaged body with some stiffness as an undamaged body with a reduced stiffness (Figure 2.25). Continuum damage theories thus attempt to quantify two values, damage and effective stiffness (B. S. Underwood, 2006).

The material can be considered as a continuous and homogeneous body because the effects of microcracks are modeled via internal state variables (Schapery, 1984). Specific microscale behaviors are ignored and, instead, a material is characterized using macroscale observations, i.e., the net effect of microstructural changes on observable properties The most convenient method to assess the effective stiffness, in the macro sense, is the instantaneous secant modulus. Damage, on the other hand, is oftentimes more difficult to quantify and generally relies on macroscale measurements combined with rigorous theoretical considerations. Schapery’s work potential theory (1987), based on thermodynamic principles, is appropriate for the purpose of quantifying damage. Within Schapery’s theory (1987), damage is quantified by an internal state variable S that accounts for microstructural changes in the material. The definition of the damage S is given in Equation (2.14).

$$S = \left(\frac{\partial W^R}{\partial S}\right)^{\alpha} \tag{2.14}$$

where W^R is the pseudostrain energy (i.e., area of the hysteresis loop considering the pseudostrain) and α is the damage evolution rate, corresponding to the slope of the relaxation modulus master curve. α can be calculated as $\alpha = \frac{1}{m} + 1$, where m is the log-log slope of the 2S2P1D mastercurve of $E'(\omega_R)$.

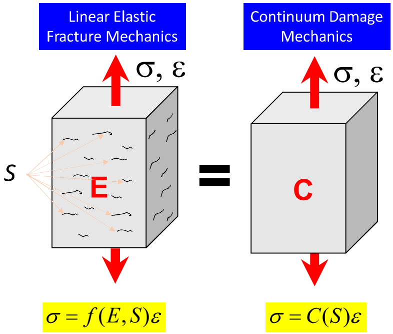

Figure 2.25. Cyclic fatigue test: continuum damage mechanics.

Time-temperature superposition principle with growing damage

Superposition is known to apply to linear viscoelastic behavior and greatly reduces characterization requirements. It was experimentally demonstrated that the principle applies even to mixtures at highly damaged states (Chehab et al., 2003; Zhao & Kim, 2003). The time-temperature superposition principle with growing damage (and viscoplastic strain) takes into account the combined effects of time/rate and temperature, even outside the viscoelastic domain of the material's behavior (Chehab et al., 2002).

Figure 2.26 shows a scheme of the stages to construct stress - log reduced-time master curves based on stress vs. strain curves from monotonic compression tests at different strain rate levels and temperatures (Zhao & Kim, 2003). The first step consists in finding for every strain level ε, the corresponding stress σ and time t at all temperatures T and for all rates $\dot{\varepsilon}$. In the second step, the stress and log time data at all test temperatures are cross plotted on one graph for the given strain level. Then, in the third step, the curves of stress vs. log time (one for each temperature at the given strain level) are horizontally shifted along the logarithmic time axis by the amounts of $log\ (a_T)$ that were determined earlier for constructing the dynamic modulus master curve (LVE characterization, Equation (2.4)). This procedure is then repeated for each of the selected strain levels.

The major benefit of t-TSP with damage is that the prediction of material behavior with growing damage can be conducted using the material behavior at a single temperature and t-T shift factors determined from the LVE tests (e.g., dynamic modulus test). Furthermore, a major reduction in testing requirement and time is possible.

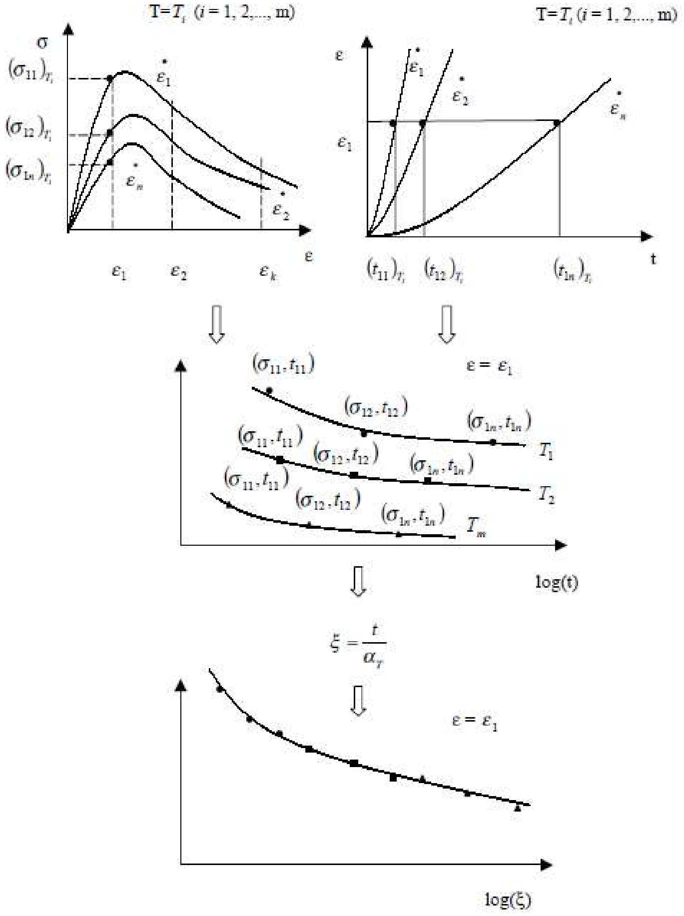

Figure 2.26. Cyclic fatigue test: constructing stress -log reduced-time master curve in damaged state (Zhao & Kim, 2003).

The simplification of the VECD model

A requirement of the rigorous VECD model is calculating and tracking the pseudostrain, pseudostiffness, and damage for the entire loading history. This requirement necessitates a computationally expensive procedure for cyclic loading. Although this task is not impossible using advanced computers, it is cumbersome and time-consuming. In addition, experimental difficulties like data storage can lead to significant errors.

In response to this problem, a simplification was introduced by B. Underwood et al. (2012) for the cyclic-loading application. The simplification lays in the evaluation of the dissipated energy using only the reduction in pseudostiffness C (Figure 2.27), instead of the enclosed area W_{max}^{R} (Equation (2.15)):

$$W^{R} = \frac{1}{2}(\varepsilon^{R})^{2}C \tag{2.15}$$

The computational simplification in the Simplified-VECD consists in calculating C piecewise instead of each data point of the cycle (except for the 1st cycle) because damage usually does not propagate much during one cycle under fatigue loading. The simplified calculation implicitly assumes that the pseudostrain is constant within a cycle. The errors of this assumption are adjusted by multiplying by an adjustment factor valid when damage growth within an individual cycle is small (R. Y. Kim et al., 2022).

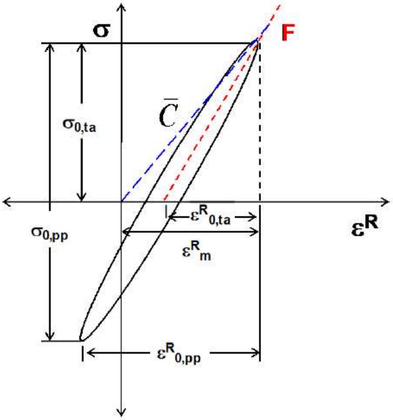

Figure 2.27. Cyclic fatigue test: simplification of the VECD model (R. Y. Kim et al., 2022).

The S-VECD output parameters

A damage evolution law is based on the elastic–viscoelastic correspondence principle, which allows the entire loading history to be taken into account for the damage calculation, as well as on the t-TSP and continuum damage mechanics. The S-VECD model applies the pseudo stiffness concept to indicate the integrity of a material under loading (Figure 2.28a). The pseudo stiffness value is normalized with the *DMR* value. Thus, pseudostiffness is 1 when the material is intact; this value decreases as damage accumulates (Figure 2.28b). The model defines a unique relationship, the so-called *damage characteristic curve* (Figure 2.28c) between normalized pseudo stiffness (*C,* Figure 2.28a) and the amount of cumulative damage (*S,* Figure 2.28b) for a given mixture. Equation (2.16) presents the power function law that expresses this relationship. This relationship is independent of mode of loading, temperature, and loading amplitude; thus, it is considered a fundamental material property (Y. D. Wang et al., 2018).

The damage characteristic curve represents the core of the S-VECD model. A mixture can be characterized by three valid test results that show overlapping C versus S curves.

$$C = 1 - C_{11} \cdot S^{C_{12}} \tag{2.16}$$

where C is pseudo stiffness; S is damage; and C_{11} and C_{12} are fitting coefficients.

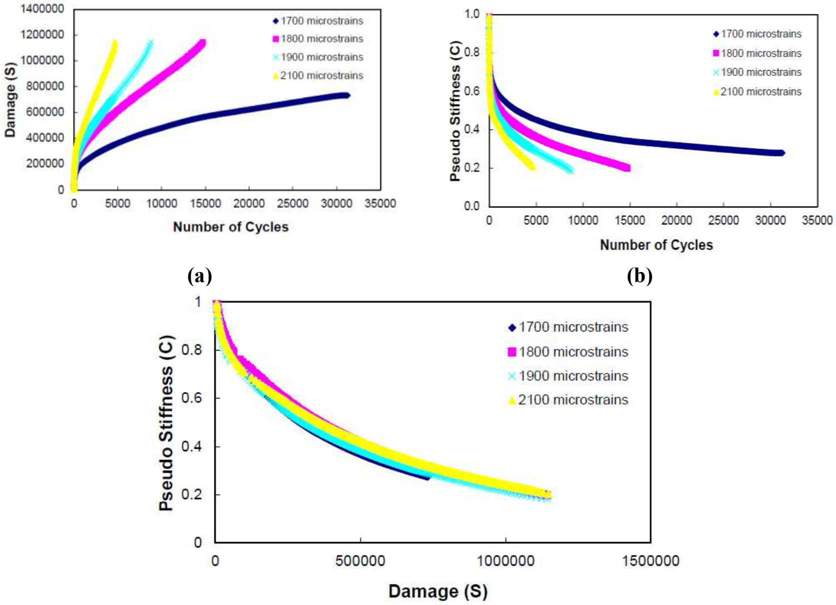

(a) **(b)**

(c)

Figure 2.28. Cyclic fatigue test: trend of (a) damage and (b) pseudostiffness during cyclic loading, and (c) resulting damage characteristic curve.

The damage characteristic curve represents how damage grows in the material; however, a failure criterion is needed to predict the failure of the material (Y. D. Wang et al., 2018). According to the reference AASHTOs, the number of cycles to failure *Nf* corresponds to the cycle in which the product of peak-to-peak stress and cycle number reaches a maximum value after a stable increase during cyclic loading (σ *N*) An example is the trend of $\sigma \cdot N$ is shown is Figure 2.29. The main advantage of this criterion is that phase angle measurement is not needed.

To characterize failure in a material, the S-VECD model adopt a pseudo energy-based fatigue model as failure criterion, called D^R, that reflects changes in the material constitutive relationship due to the development of damage (Y. D. Wang et al., 2018). The D^R failure criterion is based on experimental observations by Y. Wang & Richard Kim (2019) that the average loss of integrity per cycle throughout an asphalt mixture's fatigue life is constant regardless of temperature, mode of loading, and load amplitude:

$$D^R = \frac{\int_0^{N_f}(1-C)dN}{N_f} = \frac{sum(1-C)}{N_f} \tag{2.17}$$

According to the definition of D^R given in Equation (2.17), D^R is the slope of the linear relationship between the sum of $(1 - C)$ to failure and N_f, as demonstrated that the slope of D^R is a ductility parameter because it indicates the brittleness or ductility of a mixture. High values of D^R indicate high material toughness. To evaluate single-operator repeatability, limits on the variations of D^R values between specimens are given by AASHTOs based on the NMAS, as specified in Table 2.5.

Table 2.5. Cyclic fatigue test: single-operator repeatability on D^R.

NMAS (mm)	AASHTO T 400 (2023) Large specimens	AASHTO T 411 (2023) Small specimens
9.5	0.065	0.088
12.5	0.089	0.129
19.0	0.124	0.124
25.0	0.124	-

All these elaborations are automatically executed by the Excel-based material-level analysis program FlexMAT™_Cracking, giving as input data the .csv files obtained from the AMPT software.

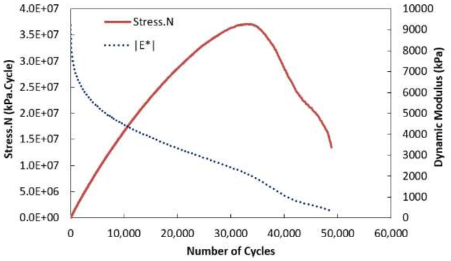

Figure 2.29. Cyclic fatigue test: identification of *Nf*.

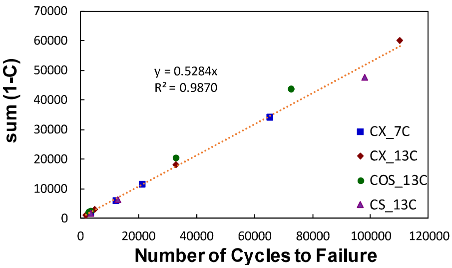

Figure 2.30. Cyclic fatigue test: failure criterion.

In summary, the S-VECD fatigue characterization of each mixture is completed when both the following criteria are met for at least three specimens:

- for each specimen:
    - ✓ middle failure (i.e., failure within the measurement area)
    - ✓ *DMR* between 0.85 and 1.15
    - ✓ duration of the test between 2000 and 80000 cycles
- for all the specimens of the same mixture:
    - ✓ overlapping *C*-*S* curves
    - ✓ D^R variation within prescribed limits.

Appendix E reports the main considerations about the S-VECD fatigue tests gained from experience.

A synthetic index, called apparent damage capacity S_{app} (Equation (2.18)), was recently developed by Y. D. Wang et al. (2022) to account for the effects of the material stiffness, damage properties and toughness on the fatigue resistance. S_{app} refers to a temperature that is based on the climatic PG of the location where the pavement is constructed.

$$S_{app} = 1000^{\left(\frac{\alpha}{2}-1\right)} \cdot \frac{a_{T(S_{app})}^{\frac{1}{\alpha+1}} \cdot \left(\frac{D^R}{C_{11}}\right)^{\frac{1}{C_{12}}}}{|E^*|^{\frac{\alpha}{4}}_{LVE,Sapp}} \tag{2.18}$$

where α is the damage growth rate, $\alpha_{T(Sapp)}$ is the time-temperature shift factor between the S_{app} temperature and the reference temperature considered for the dynamic modulus mastercurve, and $|E^*|^{\frac{\alpha}{4}}_{LVE,Sapp}$ is the reference modulus calculated at the S_{app} reference temperature and at the reduced frequency of 62.8$\cdot$ $\alpha_{T(Sapp)}$.

S_{app} values usually vary within a range of 0 to 50 (Y. D. Wang et al., 2022), and higher values indicate better fatigue resistance. The calculation is done by FlexMAT™_Cracking, after selecting the construction city.

Table 2.6. Recommended threshold values for the S_{app} fatigue index parameter (FHWA, 2019).

S_{app} limits	Traffic (million ESALs)	Tier	Designation
$S_{app} > 8$	Less than 10	Standard	S
$S_{app} > 24$	Between 10 and 30	Heavy	H
$S_{app} > 30$	Greater than 30	Very Heavy	V
$S_{app} > 36$	Greater than 30 and slow traffic	Extremely Heavy	E

2.5 The viscoplastic shift model to characterize the rutting behavior

2.5.1 Description of the test

The AM-PRS provide rutting characterization using the shift model to evaluate the susceptibility to permanent deformation of asphalt mixtures. To construct the shift model, Stress Sweep Rutting (SSR) tests have been ad-hoc calibrated. In this PhD research work, SSR tests were carried out in accordance with AASHTO TP 134 (2019), whereas the updated AASHTO TP 134 (2023) has been recently published. The few differences will be specified.

To characterize a mixture, SSR tests are performed at two testing temperatures, termed low temperature (*TL*) and high temperature (*TH*). According to AASHTO TP 134 (2019), both *TL* (Table 2.7) and *TH* are based on the climatic PG of the construction city of the pavement, whereas *TH* depends also on the depth at which the mixture will be used in the pavement structure (Equation (19)). However, the new AASHTO TP 134 (2023) recommends *TL* based on the resulting *TH.* Specifically, *TL* is equal to 20 °C for *TH* equal or lower than 45 °C, and equal to (*TH - 25 °C*) for *TH* higher than 45 °C.

Table 2.7. Stress sweep rutting tests: low test temperature according to AASHTO TP 134 (2019).

PG Low Temperature, °C	PG High Temperature, °C						
	46	52	58	64	70	76	82
	Test Temperature, °C						
–10	23	26	29	32	32	32	32
–16	20	23	26	29	32	32	32
–22	17	20	23	26	29	32	32
–28	17	17	20	23	26	29	32
–34	17	17	17	20	23	26	29
–40	17	17	17	17	20	23	26
–46	17	17	17	17	17	20	23

$$T_H = 0.87 * \left[58 + 7 * \frac{DD}{1000} - 15 * \log\left(H + 45 \right) \right] \tag{2.19}$$

where *DD* is the number of degree-days > 10°C obtained from the tool LTPPBindOnline, and *H* (mm) is the design depth to top of the course for intermediate and base layers, and it is 0 for the surface layer.

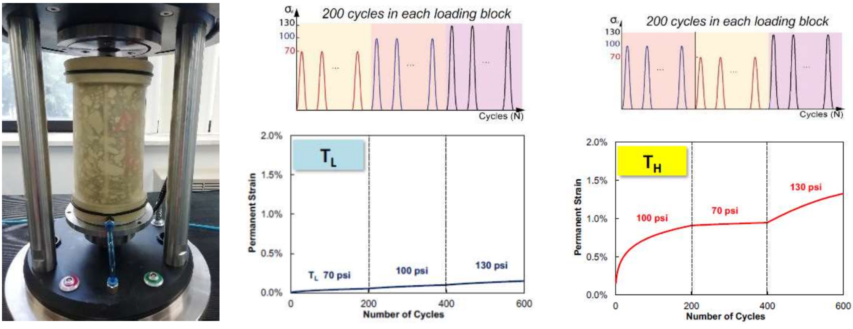

(a) **(b)** **(c)**

Figure 2.31. Stress sweep rutting tests: (a) set-up of SSR test in the AMPT, loading history and corresponding permanent strain at (b) *TL* and (c) *TH*.

The set-up of the specimen for the test provides the preparation of two greased double latex end-friction reducers. The specimen is assembled with platens in the following order from bottom to top: bottom loading platen, bottom greased double latex end-friction reducers, test specimen centered with the bottom platen, top greased double latex end-friction reducers, and top loading platen centered with the bottom platen. A latex membrane must be stretched over the specimen and loading platens, where O-ring seals are positioned to fix it. After the conditioning at the test temperature in an external climatic chamber (for at least 4 hours), the specimens and platen assembly into the AMPT (previously conditioned at the same testing temperature for at least 1 hour) with the steel ball in the center of the top loading platen. Since permanent deformations could occur even during the conditioning of the specimens, especially at high temperature, it is recommended to follow the same storage and conditioning procedure for all the specimens in order to have comparable results. A drainage line is connected to the loading platens (bottom one has a hole in the center), so that they are vented to atmospheric pressure through the bubble chamber. After the chamber has been closed and the target temperature is newly reached, the test chamber is pressurized, expressed by air bubbles coming out of the drainage lines. The specimen is left at the pre-set confining pressure for 1 hour, after that the SSR test starts. During the test, the top platen is not free to rotate. The set-up of the specimen inside the climatic chamber of the AMPT in shown in Figure 2.31a.

SSR test consists of cyclic compression tests composed by three consecutive 200-cycles loading blocks with deviatoric stresses (i.e., the difference between vertical stress and confining pressure) of 483 kPa, 689 kPa and 896 kPa (i.e., 10 psi, 100 psi and 130 psi) for *TL* (Figure 2.31b), respectively, and of 689 kPa, 483 kPa and 896 kPa (i.e., 100 psi, 70 psi and 130 psi) for *TH* (Figure 2.31c), respectively. The loading time is 0.4 s, whereas the rest period is 1.6 s for *TL* and 3.6 s for *TH*. A confining pressure of 69 kPa is applied during the test. The vertical permanent strain of the specimen is measured by the actuator, and the trends are shown in Figure 2.31. Two replicate specimens, whose difference in the permanent strain at the end of the test did not exceed 25 %, are tested for each testing temperature.

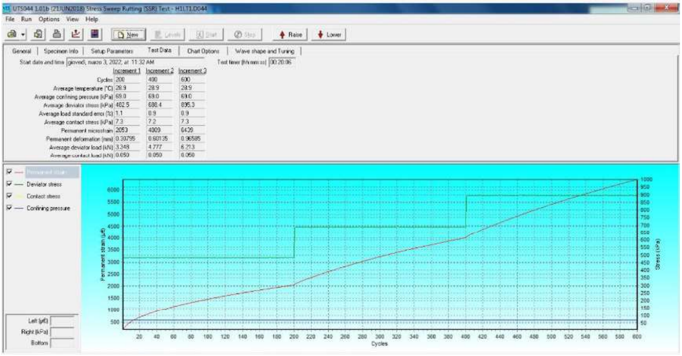

Start date and time: giovedì, marzo 3, 2022, at 11:32 AM
Test timer (hh:mm:ss): 00:20:06

	Increment 1	Increment 2	Increment 3
Cycles	200	400	600
Average temperature (°C)	28.9	28.9	28.9
Average confining pressure (kPa)	69.0	69.0	69.0
Average deviator stress (kPa)	482.5	688.4	895.3
Average load standard error (%)	1.1	0.9	0.9
Average contact stress (kPa)	7.3	7.2	7.3
Permanent microstrain	2053	4009	6439
Permanent deformation (mm)	0.30795	0.60135	0.96585
Average deviator load (kN)	3.348	4.777	6.213
Average contact load (kN)	0.050	0.050	0.050

Figure 2.32. Stress sweep rutting tests: example of output from AMPT's software (test at *TL*).

2.5.2 The viscoplastic shift model

The SSR test is designed to calibrate a mechanistic-empirical model that describes an asphalt mixture's permanent strain behavior as a function of temperature, stress, and loading time(D. Kim & Kim, 2017). The shift model is based on the concept that a standard set of conditions will produce a certain relationship between permanent deformation and the number of load cycles. Equivalent levels of permanent deformation will develop at a different number of cycles for loading conditions that differ from the reference strain curve. The reference strain curve that is created following the horizontal shift is called the permanent strain mastercurve and the amount of translation is defined as the shift factor within the time-temperature-stress superposition (t-TSSP) principle. This approach is conceptually the same as that taken to derive the dynamic modulus mastercurve and its predictions using the shift function. In general, the permanent strain mastercurve, which fits both the primary and secondary region behavior of asphalt concrete, can be expressed by the incremental model form (Equation (2.20)):

$$\varepsilon_{vp} = \frac{\varepsilon_0 \cdot N_{red}}{(N_I + N_{red})^{\beta}} \tag{2.20}$$

where ε_{vp} is the viscoplastic strain, $1 - \beta$ and ε_0 are the slope and the intercept of the permanent strain versus number of loading cycles relationship in log-log space, N_I is the number of cycles at which the secondary region begins, and N_{red} is the reduced number of cycles of a certain loading condition.

The following stages aim to make understand in a practical and simple way the procedure to construct the shift model, without going into theoretical details which can be found in D. Kim & Kim (2017) and R. Y. Kim et al. (2022). With reference to Figure 2.33:

1. Given the experimental data, the permanent strain mastercurve is obtained directly from the first loading block of the tests carried out at T_H (deviatoric stress 689 kPa) (Figure 2.33a). The parameters of the permanent strain mastercurve ε_0, N_I and β

(Equation (2.20)) are found minimizing the error between the incremental model and the experimental data.

2. The permanent strain at the last cycle of each individual loading block is horizontally shifted to match the permanent strain mastercurve (Figure 2.33b).
3. Reduced load time and vertical stress shift factors are calibrated, and the total shift factor is calculated as the sum of the reduced load time and vertical stress shift factors (Figure 2.33c).
4. The physical number of cycles N is converted to a reduced number of cycles N_{red} using the total shift factors (Figure 2.33d).

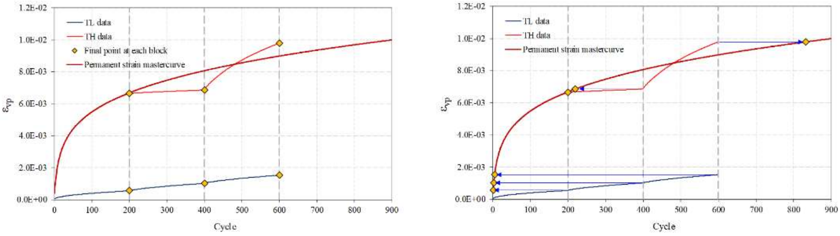

(a) **(b)**

Reduced load time shift factor:

$$a_{\xi_p} = p_1 \log(\xi_p) + p_2$$

where p_1, p_2 are coefficients of reduced load time shift factor, and ξ_p is the reduced load time.

Vertical stress shift factor

$a_{\sigma_v} = d_1 \log(\sigma_v / P_a) + d_2$

where d_1, d_2 are the coefficients of vertical stress shift factor, σ_v is the vertical stress, and P_a is the atmospheric pressure.

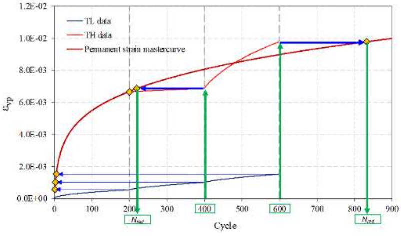

(c) **(d)**

Figure 2.33. Stress sweep rutting tests: stages to construct the shift model.

All these elaborations are automatically executed by the Excel-based material-level analysis program FlexMAT^{TM}_Rutting, giving as input data the .csv files obtained from the AMPT software. The model can estimate the response of the material under any combination of deviatoric stress and temperature by applying the shift factor equations (Figure 2.33c) along with the shift model (Equation (2.20)). Indeed, the shift model allows the prediction of asphalt mixture rutting under a wide range of temperatures, loading times, and stress levels using only four SSR tests (at two high and two low temperatures).

Analogously to the synthetic index *Sapp* for cyclic fatigue tests, a synthetic index which could resume the rutting behavior of an asphalt mixture was developed by Ghanbari et al. (2022), and named Rutting Strain Index (*RSI*). This index, adopted by FHWA, combines the effects of the material properties, the climatic conditions and the pavement structure (Ghanbari et al., 2022). The actual behavior of a mixture within the pavement can be deduced by pavement performance simulations, which however require a huge amount of time. For this reason, three standard pavement structures are considered to calculate this index (Figure 2.34). Such pavements are characterized by the same granular courses (20 cm aggregate base and subgrade) but different asphalt courses, depending on the examined asphalt mixture. If the mixture in question is for wearing course, 10 cm of such mixture are placed directly on the granular base. If the mixture is for intermediate (binder) course, 10 cm of such mixture are placed between the granular base and 7.5 cm of asphalt concrete (wearing course). If the mixture is for asphalt base course, 10 cm of such mixture are placed above the granular base and below 15 cm of asphalt concrete (7.5 cm of wearing course plus 7.5 cm of intermediate course) (Ghanbari et al., 2022). Since these standard pavement structures are considered, *RSI* is particularly useful in the design stage of a mixture, but it might not be fully representative of the performance that the mixture will have in the actual pavement. In fact, *RSI* is defined as the percentage ratio between the permanent deformation of an asphalt course and the thickness of such course at fixed boundary conditions, i.e., at the end of a 20-years period over which 30 million 80-kN ESALs are applied at a speed of 96 km/h to one of the abovementioned standard pavement structures subjected to given climatic conditions (FHWA, 2021). It is calculated by FlexMAT^{TM}_Rutting based on the shift model parameters and the outcomes of viscoelastic pavement simulations performed with the finite element method, and on the selected city of construction (AASHTO TP 134, 2023; FHWA, 2021). Threshold values of allowable traffic in terms of 80-kN ESALs are recommended based on *RSI* values (FHWA, 2021), as reported in Table 2.8.

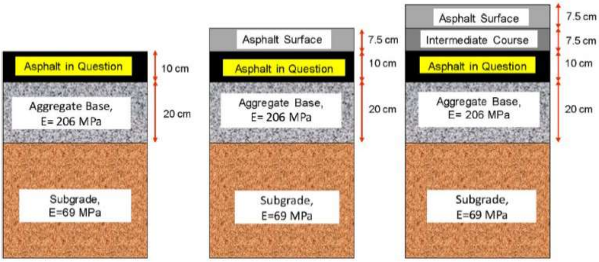

Figure 2.34. Stress sweep rutting tests: standard pavement structures to determine the *RSI* (Ghanbari et al., 2022).

Table 2.8. Stress sweep rutting tests: recommended threshold values for the *RSI* parameter (FHWA, 2021).

RSI limits (%)	Traffic (million ESALs)	Tier	Designation
RSI < 12	Less than 10	Standard	S
RSI < 4	Between 10 and 30	Heavy	H
RSI < 2	Greater than 30	Very Heavy	V
RSI < 1	Greater than 30 and slow traffic	Extremely Heavy	E

2.6 Viscoelastic and viscoplastic pavement design method using FlexPAVE^{TM}

A pavement performance prediction program, called FlexPAVE^{TM} (formerly known as the LVECD program) version 1.1Alpha, was developed under the auspices of the FHWA and it is actually under optimization, to evaluate the fatigue and rutting long-term performance of asphalt mixtures at structural level. The S-VECD model properties and shift model parameters obtained from laboratory tests are used directly as input data in FlexPAVE^{TM} (Y. D. Wang et al., 2018).

Using FlexPAVE^{TM}, the pavement is modeled as a three-dimensional layered viscoelastic structure, and the finite element method with Fourier transform is embedded to predict long-term mechanical responses (Eslaminia & Guddati, 2016). Any empirical equation is applied, but the response is just mechanical. FlexPAVE^{TM} takes into account both the moving nature of traffic loads and climatic conditions that affect the pavement.

The computational process on which FlexPAVE^{TM} is based has been developed by Eslaminia & Guddati (2016) with the aim of predicting progressive pavement distress (damage and rutting) under millions of cycles of moving vehicular loading and temperature variations. The concept is to combine Fourier transform, finite element discretization and time-scale separation. Using the observation of time-scale separation between evolution of pavement damage/rutting, temperature variation and traffic load variation, the analysis under millions of cycles is reduced to a few hundred analyses of stress and strain evolution under a single cycle of moving load (Eslaminia & Guddati, 2016). The so-called Fourier finite element (FFE) method is used for each independent stress analysis. As the name indicates, FFE is based on combining Fourier analysis and the FEM. Fourier analysis is used to eliminate the time variable as well as the spatial variable associated with traffic direction, thus limiting the analysis to the cross-section of the pavement, while still capturing all 3D and time-dependent effects. The analysis within the cross-section is performed using the FEM in order to capture potential stress-redistribution effects due to damage/rutting. Figure 2.37 shows the flowchart of the method. Essentially, Fourier analysis is used to eliminate the time dimension as well as the spatial dimension in the direction of traffic, reducing the problem to a set of two-dimensional problems, which are in turn solved using the finite element method (FEM). The FFE method is more efficient than direct three-dimensional FEM by orders of magnitude but captures the 3D effects in an accurate manner (Eslaminia & Guddati, 2016).

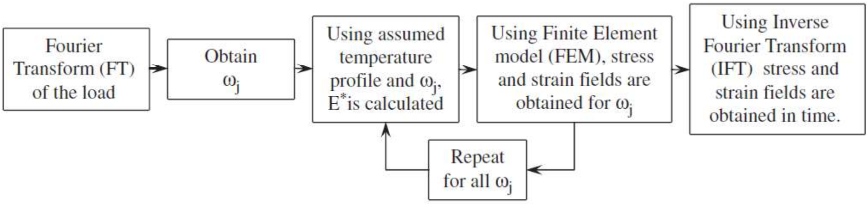

Figure 2.35. FlexPAVE^{TM} pavement performance simulation: flowchart of the FFE method (Eslaminia & Guddati, 2016).

An infinite pavement under traffic load moving applied at the top surface with a constant speed V is considered. In Figure 2.36 the directions of X, Y, Z axes in FlexPAVE$^{\mathrm{TM}}$ are indicated: X, Y, Z indicate the transversal ($x_{min} < x < x_{max}$), longitudinal of the traffic ($-\infty < y < +\infty$) and depth ($0 < z < z_{max}$), respectively.
The side boundaries are laterally constrained but allowed to have vertical displacement, and the bottom boundary is fixed (Eslaminia & Guddati, 2016):

- Side boundary conditions:

$$u_x = u_y = 0 \text{ at } x_{min} \text{ and } x_{max} \tag{2.21}$$

- Bottom boundary conditions:

$$u_x = u_y = u_z = 0 \text{ at } z = z_{max} \tag{2.22}$$

- Top boundary conditions:

$$t_r = \{\tau_{xz} \quad \sigma_{zz} \quad \tau_{zy}\}^T = p(x, t - y/V) \tag{2.23}$$

where u is the displacement vector and $p(x, y)$ is the spatial distribution of the load at *t=0*, and the argument $(y = t - y/V)$ indicates that the load is moving with constant velocity V.

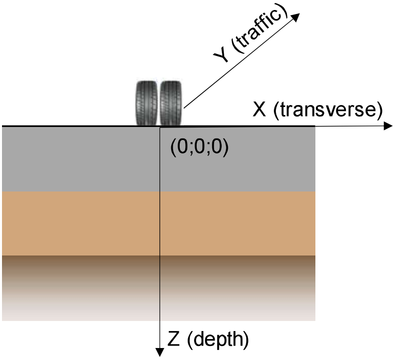

Figure 2.36. FlexPAVE$^{\mathrm{TM}}$ pavement performance simulation: coordinates system.

Specifically, the input data are the following:

1. *Design structure.* The number of layers and their thickness can be defined. FlexPAVE$^{\mathrm{TM}}$ is able to handle pavements with any number of material layers. The material of each layer can be modeled as asphalt concrete or asphalt-treated base, for which the S-VECD and shift model parameter are set (output of FlexMAT$^{\mathrm{TM}}$ files), or as aggregate or cement-treated base, that can be treated as linear elastic (elastic modulus and Poisson's ratio are required) or anisotropic elastic materials. The width of the lane is another input data.

2. *Climatic data.* The temperature data can be input four ways: from the Enhanced Integrated Climate Model (EICM) database for U.S. cities which included hour, day and months variations (one-year temperature variation), as an EICM text file, as an isothermal condition, or input manually.
3. *Traffic* The *Design vehicle* is used to carry the analysis. The geometric configuration and the characteristic of the considered ESAL can be choose axle type, wheel type, contact area of the wheel, distance between consecutive axles, axle load and design velocity. Moreover, the traffic information during the design period, such as the AADTT, growth type, lane distribution factor, monthly adjustment factor and hourly truck distribution can be inserted.

The prediction can be carried out up to 30 years of service.
Two types of analysis can be performed with FlexPAVE^{TM}: pavement response analysis and pavement performance analysis. Pavement response analysis produces only stress, strain and displacement results in the transversal cross-section area of the pavement. Pavement performance analysis gives all the information, including fatigue cracking, thermal stress, rutting data in the transversal cross-section area of the pavement. The outputs of the pavement analysis are classified into two groups: time history (i.e., temporal variation) and spatial distribution (i.e., spatial variation). Time history plots show the history of a selected response at a given evaluation point. Spatial distribution presents the so-called contours of a selected response within the pavement cross-section at any time.
The reference cross-section area within which the level of damage is composed of two overlapping triangles. Figure 2.37 illustrates these overlapping triangles. The top inverted triangle has a 170-cm wide base that is located at the top of the surface layer and a vertex that is located at the bottom of the bottom asphalt layer. The 12-cm wide base of the second triangle is located at the bottom of the bottom asphalt layer and its vertex is positioned at the surface layer (Y. D. Wang et al., 2018). Indeed, both top-down and bottom-up cracking are evaluated.

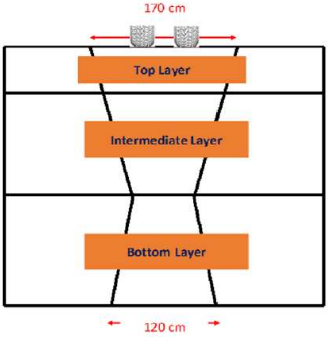

Figure 2.37. FlexPAVE^{TM} pavement performance simulation: reference area where the *%damage* is calculated (Y. D. Wang et al., 2018).

For fatigue characterization, one of the most analyzed outputs in this PhD work is the spatial distribution response of the damage factor. The damage factor DM is defined as the ratio of the current number of cycles (N) to the number of cycles at failure (N_f). The damage factor ranges from 0 to 1, with 1 indicating an asphalt element that is completely cracked. Figure 2.38 shows an example of contour of the DM, where both top-down cracking and bottom-up cracking is visible.

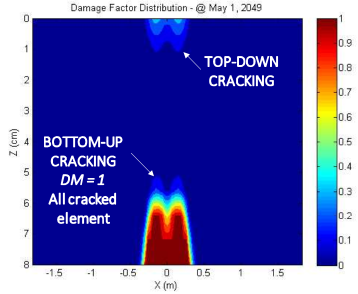

Figure 2.38. FlexPAVE^{TM} pavement performance simulation: contour of the damage factor at a fixed time.

Moreover, the time history (or evolution) of the percentage of damage, defined as the ratio of the sum of the damage factors within the cross-section area to the total area, also was evaluated in this study. Equation (2.23) defines the percentage of damage *(%damage*). Specifically, FlexPAVE^{TM} calculates the *%damage* based on a reference cross-section area affected by stresses and strains due to traffic loading (Figure 2.37)(Y. D. Wang et al., 2018).

$$\%Damage = \frac{\sum_{i=1}^{M}(DM)_i \cdot A_i}{\sum_{i=1}^{M} A_i} = \frac{\sum_{i=1}^{M}(N/N_f)_i \cdot A_i}{\sum_{i=1}^{M} A_i} \tag{2.23}$$

where i is the nodal point number in the finite element mesh; M is the total number of nodal points in the finite element mesh; and A_i is the area that corresponds to the nodal point i in the finite element mesh.

Equation (2.24) presents the sigmoidal transfer function proposed by Y. D. Wang et al. (2021) that was used to create a relationship between the *%damage* in the cross-section provided by FlexPAVE^{TM} and the percentage of cracking (*%cracking*) on the surface of the pavement. certain value. *%cracking* is the ratio of the fatigue cracking area over the whole lane area. The maximum *%cracking* is 50% (numerator in Equation (2.24)), since it is assumed that the fatigue cracks involve each wheel path throughout the lane in the longitudinal direction, and both wheel paths width is half of total lane width. For example, if each wheel path is 1-m wide and the lane is 4-m wide, the maximum *%cracking* is $2 \cdot (1\,m)/(\,4\,m) = 50\%$. Since engineering judgment also suggests that after *%cracking* has accumulated to a certain level, the cracking growth will slow down, an S-shaped curve or sigmoidal function was considered, as the transfer function used in Pavement MEPD. However, it must be underlined that the formulation of *%cracking* is calibrated with limited field data, so some assumptions based on engineering judgment were to be made to develop such viable transfer function (Y. D. Wang et al., 2021).

$$\%cracking = \frac{50}{1+C_{f1}\cdot\exp\left[C_{f2}\cdot\left(\log C_{f3}-\log \%damage\right)\right]} \tag{2.24}$$

where 50 is the maximum *%cracking,* C_{f1}, C_{f2}, and C_{f3} are calibration factors whose values are 0.342, 13.97, and 16.38, respectively.

For the rutting characterization, one of the most analyzed outputs in this PhD work is the time-history of the rut depth evolution during service for each layer. Figure 2.39 shows an example.

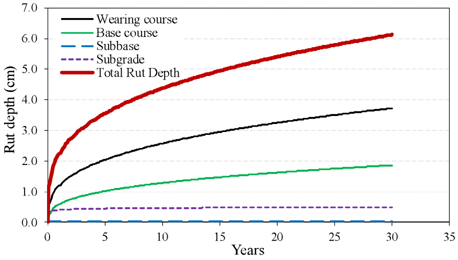

Figure 2.39. FlexPAVE^{TM} pavement performance simulation: rut depth evolution during service.

Finally, it should be noted that up to-date FlexPAVE^{TM} is not able to consider the ageing of the mixtures and the redistribution of the stresses as the damage increases. Such main topics are currently under development and will be considered in the new version 2.0.

Chapter 3.

S-VECD characterization of asphalt mixtures containing polymeric compounds added with dry method

3.1 Background and objectives

Within the framework of pavement engineering, new processes and materials are currently studied to improve environmental sustainability and lower production costs and thus improve affordability for industries and asphalt plants. To enhance the mixture's rutting and fatigue resistance and mitigate its susceptibility to temperature variations, polymer materials, such as styrene-butadiene-styrene (SBS) and ethylene vinyl acetate (EVA), are widely used as bitumen modifiers (Airey, 2004; Lin et al., 2019; Sengoz & Isikyakar, 2008). Such polymers usually are *ad hoc* engineered and added to the asphalt binder using the 'wet' modification method, which consists of blending the polymer with the binder first at a high temperature and then mixing the modified bitumen with the aggregate. Since the wet method usually consists in a chemical modification due to a complete dispersion of the polymer in the bitumen, the melting point of the polymers should be lower than the production temperature. Moreover, a special equipment is needed during transport and storage to avoid phase separation (Wu & Montalvo, 2021; Zani et al., 2017).

The dry method could be a potential alternative to the wet method to produce asphalt mixtures. The dry method consists in the addition of the polymer is added with hot aggregate directly in the asphalt plant prior to the addition of the binder (Wu & Montalvo, 2021). Therefore, this modification method is suitable also for polymers with a melting point comparable to the production temperature, such as hard plastics. Moreover, there is no risk of phase separation, reducing costs and energy consumption with respect to the wet method (Chavez et al., 2019; Ranieri et al., 2017). The main disadvantage is that the dry method implies less control of the binder/mixture properties, so that an in-depth investigation is needed.

In addition, the dry method can employ polymer compounds obtained from waste plastics, currently sent to incineration facilities or landfills (Wu & Montalvo, 2021; Zulkernain et al., 2021), improving pavement sustainability. Waste plastics are complex materials typically composed of many different grades of plastic, which can complicate their homogenization within the asphalt mixture and compatibility with bitumen (Awoyera & Adesina, 2020; Wu & Montalvo, 2021). The most common plastics found in municipal solid waste are polyethylene and polypropylene (Awoyera & Adesina, 2020), both of which are known to increase the stiffness and rutting resistance of asphalt mixtures and reduce their susceptibility to thermal loading (Angelone et al., 2016; Lastra-González et al., 2016; Sangita et al., 2011; Vasudevan et al., 2012). However, to date, researchers have not reached consensus regarding the impact of polymer compounds on the fatigue and cracking resistance of asphalt mixtures, which could be strongly influenced by the increased stiffness (Ranieri et al., 2017). Moreover, the gap in understanding the long-term performance and the lack of proper guidelines and technical standards (Awoyera & Adesina, 2020) could limit the use of waste plastics in bituminous mixtures.

Given this background, the S-VECD modeling approach was applied to three dense-graded asphalt and one open-graded asphalt mixture. Regarding the dense-graded asphalt mixtures, a reference mixture (coded as H) that contains SBS polymer-modified bitumen represents the wet modification method and two mixtures that contain compounds (coded as GC and PC, respectively) represent the dry modification method. The GC compound was made of recycled plastic with graphene and the PC compound was made of plastomeric polymers. The open-graded mixture (coded as OG) is used in wearing layer in Italy and contains SBS polymer-modified bitumen. Laboratory-compacted mixture specimens and specimens from a full-scale field test trial were tested. Finally, pavement simulations were carried out using FlexPAVE^{TM} under different scenarios in which the material properties of the asphalt layers were varied.

This study is part of a larger project in which, first, D’Angelo et al. assessed the rheological behavior and adhesion properties of the same modified binders in this study (D’Angelo et al., 2022). Then, the investigation was carried out at mixture level by Cardone et al. applying a traditional performance-related approach based on conventional tests (i.e., indirect tensile tests and triaxial cyclic tests) and performed falling weight deflectometer (FWD) tests at the field test trial (Cardone et al., 2022).

Most of the data presented and discussed in the following sections are published in Spadoni, Ingrassia, Mocelin, et al. (2022).

3.2 Materials

Three dense-graded asphalt mixtures, coded as H, GC, and PC were investigated. An open-graded mixture, coded as OG, was investigated, too.

3.2.1 The reference SBS modified asphalt mixtures

The dense-graded mixture H currently serves as the reference mixture for Italian motorway pavements. The aggregate gradation (Figure 3.) of the H is typical for base course. However, in Italy, it is currently used for both binder and base courses, as permitted by the Technical Specification [NTC 2022]. This practice decreases the costs of pavement construction since only one mixture must be produced at the asphalt plant. The nominal maximum aggregate size (NMAS) is 20 mm. 30% of unfractioned 0/16 of RAP, unfractioned, deriving from old binder and base motorway courses, by aggregate weight was added to the limestone virgin aggregate. The total binder content (virgin bitumen plus bitumen from RAP) is 4.3% by aggregate weight. The virgin bitumen, produced with SBS polymer-modified bitumen with 3.8% polymer by binder weight, is 3.0% by aggregate weight. The characteristics of such SBS modified bitumen are reported in Table 3. as declared by the producer. The expected PG of the bitumen is PG 76-16. The maximum density of mixture H is 2,503 g/cm^3.

Table 3.1. Properties of the virgin bitumen of mixtures H and OG.

Characteristic	Measure unit	NTC 2022 values	Value	Standard	Class (EN 14023)
Penetration at 25 °C	0.1 mm	50 – 70	50	EN 1426	4
Softening point	°C	70 – 90	77.8	EN 1427	4
Fraass breaking point	°C	≤ -12	-	EN 12593	-
Viscosity at 160 °C	Pa·s	≥ 0.15 ≤ 0.80	0.387	EN 13302	-
Elastic recovery at 25 °C (50 mm/min)	%	≥ 80	97	EN 13398	2
Storage stability (Δ softening point)	°C	≤ 3	1.4	EN 13399	-
Cohesion (Force ductility)	J/cm^2	≥ 3	4.32	EN 13589 EN 13703	-
After Rolling Thin Film Oven Test					
Retained penetration at 25 °C	%	≥ 40	52	EN 1426	3
Increasing in softening point	°C	≤ 5	2.1	EN 1427	2
Change of mass	%	≤ 0.8	0.4	EN 12607-1	4

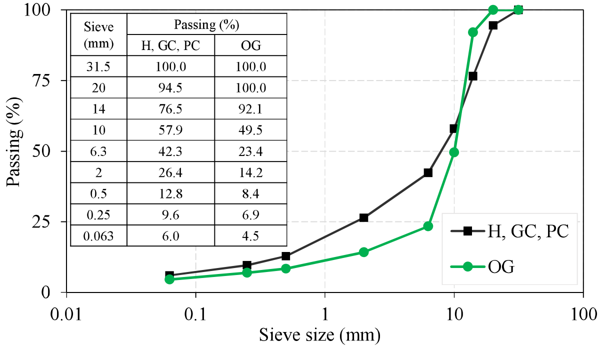

Sieve (mm)	Passing (%)	
	H, GC, PC	OG
31.5	100.0	100.0
20	94.5	100.0
14	76.5	92.1
10	57.9	49.5
6.3	42.3	23.4
2	26.4	14.2
0.5	12.8	8.4
0.25	9.6	6.9
0.063	6.0	4.5

Figure 3.1. Aggregate gradations of investigated mixtures.

The open-graded mixture OG currently serves as the reference mixture for Italian motorway pavements in porous wearing course. Porous wearing courses are employed in 80% of Italian motorway pavements. The remaining 20% is in areas subjected to cold weather, where porous mixtures cannot be used due to the water filling air voids, that would freeze and would break the mixtures due to volume increase. The aggregate gradation of OG, characterized by a NMAS of 14 mm, is reported in Figure 3.. The mixture contains 15% of unfractioned 0/16 RAP, deriving from old wearing motorway courses, combined with the basaltic aggregates. The total binder content (virgin bitumen plus bitumen from RAP) is 5.1% by aggregate weight. The virgin bitumen, produced with SBS polymer-modified bitumen with 3.8% polymer by binder weight, is 4.5% by aggregate weight. The virgin bitumen is modified with

SBS dosed at 3.8% by bitumen weight, obtaining the same properties indicated in Table 3. A dosage equal to 0.3% by aggregate weight of cellulose and glass fiber was added to prevent drain-down issues. The maximum density of mixture OG is 2,481 g/cm^3.

3.2.2 Asphalt mixtures with compound added using the dry method

The dense-graded mixtures GC and PC were produced using the same aggregate gradation of H (Figure 3.), typical for base course, containing 30% of unfractioned 0/16 of RAP (deriving from old binder and base motorway courses). The total binder content (virgin bitumen plus bitumen from RAP) is 4.3% by aggregate weight for all the mixtures, as for H, even in the presence of the compound. The GC and PC mixtures were produced using a neat 50/70 penetration grade bitumen and then adding the two compounds via the dry method, with a dosage of 5.2% by total binder weight. The plain 50/70 bitumen had a penetration value of 52 dmm and a softening point equal to 48.9 °C. The compounds, supplied in the form of hard pellets with a diameter less than 5 mm, consisted of hard recycled plastic and graphene for the GC mixture and a blend of plastomeric polymers for the PC mixture. The chemical characterization of the compounds carried out by D'angelo et al. (2022) showed that both compounds were made mostly of polyethylene and polypropylene, with the small addition of graphene for the GC mixture which should be able to improve the performance of the mixture because of the formed graphene networks (Ahmad Nazki et al., 2020; L. Yang et al., 2020). Moreover, it was found that the differential thermal profiles of the compound in PC and GC P showed the presence of two endothermic peaks placed at 127 and 161 °C, and 141 and 167 °C respectively, due to the melting of the polymer crystalline parts. Since the higher melting temperatures of the plastics are very close to the temperatures typically used in production, lay-down and compaction of asphalt mixtures (i.e. 160–170 °C), potential effects on the mixture workability are expected. The dosage of the compound was 5.2% by total bitumen weight.

(a) **(b)**

Figure 3.2. Polymeric compound of the mixtures (a) GC and (b) PC.

The production with the dry process of the compound modified mixtures was executed in the asphalt plant at 170 °C. The RA was incorporated into the pre-heated virgin aggregates through the RA conveyor. The same RA conveyor was used to introduce the plastomeric compounds, so that they stayed away from the direct contact with the burner flame of the drum. Finally, the bitumen was added and mixed with the hot aggregate blend containing compounds (i.e., dry method) (Cardone et al., 2022).

3.2.3 Field test trial

A 600-m full-scale field test trial was constructed in September 2020 as part of the A12 Italian motorway in the city of Fiumicino and consists of milled and reconstructed asphalt layers (Cardone et al., 2022). The field test trial is composed of three 200-m sections, each characterized by the same pavement structure, as follows:

- An open-graded wearing layer with nominal thickness of 4 cm, constructed with the OG mixture for all three sections.
- A dense-graded layer with a total nominal thickness of 25 cm, constructed with a different material for each section, i.e., the reference mixture H (representing the wet modification method), and the GC and PC mixtures modified via the dry method. The construction was carried out via the consecutive compaction of two layers within one morning: a 15-cm lower layer on the foundation, hereafter called *Field_inf*, and a 10-cm upper layer, hereafter called *Field_sup*. As a consequence, it is likely that the *Field_inf* course was subjected to a sort of additional compaction effort, which may cause a lower air void content than *Field_sup*.

An unbound foundation layer with nominal thickness of 35 cm (checked by an exploratory pit) was placed on the subgrade.

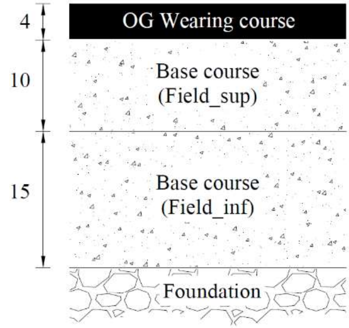

Figure 3.3. Pavement structure of the field test trial.

3.3 Testing program and procedures

Figure 3.4 presents the testing program, which was divided into three stages. In the first stage, laboratory-compacted specimens of all the study mixtures were investigated. The specimens were produced using the same mixtures that were used for the field test trial. The loose mixtures were produced at 170°C at the asphalt plant and then sampled and immediately compacted at 160°C by a gyratory compactor in accordance with EN 12697-31(2019). As prescribed by AASHTO R 83, the gyratory-compacted samples had a diameter of 150 mm and height of 180 mm. Then, one large (100-mm diameter, 150-mm height) test specimen or four small (38-mm diameter, 110-mm height) test specimens were vertically extracted from the inner portion of the gyratory-compacted sample (Section 2.2.1). Due to their high air void contents, only the large specimens were considered for the OG mixture.

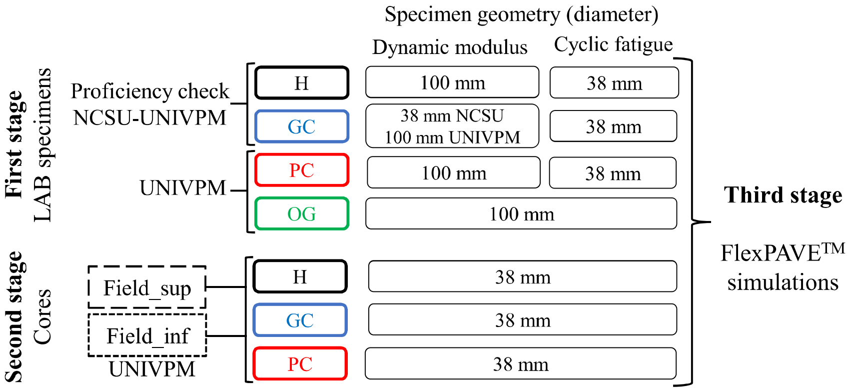

Figure 3.4. Testing program.

First, given the peculiarities of the investigated materials, proficiency checks were carried out by the North Carolina State University (NCSU, USA) research team and the Università Politecnica delle Marche (UNIVPM, Italy) research team with the aim of comparing the results for the same mixtures, H and GC, obtained from the two institutions' individual laboratories. Then, all the remaining tests were carried out at the UNIVPM laboratory.

During the second stage of the testing program, the dense-graded cores extracted from the field test trial (*Field_sup* and *Field_inf*) were studied to assess the effects of *in situ* compaction. A set of 200-mm diameter cores was extracted from each field test section in February 2021. After cutting the layers at the interface, small specimens were horizontally extracted from the *Field_sup* and *Field_inf* layers (Section 2.2.2). Figure 3.5 shows the scheme of how the cores were cut and cored in order to obtain the small specimens from the *Field_sup* and *Field_inf* courses. It was possible to obtain a maximum of three and nine specimens from *Field_sup* and *Field_inf* courses, respectively. The open-graded wearing layer was not included in the investigation due to its limited thickness.

During the first and second stages of the testing program, the fatigue behavior at the material level was evaluated using the S-VECD model approach by carrying out dynamic modulus tests and cyclic fatigue tests (Section 2.3-2.4).

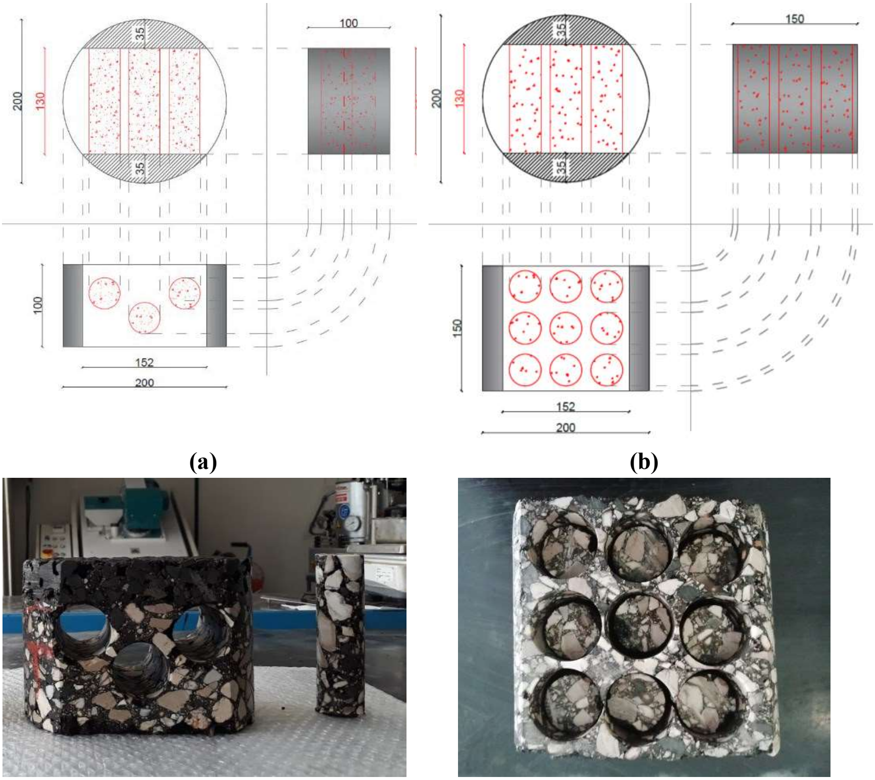

(a) (b)

(c) (d)

Figure 3.5. Small specimens from field cores: scheme and cores form (a,c) *Field_sup* and (b,d) *Field_inf*.

Specifically, with reference to Section 2.3, dynamic modulus tests were carried out by means of an AMPT. For the DG mixtures, the investigated temperatures were 4 °C, 20 °C, and 40 °C, selected in accordance with the reference standards based on the bitumen PG 76-16. For OG mixture, the investigated temperatures were 4 °C, 15 °C, 25 °C and 40 °C. The frequencies investigated for each temperature were 0.1 Hz, 0.5 Hz, 1 Hz, 5 Hz, and 10 Hz, plus 0.01 Hz at 40°C. The single-operator precision requirements were checked and verified. With reference to Section 2.4, cyclic fatigue tests were carried out on small specimens for DG mixtures, and on large specimens for OG mixture due to its high air void content. For all of them, the testing temperature (based on the bitumen PG) was equal to 21 °C. In order to obtain tests with the proper duration, the peak-to-peak on-specimen amplitude of the sinusoidal strain was selected to be between 190 με and 300 με for DG mixtures, and between 230 με and 290 με for OG.

S_{app} is determined at a specific temperature that is based on the climatic PG of the location where the pavement is constructed. Given that the field test trial is located in a PG 58-10 climatic zone (Giuliani, 2006), the S_{app} reference temperature used in this study was 21°C.

Finally, in the third stage, the fatigue performance of the mixtures was investigated at the structural level by performing FlexPAVE^{TM} pavement simulations (Section 2.6) based on the laboratory test results.

3.4 Results and analysis

3.4.1 Proficiency check with NCSU

The proficiency checks, which aimed to check for the reproducibility of the tests that were conducted at the NCSU and UNIVPM laboratories, involved laboratory-compacted specimens of the H and GC mixtures. The results are reported in detail in Appendix A.
First, the large specimen geometry (100-mm diameter) was selected, because the NMAS of the mixtures was slightly higher than 19 mm, which is the maximum NMAS prescribed by the reference standards for small specimens. However, to assess the feasibility of using the small specimen geometry (38-mm diameter), small specimens were considered for the dynamic modulus tests of the GC specimens at NCSU (see Figure 3.4). In order to exclude the influence of the volumetric properties, the tested specimens had air void contents within the range of 2.2% and 3.3%. The density of the specimens was measured using the automatic sealing method (AASHTO T 331, 2023) at NCSU and the saturated surface dry method (EN 12697-6, 2020) at UNIVPM. According to AASHTO PP 99, these two methods can be used indifferently for calculating the density of dense-graded asphalt specimens.

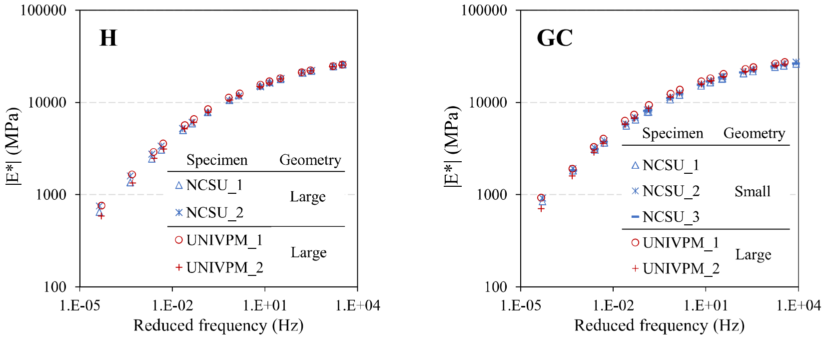

(a) **(b)**

Figure 3.6. Proficiency check results: dynamic modulus mastercurves for individual specimens of (a) mixture H and (b) mixture GC at 21.1°C.

Figure 3.6a and Figure 3.6b respectively show the dynamic modulus mastercurves of the H and GC specimens tested at NCSU and UNIVPM. The results at the reference temperature of 21.1°C (70°F) overlap for both mixtures at both laboratories, demonstrating the good reproducibility and repeatability of the dynamic modulus tests.

In addition, the overlapping results of the GC mixture obtained from specimens with different geometries, i.e., the large specimens tested at UNIVPM and the small specimens tested at NCSU (see Figure 3.4), demonstrate that the small specimen geometry complies with the representative volume element despite the NMAS of 20 mm. As a consequence, the small specimen geometry was adopted for the cyclic fatigue tests.

Figure 3.7a and Figure 3.7b respectively show the damage characteristic curves of H and GC obtained at NCSU and UNIVPM. Considering that the damage characteristic curve is a fundamental property of the material, and that it is not influenced by the testing and boundary conditions (Daniel et al., 2002), the overlap of the *C* versus *S* curves indicates good reproducibility and repeatability of the fatigue tests.

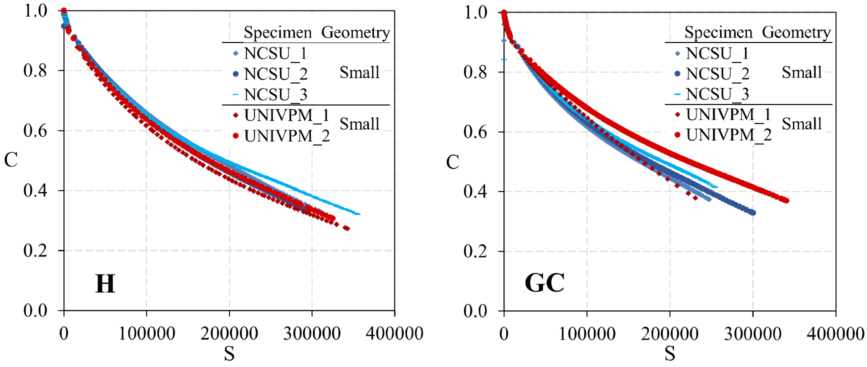

(a) **(b)**

Figure 3.7. Proficiency check results: damage characteristic curves for individual specimens of (a) mixture H and (b) mixture GC.

3.4.2 Laboratory specimens

As a follow-up to the successful proficiency checks, laboratory specimens PC and OG also were investigated by means of dynamic modulus and cyclic fatigue tests. The following Sections 3.4.2.1 and 3.4.2.2 present comparisons of the results obtained from the laboratory-compacted dense-graded mixtures, H, GC, and PC, and the results obtained for the open-graded mixture, OG, respectively.

3.4.2.1 Dense-graded mixtures

Figure 3.8a and Figure 3.8b respectively show the storage modulus mastercurves based on the 2S2P1D model and the phase angle mastercurves at the reference temperature of 21.1°C for all the dense-graded mixtures. Table 3.2 reports the parameters of the 2S2P1D model. Obviously, the 2S2P1D model predictions would be less accurate for very low and very high reduced frequencies, i.e., for conditions that are significantly different from those investigated in the laboratory (approximately between 10^{-5} Hz and 10^{4} Hz). Note that the H, GC, and PC mixtures were characterized by the same volumetric properties.

Figure 3.8a shows that the dynamic modulus mastercurves basically overlap, meaning that H, GC, and PC have comparable stiffness values overall. Specifically, H exhibits a slightly lower stiffness value within a wide range of reduced frequencies compared to the mixtures modified by the dry method, whereas the PC and GC curves have slightly different dynamic modulus mastercurve shapes In particular, in comparison with H, it is noticeable the different η value of GC (Table 3.2), which rules the proportional between the two parable elements, and the different $log\ \tau$ value (Table 3.2), which leads to a rigid translation of the curve. Figure 3.8a also reports the average air void contents (%AV) of each mixture, calculated using the saturated surface dry method.

The phase angle mastercurves presented in Figure 3.8b confirm that the mixtures modified by the dry method (especially PC) are more elastic and less viscous than the reference mixture H, as denoted by their lower phase angle values. Even at the binder level, D'angelo et al., (2022) observed a predominance of the elastic component of the dynamic modulus for the GC and PC binders compared to the H binder, especially at high temperatures. Moreover, lower phase angle values can be observed for the binders modified with the compounds compared to the polymer-modified bitumen (D'Angelo et al., 2022).

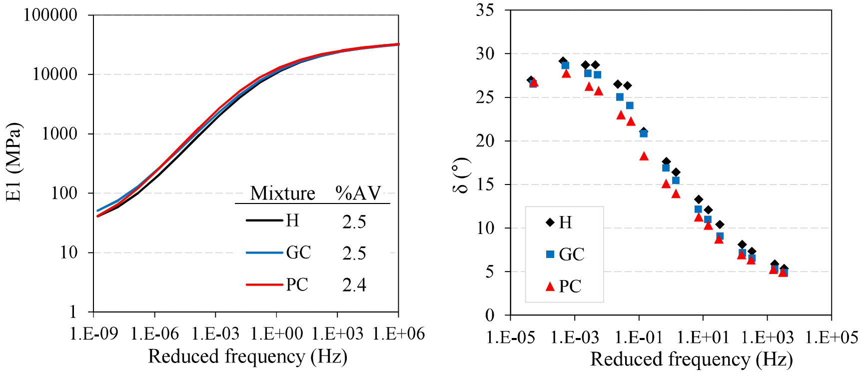

(a) **(b)**

Figure 3.8. Laboratory specimens, dense-graded mixtures: (a) storage modulus mastercurves (2S2P1D model) and (b) phase angle mastercurves at 21.1 °C.

Table 3.2. Laboratory specimens, dense-graded mixtures: parameters of the 2S2P1D models for the storage modulus.

Mixture	$E_{1,0}$ (MPa)	$E_{1,\infty}$ (MPa)	ξ	k	h	β	$log\ \tau$
H	28	40000	1.54	0.14	0.38	1E+12	-0.91
GC	32	40000	1.33	0.12	0.36	1E+12	-0.94
PC	24	40000	1.59	0.13	0.39	1E+12	-0.49

Figure 3.9 shows the three replicates overlapping damage characteristic curves obtained from different specimens for each mixture, then used to construct the fit. Figure 3.10a shows the fit of the *C* versus *S* curves for each mixture, and in Table 3.3 their regression coefficients are reported. The figure also reports the average air void contents of the specimens investigated in the fatigue tests. Note that these average air void contents are close to those of the specimens used in the dynamic modulus tests; see Figure 3.8a. The curves are similar for all the dense-graded mixtures, which is probably due to their comparable stiffness values, also shown in Figure 3.8. The C11 and C12 parameters confirm the comparable shapes, too (Table 3.3). Nevertheless, H and PC reached lower pseudo stiffness values at failure compared to GC, suggesting their greater capacity to tolerate damage. It is underlined that the fatigue resistance of the mixture cannot be evaluated solely based on the position of the damage characteristic curve (which mainly depends on the mixture's stiffness). The damage characteristics provided by the *C* versus *S* curve should be always combined with the mixture's toughness, quantified by the D^R value. This is possible thanks to the S_{app} parameter, which allows to predict the fatigue performance of the mixture within the pavement.
Figure 3.10b shows the results based on the failure criterion D^R. The dense-graded mixtures basically are characterized by similar values. However, the slightly higher value observed for H (i.e., 0.496) indicates its greater ability to absorb energy before failure compared to GC and PC. This outcome could be ascribed to the different binder phases of the mixtures, i.e., the polymer-modified bitumen for mixture H versus the neat bitumen for mixtures GC and PC.

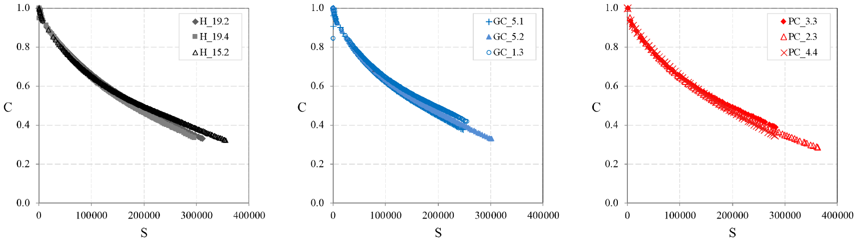

(a) **(b)** **(c)**

Figure 3.9. Laboratory specimens, dense-graded mixtures: damage characteristic curves for mixture (a) H, (b) GC and (c) PC used for the fit.

Table 3.3. Laboratory specimens, dense-graded mixtures: parameters of the damage characteristic curves.

Mixture	C11	C12
H	3.05E-04	6.09E-01
GC	4.08E-04	5.89E-01
PC	4.23E-04	5.83E-01

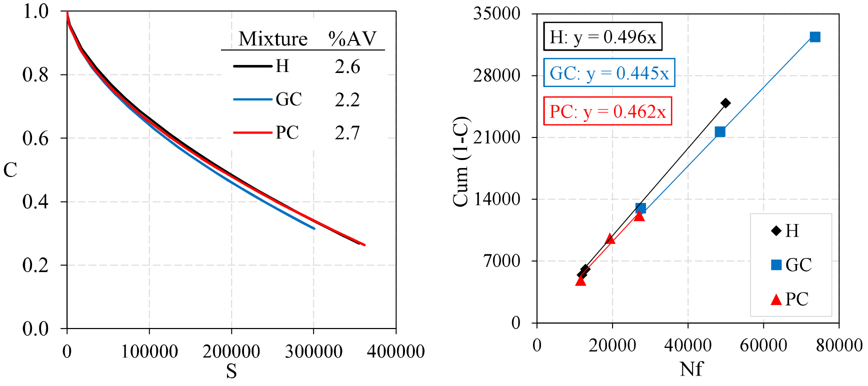

(a) **(b)**

Figure 3.10. Laboratory specimens, dense-graded mixtures: (a) fit of damage characteristic curves and (b) D^R failure criterion.

Figure 3.11 presents the S_{app} values and average air void contents obtained from the dynamic modulus and fatigue tests of the three dense-graded mixtures, which confirmed the rankings given by the D^R values. H is characterized by the highest value followed by PC and GC, suggesting that the fatigue resistance of the reference mixture is slightly better than that of the mixtures modified by the dry method.

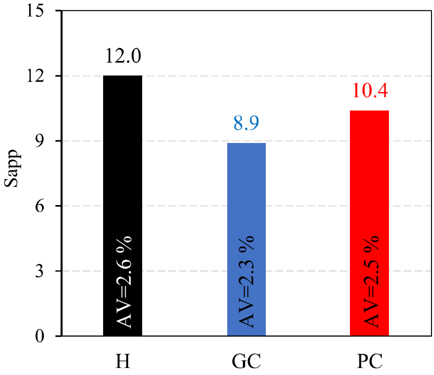

Figure 3.11. Laboratory specimens, dense-graded mixtures: S_{app} values.

3.2.2. Open-graded mixture

As mentioned, the open-graded mixture OG also was investigated through dynamic modulus and cyclic fatigue tests (see Figure 3.4). The S-VECD model and the related transfer functions have been mainly calibrated for dense-graded mixtures. Moreover, the service life of open-graded wearing layers mainly depends on functional aspects, as they are usually replaced due to ravelling and/or clogging. However, the determination of the viscoelastic and damage properties of the OG mixture was necessary in order to run FlexPAVE^{TM} simulations for the study pavement that includes the OG mixture as the wearing layer.

Figure 3.12a shows the OG storage modulus mastercurve based on the 2S2P1D model at the reference temperature of 21.1°C, and in Table 3.4 its parameters are reported. Figure 3.12c shows the fit of the OG damage characteristic curve obtained from the four replicates overlapping *C* versus *S* curves shown in Figure 3.12b. These figures also report the average air void contents of the tested OG specimens, calculated using the geometric method (EN 12697-26, 2018). Table 3.5 finally reports the C_{11} and C_{12} values.

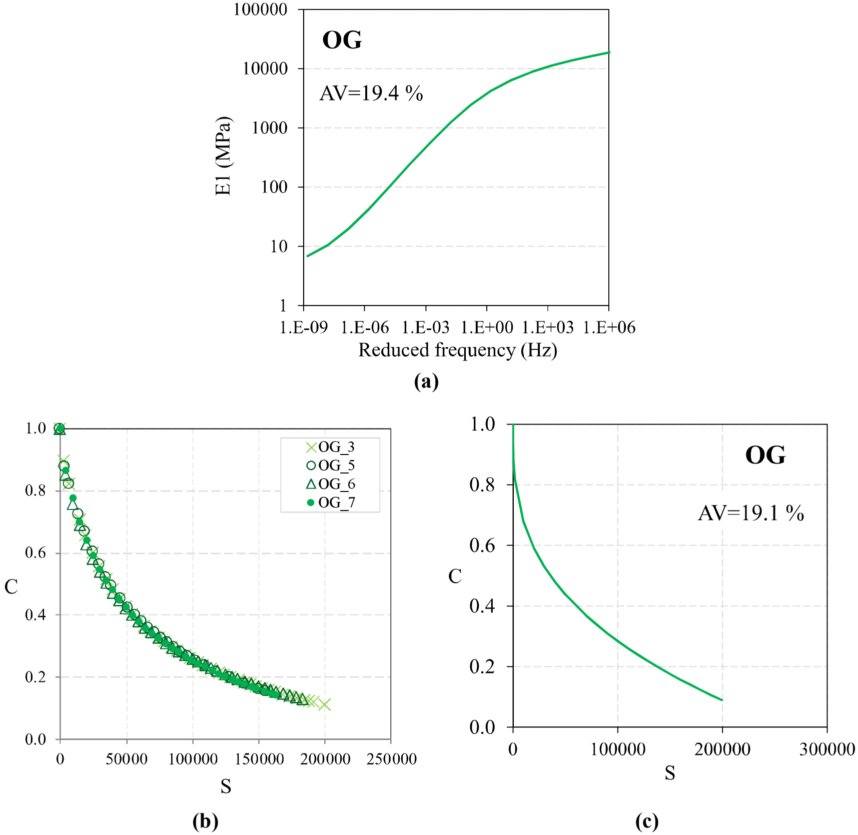

(a)

(b) **(c)**

Figure 3.12. Mixture OG: (a) storage modulus mastercurve (2S2P1D model) at 21.1°C, and damage characteristic curves (b) of the specimens and (c) fit.

Table 3.4. Mixture OG: parameters of the 2S2P1D model for the storage modulus.

Mixture	$E_{1,0}$ (MPa)	$E_{1,\infty}$ (MPa)	ξ	k	h	β	$log\ \tau$
OG	4	40000	3.74	0.11	0.40	1E+12	-2.23

Table 3.5. Mixture OG: parameters of the damage characteristic curve.

Mixture	C11	C12
H	1.29E-02	3.49E-01

3.4.3 Field specimens

Figure 3.13a, Figure 3.13b and Figure 3.13c present comparisons of the storage modulus mastercurves for the field and laboratory specimens for each of the three mixtures, respectively, obtained based on the 2S2P1D model at the reference temperature of 21.1°C. The figures also report the average air void content for each mixture. Table 3.6 reports the parameters to construct such mastercurves.

Note that, in the case of the *Field_inf* layer, the air void content is comparable to that of the laboratory specimens only for H, whereas both GC and PC show higher air void contents for the field specimens. Moreover, for all the mixtures, the air void content of the *Field_sup* layer is higher than that of the *Field_inf* layer and significantly higher than that of the laboratory specimens. As discussed in depth by Cardone et al. (2022), the *Field_inf* layer of mixture H underwent additional compaction when *Field_sup* was constructed over it, whereas the workability of the GC and PC mixtures was diminished by the presence of the compounds, whose melting points are comparable to the compaction temperature (i.e., 160°C). Therefore, unlike the laboratory specimens (characterized by similar volumetric properties for all mixtures), the effect of the different air void contents must be considered when analyzing the behavior of field specimens.

Figure 3.13a, Figure 3.13b and Figure 3.13c also show that all the mixtures exhibit a similar trend whereby the stiffness values of the laboratory specimens are higher than those of the *Field_sup* specimens, whereas the *Field_inf* specimens exhibit an intermediate stiffness value. The lowest stiffness value of the *Field_sup* specimens is due to the high air void content observed for all the mixtures. Regarding the *Field_inf* results, the dynamic modulus values are comparable to those of the laboratory specimens at high reduced frequencies and comparable to those of the *Field_sup* specimens at low reduced frequencies (even though the 2S2P1D model predictions could be less accurate at particularly low and high reduced frequencies). These findings indicate a faster transition from predominantly elastic behavior to predominantly viscous behavior. Moreover, recall that the dynamic modulus tests were conducted using large specimens under laboratory conditions and small specimens under field conditions. Therefore, the test geometry might emphasize the difference at low frequencies (Castorena et al., 2017).

Different from the compound-modified mixtures, GC and PC, the intermediate stiffness values of the *Field_inf* specimens for the H mixture with SBS-modified bitumen could not be justified by the intermediate air void contents, because the laboratory and *Field_inf* specimens had similar air void contents of around 2.5%; see Figure 3.13a. As a possible explanation, the mixtures were compacted by a gyratory compactor at a fixed height (180 mm) in the laboratory, whereas the lower 15-cm layer reached this compaction level in the field gradually thanks to the progressive passage of rollers on the pavement. The two compaction methods can imply different compaction energy and lead to different aggregate packing. In addition, the laboratory specimens were cored vertically from the gyratory-compacted samples, whereas the field specimens were cored horizontally within the layer (i.e., different orientation of the principal stresses).

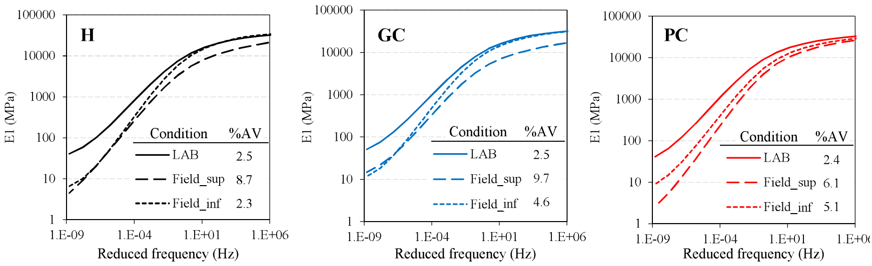

(a) **(b)** **(c)**

Figure 3.13. Field vs. laboratory specimens: storage modulus mastercurves (2S2P1D model) of (a) H, (b) GC, and (c) PC at 21.1°C.

Table 3.6. Field specimens: parameters of the 2S2P1D models for the storage modulus.

Mixture	$E_{1,0}$ (MPa)	$E_{1,\infty}$ (MPa)	ξ	k	h	β	$log\ \tau$
Field_sup_H	2	40000	3.13	0.11	0.41	1E+12	-1.80
Field_inf H	5	40000	2.12	0.18	0.48	1E+12	-0.85
Field_sup_GC	10	40000	3.50	0.09	0.38	1E+12	-1.99
Field_inf GC	8	40000	1.96	0.14	0.44	1E+12	-0.86
Field_sup_PC	1	40000	2.62	0.13	0.46	1E+12	-1.42
Field_inf PC	5	40000	2.04	0.13	0.43	1E+12	-1.18

Figure 3.14 shows the three replicates overlapping damage characteristic curves obtained from different specimens for each mixture, then used to construct the fit whose regression coefficient are in Table 3.7. Figure 3.15a, Figure 3.15b and Figure 3.15c present comparisons of the fit of the damage characteristic curves obtained from the *Field_sup* and *Field_inf* specimens and from the laboratory specimens for each of the three mixtures, respectively. The figures also report the average air void contents of the specimens subjected to fatigue tests, which are comparable to the air void contents of the dynamic modulus specimens shown in Figure 3.13. Figure 3.15 shows that, for all three dense-graded mixtures, the curve of the laboratory specimens is in the highest position, followed by that of *Field_inf* and then *Field_sup*. These results are consistent with the stiffness properties and air void contents (in general, the curve of softer mixtures tends to stay below that of stiffer mixtures). Regarding mixture H, note that the LAB curve is above the *Field_inf* curve despite their similar air void contents, confirming that C versus S curves are dependent on the stiffness property, which in turn is affected by the compaction and coring conditions, as mentioned earlier.

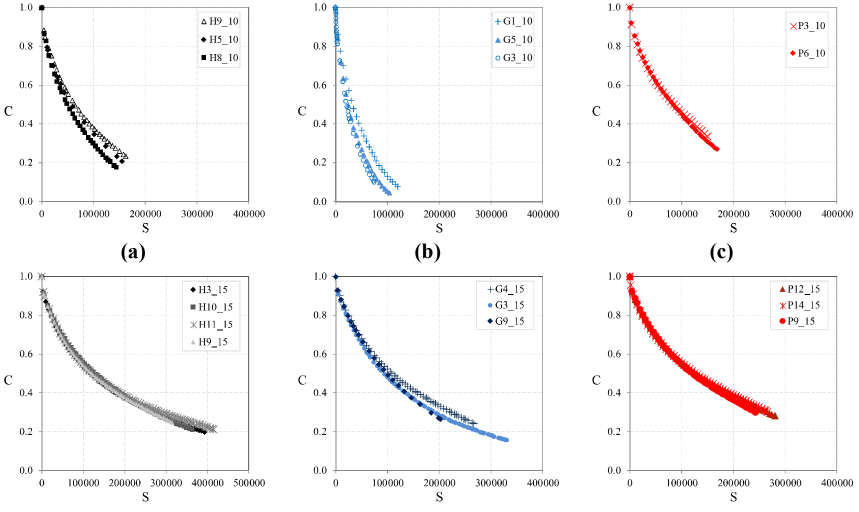

(a) (b) (c)

(d) (e) (f)

Figure 3.14. Field specimens: damage characteristic curves for mixture (a,d) H, (b,e) GC and (c,f) PC of *Field_sup* and *Field_inf*, respectively used for the fit.

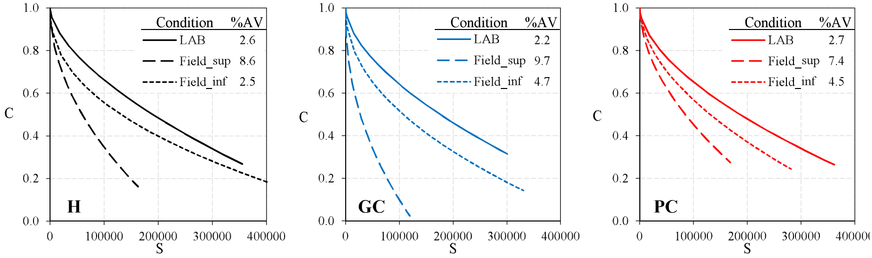

(a) (b) (c)

Figure 3.15. Field vs. laboratory specimens: fit of damage characteristic curves for (a) H, (b) GC, and (c) PC.

Table 3.7. Field specimens: parameters of the damage characteristic curves.

Mixture	C11	C12
Field_sup_H	1.77E-03	5.14E-01
Field_inf H	2.84E-03	4.39E-01
Field_sup_GC	2.36E-03	5.23E-01
Field_inf GC	1.98E-03	4.78E-01
Field_sup_PC	1.09E-03	5.40E-01
Field_inf PC	8.42E-04	5.42E-01

The H and GC field specimens reached lower C values at failure than the laboratory specimens, suggesting the field specimens' greater tolerance to damage, which could be ascribed to the different volumetric properties and/or compaction method (whose effects are discussed above). Moreover, the high value of S at failure observed for H in the *Field_inf* condition suggests that this mixture is able to tolerate a greater amount of damage compared to all the other investigated mixtures. However, recall that the C versus S curve alone does not provide complete information on the fatigue resistance and thus should be always combined with D^R into the S_{app} value. The curve of *Field_sup* for the GC mixture, which is characterized by the C value at failure that is close to 0, is considered unreliable due to the high air void content (i.e., 10%), which could lead to problems related to the representativeness of the small specimen geometry. Conversely, for PC, all the curves can be characterized by similar pseudo stiffness values at failure.

Table 3.8 presents the D^R values for all the mixtures. The toughness, i.e., the ability to absorb energy before fracture, of the field specimens is always significantly greater than that of the laboratory specimens, suggesting that the laboratory compaction process leads to a reduction in toughness (i.e., possible over-compaction causing some broken aggregate, especially within the RAP fraction). The extremely high D^R value (0.876) observed for *Field_sup* of GC confirms the unrealistic results for this mixture. No clear trend related to air void content was observed in terms of D^R.

Table 3.8. Field vs. laboratory specimens: D^R values.

Condition	H	GC	PC
Laboratory	0.496	0.445	0.462
Field_sup	0.619	0.876	0.481
Field_inf	0.610	0.581	0.514

The S_{app} values in Figure 3.16a-b-c confirm the findings from the damage characteristic curves and D^R failure criterion for the three mixtures. The figures also report the average air void contents of all the specimens used for the dynamic modulus and fatigue tests. Better fatigue resistance can be expected from the field specimens, especially from *Field_inf* specimens, which are characterized by an intermediate stiffness value that ensures good distribution of the stress within the pavement without compromising the mixture's toughness. The highest S_{app} value of 22.4, observed for H in the *Field_inf* condition, can be associated with the high S value at failure observed for this mixture; see Figure 3.15a.

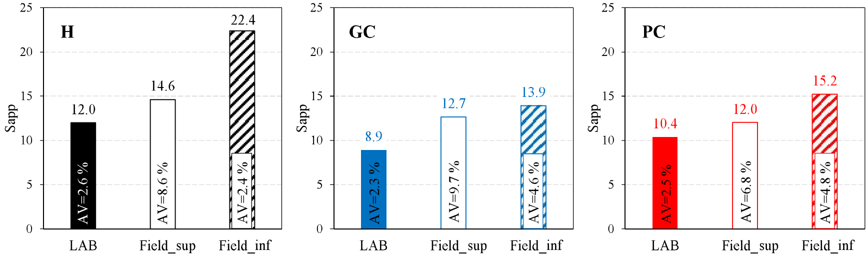

(a) **(b)** **(c)**

Figure 3.16. Field vs. laboratory specimens: S_{app} values for (a) H, (b) GC, and (c) PC.

Overall, based on the analysis of the mixtures at the material level, the compound-modified mixtures, GC and PC, show similar performance, which is slightly worse than the performance of the reference mixture, H. Moreover, the analysis results indicate that an intermediate material stiffness value can lead to better fatigue resistance of the pavement, as expressed by the S_{app} parameter.

3.5 Comparison with the traditional approach results

The stiffness of laboratory compacted specimens and of field cores of dense-graded mixtures was evaluated with the ITSM tests (EN 12697-26, 2022). ITSM was determined at 20 °C and setting a target horizontal deformation of 5 ± 2 µm. The frequency is fixed by the Standard at 2 Hz. The specimens had a nominal height of 60 mm and a diameter of 100 mm. Six replicates were tested for each mixture. The results are shown in Figure 3.17 (Cardone et al. 2022).

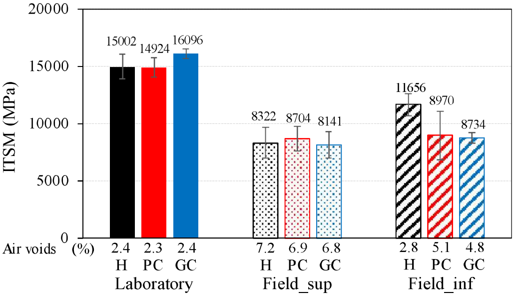

Figure 3.17. Traditional approach results, stiffness: ITSM.

Such results are in good agreement with those obtained from the storage modulus mastercurves (Figure 3.8a, Figure 3.13). Regarding the laboratory specimens, under the same volumetric properties, the mixtures present similar indirect tensile stiffness modulus values, as observed in Figure 3.8a. This is confirmed for *Field_sup* specimens, whose stiffness is lower due to higher AV. In the *Field_inf* course, the higher stiffness modulus of the reference mixture with respect to the compound modified mixtures was justified by the lower air voids content of the specimens H (i.e. 2.8%) as compared to specimens PC and GC (i.e. 5.1 and 4.8%, respectively).

The fatigue resistance of laboratory compacted specimens and of field cores of dense-graded mixtures was evaluated with the ITFT (EN 12697-24, 2018, Annex F) at 20 °C. The specimens were the same previously subjected to ITSM tests (diameter 100 mm – height 60 mm). The results are shown in Figure 3.18 (Cardone et al. 2022), together with the ε_6 which is the deformation corresponding to one million cycles. A comparison between such results and the S_{app} values (Figure 3.11, Figure 3.16) can be carried out.
The ε_6 and S_{app} values for the laboratory specimens are not in agreement, since a better performance should be expected from PC (ε_6 = 107 με) and H (S_{app} = 12.0), respectively. Conversely, the higher fatigue resistance for H compacted in the field is actually expressed by both the considered parameters (ε_6 = 140 με, $S_{app,average}$ = 18.5). A similar behavior can be attributed to GC and PC.

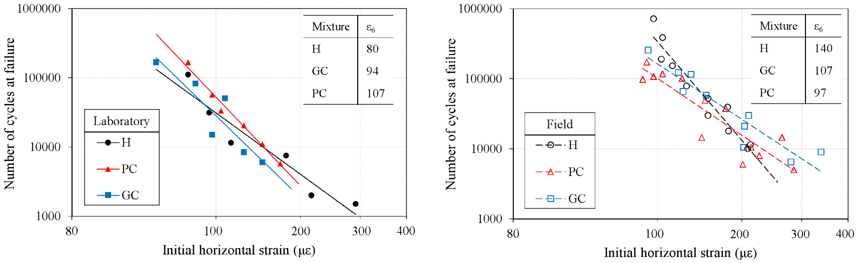

(a) **(b)**

Figure 3.18. Traditional approach results, fatigue: ITFT.

3.6 Pavement performance simulations

3.6.1 Input data

In this study, FlexPAVE^{TM} analysis was performed for a 30-year pavement service life under both thermal effects and traffic loading. The structure of the simulated pavement is the same as the Fiumicino field test track and consists of a 4-cm open-graded wearing layer, a 25-cm dense-graded asphalt layer, and a 35-cm foundation on the subgrade (Figure 3.3). Table 3.9 presents a summary of the three scenarios evaluated in the simulations. For all three scenarios, the upper 4-cm layer is modeled based on the OG results, whereas the material properties of the 25-cm layer used as input differ. Note that, in the context of FlexPAVE^{TM} simulations, a 25-cm layer is equivalent to two separate layers of 10 cm (*Field_sup*) and 15 cm (*Field_inf*) with the same properties, presenting perfect bonding at the interface, as preliminarily verified in this study. The decision to consider a single layer with 25-cm thickness was based on the fact that it requires less computational time. In Scenario 1, the dense-graded layer was modeled using the results of the laboratory specimens. In Scenario 2 and Scenario 3, the dense-graded layer was modeled using the results of *Field_sup* (excluding GC for the reasons mentioned in Section 3.4.3) and *Field_inf* specimens, respectively. The foundation and the subgrade were modeled as linear elastic materials with stiffness modulus values of 400 MPa and 150 MPa, respectively, determined from FWD tests (Cardone et al., 2022).

Table 3.9. Pavement performance simulations: material properties considered for each scenario.

Scenario	Wearing layer (4 cm)	Dense-graded layer (25 cm)	Foundation (35 cm)	Subgrade
1	OG	LAB (H, GC, PC)	$E = 400$ MPa	$E = 150$ MPa
2	OG	*Field_sup* (H, PC)	$E = 400$ MPa	$E = 150$ MPa
3	OG	*Field_inf* (H, GC, PC)	$E = 400$ MPa	$E = 150$ MPa

As for the climatic conditions, based on a comparison of the annual temperatures and precipitation, the Italian city of Fiumicino (where the field test track is located) best matches San Luis Obispo in California (whose climatic data are present in the FlexPAVE^{TM} database). Regarding the loading conditions, as revealed from traffic data studies conducted in 2019, the field test track is subjected to one million equivalent standard axle loads (ESALs) per year, where the reference ESAL is a 120-kN single axle with dual wheels. In order to assess the damage caused by motorway heavy traffic, a speed of 90 km/h and a tire inflation pressure of 800 kPa were considered. The tire-pavement contact area was set as circular, and linear traffic growth of 0.4% per year was estimated.

3.6.2 FlexPAVE^{TM} results

Figure 3.19a-b-c present the damage contours of H, GC, and PC, respectively, for Scenario 1 (i.e., with the material properties of the laboratory specimens for the dense-graded asphalt layer) after 30 years of service. Recall that the H, GC, and PC laboratory specimens present analogous volumetric properties, i.e., air void contents around 2.5%, as reported also in Figure 3.19. Figure 3.19 clearly indicates that the damage is concentrated mainly in the upper part of the asphalt layers, in particular under the 4-cm wearing layer. This damage distribution is likely attributable to the thermal effects that are due to the difference in stiffness values between the open-graded and dense-graded layers. Note, too, that thermal loading is similar to the loading applied in a displacement-controlled test, and the resistance of the mixture to thermal loading depends on the mixture's capacity to relieve the stress and resist the damage that is due to the induced stress (Saleh et al., 2020). Mixture H is less prone to thermal damage than GC and PC, because the latter mixtures are slightly stiffer and more brittle (i.e., greater induced stress and lower tolerance to damage) and have lower phase angle values (i.e., less capacity to relieve stress) than H (Figure 3.8a). Bottom-up cracking, which relates strictly to fatigue stress, is limited in all the cases because of the significant stiffness of the laboratory specimens (Figure 3.8ba), which determined the low tensile strain at the bottom of the asphalt layers.

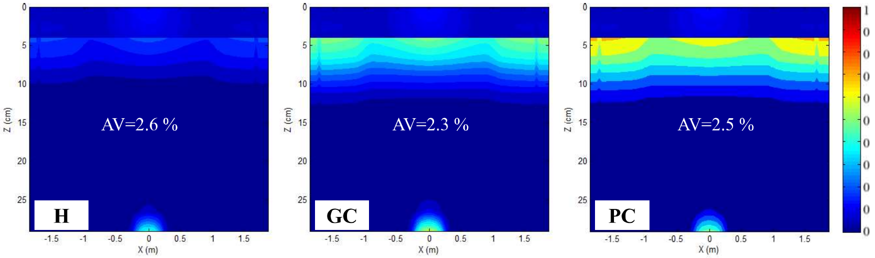

(a) **(b)** **(c)**

Figure 3.19. Scenario 1: damage contours of (a) H, (b) GC, and (c) PC after 30 years.

Figure 3.20a illustrates the Scenario 1 damage evolution within the pavement during the 30 years of service, whereas Figure 3.20b reports the percentage of damage and the percentage of cracking after the 30 years of service.

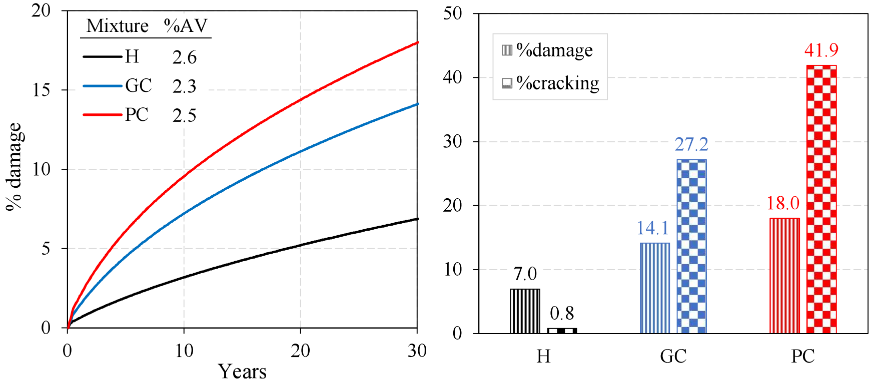

Figure 3.20. Scenario 1: (a) damage evolution, and (b) percentages of damage and cracking after 30 years.

The percentage of damage at the end of 30 years for H, GC, and PC is 7.0, 14.1 and 18.0%, respectively. After applying the transfer function proposed by Wang et al. (2021), the percentage of cracking is 0.8%, 27.2%, and 41.9% for H, GC, and PC, respectively. The ratios of *%Damage* and *%Cracking* between GC and PC are about the same. However, *%Cracking* of H is much smaller than the *%Damage*. In fact, according to the considered transfer function, when *%Damage* is lower than 10%, the corresponding *%Cracking* increases slowly and usually remains lower than 5%. Instead, when *%Damage* is higher than 10%, *%Cracking* increases dramatically (Y. D. Wang et al., 2021). The reason is that

%*Damage* is calculated from the pavement cross-section whereas %*Cracking* is measured from pavement surface. That is, fatigue cracking cannot be seen on the pavement surface while fatigue damage grows within the asphalt layer. Overall, the better performance of H can be attributed to its polymer-modified bitumen.

Figure 3.21a-b-c respectively present the damage contours for the PC mixture in Scenario 1 (laboratory specimens), Scenario 2 (*Field_sup* specimens), and Scenario 3 (*Field_inf* specimens) after 30 years of service, together with the average air void contents of the specimens. As stated earlier, in Scenario 1, the damage involves a large area under the wearing layer due to the difference in stiffness values between the layers, which led to significant thermal damage. In Scenario 2, the damage is shown to be concentrated mostly at the bottom of the asphalt layer (i.e., bottom-up cracking), even though the involved area is only 6 cm to 7 cm thick. This behavior is due to the lower stiffness values of the *Field_sup* specimens compared to the laboratory specimens (Figure 3.13a) and relates strictly to the higher air void content. Finally, in Scenario 3, an intermediate behavior (that falls between the other two scenarios) can be observed whereby the pavement is subjected to limited damage at the bottom of the asphalt layer (bottom-up cracking) and the upper part of the asphalt layer (top-down cracking). However, the damage level observed for the open-graded wearing layer might not be fully reliable due to the limited data available in the literature regarding the S-VECD model characterization of open-graded mixtures. These findings suggest that the best performance at the structural level can be expected from dense-graded mixtures characterized by an intermediate stiffness level, which ensures a limited stress-strain level within the pavement without negatively affecting the mixture's toughness and thermal resistance. Similar observations could be made for H and GC, and thus, the results for H and GC are not shown.

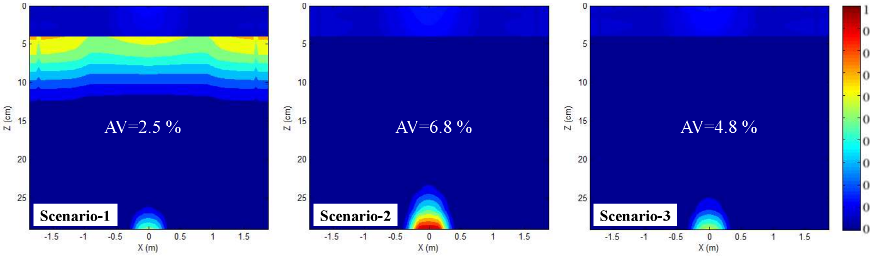

(a) **(b)** **(c)**

Figure 3.21. Damage contours for PC mixture: (a) Scenario 1, (b) Scenario 2, and (c) Scenario 3.

Figure 3.22a shows the damage evolution within the pavement during 30 years of service for the PC mixture, whereas Figure 3.22b reports the percentage of damage and the percentage of cracking after the 30 years of service for each Scenario. For the specimens obtained from the field test track, the percentage of damage after 30 years reached between 5% and 10%, corresponding to a very low percentage of surface cracking (lower than 3.2%), as explained earlier. A comparison of Figure 3.21 and Figure 3.22 shows that the wide difference in the percentage of cracking between the LAB and field conditions can be ascribed to the damage that is due to thermal stress. Given that only mixture H did not suffer thermal damage (see Figure 3.19), the viscoelastic properties derived from the modification of the binder can reasonably be assumed to provide beneficial effects, which are not provided through the dry modification of neat bitumen.

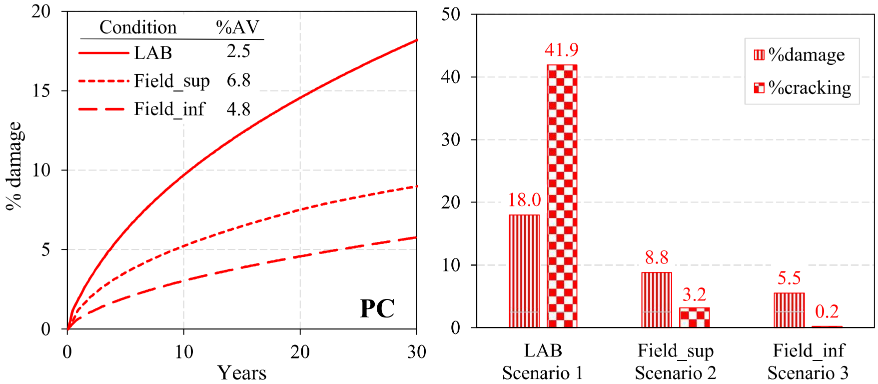

Figure 3.22. PC mixture: (a) damage evolution, and (b) percentages of damage and cracking after 30 years under the three scenarios considered.

3.7 Summary of the findings

This study aimed to compare the fatigue performance of a reference mixture (H) that contains bitumen modified via the wet method and two compound mixtures (GC and PC) modified via the dry method. The mixtures were produced at an asphalt plant and were used to construct a 25-cm base layer (placed and compacted in two separate steps, 15 cm + 10 cm) in a field test track as part of an Italian motorway. Part of the mixtures also were compacted in the laboratory.

This study demonstrates the applicability of the S-VECD modeling approach also to non-conventional materials such as asphalt mixtures modified with plastics via the dry method.

Under the same volumetric properties, the investigated mixtures show comparable stiffness values and fatigue resistance overall, even though the mixtures with the compounds are slightly stiffer and less viscous than the reference mixture. However, based on the FlexPAVE^{TM} simulations, the mixtures with the compounds are much more prone to thermal damage compared to the reference mixture. This outcome is due mainly to the greater difference in stiffness values with the open-graded wearing layer. Compared to the laboratory specimens, the field specimens can be characterized by less stiffness as a consequence of their higher air void contents and different compaction conditions. In particular, the intermediate stiffness level, which characterizes the *Field_inf* specimens of all the mixtures, correlates with several positive effects: greater damage tolerance and toughness at the material level and less thermal damage and limited bottom-up cracking at the structural level. Taking into account also the workability issues of GC and PC that are related to the melting point of plastics, the findings suggest that the performance of the reference mixture with the polymer-modified bitumen (H) is slightly better than the performance of the mixtures modified using the dry method (GC and PC). However, the addition of the polymeric compounds certainly improves the performance of mixtures with neat bitumen, even though graphene does not seem to add any positive contribution. Moreover, the environmental benefits generated from the dry modification method, i.e., reduced operational effort and the possibility of recycling waste plastics, also should be taken into consideration. Monitoring the existing motorway field test track over time will provide further data regarding the behavior of the mixtures in the field.

Chapter 4.
S-VECD characterization and application of the viscoplastic shift model of Polish asphalt mixtures

4.1 Background and objectives

In order to enlarge the reliability of the VECD approach from Italian mixtures to European ones, the research also provided a two-month stay abroad in Poland (July-August 2022). Specifically, the cooperation was with the research team of Gdańsk University of Technology, guided by Professor Piotr Jaskuła, who is currently interested in the AM-PRS developed in the US. In fact, even in Poland the pavement design is currently based on the elastic-method, as in Italy. However, the SBS modified bitumen has started to be proposed by the producers since it could strongly enhance the asphalt mixtures' behavior. Moreover, given the interesting results, such research was then successfully presented at the European Asphalt Technology Association (EATA) 2023, held right in Gdańsk in June.

In Poland, SBS polymer is currently used as bitumen modifier, since it can improve the fatigue and rutting performance of the pavement (Zofka et al., 2021), even though there is some skepticism about its use, yet. In fact, SBS modified bitumen is always used to produce Stone Mastix Asphalt for wearing course (Błazejowski, 2016), but not so used for DG mixtures for binder and base courses even if Highly Modified Asphalt (HiMA) is currently in production (Błażejowski et al., 2020).
So, the pavement materials are in development, but their improved properties cannot be totally taken into account by the pavement design stage. In fact, the current Polish pavement structure design approach, similarly to other countries worldwide, is simply based on the elastic properties of the materials and requires as inputs only the stiffness modulus, the Poisson's coefficient and the volumetric properties of the asphalt mixtures (Judycki et al., 2014, 2017). The application of such conservative elastic approach does not allow to take into account the actual fatigue and rutting behavior of the mixtures in a wide range of temperatures (climatic conditions) and frequencies (traffic load), often resulting in overestimated pavement thickness, thus adding unnecessary construction time, material, and cost (Kluttz et al., 2018). This problem is further emphasized in the case of high-performance materials, whose actual contribution to the pavement service life could not be caught with conventional elastic-based design methods (Kluttz et al., 2018; Ryś et al., 2019).
Since a potential solution to the deficiencies of such design methods can be the application of the viscoelastic continuum damage (VECD) theory to investigate the fatigue performance, and the viscoplastic theory to characterize the rutting resistance, this research was focused on the application of the AM-PRS to four typical Polish asphalt mixtures. This advanced

methodology could reduce the risk of overdesigning the pavement structures thanks to an accurate evaluation and modelling of the mixture properties.

To this purpose, four typical Polish asphalt mixtures with neat or SBS modified bitumen, currently employed in motorways and expressways, were studied by considering the advanced AM-PRS framework developed in the USA. With this aim, laboratory-compacted specimens (prepared with the mixtures produced in asphalt plants) were subjected to dynamic modulus and cyclic fatigue tests, whose results were used to determine the viscoelastic and damage properties of the mixtures applying the S-VECD theory. The rutting properties were determined by carrying out Stress Sweep Rutting (SSR) tests, based on the viscoplastic theory. Finally, synthetic indices, representative of the expected performance of the mixtures in the pavement, were calculated. The results and parameters from the laboratory tests were used to carried out FlexPAVE^{TM} pavement performance simulations varying the thickness of the pavement structures. The expected service life was then compared with the one obtained with the traditional elastic design method.

Most of the data presented and discussed in the Section 4.4 are published in Spadoni et al. (2023).

4.2 Materials

Four mixtures, usually employed in motorways and expressways in Poland (Judycki et al., 2017), were investigated. The job mix formulas (JMFs) of all the mixtures had been previously studied and optimized through conventional laboratory tests according to European Standards and Polish technical guidelines for heavy traffic pavements. The research involved:

- *SMA 11_PmB:* a Stone Mastic Asphalt for wearing course, designed according to EN 13108-5 (2016) and the Polish technical guidelines WT-2 (2014), with the aggregate gradation 0-11 mm;
- *AC 16_PmB* and *AC 16_35/50*: two dense-graded (DG) mixtures for binder course, designed according to EN 13108-1 (2016) and the Polish technical guidelines WT-2 (2014), with the aggregate gradation 0-16 mm;
- *AC 22_35/50*: a DG mixture for asphalt base course, designed according to EN 13108-1 (2016) and the Polish WT-2 (2014), with the aggregate gradation 0-22 mm.

Figure 4.1 presents the aggregate gradations, made of 100% crushed granite aggregate (virgin) from Norway. The NMAS, corresponding to 90% of passing, is reported in the same figure. *SMA 11_PmB* was characterized by a gap-graded curve with about 10% by aggregate weight of filler. The aggregate gradation of *AC 16_PmB* and *AC 16_35/50* differed mainly for the passing through the 2 mm sieve, since 3% of artificial aggregate made of copper slags was added in *AC 16_PmB*.

Table 4.1 reports the main properties of the mixtures. An adhesion promoter was used in order to enhance the adhesion between bitumen and granite, which would be otherwise penalized by the siliceous nature of the aggregate. The adhesion promoter was a liquid anti-stripping additive based on amino-acids, dosed at 0.3% by bitumen weight. The stabilizer used for the *SMA 11_PmB* mixture (Table 4.1) was a bitumen-coated fiber pellet made of 90% natural cellulose fibers and 10% of 50/70 bitumen, dosed at 0.3% by mixture weight.

The Polymer modified Bitumen (PmB) in the *SMA 11_PmB* mixture was obtained by adding 3.6% of SBS by bitumen weight to a 70/100 base bitumen, whereas the PmB in the *AC 16_PmB* mixture was obtained by adding 2.6% of SBS by bitumen weight to a 35/50 base bitumen. A neat 35/50 bitumen was employed in *AC 16_35/50* and *AC 22_35/50* mixtures. The Performance Grade (PG) values were determined according to AASHTO M 320 (2022). The maximum densities (Gmax) of the mixtures were checked through the pycnometer method (EN 12697-5, 2018).

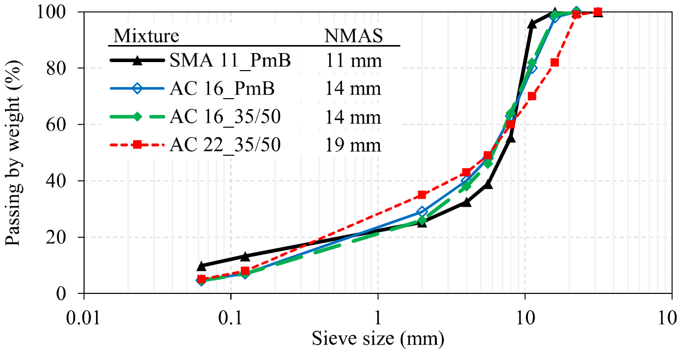

Figure 4.1. Aggregate gradations of investigated mixtures.

Table 4.1. Main properties of the investigated mixtures.

	SMA 11_PmB	*AC 16_PmB*	*AC 16_35/50*	*AC 22_35/50*
% bitumen by asphalt mixture weight	6.4	4.4	4.5	3.9
% SBS polymer by bitumen weight	3.6	2.6	-	-
Bitumen class	45/80-55 (EN 14023)	25/55-60 (EN 14023)	35/50 (EN 12591)	35/50 (EN 12591)
Performance Grade (AASHTO M 320)	PG 76-22	PG 82-16	PG 70-22	PG 70-22
Additives	Adhesion promoter and stabilizer	Adhesion promoter	Adhesion promoter	Adhesion promoter
Gmax (g/cm^3)	2.473	2.570	2.543	2.622

According to the JMFs, the production and compaction temperatures were 185 °C and 145 °C for the PmB mixtures (*SMA 11_PmB* and *AC 16_PmB*), and 190 °C and 135 °C for the mixtures with neat bitumen (*AC 16_35/50* and *AC 22_35/50*), respectively. The mixtures were produced in different asphalt plants located in the northern part of Poland.

4.3 Testing program and procedures

The first step of the experimental program was the laboratory compaction of the mixtures. Since the loose mixtures arrived cold from the asphalt plants, they were heated for three hours at the compaction temperature before the compaction of gyratory samples (EN 12697-31, 2019) with a height of 170 mm and a diameter of 150 mm. The material needed for the gyratory samples (Figure 4.2a) was adjusted in order to achieve the target AV of the test specimens, which were cored from the inner part of the gyratory samples (Figure 4.2b). An average of 10 gyratory samples were compacted for each mixture. The stiffness, fatigue and rutting properties of the test specimens were investigated through dynamic modulus, VECD fatigue tests and SSR tests carried out by means of the Simple Performance Tester (SPT) in the Road Research Laboratory of Gdańsk University of Technology (Figure 4.3). Since the NMAS of all the mixtures was less than or equal to 19 mm (see Figure 4.1), the small specimen geometry was considered to perform dynamic modulus and VECD fatigue tests.
Table 4.2 reports the AV of the test specimens and the average number of gyrations (N_{gyr}) needed to compact the gyratory samples. Regarding the dynamic modulus and VECD fatigue tests, the target AV were the typical field values. Regarding the SSR tests, the target AV simulated a poor field compaction.

Table 4.2. Target AV of the test specimens.

		SMA 11_PmB	*AC 16_PmB*	*AC 16_35/50*	*AC 22_35/50*
Target AV (%)	Dynamic modulus and VECD fatigue tests	3.5 ($N_{gyr} = 14$)	5.0 ($N_{gyr} = 108$)	5.0 ($N_{gyr} = 41$)	5.5 ($N_{gyr} = 36$)
	Stress Sweep Rutting tests	4.5 ($N_{gyr} = 14$)	7.0 ($N_{gyr} = 61$)	7.0 ($N_{gyr} = 25$)	7.0 ($N_{gyr} = 20$)


(a) **(b)**

Figure 4.2. (a) Gyratory samples and (b) test specimens cored from them.

Figure 4.3. SPT at the Road Research Laboratory of Gdańsk University of Technology.

The viscoelastic properties of the test specimens, i.e., dynamic modulus $|E^*|$ and phase angle δ, were determined at the testing temperatures of 4 °C, 20 °C and 40 °C on the basis of the bitumen PG (Table 4.1). For each temperature, the frequencies investigated were 0.1 Hz, 0.2 Hz, 0.5 Hz, 1 Hz, 2 Hz, 5 Hz, 10 Hz and 20 Hz. Three replicate specimens were tested for each mixture, ensuring that the single-operator precision requirements were met.

The testing temperature for cyclic fatigue tests, based on the bitumen PG, resulted of 21 °C for all the mixtures. were carried out on small specimens for DG mixtures, and on large specimens for OG mixture due to its high air void content. For all of them, the testing temperature (based on the bitumen PG, Table 4.1) was equal to 21 °C. In order to obtain tests with the proper duration, the peak-to-peak on-specimen amplitude differed for each mixture and is shown in the next Sections.

S_{app} refers to a temperature that is based on the climatic PG of the location where the pavement is constructed. The city of Gdańsk was considered, which falls in a PG 52-28 climatic zone with a probability level of 98 % (Pszczoła et al., 2017). Therefore, the S_{app} reference temperature resulted equal to 9°C.

Table 4.3 reports the testing temperatures for SSR tests for the investigated mixtures. Both *TL* and *TH* are based on the climatic PG of the city of Gdańsk (PG 52-28 climatic zone), whereas *TH* depends also on the depth at which the mixture will be used in the pavement structure. For this purpose, a 28 cm pavement structure (Judycki et al., 2017) was considered, made of 4 cm of *SMA 11_PmB*, 8 cm of *AC 16_PmB* or *AC 16_35/50*, and 16 cm of *AC 22_35/50*. Such structure was then considered for the pavement performance simulation. In this study, the *RSI* was calculated for each mixture considering the corresponding course within the pavement (wearing, intermediate or base, see Section 3.2) and the climatic conditions of Gdańsk.

Table 4.3. SSR testing temperatures for investigated mixtures.

	SMA 11_PmB	*AC 16_PmB*	*AC 16_35/50*	*AC 22_35/50*
TL (°C)	17	17	17	17
TH (°C)	40	36	36	32

Finally, fatigue resistance and rutting resistance of the mixtures were investigated at the structural level by performing FlexPAVE^{TM} pavement simulations based on the laboratory test results.

4.4 Results and analysis

4.4.1 Dynamic Modulus

Figure 4.4 shows the storage modulus mastercurves (experimental data and related 2S2P1D model) at 21.1 °C for the investigated mixtures. The average AV of the tested specimens (‘%AV’), measured using the saturated surface dry method in accordance with EN 12697-6 (2020), is reported in the same figure. Table 4.4 reports the parameters of the 2S2P1D models. *SMA 11_PmB* is characterized by significantly lower stiffness in a wide range of reduced frequency with respect to the DG mixtures due to its higher amount of softer bitumen (i.e., 6.4 % of PmB 45/80-55, see Table 4.1) and different aggregate gradation (see Figure 4.1), despite its lower AV. Under the same volumetric properties, *AC 16_PmB* is slightly stiffer than *AC 16_35/50*, likely due to the polymer modification (in accordance with literature data (Behnood & Modiri Gharehveran, 2019)). Specifically, the higher stiffness of *AC 16_PmB* at low reduced frequency can enhance the resistance against permanent deformations. The higher stiffness of *AC 22_35/50* is justified by the presence of coarser aggregates (see Figure 4.1) and the lower bitumen content (i.e., 3.9 %, see Table 4.1).

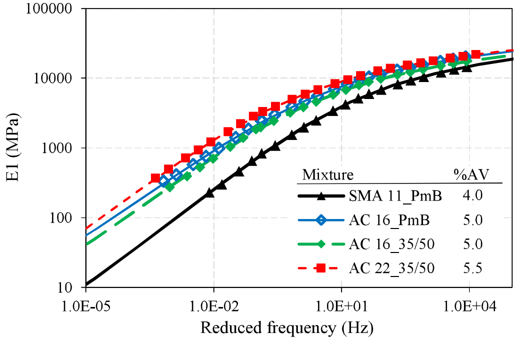

Figure 4.4. Dynamic modulus results: storage modulus mastercurves (experimental data and 2S2P1D model) at 21.1 °C.

Table 4.4. Dynamic modulus results: parameters of the 2S2P1D models for the storage modulus.

Mixture	$E_{1,0}$ (MPa)	$E_{1,\infty}$ (MPa)	ξ	k	h	β	$log\ \tau$
SMA 11_Pmb	1	40000	2.93	0.16	0.48	1E+12	-3.04
AC 16_PmB	5	40000	1.44	0.16	0.44	1E+12	-2.11
AC 16_35/50	4	40000	2.99	0.15	0.45	1E+12	-2.20
AC 22_35/50	1	40000	2.92	0.16	0.45	1E+12	-1.52

Figure 4.5a shows the experimental phase angle mastercurves at 21.1 °C. The high amount of PmB in *SMA 11_PmB* leads to a more viscous behavior of the mixture, as denoted by δ values up to 37°. With respect to *SMA 11_PmB*, the DG mixtures present down-shifted phase angle mastercurves, indicating a more pronounced predominancy of the elastic component of the dynamic modulus. Moreover, as can be seen from the similar values of δ, the DG mixtures have broadly comparable viscoelastic behavior. More in detail, *AC 16_35/50* and *AC 22_35/50* (which contain neat bitumen) exhibit a sub-horizontal phase angle trend at low reduced frequencies, whereas a decreasing phase angle trend can be observed in the PmB mixtures, *SMA 11_PmB* and *AC 16_PmB*, as the frequency is reduced. The latter aspect denotes a rubber-like elastic behavior at very high temperatures in the presence of PmB, which contributes to the improvement of the rutting resistance.

Figure 4.5b shows the time-temperature shift factors and the equations of the related polynomial regressions. The broadly overlapping of the curves, as well as the similar regression coefficients values indicate that the mixtures have broadly the same thermal susceptibility.

In summary, as for the viscoelastic properties, it can be concluded that the experimental results are in good agreement with the composition (aggregate gradation, bitumen type and dosage) of the studied mixtures.

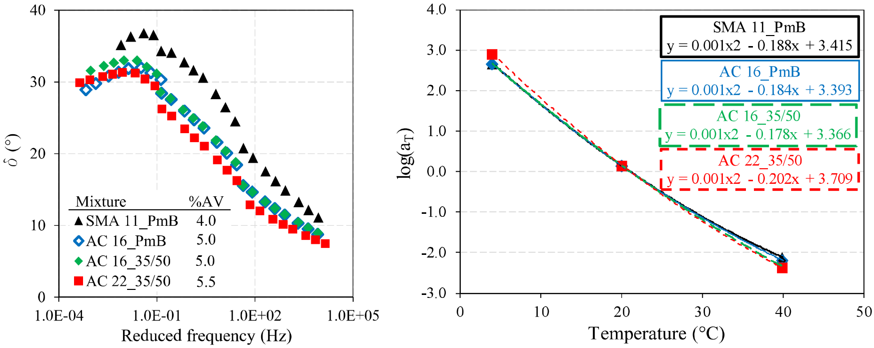

(a) **(b)**

Figure 4.5. Dynamic modulus results: (a) phase angle mastercurves at 21.1 °C and (b) time-temperature shift factors.

4.4.2 Cyclic Fatigue

Table 4.5 summarizes the main parameters of the fatigue tests carried out for the S-VECD characterization of the mixtures. The limits on DMR, number of cycles at failure N_f and D^R variation were met for all tests reported in Table 6 (all characterized by middle failures). The input peak-to-peak strain needed to obtain proper and different durations of the tests can be also observed in the table: specifically, the input strain value increases as the stiffness of the specimen ($|E^*|_{fp}$) decreases. Moreover, the width of the considered strain interval also increases as the stiffness decreases.

Table 4.5. Fatigue properties: main parameters of the S-VECD fatigue tests.

	$|E^*|_{fp}$ (MPa)	DMR	Input strain ($\mu\varepsilon$)	N_f	Cum(1-C)	D^R
SMA 11_PmB-1	4035	0.94	900	12690	10522	0.829
SMA 11_PmB-2	3922	0.92	1150	2600	1995	0.767
SMA 11_PmB-3	4008	0.94	1000	6990	5631	0.806
SMA 11_PmB-4	4114	0.97	900	14060	11777	0.838
AC 16_PmB-1	7121	0.87	400	50640	37272	0.736
AC 16_PmB-2	8033	1.00	430	10320	6994	0.678
AC 16_PmB-3	7858	0.97	450	16310	11888	0.729
AC 16_35/50-1	7088	1.03	400	11490	7491	0.652
AC 16_35/50-2	6516	0.94	430	6060	4001	0.660
AC 16_35/50-3	6660	0.97	380	30050	20126	0.670
AC 22_35/50-1	9671	1.03	230	29520	15167	0.514
AC 22_35/50-2	9525	1.02	210	17880	8667	0.485
AC 22_35/50-3	9534	1.02	230	13020	6222	0.478

Figure 4.6a-b show respectively the experimental damage characteristic curves and their fits with the power function law, whose C11 and C12 values are in Table 4.6. The average AV of the tested specimens, reported in Figure 4.6b, was analogous to that of the specimens tested in the dynamic modulus tests, as prescribed by AASHTO T 411 (2023).

As required, the *C-S* curves related to different specimens of the same mixture overlap. *SMA 11_PmB* and *AC 16_PmB* present damage characteristic curves with similar concavity, denoting a comparable evolution of the damage within the material, due to the presence of PmB in both mixtures. Moreover, the upper position of *AC 16_PmB* curve, followed by that of *AC 16_35/50* and finally *SMA 11_PmB*, confirms that the *C-S* curves of stiffer mixtures (see Figure 4.4) tend to stay above the curves of the softer ones. Comparing the two mixtures for binder course at failure conditions, the significantly higher amount of damage *S* of *AC 16_PmB* curve indicates a lower rate of fatigue resistance loss during cyclic loading, and its lower *C* value means a higher capacity to withstand the damage, ascribable to the polymer modification of the bitumen.

The *C-S* curve of *AC 22_35/50* instead presents a very fast drop of the pseudostiffness (*C*) during the propagation of the microcracks (associated to the evolution of the damage parameter *S*), denoting a brittle behavior and lower tolerance to damage. In addition, it reaches the highest *C* and lowest *S* values at failure, suggesting premature fatigue failure. These outcomes are probably related to the low content of neat bitumen and to the coarse aggregate gradation of this mixture.

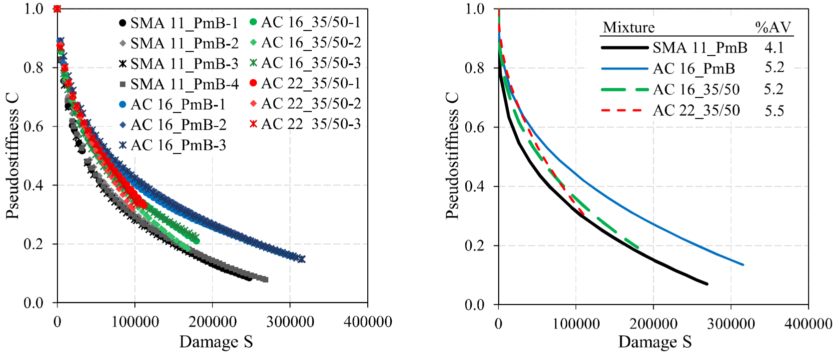

(a) **(b)**

Figure 4.6. Fatigue properties: (a) experimental damage characteristic curves and (b) fits of the damage characteristic curves.

Table 4.6. Fatigue properties: parameters of the damage characteristic curves.

Mixture	C11	C12
SMA 11_Pmb	1.92E-02	3.01E-01
AC 16_PmB	7.20E-03	3.78E-01
AC 16_35/50	7.10E-03	3.91E-01
AC 22_35/50	1.80E-03	5.13E-01

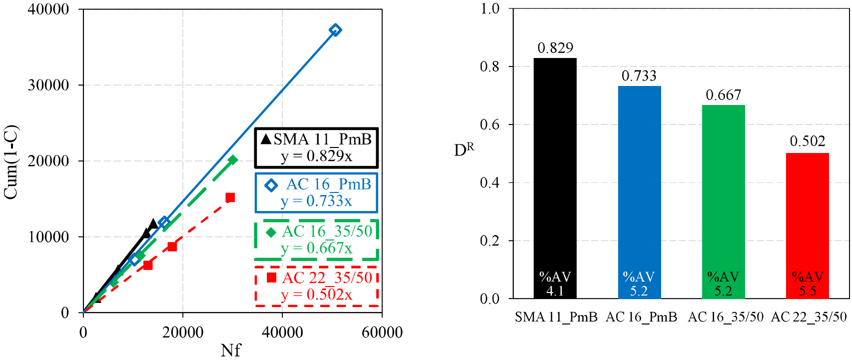

(a) **(b)**

Figure 4.7. Fatigue properties: (a) failure envelopes and (b) D^R values.

Figure 4.7a-b show respectively the failure envelopes and the corresponding D^R values for the investigated mixtures. Figure 4.4b also reports the average AV of the specimens subjected to the fatigue tests. Recalling that a higher D^R value means a higher toughness of the mixture, a clear ranking can be observed. *SMA 11_PmB* showed the greatest ability to absorb energy before fracture (i.e., $D^R = 0.829$) due to the beneficial effects of the high amount of PmB, which makes the mixture softer and more viscous (Figure 4.4 and Figure 4.5a) as well as more resistant during cyclic loading. *SMA 11_PmB* is followed by *AC 16_PmB*, which is also produced with PmB but with a lower bitumen content and a lower percentage of polymers (see Table 4.1). The lower toughness of *AC 16_35/50* is ascribable to the neat bitumen, which has worse fatigue performance with respect to the PmB. Finally, *AC 22_35/50* was characterized by the lowest capacity to absorb energy without fracturing, confirming the observations derived from its *C-S* curve (Figure 4.6b).

Overall, the intrinsic fatigue properties of the investigated mixtures, which are influenced by the aggregate and bitumen properties, are effectively expressed by the S-VECD parameters.

4.4.3 Stress Sweep Rutting

Figure 4.8a shows the experimental permanent viscoplastic strain (ε_{vp}) growth obtained from the SSR tests. The average AV of the two replicates tested at each temperature, reported in the same figure, was similar to the target AV (Table 4.2). Regarding the tests at *TL*, the ε_{vp} evolution and the final values were similar and lower than 2500 με for all mixtures, likely also due to the same testing temperatures (Table 4.3). The different behavior of the mixtures emerged at *TH*, since *SMA 11_PmB* manifested a final ε_{vp} value almost double than *AC 16_35/50*, which in turn reached a value almost double than *AC 16_PmB* and *AC 22_35/50*. Figure 4.8b shows the permanent strain mastercurves, derived from the application of the shift model. The permanent strain mastercurve can fit both the primary and secondary region behaviors of a mixture (D. Kim & Kim, 2017), and represents the rut depth evolution which would be obtained at a single deviatoric stress, pulse time, rest period, confining pressure (i.e., 689 kPa, 0.4 s, 3.6 s, 69 kPa, respectively) at *TH* temperature (see Table 4.3). The markers indicate the shifted strain at the end of each block. The ε_{vp} growths reflect the ones obtained from SSR tests performed at *TH*. *SMA 11_PmB* showed the worst rutting resistance, as denoted by a rapid increase of the rut depth in the primary region and a high slope of the quasi-linear secondary region. This outcome could be somehow unexpected, since it is generally believed that SMA mixtures have good resistance against rutting due to the high coarse aggregate content and strong skeleton of interlocked aggregate particles, despite their high bitumen content (Błazejowski, 2016). However, the main reason of such behavior might be attributable to the high amount of soft bitumen employed (i.e., 6.4 % of PmB 45/80-55, see Table 4.1) and to the AV of the tested specimens, representing the condition of poor compaction, as denoted also by the low N_{gyr} values in Table 4.2. In fact, the behavior emerged from the tests can be correlated with a fast densification of the mixture until the aggregate interlocking is reached (Choi & Kim, 2014; Habbouche et al., 2022), which is justified also by the higher voids in the mineral aggregate (VMA) with respect to the DG mixtures (i.e., 17.7 % vs. 14-15 %). Given the limited literature data about SSR tests conducted on SMA mixtures, further study may be necessary to verify the suitability of the test for such type of mixtures. In fact, it was demonstrated that the rutting behavior of SMA mixtures significantly depends on the performed test, and the laboratory observations may not correspond to the in-field ones (Batioja-Alvarez et al., 2020; Habbouche et al., 2022).

The comparison of the performance between the two binder mixtures, at the same testing conditions and similar volumetric properties, highlights that the SBS polymer significantly enhances the rutting resistance, ensuring a lower permanent strain accumulation in the primary and secondary regions of the curve. Even *AC 22_35/50*, whose reference curve basically overlaps the *AC 16_PmB* one, presents a high resistance to permanent deformations likely due to its aggregate gradation and low bitumen content.

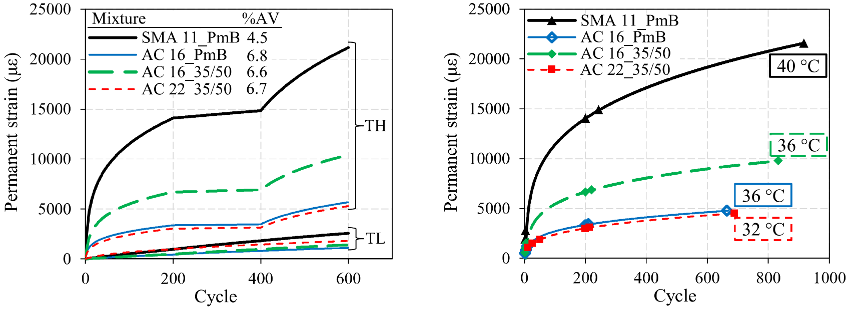

(a) **(b)**

Figure 4.8. Rutting properties: (a) experimental permanent strain growth in SSR tests and (b) permanent strain mastercurves.

In general, the SSR results are in agreement with the composition of the mixtures, especially for the DG mixtures for binder and asphalt base courses. For *SMA 11_PmB*, instead, the outcomes of the tests are likely influenced by the volumetric properties considered for the SSR specimens.

4.4.4 Synthetic indices

Figure 4.9 shows the S_{app} fatigue index and the *RSI* rutting index, often used by road agencies for asphalt mixture design and quality controls. The suggested threshold values are reported with grey horizontal lines, and the corresponding designations (S, H, V, E) are indicated as well. The grey areas represent the range where the mixtures' fatigue and rutting performance falls in the same category.

A better fatigue performance can be expected from the *SMA 11_PmB* mixture, followed by *AC 16_PmB*, *AC 16_35/50*, and *AC 22_35/50*. According to literature (Wang et al., 2022), the S_{app} maximum value is usually 50, which suggests that the definition of this synthetic index for SMA mixtures may need further calibration to better take into account the peculiar mix design of such type of mixtures. Moreover, it should be underlined that all the S_{app} values are relatively high for the presence of only virgin aggregate (i.e., no reclaimed asphalt), and higher values are obtained with finer gradation, increased bitumen content and polymer modification, which is consistent with FHWA-HIF-19-091 (2019). It is also worth pointing out that such results are in agreement with the ones obtained from conventional fatigue tests (i.e., four-point bending tests) carried out on the same mixtures (Błażejowski et al., 2020).

RSI predicts the overall rutting performance of a mixture within a given pavement subjected to fixed traffic conditions and known climatic conditions (climate of Gdańsk in this study). Since it is calculated considering standard pavement structures which differ depending on the position of the mixture in question (see Section 2.5), only *AC 16_PmB* and *AC 16_35/50* are directly comparable in terms of *RSI*.

SMA 11_PmB is characterized by *RSI* value equal to 4.88 %, corresponding to a *Standard* tier of rutting resistance. However, it should be noted that the thickness of the wearing course in the considered standard pavement (i.e., 10 cm, see Section 3.6.1) does not represent the actual thickness of 4 cm usually adopted in Poland (Błazejowski, 2016) and recommended by the specifications in Germany (where such mixtures were originally developed). Comparing the performance of the two binder mixtures, the rutting resistance of *AC 16_PmB* is expected to be about two times higher than *AC 16_35/50*, due to the higher stiffness at low reduced frequencies (Figure 4.4) and the lower thermal susceptibility (**Figure 4.5**b) provided by the PmB. Differently from the other mixtures, the predicted ε_{vp} of *AC 22_35/50* does not reflect the ranking obtained at *TH* (Figure 4.8). However, the expected ε_{vp} after 20 years is very low also in this case (*RSI* = 1.44 %).

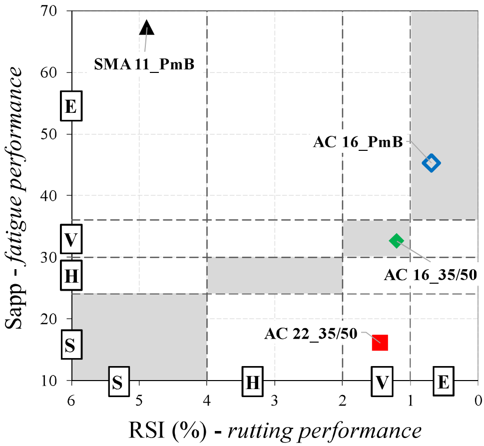

Figure 4.9. Synthetic indices

In conclusion, *SMA 11_PmB* is classified as *Standard* against rutting and *Extremely Heavy* against fatigue cracking, underlining that its high amount of soft bitumen may have negative effects on the permanent deformation behavior but beneficial effects on the resistance to cyclic loading. Therefore, this analysis suggests that rutting is the predominant distress for *SMA 11_PmB*. However, it should be recalled that, for such mixture, the outcomes of the SSR tests were influenced by the volumetric properties of the specimens representing a poor compaction. In addition, the *RSI* calculation considers a layer thickness of 10 cm instead of the typical thickness of 4 cm. *AC 16_PmB* and *AC 16_35/50* fall in the *Extremely Heavy* and *Very heavy* tiers respectively for both fatigue and rutting, meaning that the design of both mixtures is well balanced and there is no predominant distress. Moreover, the polymer modification leads to a better overall performance. *AC 22_35/50* results in the *Very heavy* tier for rutting and in the *Standard* tier for fatigue, which thus represents the predominant distress. The coarser aggregate and the low bitumen content stiffen the mixture, increasing the rutting resistance, but penalizing the behavior against cyclic loading at intermediate temperatures.

4.5 Pavement performance simulations

4.5.1 Simulations of a typical motorway section

To evaluate the performance of a typical motorway section, FlexPAVE^{TM} analysis was performed for a 30-year pavement service life under thermal effects, traffic loading and rutting distress. The reference catalogue of Polish flexible pavement is the "Katalog Typowych Konstrukcji Nawierzchni Podatnych i Polsztywnych" (KTKNPiP-2012), where the pavement structures are divided into 7 types (KR1-KR7), based on the traffic to which it will be subjected. Other details will be given in the next Section 4.5.2.

The structure of the simulated pavement belongs to KR6, consisting of a 4-cm wearing layer, a 8-cm binder layer, a 16-cm base layer, and a 20-cm foundation on the subgrade (Figure 4.10). The design traffic level for KR6-roads is between 22 and 52 million ESALs during the design life of 30 years. For this study, the upper limit was chosen, i.e., 52 million 100-kN ESALs. The Polish reference ESAL, put as input in FlexPAVE^{TM}, is a 100-kN single axle with single wheel. A speed of 60 km/h, a tire inflation pressure of 850 kPa considered. The tire-pavement contact area was set as circular, and any traffic growth was considered.

Table 4.7 presents the material properties of the two scenarios evaluated in the simulations. For all two scenarios, the upper 4-cm layer and the 16-cm base layer are modeled based on the SMA 11_PmB and AC 22_35/50, respectively, whereas the material properties of the 8-cm binder layer used as input differ: in Scenario 1, the binder layer is modeled with the AC 16_35/50, whereas in Scenario 2 with AC 16_PmB. The foundation and the subgrade were modeled as linear elastic materials with stiffness modulus values of 400 MPa (unbound material 0/31) and 120 MPa (improved subgrade), respectively, determined from FWD tests (Cardone et al., 2022).

As for the climatic conditions, based on a comparison of the annual temperatures and precipitation, the city of Gdańsk is usually matched with Chicago in Illinois (whose climatic data are present in the FlexPAVE^{TM} database).

Table 4.7. Simulations of a typical motorway section: material properties considered for each scenario.

Scenario	Wearing layer (4 cm)	Binder layer (8 cm)	Base layer (16 cm)	Foundation (20 cm)	Subgrade
1	SMA 11_PmB	AC 16_35/50	AC 22_35/50	E = 400 MPa	E = 120 MPa
2	SMA 11_PmB	AC 16_PmB	AC 22_35/50	E = 400 MPa	E = 120 MPa

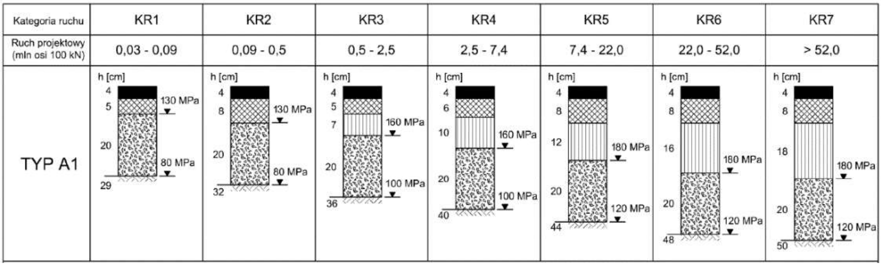

Figure 4.10. Typical pavement structures in Poland (Judycki et al., 2014).

Regarding the simulations considering the thermal effects and the fatigue loading, Figure 4.11a-b present the damage contours of Scenario 1 (i.e., with the material properties of the binder with neat bitumen) and Scenario 2 (i.e., with the material properties of the binder with PmB), respectively, after 30 years of service. Figure 4.11c-d present the damage evolution and the corresponding cracking evolution on the surface, respectively.

For both the Scenarios, it is clear that the damage is mainly concentrated at the bottom of the asphalt layers, strictly due to the cyclic loading. It should be noted that after 30 years of service, such damage leads to the complete failure of 3-4 cm of asphalt concrete at the bottom (dark red area, DF =1).

Moreover, it is possible to observe the area of the wearing layer slightly damaged in correspondence of the wheel. In Scenario 2, such area even involves the binder layer, right under the wearing layer. This damage distribution is likely attributable to both top-down cracking and thermal effects. The top-down cracking is broadly the same in both the Scenarios, since it involves the wearing layer with the SMA 11_PmB (Table 4.7). The thermal effects, which represent a loading applied in a displacement-controlled test (Saleh et al., 2020), depends on the mixture's capacity to relieve the stress. The slightly higher damaged area is in Scenario 2, even away from the wheel load, and it is ascribable to the difference in stiffness between the binder and wearing layers (higher for AC 16_PmB, see Figure 4.4).

Overall, the damage evolution is comparable for both the Scenario, as clearly visible in Figure 4.11c. The cracking evolution, too (Figure 4.11d), follows of course the same comparable trend, even though a slightly higher value after 30 years is registered for the Scenario 2, due to the higher damage in the upper part of the pavement. The percentage values after 30 years are about 5.0%, highlighting a very good fatigue performance of the pavement, ensuring the service life of 30 years for which has been designed by the Polish catalogue KTKNPiP.

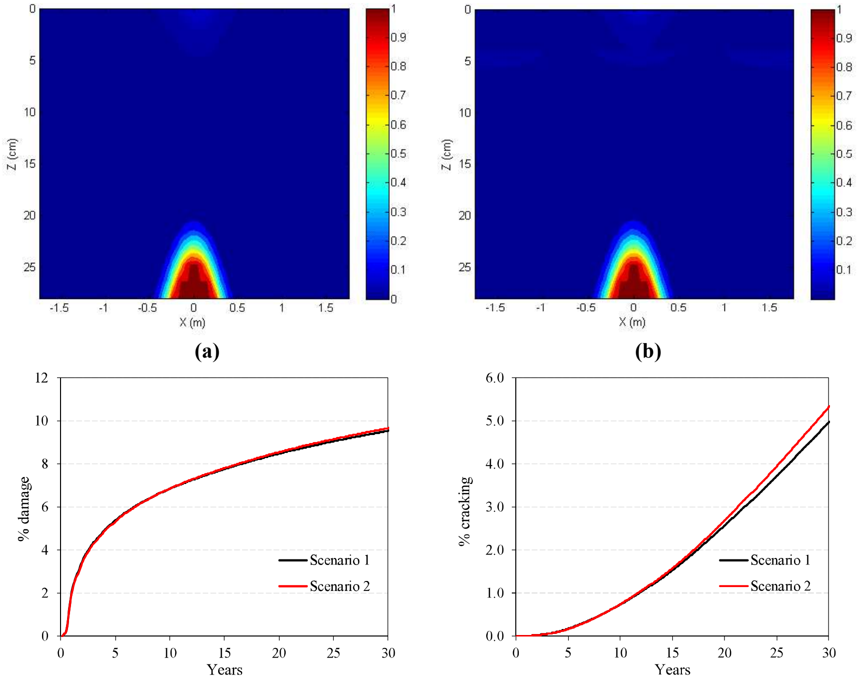

(a) (b)

(c) (d)

Figure 4.11. Simulations of a typical motorway section: damage contours of (a) Scenario 1 and (b) Scenario 2 after 30 years; (c) damage evolution and (d) cracking evolution.

Regarding the simulations of the rutting performance, Figure 4.12a-b present the rut depth evolutions of each layer and the sum for Scenario 1 and Scenario 2, respectively. For comparison purpose, the limit of the rut depth provided by the AASHTO regarding the M-PEDG method (Guide for Mechanistic-Empirical Design of New and Rehabilitated Pavement Structures, 2004) was chosen. Such limit of 1.27 cm (0.5 inches) refers to motorway pavement and it is the upper limit to not have the aqua-planing phenomenon at a speed of 90 km/h.

Both the Scenarios provide a very good performance against rutting, since the limit should be reached after more than 15 years. An higher performance could be expected from the structure of Scenario 2, where the service life of pavement increases of about 5 years with respect to Scenario 1. Even the rut depth value after 30 years of Scenario 2 (1.48 cm) is slightly higher than the one of Scenario 1 (1.38 cm). Observing the rut depth evolutions of each course, it is clear that such higher performance is due to lower permanent deformation of AC 16_PmB thanks to the polymer modification (in according with the lower *RSI* value, see Figure 4.9). The rut depth evolutions of the other courses are comparable. It should be noted that SMA 11_PmB presents a satisfactory performance, despite the high *RSI* value (i.e., 4.88, Figure 4.9). This highlight that the synthetic indices should be considered only for comparison purpose between similar mixtures (for example varying the bitumen), but pavement simulations should be performed to totally catch the actual mixture behavior in the pavement.

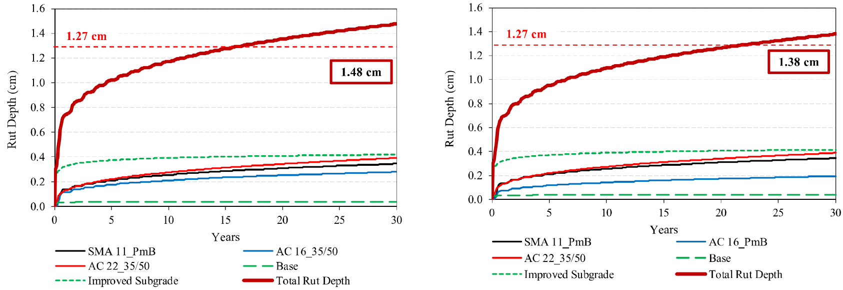

(a) **(b)**

Figure 4.12. Simulations of a typical motorway section: rut depths evolutions in (a) Scenario 1 and (b) Scenario 2.

4.5.2 Comparison with the conventional linear elastic design method

The conventional linear elastic design method

As in many Countries in Europe, in Poland the conventional pavement design tool is based on the elastic theory. The method is very simple and user-friendly, but the actual material properties cannot be totally taken into account. Moreover, the prediction of the service life is based on empirical equations calibrated on the field, so they are may not reliable for all the cases.

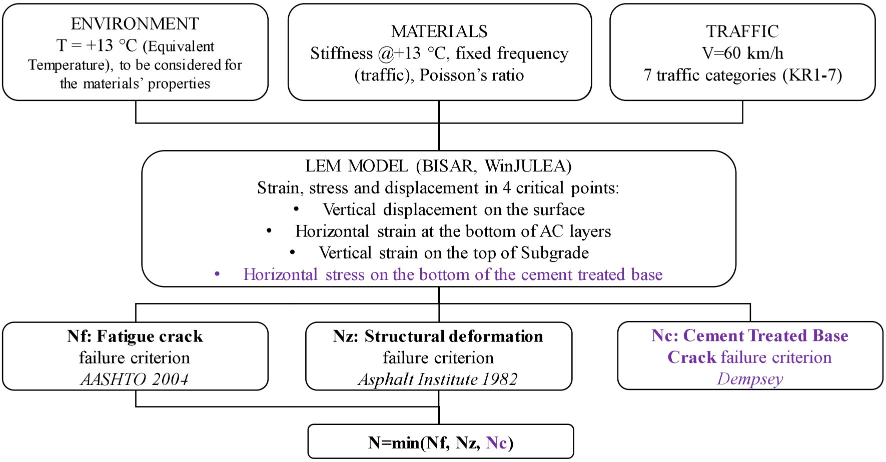

Figure 4.13. Summary of the conventional design approach in Poland.

The conventional pavement design method for flexible pavements is deeply explained in (Judycki et al., 2014) A summary is represented in Figure 4.13. The input data are the following:

- Environment. The climatic conditions are taken into account by the temperature at which the stiffness of the asphalt concrete must be evaluated. In Poland, the so-called "equivalent temperature" is considered, equal to +13 °C (Pszczola, 2019).
- Traffic. The loading conditions, specifically the design number of 100-kN ESALs, are the basis on which the pavement structures are differentiated in the Polish catalogue (Figure 4.10, KTKNPiP). The design speed is the one of the heavy vehicles of 60 km/h.
- Materials. The asphalt mixtures' properties are the stiffness and the Poisson's ratio. This last one is assumed of 0.3. The stiffness should be evaluated at the equivalent temperature and at a frequency characteristic of the traffic. The stiffness can be tested through any method. For this study, as shown in Table 4.8, the complex modulus data from the mastercurve and ITSM (at +13 °C, EN 12697-26, 2022) were available. Since the conventional 4PB test, usually employed to evaluate the fatigue resistance in Poland, is performed at the frequency of 10 Hz, it was chosen to use $E^*|_{+13\ °C,\ 10\ Hz}$. Moreover, such values are the most comparable with the ones given by the Polish Catalogue (KTKNPiP). For the unbound layers, the stiffness and the Poisson's ratio are requested as well. These values are suggested by the Polish Catalogue, based on the traffic category (Figure 4.10).

Table 4.8. Stiffness data of asphalt mixtures for conventional design method.

Mixture	Km/h	Hz	$E^*|_{+13\ °C}$ (MPa)	$ITSM|_{2Hz}$ (MPa)
SMA 11_PmB	60	10 50	8146 10722	4036
AC 16_PmB	60	10 50	12853 15820	6172
AC 16_35/50	60	10 50	11032 13634	5731
AC 22_35/50	60	10 50	14517 17419	9213

Then, the pavement structure with the materials' properties for each course is put as input in a LEM software. In this study, WinJULEA was used (Figure 4.14). The strain, stress and displacement are evaluated in four critical points of the pavement to calculate the service life:

- Vertical displacement on the surface. It is used to check the maximum permanent deformation on the surface.
- Horizontal strain at the bottom of AC layers. It is used to calculate the service life due to fatigue, following the failure criterion given by AASHTO 2004 (Equation 4.1):

$$N_{f1} = 7.3557(10^{-6})Ck_1'\left(\frac{1}{\varepsilon_t}\right)^{3.9492}\left(\frac{1}{E}\right)^{1.281} \tag{4.1}$$

where ε_t is the horizontal strain at the bottom of AC layers, k_1' is a calibration constant depending on the asphalt layer thickness and type of fatigue cracking (it takes into account that thin pavements works in strain mode and thick pavements in stress mode), E is the stiffness of the lowest AC layer (i.e., base layer), $C = 10^M$ is a coefficient depending on the volumetric parameters of the lowest AC layer (i.e., base layer) with

$$M = 4.84\left(\frac{V_b}{V_a + V_b} - 0.69\right) \tag{4.2}$$

where V_b is the bitumen void content, $V_a$is the air void content.
Then, N_{f1} must be multiplied by the acceptable fatigue cracking on the surface (FC), calculated as (Equation 4.3):

$$FC_{bottom} = \left(\frac{100}{1 + e^{\left(-2C_2' + C_2' \, log_{10}(D \cdot 100)\right)}}\right) \tag{4.3}$$

where D is the damage on the cross-section area and $C_2' = -2.40874 - 39.748(1 + h_{AC}/2.54)^{-2.856}$ where h_{AC} is the thickness of the AC layers.
So, the service life due to fatigue is finally calculated as $N_f = FC_{bottom} \cdot N_{f1}$.

- Vertical strain on the top of the subgrade. It is used to calculate the service life due to structural deformation, following the failure criterion given by the Asphalt Institute (1982) (Equation 4.4):

$$N_z = 0.0105\left(\frac{1}{\varepsilon_v}\right)^{4.484} \tag{4.4}$$

where ε_v is vertical strain on the top of subgrade.
- Horizontal stress on the bottom of the cement treated base (not in this study), that is used according to the Dempsey criterion.

The service life of the pavement is the minimum between the ones due to fatigue and to structural deformation.

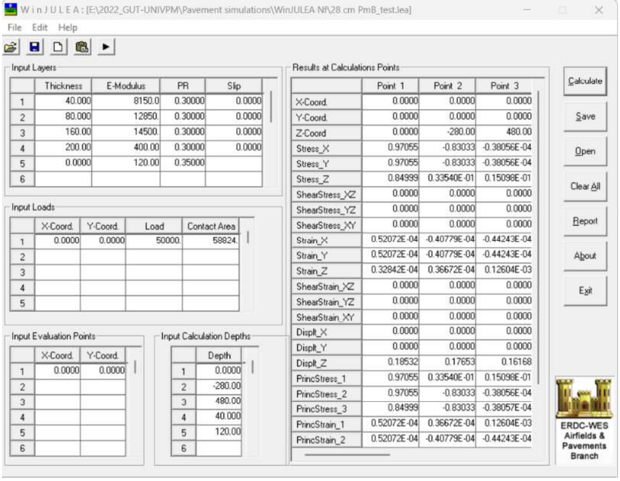

Input Layers

	Thickness	E-Modulus	PR	Slip
1	40.000	8150.0	0.30000	0.0000
2	80.000	12850.	0.30000	0.0000
3	160.00	14500.	0.30000	0.0000
4	200.00	400.00	0.30000	0.0000
5	0.0000	120.00	0.35000	
6				

Input Loads

	X-Coord.	Y-Coord.	Load	Contact Area
1	0.0000	0.0000	50000.	58824.
2				
3				
4				
5				

Input Evaluation Points

	X-Coord.	Y-Coord.
1	0.0000	0.0000
2		
3		
4		
5		
6		

Input Calculation Depths

	Depth
1	0.0000
2	-280.00
3	480.00
4	40.000
5	120.00
6	

Results at Calculations Points

	Point 1	Point 2	Point 3
X-Coord.	0.0000	0.0000	0.0000
Y-Coord.	0.0000	0.0000	0.0000
Z-Coord	0.0000	-280.00	480.00
Stress_X	0.97055	-0.83033	-0.38056E-04
Stress_Y	0.97055	-0.83033	-0.38056E-04
Stress_Z	0.84999	0.33540E-01	0.15098E-01
ShearStress_XZ	0.0000	0.0000	0.0000
ShearStress_YZ	0.0000	0.0000	0.0000
ShearStress_XY	0.0000	0.0000	0.0000
Strain_X	0.52072E-04	-0.40779E-04	-0.44243E-04
Strain_Y	0.52072E-04	-0.40779E-04	-0.44243E-04
Strain_Z	0.32842E-04	0.36672E-04	0.12604E-03
ShearStrain_XZ	0.0000	0.0000	0.0000
ShearStrain_YZ	0.0000	0.0000	0.0000
ShearStrain_XY	0.0000	0.0000	0.0000
Displt_X	0.0000	0.0000	0.0000
Displt_Y	0.0000	0.0000	0.0000
Displt_Z	0.18532	0.17653	0.16168
PrincStress_1	0.97055	0.33540E-01	0.15098E-01
PrincStress_2	0.97055	-0.83033	-0.38056E-04
PrincStress_3	0.84999	-0.83033	-0.38057E-04
PrincStrain_1	0.52072E-04	0.36672E-04	0.12604E-03
PrincStrain_2	0.52072E-04	-0.40779E-04	-0.44243E-04

Figure 4.14. Example of WinJULEA calculation.

In this study, the scenarios presented in Table 4.9 were evaluated. The volumetric properties reported in this table are the ones of the base layer since it is the only considered in this method. All the scenarios provide the same data of the unbound base and of the subgrade, according to Judycki et al. (2017). The scenario "Edefault 7%AV" considers all the data given by the Polish Catalogue (KTKNPiP). The scenario "Edefault 5.5%AV" considers the stiffness value according to Judycki et al. (2017) and the volumetric properties (AV and V_b) of the investigated mixtures. The scenarios "Etest-neat" and "Etest-PmB" consider the stiffness and volumetric data of the investigated mixtures (Scenario 1 and 2, respectively, of Table 4.7).

Table 4.9. Conventional linear elastic design: conditions evaluated.

Scenario	E default 7%AV	E default 5.5%AV	Etest-neat	Etest-PmB
Volumetric properties	AV=7% V_b=10%	AV=5.5% V_b=9.25%	AV=5.5% V_b=9.25%	AV=5.5% V_b=9.25%
SMA 11_PmB	7300 MPa ν=0.3	7300 MPa ν =0.3	8150 MPa ν =0.3	8150 MPa ν =0.3
AC 16_35/50 (Scenario 1)	10300 MPa ν =0.3	10300 MPa ν =0.3	11000 MPa ν =0.3	-
AC 16_PmB (Scenario 2)			-	12850 MPa ν =0.3
AC 22_35/50	9820 MPa ν =0.3	9820 MPa ν =0.3	14500 MPa ν =0.3	14500 MPa ν =0.3
Unbound Base (UM 0/31)	400 MPa ν =0.3	400 MPa ν =0.3	400 MPa ν =0.3	400 MPa ν =0.3
Improved Subgrade	120 MPa ν =0.35	120 MPa ν =0.35	120 MPa ν =0.35	120 MPa ν =0.35

Element of comparison: fatigue cracking on the surface

The identified element for the comparison of the service life was the fatigue cracking on the surface (so called *FC* in the conventional Polish approach, *%cracking* in VECD approach). In fact, the thicknesses of the typical pavement structure of Figure 4.10 of the KTKNPiP were calculated assuming a maximum FC of 15% (Equation 4.3), as shown in Figure 4.15 (curve referred to AASHTO FC=15%).

Equation 4.3 is a sigmoidal function, as represented in Figure 4.16, as well as the transfer function proposed by Wang et al. (2021) for the FlexPAVE^{TM} results.

It should be underlined that, differently from the FC applied to the FlexPAVE^{TM} results (Y. D. Wang et al., 2021), FC of Equation 4.3 can only take into account bottom-up cracking and not top-down cracking, based on the development of Equation 4.1 which consider only bottom-up cracking. Moreover, the maximum value of FC is 50%, given by a damage *D* of 100% (log2), differently from the *%cracking* function.

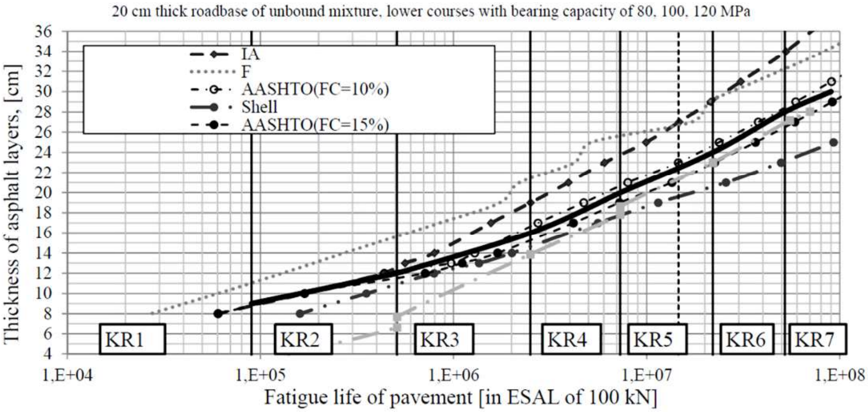

Figure 4.15. Conventional linear elastic design: thickness of asphalt layers considering FC = 15% (Judycki et al., 2014).

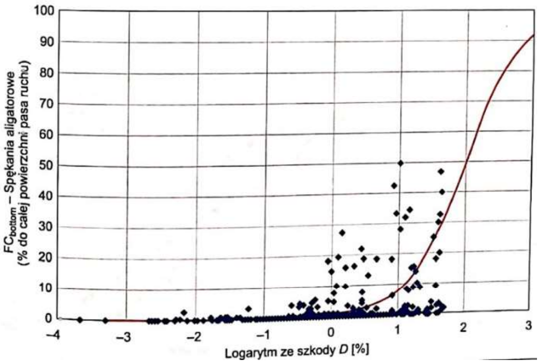

Figure 4.16. Conventional linear elastic design: function for the fatigue cracking (Judycki et al., 2014).

Comparison between the two methods

Pavement performance simulations were carried out applying the conventional linear elastic approach in the scenarios presented in Table 4.9, and with the viscoelastic approach using FlexPAVE^{TM}. The objective was to compare the fatigue resistance, whereas the rutting performance was not investigated (it was only checked that the service life due to fatigue was lower than the one due to fatigue according to the elastic method).

Pavement performance simulations with FlexPAVE^{TM} were carried out with the same two scenarios explained in Section 4.5.1, now called "VECD-neat" and "VECD-PmB", with the only difference that an isothermal of +13°C (equivalent temperature) was considered for the climatic conditions. Indeed, such two scenarios are comparable with "Etest-neat" and "Etest-PmB" of Table 4.9.

The simulations were carried out considering increasing thickness of the AC layers. Specifically, the AC layers thickness varied from 20 cm to 30 cm with step of 2 cm. At each step, 2 cm was added to the base layer, according to traffic category KR5-KR6-KR7 (Figure 4.10), whereas the wearing and binder layers were constantly 4 cm and 8 cm thick, respectively.

In the conventional linear elastic method, the service life in terms of N_f was calculated with the previous formulas (Equation 4.1-4.3).

Differently, in FlexPAVE^{TM} the service life in terms of ESAL must be an input data. For this reason, the adopted procedure consisted in carrying out simulation setting a number of daily ESALs to which correspond a fatigue cracking at 30 years higher than 15% (Figure 4.17). Finally, N_f was calculated as the product between the year to which corresponds *%cracking* of 15% and the input daily ESALs (properly multiplied by the number of months and days). It must be underlined that this procedure can be applied because the used version of FlexPAVE^{TM} does not include the ageing phenomena.

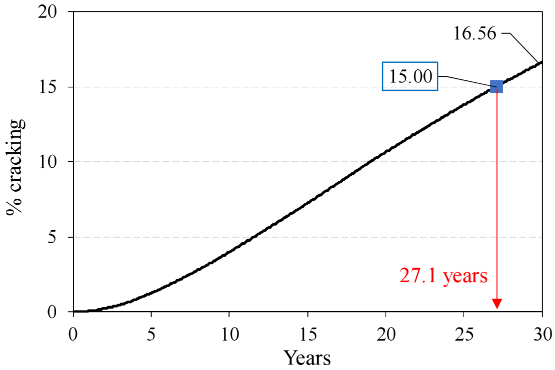

Figure 4.17. Adopted procedure to obtain N_f from FlexPAVE^{TM} corresponding to %cracking = 15%.

The results of the comparison between the prediction of the service life based on the linear elastic and VECD approach are shown in Figure 4.18a-b. In Figure 4.18a, the N_f are reported for each of the scenario in Table 4.9, compared with the two VECD scenarios (VECD-neat Scenario 1; VECD-PmB-Scenario 2).

First, comparing “Edefault 7%AV” and “Edefault 5.5%AV” results, it is possible to observe that decreasing the AV content and the bitumen content maintaining the stiffness given by the Polish Catalogue (KTKNPiP), the estimated N_f increases due to the AC’s more dense structure.

Comparing “Etest-neat” and “Etest-PmB” results, i.e., looking at the effect of the polymer modification in the binder mixture at the same volumetric properties, it is clear that the beneficial effect of the SBS is slightly detectable in terms of N_f. This is likely due to the higher stiffness provided by the modification (see Table 4.9), so that the binder layer absorbs

a slightly higher load stress decreasing the strain occurring at the bottom of the AC layers. Such interpretation is then confirmed by the comparison of these results with “Edefault 5.5%AV”. The increase of N_f is about 25% for all the AC layers thickness, and it is ascribable to the higher stiffness of all the layers (Table 4.9), at the same volumetric properties.
Comparing the VECD results, even in this case the beneficial effect of the polymer modification is slightly visible, as observed in Section 4.5.1.

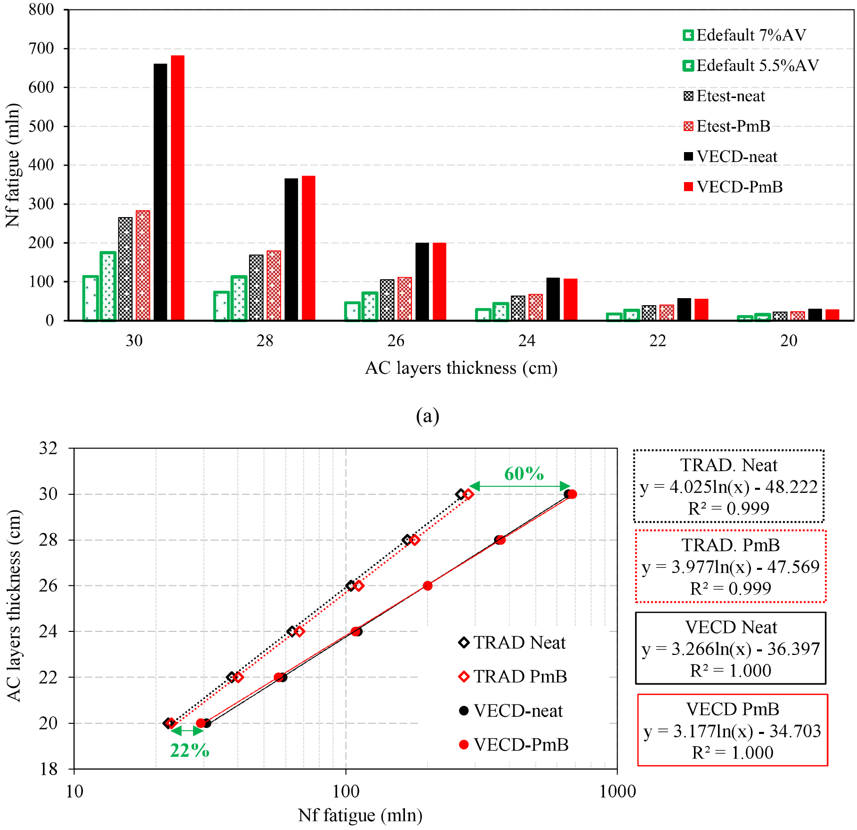

(a)

(a)

Figure 4.18. Comparison between linear elastic and VECD approaches in predicting the service life varying the AC layer thickness.

Finally, the most interesting results emerge from the comparison between the VECD and linear elastic approach results (plain vs. dotted columns in black/red). It was observed that both methods provide a logarithmic relation between the predicted N_f and the AC layer thickness, as shown by the regression equations in Figure 4.18b characterized by a coefficient of determination R^2 equal to 1 (or very close). The prediction of the service life with the VECD method is strongly higher than the one with the elastic approach. In particular, as indicated in Figure 4.18b, the increase goes from to 20% for the pavement thickness to 20 cm up to 60% for the 30 cm-thick pavement. This underlines the major benefits in using a software capable to fully taken into account the actual viscoelastic properties of the asphalt mixtures employed in the pavement. However, it must be always recalled that up to date FlexPAVE^{TM} is not capable to consider the ageing, so such results are not completely realistic.

4.6 Summary of the findings

The objective of this study was to evaluate the reliability of the advanced asphalt mixture performance-related specifications (AM-PRS) for the characterization of the fatigue and rutting behavior of typical Polish asphalt mixtures, currently used for heavy traffic pavements in motorways and expressways, and carry out pavement performance simulations evaluating different scenarios in comparison with the conventional linear elastic approach, too. The studied mixtures, produced in the asphalt plant and compacted in the laboratory, included a SMA mixture for wearing course, two mixtures for binder course with neat bitumen or PmB, and a mixture for asphalt base course with neat bitumen.

The laboratory results showed that the SMA mixture was very tough against fatigue cracking (S_{app} classification: extremely heavy traffic), but also more prone to rutting (*RSI* classification: standard traffic), which resulted as the predominant distress. The main reasons of this outcome lay in the composition of the mixture, i.e., high amount of relatively soft PmB and high VMA. The suitability of the SSR test and the *RSI* parameter for SMA mixtures may also need further study, given the limited data currently available in literature. The two binder mixtures exhibited no predominant distress, indicating a well-balanced mix design. However, the mixture with neat bitumen was classified as resistant to very heavy traffic, whereas the mixture with PmB was resistant to extremely heavy traffic. As expected, the polymer modification enhanced the resistance to both distresses thanks to a higher toughness and a higher stiffness at high temperatures. The base mixture is expected to suffer fatigue cracking (S_{app} classification: standard traffic) more than rutting (*RSI* classification: very heavy traffic), likely due to the low amount of bitumen and coarser aggregate gradation. Such factors led to a higher stiffness, which on one hand enhanced the rutting resistance but on the other hand decreased the damage tolerance.

The pavement performance simulations with the software FlexPAVE^{TM} considering the actual climatic and traffic conditions on the structure provided by the Polish Catalogue highlighted the excellent fatigue performance with service life more than 30 years. Conversely, the permanent deformations occurring on the surface would lead to a service life of about 15 years and then a maintenance operation would be needed to avoid the aqua-planing phenomenon. The beneficial effect of the polymer modification in the binder layer is present but slightly visible. Since the cracking failure does not reach the binder layer, its higher fatigue resistance cannot be expressed; its positive contribution for both fatigue and rutting distresses is mainly ascribable to its slightly higher stiffness instead.

Finally, from the comparison of the VECD approach with respect to the conventional elastic method emerged that the VECD approach can lead to an increase of the service life from 20% up to 60% for thick pavement thanks to the evaluation of the more realistic stress and strain in the viscoelastic domain.

It can be concluded that these findings were consistent with the composition of the studied mixtures, demonstrating the reliability and applicability of the AM-PRS developed in the USA even for typical Polish mixtures.

Chapter 5.
S-VECD characterization of warm mix asphalts after six years of service

5.1 Background and objectives

With the increasingly stringent environmental limitations, all industries are reconsidering their production methods in order to minimize impacts. Within the framework of transportation infrastructures, the conventional hot mix asphalt (HMA) is produced and laid down at high temperatures (140-180 °C), which imply non-negligible emissions and energy consumption (Cheraghian et al., 2020; Rubio et al., 2012). For these reasons, in the last decade, warm mix asphalt (WMA) technology has undergone a strong development (Abed et al., 2019). WMA are mixtures produced and compacted at lower temperature (i.e., 100-140 °C) (Behnood, 2020), through three main methodologies: foaming processes, organic additives and chemical additives (Behnood, 2020; S. D. Capitão et al., 2012; Cheraghian et al., 2020; Rubio et al., 2012). It has been demonstrated that the use of chemical additives, which are usually a combination of surfactants, polymers, emulsification agents and aggregate coating promotors, guarantees better performance in terms of workability and moisture susceptibility, ensuring also less binder ageing (Behnood, 2020; Cheraghian et al., 2020; Ingrassia et al., 2018; Kusam et al., 2017; Pereira et al., 2018; Yu et al., 2022). Moreover, the reduction of temperature has many beneficial effects, such as reduced emissions and energy savings (environmental and economic benefits), increased haul distance and extended paving season (technical benefits), improved working conditions (benefits for the human health) (Almeida-Costa & Benta, 2016; Almusawi et al., 2022; Stimilli, Frigio, Canestrari, et al., 2017; Vaitkus et al., 2016; X. Yang et al., 2019).

However, it is well-known that low temperature production results in less oxidative hardening of the binder, which could lead to a greater rutting potential (Behnood, 2020; S. D. Capitão et al., 2012). Since in Europe styrene-butadiene-styrene (SBS) polymer modified bitumen (PMB) is widely used to increase the rutting and fatigue resistance of asphalt mixtures (Airey, 2003, 2004; Behnood & Modiri Gharehveran, 2019; Lin et al., 2019), some researchers investigated the effect of chemical additives on SBS modified WMA mixtures. Many studies showed the effectiveness and compatibility between these materials, which overall provide improved performance for WMA mixtures, despite the fact that SBS bitumen usually requires high production and compaction temperatures to gain proper workability (Kataware & Singh, 2020; Stimilli, Virgili, et al., 2017; Zhang et al., 2021). Chemical additives have no noticeable influence on the rheological properties of SBS bitumen and Fourier transform infrared spectroscopy analysis showed broadly unaltered chemical composition for the binders (Ferrotti et al., 2017). Moreover, in the case of chemical additives, the workability is ensured by better interactions between bitumen and aggregates rather than by lower bitumen viscosity (Ingrassia et al., 2018; Stimilli, Virgili, et al., 2017).

The rutting resistance and the elastic response at high temperature are enhanced due to a reduced temperature susceptibility (Ferrotti et al., 2017; Morea et al., 2012). In addition, the chemical additives positively affect the short-term ageing, resulting in a potential increase in fatigue resistance of the pavement (Ragni et al., 2018). The good pavement performance is demonstrated also by in-situ investigations (Frigio et al., 2017; Stimilli, Frigio, Cardone, et al., 2017). However, there is limited data on the long-term performance, which remains still an open issue, especially in the case of warm recycled mixtures produced with SBS polymer modified bitumen.

Another advantage of production at lower temperature is the possibility to incorporate high percentages of reclaimed asphalt pavement (RAP). This could lead to environmental and technical benefits, such as the reduced demand for non-renewable resources, virgin aggregates and production energy, and improved rutting performance (Behnood, 2020; Cheraghian et al., 2020; Guo et al., 2020; Rathore et al., 2022). One of the major challenges is to produce 100% RAP asphalt mixtures, which can be obtained only by using WMA additives and rejuvenators, capable to adjust the properties of the aged RAP binder (Rathore et al., 2022). Moreover, the workability issues of mixtures containing RAP are counterbalanced by the WMA additives, which reduce the viscosity of the binder and/or the friction at the binder-aggregate interface (Ingrassia et al., 2018), ensuring comparable or better workability with respect to mixtures with only virgin aggregate (Guo et al., 2020; Xiao et al., 2019). However, the long-term effectiveness of these products and their interaction with the asphalt binder during in-service life are very uncertain, and, as a consequence, road agencies allow relatively low percentages of RAP in the mixtures. In addition, due to the intrinsic heterogeneity of RAP (Antunes et al., 2019), researchers did not find consensus on fatigue response (Guo et al., 2020). In fact, the fatigue resistance of recycled WMA depends on several factors, such as the type of WMA technology, the mixing method, the performance grade of the binder, the type and amount of additive/ rejuvenator, as well as the source and amount of RAP (Lu et al., 2019; Xiao et al., 2019). The combination and the equilibrium between these variables must be studied case by case in order to make specific recommendations (Hettiarachchi et al., 2019). No firm conclusion was obtained about the use of organic additives (Singh et al., 2017; D. Wang et al., 2021), foaming process (Perez-Martinez et al., 2016) and chemical additives (Lu et al., 2019; Perez-Martinez et al., 2016). For example, in (Lu et al., 2019) recycled WMA produced with chemical additive showed a lower fatigue resistance than the same WMA mixture produced with rejuvenator. In Perez-Martinez et al. (2016), the fatigue resistance of WMA produced with chemical additive was higher at short-term but had a faster decrease with ageing as compared to the control HMA mixture. In addition, it should be underlined that in all the abovementioned studies (Lu et al., 2019; Perez-Martinez et al., 2016; Singh et al., 2017; D. Wang et al., 2021), a neat bitumen was employed, whereas the fatigue resistance evaluation of WMA with modified bitumen is very limited, to date.

In literature, there are few studies on WMA containing RAP based on the VECD model, and all experiments were carried out only on laboratory specimens (D. Kim et al., 2017; Padula et al., 2019; Sabouri et al., 2016). In Kim et al. (2017), WMAs produced with 35% of RAP using an organic additive, a chemical additive and foaming technique showed lower stiffness and ageing than the reference HMA, but the fatigue resistance was penalized, except for the mixture with the chemical additive. According to Sabouri et al. (2016) and Padula et al.

(2019), a longer fatigue life was proved for WMA with 40÷50 % RAP using rejuvenators or through the foaming process. None of these studies considered a SBS polymer modified bitumen.

Given this background, this study presents the evolution over six years of the stiffness and fatigue properties of a WMA recycled pavement in comparison with a hot recycled pavement, both produced with SBS polymer modified bitumen and constructed along an Italian motorway. This study can improve the current knowledge of WMA scenario, towards a more conscious use of WMA produced with chemical additives and containing SBS modified bitumen and RAP. Moreover, the experimental outcomes provide valuable data on the long-term performance of a pavement constructed with such materials and subjected to actual motorway heavy traffic. Most of the data presented and discussed in this Chapter are published in (Spadoni, Ingrassia, Mariani, et al., 2022) and (Ingrassia et al., 2023).

5.2 Materials

Four dense-graded asphalt mixtures produced in 2016 were investigated in this study, namely a HMA and a WMA for binder courses, and a HMA and a WMA for base courses. Table 5.1 reports the aggregate gradation of the investigated mixtures as determined by bitumen extraction (EN 12697-1:2020). The nominal maximum aggregate size (NMAS) was equal to 16 mm. It can be noted that the aggregate gradation for binder and base courses are very similar, demonstrating that the practice of the same granulometry was adopted.

Table 5.1. Aggregate gradation of the investigated mixtures.

Sieve (mm)		31.5	20	16	10	6.3	2	0.5	0.25	0.063
Passing (%)	Binder course	100	97.3	90.4	68.8	45.8	29.4	14.8	12.1	6.7
	Base course	100	96.9	91.7	68.2	44.8	28.0	13.5	11.4	6.4

Unfractioned 0/14 RAP deriving from the milling of old motorway pavements was used to produce the mixtures. The amount of bitumen contained in the RAP, evaluated by bitumen extraction (EN 12697-1:2020), was equal to 5.0 % by aggregate weight. For all the mixtures, the virgin and RAP bitumen were SBS polymer modified with 3.8 % polymer content by bitumen weight. Table 5.2 reports the properties of the virgin SBS polymer modified before and after short-term ageing simulated with the RTFOT. The virgin SBS modified bitumen is the same of the reference mixtures, usually used for motorway mixtures. In fact, the properties in Table 5.2 are very similar to those in Table 3..

Binder course mixtures contained 25 % by aggregate weight of RAP and 4.8 % by aggregate weight (4.5 % by mixture weight) of total bitumen content (virgin bitumen plus bitumen from RAP). Base course mixtures contained 30 % of RAP and 4.2 % by aggregate weight (4.0 % by mixture weight) of total bitumen content.

Table 5.2. Properties of the virgin SBS polymer modified bitumen.

	Measured value	Reference Standard
Needle penetration at 25 °C	54 dmm	EN 1426
Softening point (R&B method)	71 °C	EN 1427
Elastic recovery at 25 °C; 25 cm/min	89%	EN 13398
Viscosity at 135 °C	1.24 Pa·s	ASTM D4402
Change in mass after RTFOT	0.05%	EN 12607-1
Needle penetration at 25 °C after RTFOT	27 dmm	EN 1426
Softening point (R&B method) after RTFOT	77 °C	EN 1427

The WMA mixtures were produced with a chemical additive (C1) mainly composed of ammine substances which act as adhesion enhancers and surfactants due to their polarized extremities (Ingrassia et al., 2021; Stimilli, Frigio, Canestrari, et al., 2017). The chemical additive C1 is characterized by a pour point of about -8 °C and a flash point higher than 140 °C. At 25 °C, it is a viscous liquid with a density of about 1.0 g/cm^3. The dosage of C1 was equal to 0.50 % and 0.55 % by virgin bitumen weight for the binder course and the base course, respectively. These dosages were designed in accordance with the recommendations of producer and based on the actual “working” bitumen content (i.e., the sum of virgin bitumen and re-activated RAP bitumen, in order to consider the different amount of RAP in the binder and base courses (Ingrassia et al., 2021; Stimilli et al., 2015).

The production and compaction temperatures were 130 °C and 120 °C for the WMA mixtures, and 170 °C and 160 °C for the HMA mixtures.

The gradations of HMA for binder course (Table 5.1) comparable to the one of the reference SBS modified asphalt mixture presented in Section 3.2.1 (Figure 3.), as well as the similar bitumen properties and the same RAP content, make such mixture (produced in 2016) almost assimilable to H (produced in 2021).

5.2.1 Field test trial

These materials were used to construct a full-scale field trial in April 2016 along the A1 motorway (South carriageway) in central Italy. All the details about the production of these mixtures and the construction of the field trial can be found in Stimilli, Frigio, Canestrari, et al. (2017). The construction activities consisted in the milling and re-construction of the asphalt courses of the slow lane. The field trial includes two consecutive 200-m sections, one constructed with the HMA mixtures and the other one with the WMA mixtures. The pavement structure, typical of motorway pavements, is as follows:

- Wearing course, made of an open-graded mixture, with nominal thickness of 4 cm (not investigated in this study due to its limited thickness);
- Binder course with nominal thickness of 10 cm;
- Base course with nominal thickness of 15 cm;
- Cold recycled subbase course with nominal thickness of 25 cm and stiffness of 1200 MPa derived from previous FWD campaign (Stimilli, Frigio, Canestrari, et al., 2017).

Indeed, the thicknesses of the asphalt courses are the same of those in Figure 3.3.

Traffic analyses indicate that the full-scale field trial is subjected to 8.5 million equivalent single axle loads (ESALs) per year (calculated considering a 120 kN reference axle with twin wheels).

5.3 Testing program and procedures

From the year of construction of the field test trial in 2016, the section was continuously monitored through laboratory tests on cores to determine the evolution of the stiffness properties and the fatigue resistance. Figure 5.1 shows the history of the testing program, whose results are partially presented in the following sections for comparison purpose with the VECD results.

Specifically, cored samples of the asphalt courses were extracted from the field trial in April 2016 (after one week from the construction and before the re-opening to traffic), in November 2019 and in January 2022 at different positions in the middle of the lane. In 2016 and 2019, 100 mm diameter cores were extracted from each section. Then, each core was cut to obtain two 50 mm height specimens from the binder and base courses, respectively. ITSM (EN 12697-26, 2022) tests and ITFT (EN 12697-24, 2018) were carried out on specimens from the binder course in 2016 and on specimens from both the binder and base courses in 2019. In 2022, 150-mm diameter cores were extracted from each section (Figure 5.2), afterwards “small” specimens (diameter of 38 mm and height of 110 mm) were horizontally cored from both the binder and base courses, after isolating each course cutting at the interfaces (Figure 5.3). VECD characterization was carried out on the latter specimens cored in 2022. It was possible to obtain a maximum of three and six specimens from *Binder* and *Base* courses, respectively. The open-graded wearing layer was not included in the investigation due to its limited thickness.

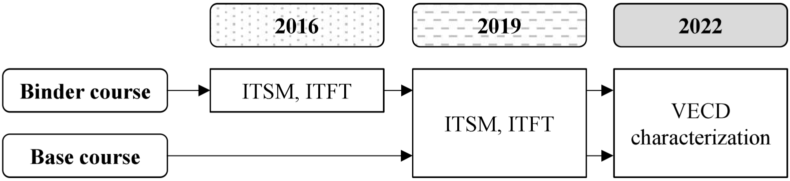

Figure 5.1. History of the testing program on cored samples taken from the field trial.

Figure 5.2. Cores of all the asphalt courses extracted in 2022.

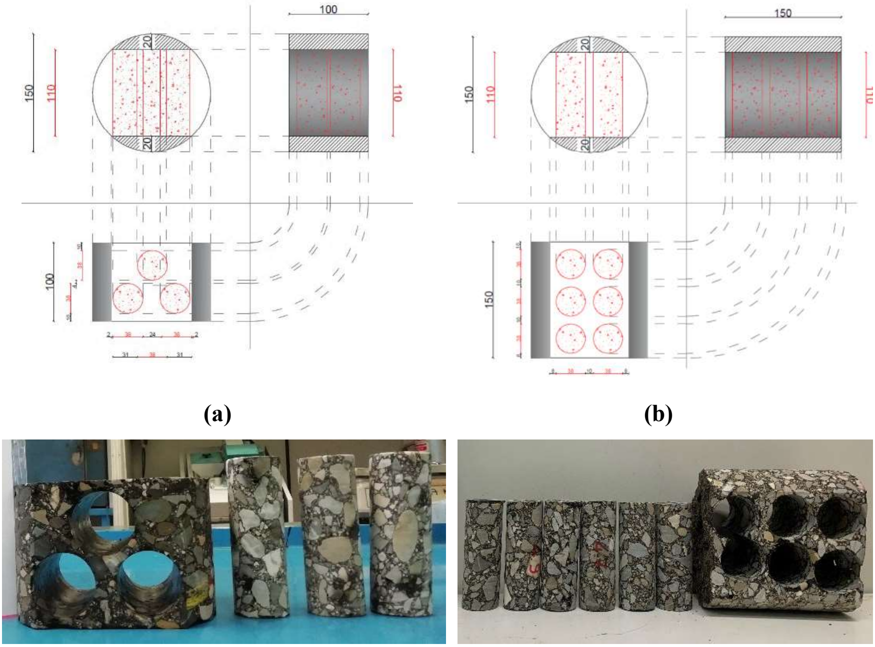

(a) (b)

(c) (d)

Figure 5.3. Small specimens from field cores: scheme and cores form (a,c) *Binder* and (b,d) *Base* courses.

The norm of the dynamic modulus |E*|and the phase angle θ were determined at 4 °C, 20 °C and 40 °C with the AMPT. The selected frequencies for each temperature were 0.1 Hz, 0.5 Hz, 1 Hz, 5 Hz, 10 Hz and 20 Hz. The amplitude of the sinusoidal axial compression load was adjusted to maintain an average strain level between 50 and 75 µε. The single-operator precision requirements were checked and verified.

The testing temperature of the cyclic fatigue tests was 21 °C, since the expected PG of the binder in the recycled mixtures was PG 76-16. The deformation levels set as input in order to obtain the target duration were in the range between 230 µε and 300 µε for all the mixtures. S_{app} refers to a temperature which is determined as the average climatic PG temperature of the pavement location, minus 3 °C. Since the field trial is in a PG 58-10 climatic zone (Giuliani, 2006), S_{app} reference temperature was equal to 21 °C.

5.4 Results and analysis

5.4.1 Binder course

Figure 5.4a-b show the storage modulus and phase angle mastercurves at 21.1 °C, respectively, for the mixtures tested in 2022 according to the S-VECD approach. Table 5.3 reports the parameters of the 2S2P1D models. Figure 5.4a also reports the average AV of the tested specimens, which had similar volumetric properties for the two mixtures. It is possible to notice that HMA exhibited higher stiffness, confirming that the higher RAP oxidation and faster in-service ageing affected its stiffness properties in a wide range of frequencies. Moreover, the higher phase angle values of WMA (Figure 5.4b) highlighted a more viscous and less elastic behavior with respect to HMA. Figure 5.4c reports the shift factors and the equations of the related regressions. The overlapping polynomial trendline indicate that the mixtures were characterized by the same thermal susceptibility, which did not depend on the different production process but can be mainly related to the bituminous components (virgin bitumen and bitumen from RAP), which are the same for both mixtures. This outcome confirms that chemical additives usually do not significantly affect the rheological properties of the binder itself (Behnood, 2020; Ferrotti et al., 2017).

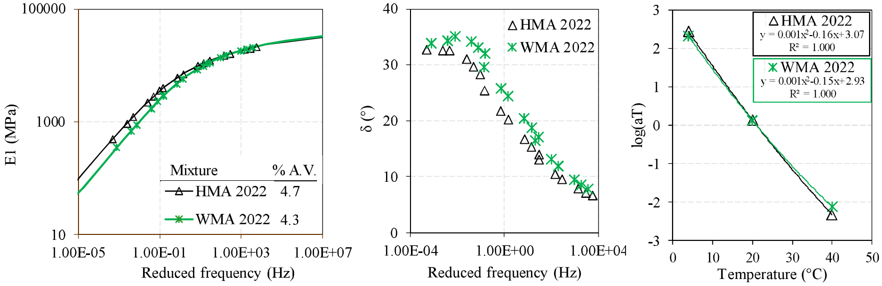

(a) **(b)** **(c)**

Figure 5.4. Binder course mixtures: (a) storage modulus mastercurves (2S2P1D model) and (b) phase angle mastercurves at 21.1 °C, (c) shift factors.

Table 5.3. Binder course mixtures: parameters of the 2S2P1D models for the storage modulus.

Mixture	$E_{1,0}$ (MPa)	$E_{1,\infty}$ (MPa)	ξ	k	h	β	$log\ \tau$
HMA2022	3	40000	2.39	0.14	0.44	1E+12	-1.43
WMA2022	7	40000	2.25	0.16	0.47	1E+12	-1.79

Figure 5.5a presents the fitting of the damage characteristic curves, obtained from three overlapping experimental curves, along with the values of fitting coefficients. The AV of the specimens investigated in the fatigue tests, reported in the same figure, was similar to that of the specimens investigated in dynamic modulus tests (Figure 5.4a). The shape of the C versus S curves for the two mixtures was comparable, indicating that the evolution of the damage in the materials was broadly the same. Nevertheless, the curve of WMA was characterized by lower pseudo stiffness value C and higher amount of damage S at failure with respect to

HMA, indicating a higher tolerance to damage and a postponed failure. Figure 5.5b presents the D^R failure envelopes. The D^R values are the slopes of the linear relationships reported in the figure. WMA showed a slightly higher D^R value (0.736), which indicates a higher toughness, i.e., better ability to absorb energy before failure. Figure 5.5c shows the S_{app} values, together with the average AV of all tested specimens (dynamic modulus and cyclic fatigue tests). The S_{app} ranking reflects the previous observations on the C versus S curves and D^R values, highlighting that a better fatigue performance can be expected from WMA.

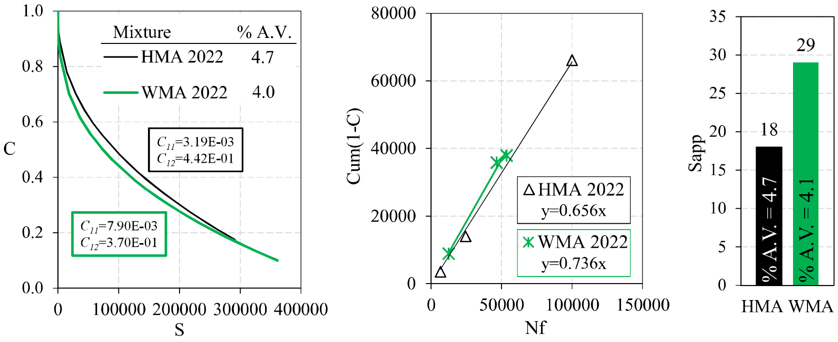

(a) **(b)** **(c)**

Figure 5.5. Binder course mixtures: (a) fitting of the damage characteristic curves, (b) D^R failure criterion and (c) S_{app} values.

5.4.2 Base course

Figure 5.6a presents the storage modulus mastercurves at 21.1 °C and the average AV of the specimens tested in 2022. Table 5.5 reports the parameters of the 2S2P1D models for the storage modulus.

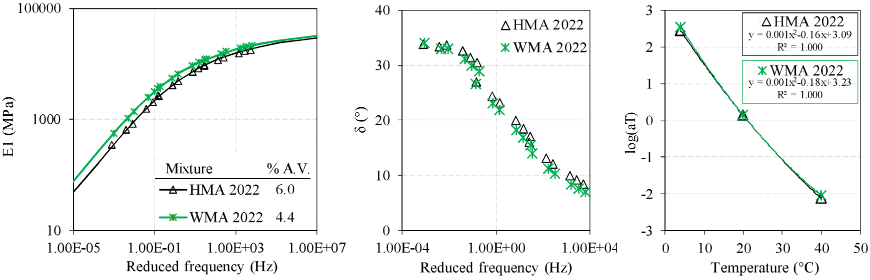

(a) **(b)** **(c)**

Figure 5.6. Base course mixtures: (a) storage modulus mastercurves (2S2P1D model) and (b) phase angle mastercurves at 21.1 °C, (c) shift factors.

Table 5.4. Base course mixtures: parameters of the 2S2P1D models for the storage modulus.

Mixture	$E_{1,0}$ (MPa)	$E_{1,\infty}$ (MPa)	ξ	k	h	β	$log\,\tau$
HMA2022	3	40000	2.78	0.15	0.46	1E+12	-1.93
WMA2022	1.49	40000	2.54	0.16	0.45	1E+12	-1.51

WMA showed higher stiffness with respect to HMA, mainly due to the lower AV of the WMA mixture. Figure 5.6 b presents the phase angle mastercurves at 21.1 °C. It can be observed that the phase angle values are broadly the same for the two mixtures. Figure 5.6c reports the shift factors and the equations of the related regressions. The shift factor values and regression curves basically overlapped and were also similar to those obtained for the binder course (Figure 5.4c). This confirms that thermal susceptibility is mainly affected by the bitumen properties, which do not change even in the presence of the additive.

Figure 5.7a presents the fit of the damage characteristic curves, obtained from at least three overlapping experimental curves, along with the average AV of the specimens tested and the values of the fitting coefficients. First, it should be noted that the different in-situ AV of the mixtures (i.e., about 2.5 %) significantly influenced their fatigue behavior, as discussed in detail below. The higher position of the WMA curve was consistent with the stiffness properties and AV, confirming that the curve of softer mixtures tends to stay below that of stiffer mixtures (Hou et al., 2010).

Both curves showed similar pseudo stiffness *C* at failure, indicating a comparable tolerance to damage, whereas WMA curve reached higher *S* value at failure, indicating a lower rate of fatigue resistance loss during the in-service life. Figure 5.7b presents the failure envelopes, whose slope corresponds to D^R. A higher D^R value was observed for the HMA mixture, denoting its greater ability to absorb energy before failure, which is strictly related to its lower stiffness (Figure 5.6a) mostly due to the higher AV. Figure 5.7c shows the S_{app} values and the average AV of all tested specimens (dynamic modulus and cyclic fatigue tests). In this case, the S_{app} ranking did not confirm the D^R ranking, because the S_{app} value depends also on the stiffness properties and the damage characteristics. The higher S_{app} value obtained for WMA can be explained by considering that the WMA mixture has better damage properties (Figure 5.7a) and its higher stiffness (Figure 5.6a), linked to the AV, ensures a better distribution of the strains/stresses within the pavement. Analogously to the binder course, a better fatigue performance can be thus expected from WMA even for the base course.

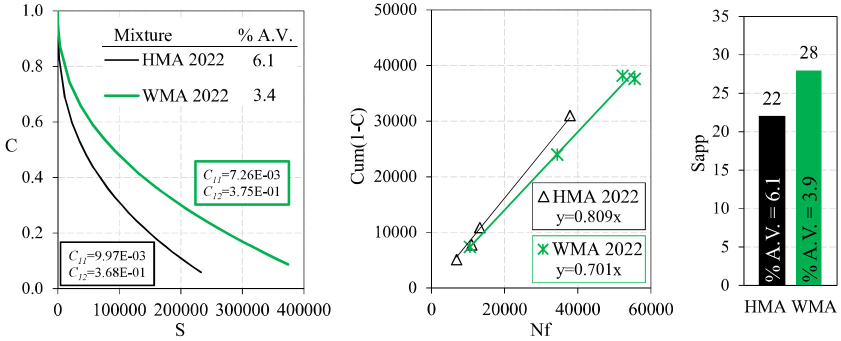

(a) **(b)** **(c)**

Figure 5.7. Base course mixtures: (a) fitting of the damage characteristic curves, (b) D^R failure criterion and (c) S_{app} values.

This finding corroborates the beneficial effect of the WMA additive on the volumetric properties of the mixture, despite the higher RAP content and the lower bitumen content of the base course with respect to the binder course.

5.5 Comparison with the traditional approach results

5.5.1 Binder course

Figure 5.8 presents the evolution of the stiffness modulus values during the six years of the pavement in-service life for both mixture types (HMA and WMA). The average AV of the tested specimens is also indicated. For the 2016 and 2019 data, the stiffness moduli refer to the average measured ITSM values, and the standard deviation is reported as well. For comparison purposes, for the 2022 data, the stiffness moduli refer to the dynamic modulus values calculated through the 2S2P1D model at the same testing conditions as for the ITSM tests (temperature of 20 °C, frequency of 2 Hz). Since these values come from a model fitted to already averaged experimental values, no standard deviation is available.

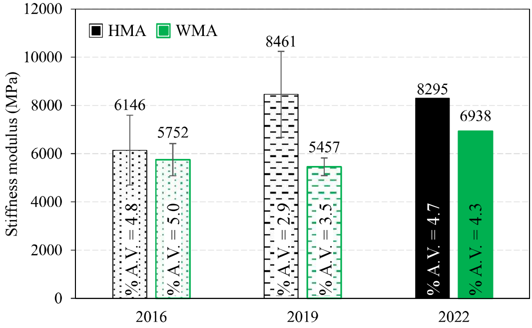

Figure 5.8. Binder course mixtures: stiffness modulus values in 2016, 2019 and 2022 (error bars represent the standard deviation).

As can be observed, cores extracted in 2016 were characterized by similar volumetric properties and similar stiffness moduli. These data demonstrate that the WMA additive ensures a compactability comparable to HMA despite the reduced production and compaction temperatures (i.e., 40 °C lower), and does not negatively affect the stiffness properties (Ingrassia et al., 2021), which are strictly related to the volumetric ones. Comparing the cores extracted in 2019 to those extracted in 2016, HMA showed significantly higher stiffness modulus in 2019, whereas WMA showed broadly unchanged results. The higher stiffness of HMA can be ascribable to a higher in-service ageing rate. The higher data dispersion of HMA in both 2016 and 2019 can be likely due to the presence of highly oxidized RAP not homogenously distributed within the mixture at the specimen scale. The high oxidation of RAP can be caused by the typical HMA production and compaction temperatures (Ingrassia et al., 2021; D. Kim et al., 2017). As for the 2022 data, it must be kept in mind that such stiffness values were measured in compression mode, which usually leads to higher stiffness values than those obtained in indirect tensile mode (2019 data). For WMA a higher stiffness was observed in 2022 as compared to 2019, whereas this was not observed for HMA. The high data variability found for HMA in 2019 can justify this finding. Moreover, the stiffness results of 2022 confirmed the trend of 2019, denoting a higher stiffness for the HMA mixture with respect to the WMA mixture, despite their comparable volumetric properties.

Figure 5.9 presents the fatigue curves obtained from the specimens extracted in 2016 and 2019, whose average AV is indicated as well, whereas Table 5.5 reports the fitting parameters and the ε_6 values. The experimental data were used to construct the linear regression in a bi-logarithmic plane:

$$\log N_f = a - b \cdot \log \varepsilon_{h,0} \tag{5.1}$$

where a and b are material parameters, and $\varepsilon_{h,0}$ was measured at the 100th load cycle.

In both 2016 and 2019, the linear regressions were characterized by similar slope, as demonstrated by the *b* values in Table 5.5 (see Equation (5.1)). This outcome means that the two mixtures (HMA and WMA) had comparable sensitivity to the strain level, which did not change significantly during the first years of in-service life. However, the comparison of the curves (Figure 5.9) shows the enhanced fatigue response of WMA, as also confirmed by the higher ε_6 values in both 2016 and 2019 (Table 5.5). This indicates a better resistance to cyclic loads for WMA, which can be ascribable to its lower stiffness with respect to HMA (Figure 5.8), especially in 2019. Conversely, the higher stiffness of HMA, combined with its heterogeneity caused by the highly oxidized RAP, led to a more brittle behavior.

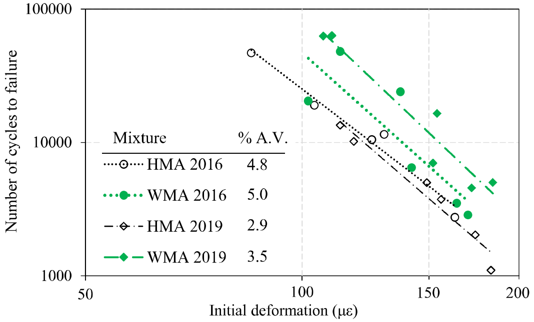

Figure 5.9. Binder course mixtures: fatigue curves in 2016 and 2019.

The comparable sensitivity to the strain level, denoted by the similar slope of the fatigue curves in 2016 and 2019 (Figure 5.9) and expressed by the *b* values (Table 5.5), can be compared with the similar shape of the *C* versus *S* curves for the two mixtures (Figure 5.5a), indicating that the evolution of the damage in the materials was broadly the same.
Moreover, the higher ε_6 values for WMA extrapolated from the fatigue curves in 2016 and 2019 (Table 5.5) can be associated with the lower pseudo stiffness value *C* and higher amount of damage *S* at failure in the damage characteristic curve with respect to HMA (Figure 5.5), both indicating a higher fatigue resistance at failure.

Table 5.5. Binder course mixtures: fitting parameters of the fatigue curves.

		a	*b*	R^2	ε_6
2016	HMA	12.675	4.138	0.965	41
	WMA	14.344	4.836	0.724	53
2019	HMA	13.741	4.670	0.954	45
	WMA	15.203	5.115	0.927	63

5.5.2 Base course

Figure 5.10 presents the stiffness modulus values obtained from the specimens cored in 2019 and 2022 for both types of mixture (HMA and WMA). The average AV is indicated in the figure as well. The average ITSM values and the related standard deviations are reported for the 2019 specimens, whereas the dynamic modulus values derived from the 2S2P1D model at the same testing conditions as for the ITSM tests are reported for the 2022 specimens (as already explained in Section 5.4.1). First, it is worth pointing out that WMA reached an average AV about 1% lower than HMA. This can be likely due to the chemical additive used for the WMA production, which ensured a proper compactability of the mixture.

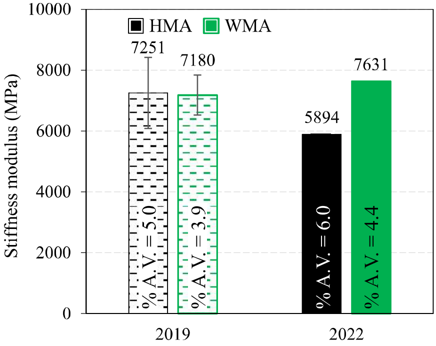

Figure 5.10. Base course mixtures: stiffness modulus values in 2019 and 2022 (error bars represent the standard deviation).

In 2019, cored samples of both mixtures showed similar stiffness despite the different volumetric properties. This can be attributed to the stronger RAP oxidation during the production and construction phases and the faster in-service ageing rate undergone by the HMA mixture as compared to the WMA mixture. As for the comparison between 2019 and 2022 results, recall that the stiffness moduli were obtained in compression mode in 2022 versus indirect tensile mode in 2019. As already mentioned in Section 5.4.1, the compression mode should imply higher stiffness values. A higher stiffness was observed for WMA in 2022 as compared to 2019, whereas HMA showed a stiffness decrease of about 18% in the same period. This decrease can be ascribable to a certain extent to the different AV observed for HMA in 2019 and 2022, even though the inhomogeneity of the HMA mixture is considered as the main cause. As anticipated in Section 3.1, the samples were obviously cored in different positions of the trial section. In this regard, the properties of the HMA section seem to change more from point to point, as denoted by the higher standard deviation (Figure 5.10), although the production and construction phases were strictly controlled. These results support that WMA is a more homogenous material with comparable performance along the pavement.

Figure 5.11 presents the fatigue curves obtained from the specimens cored in 2019, whose average AV is also indicated, whereas Table 5.6 reports the fitting parameters and the ε_6 values. The linear regression of HMA was characterized by a lower slope, which means a lower sensitivity to the applied deformation level. On the other hand, WMA exhibited a significantly higher ε_6 value (i.e., 60 με vs. 28 με), which suggests a longer fatigue life for small deformations (such as those to which a thick pavement is typically subjected). Moreover, in 2019, WMAs of binder and base courses were characterized by similar AV (Figure 5.9, Figure 5.11) and similar fatigue behavior, as expressed by *a* and *b* values of Equation (5.1) and ε_6 value (Table 5.5, Table 5.6). In this regard, the chemical additive allowed to reach similar properties for the binder and base courses, even though the base mixture was characterized by higher RAP content and lower virgin bitumen content with respect to the binder mixture (in the light of a comparable aggregate gradation, see Section 5.2). On the contrary, for the HMAs, the volumetric properties and mechanical behavior of the binder and base courses were different. In this case, the compactability of the base course was penalized by the higher RAP content and the lower virgin bitumen content as well as the greater layer thickness with respect to the binder course.

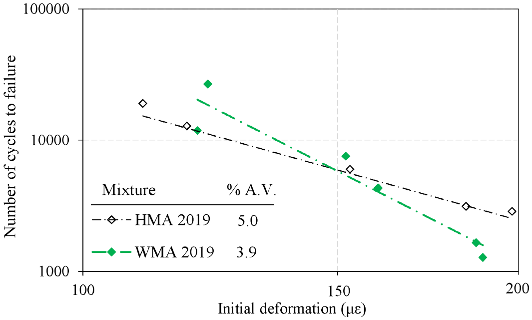

Figure 5.11. Base course: fatigue curves in 2019.

The higher ε_6 value observed for WMA from the 2019 fatigue curves (Table 5.6) can be associated with the higher damage S value at failure reached by the WMA damage characteristic curve with respect to HMA (Figure 5.7a), both indicating a lower rate of fatigue resistance loss during the in-service life, thus suggesting a longer fatigue life for WMA.

Table 5.6. Base course mixtures: fitting parameters of the fatigue curves.

		a	*b*	R^2	ε_6
2019	HMA	10.435	3.062	0.905	28
	WMA	15.995	5.621	0.913	60

5.6 Pavement performance simulations

5.6.1 FlexPAVE^{TM} results considering different subbase stiffness

Input data

Table 5.7 shows the investigated conditions with simulations. Each simulation is coded with the following information:

- HMA/WMA: the considered HMA or WMA material properties of the binder and base courses, respectively.
- IS/CS: if the condition of Intact Subbase with stiffness of 1200 MPa (from FWD campaign) or Cracked Subbase with stiffness of 400 MPa (typical of granular materials) was considered, respectively. The intact condition simulates the initial stage of the in-service life of the cold recycled subbase, i.e., when it behaves as a bound material.
- F+T/F: if the simulation were carried out considering both the fatigue and thermal damage or only the fatigue damage, respectively.

Table 5.7. Overview of the FlexPAVE^{TM} performance simulations.

Simulation	OGFC (4 cm)	Binder (10 cm)	Base (15 cm)	Subbase (25 cm) E (MPa)	Subgrade E (MPa)
HMA_IS_F+T	OG	HMA-BINDER	HMA-BASE	1200	100
HMA_IS_F	OG	HMA-BINDER	HMA-BASE	1200	100
WMA_IS_F+T	OG	WMA-BINDER	WMA-BASE	1200	100
WMA_IS_F	OG	WMA-BINDER	WMA-BASE	1200	100
HMA_CS_F+T	OG	HMA-BINDER	HMA-BASE	400	100
HMA_CS_F	OG	HMA-BINDER	HMA-BASE	400	100
WMA_CS_F+T	OG	WMA-BINDER	WMA-BASE	400	100
WMA_CS_F	OG	WMA-BINDER	WMA-BASE	400	100

The pavement structure is the typical of Italian motorway pavements and, thus represents also the structure of the field trial (see Section 5.2.1). The asphalt courses were a 4-cm open graded friction course (OGFC), a 10-cm dense-graded binder course and a 15-cm dense-graded base course. For the OGFC, in absence of the actual results of the field trial, the results on the HMA OG in the research presented in Chapter 3 were used (Figure 3.12a-c). For binder and base courses, the laboratory results of HMA and WMA were used (Section 5.4.1 and 5.4.2, respectively). The subbase was modeled as linear elastic with different stiffness values (IS/CS), and the actual thickness of 25 cm determined by an exploration pit. The subgrade was modeled as linear elastic, with a stiffness value of 100 MPa derived from FWD campaign (Stimilli, Frigio, Canestrari, et al., 2017)

Regarding the traffic conditions, 8.5 million 120-kN ESALs (single axle, dual wheels) per year were considered, determined by previous traffic analyses. The speed traffic of 90 km/h of the heavy load was considered. The tire inflation pressure was 800 kPa and the contact area was set as circular.

The climatic conditions of the city of San Jose (California) were considered, deriving from a comparison of the average precipitation and minimum and maximum temperatures with the location of the field trial, as shown in Figure 5.12.

All the simulations analyzed the maximum timespan of 30 years.

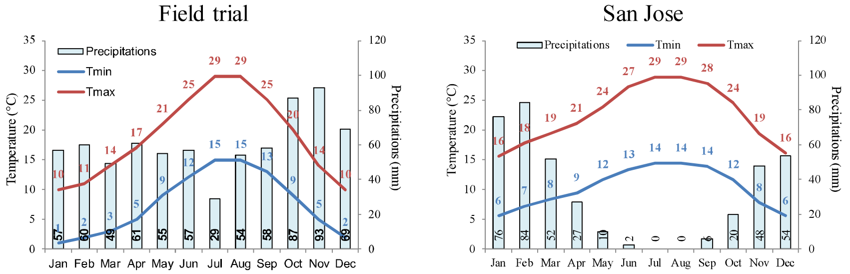
Field trial

San Jose

(a) (b)

Figure 5.12. Climatic conditions: comparison between the conditions of the field trial location and the considered San Jose in California.

Results

Figure 5.13 presents the damage contours for the two trial sections after 30 years in the condition of intact subbase. Observing the results obtained considering both fatigue and thermal damage (F+T), it can be seen that both HMA and WMA sections should experience both bottom-up cracking and comparable top-down cracking in the upper 5 cm of the pavement (Figure 5.13a-c). However, bottom-up cracking involves about 9 cm of asphalt concrete in HMA section (Figure 5.13a) and about 6÷7 cm in WMA section (Figure 5.13c), highlighting the better performance of WMA materials in enhancing the fatigue resistance of the pavement. The limited top-down cracking is mainly ascribable to thermal effects, since there is almost no damage in the upper part of the pavement when only the stresses and strains induced by traffic loads are considered (Figure 5.13b-d). Moreover, such distress is comparable for both sections, since it is likely due to the properties of the OGFC which is the same for both (Table 5.7) of them.

Figure 5.14 shows the damage contours obtained in the case of Cracked Subbase after 30 years. As expected, in each case the level and extent of damage are higher with respect to the corresponding simulation with intact subbase in Figure 5.13 due to a lower bearing capacity of the subbase. Specifically, in the HMA section (Figure 5.14a), bottom-up cracking and top-down cracking affect respectively about 14 cm and 8 cm of asphalt concrete. The damage factor reaches the 0.9 value in the lowest area of the asphalt concrete, meaning an almost completely cracked element.

(a) HMA_IS_F+T **(b) HMA_IS_F**

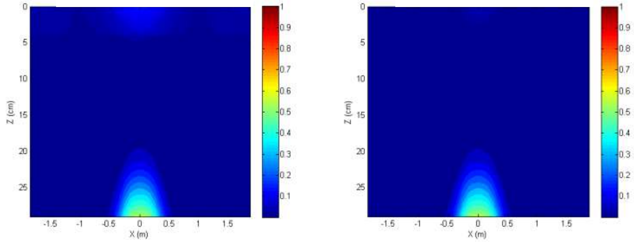

(c) WMA_IS_F+T **(d) WMA_IS_F**

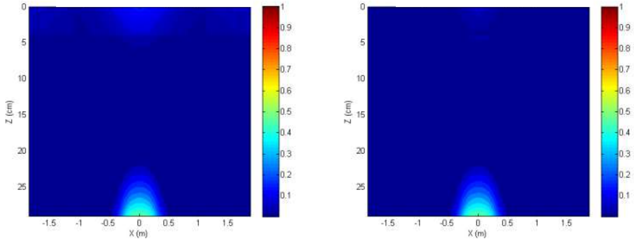

Figure 5.13. Damage contours in the condition of Intact Subbase (IS) after 30 years.

(a) HMA_CS_F+T **(b) HMA_CS_F**

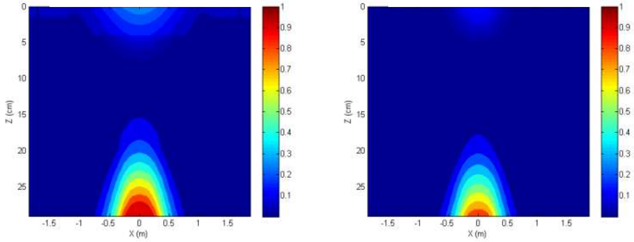

(c) WMA_CS_F+T **(d) WMA_CS_F**

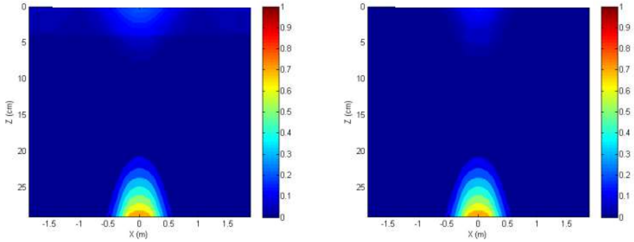

Figure 5.14. Damage contours in the condition of Cracked Subbase (CS) after 30 years.

In absence of the thermal effects (Figure 5.14b), it can be seen that the amount of damage in the upper part of the pavement is significantly reduced, and in minor measure the damage in the lower part, too, likely due to a more intact OGFC capable to absorb the cyclic stresses. Analogously to the condition of intact subbase, the WMA section clearly exhibits a lower amount and extent of damage with respect to the HMA section (see Figure 5.14c-d). In fact, the bottom-up cracking in the actual climatic and traffic conditions (F+T) leads to damage factor value not higher than 0.7 after 30 years (Figure 5.14c) vs. 0.9 in the HMA section (Figure 5.14a). The areas affected by bottom-up cracking and top-down cracking are both about 8-cm thick (Figure 5.14c). Moreover, for the WMA section, thermal damage mainly affects the upper part of the pavement, whereas it has a negligible effect on bottom-up cracking (see Figure 5.14d vs. Figure 5.14c).

Figure 5.15a-b show the evolution of *%Damage* over 30 years in the case of Intact Subbase and Cracked Subbase, respectively. In Figure 5.16 the contributions to traffic (fatigue) and thermal (climatic) damage can be identified in the total damage. In the case of Intact Subbase (Figure 5.15a), it can be observed that the increase is mostly concentrated in the first 3 years of service, and then the *%Damage* assumes a linear trend with a similar slope for all the scenarios. After 30 years, the percentage of damage induced by traffic loads plus thermal effects is low for both HMA and WMA sections: it is about 7% for the first one and 5% for the second one. Moreover, for both trial sections, 75÷80% of such damage is due to the traffic loads (i.e., pure fatigue damage), whereas the remaining 20÷25% of such damage is due to thermal effects (Figure 5.16) and is mainly concentrated in the upper part of the pavement, as discussed above.

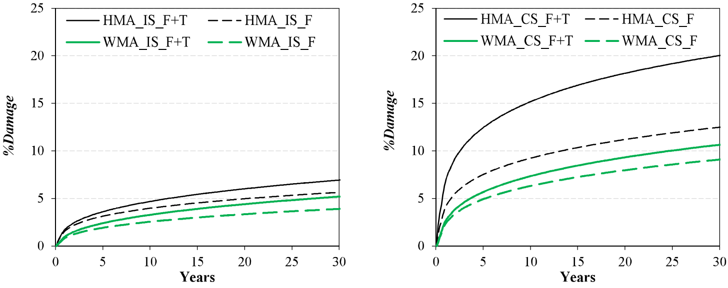

(a) **(b)**

Figure 5.15. Damage evolution on the pavement cross-section over 30 years: (a) intact subbase (IS) condition, (b) cracked subbase (CS) condition.

As expected, Figure 5.15b confirms that in all cases *%Damage* is higher in the Cracked Subbase condition with respect to the Intact Subbase condition, as already observed from the comparison between Figure 5.13 and Figure 5.14, due to the higher bearing capacity of the unbound material (400 MPA vs. 100 MPa, see Table 5.7). Even in this condition, the percentage of damage due to fatigue and climatic effects increases in the initial 5 years of the service, and it is notably higher in the HMA section (Figure 5.15b). After 30 years, the

%Damage is about 20% for the HMA section and 10% for the WMA section. For the WMA section, 85% of such damage is due to the traffic loads, whereas only 15% of such damage, concentrated in the upper part of the pavement, is due to thermal effects (Figure 5.15). Conversely, for the HMA section, the influence of thermal damage over the total damage is higher (38%, see Figure 5.15). In fact, from Figure 5.14a and Figure 5.14b, it was already observed that thermal damage contributes both to top-down cracking and bottom-up cracking for the HMA section with Cracked Subbase, meaning that the HMA materials are more susceptible to thermal changes.

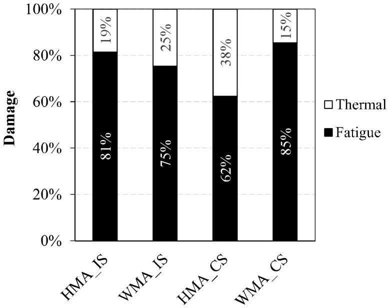

Figure 5.16. Influence of fatigue damage and thermal damage over the total damage obtained after 30 years (Ingrassia et al., 2023).

The *%Damage* was then used to predict the *%Cracking* on the pavement surface.

The *%Damage* in the Intact Subbase condition is so low for all the scenario that the *%Cracking* is always lower than 1% after 30 years. For this reason, it is not shown. All simulations with intact subbase would lead to a service life much longer than 30 years (*%Cracking* lower than 1% after 30 years).

Regarding the Cracked Subbase condition, Figure 5.17 shows the evolution of *%Cracking* over 30 years. Considering both the damage induced by traffic loads and thermal damage (F+T), it should be noted that the HMA section experiences a very fast increase of *%Cracking*, highlighted by the sigmoidal function completely developed, and with a very fast increase during the first years of service. After 30 years, the predicted *%Cracking* is about 45%. Conversely, the *%Cracking* for the WMA section slowly increases, leading to a value slightly lower than 10% after 30 years. In fact, according to the considered sigmoidal transfer function of Y. D. Wang et al. (2021), when *%Damage* is lower than 10%, the corresponding *%Cracking* is lower than 5%. Conversely, when *%Damage* is higher than 10%, *%Cracking* increases dramatically. This feature of the transfer function is due to the fact that fatigue cracking is not observed on the pavement surface while fatigue damage is still growing within the asphalt courses (Spadoni, Ingrassia, Mocelin, Richard Kim, et al., 2022; Y. D. Wang et al., 2021).

A percentage of cracking of 10% on the pavement surface was considered to define the service life of the pavement. The results regarding the cracked subbase condition are summarized in Table 5.8. Considering both traffic and climatic damage, the HMA section

should reach the end of service life after just 3 years, whereas the WMA section should maintain an acceptable performance for about 30 years.
Considering only the fatigue damage, the service life of the HMA and WMA sections would be equal to 18 years and greater than 30 years, respectively (Table 5.8).

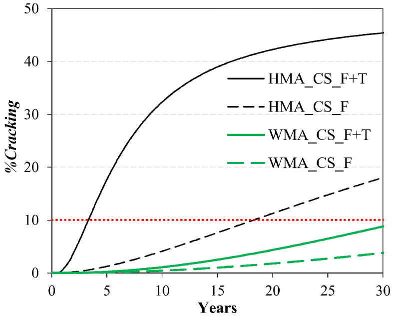

Figure 5.17. Cracking evolution on the pavement surface over 30 years in the case of cracked subbase (CS) (Ingrassia et al., 2023).

Table 5.8. Prevision of service life in the case of cracked subbase.

Simulation	Service life (years)
HMA_CS_F+T	3
HMA_CS_F	18
WMA_CS_F+T	≈ 30
WMA_CS_F	> 30

Although the prediction of the *%Cracking* derived from the FlexPAVE^{TM} results may not be totally realistic (the ageing is not taken into account) and would need to be validated based on field observations, the results clearly state that the expected service life of the WMA section is much longer than that of the HMA section.

5.6.2 Comparison with the conventional linear elastic design method

Analogously to Poland and the majority of Countries in Europe, even Italian conventional pavement design tools are based on the elastic theory. They allow a fast design of the pavement structure, and the required knowledge of the use of the dedicated software, as well as of the material properties, is very limited. The flow of the design process is very similar to the one adopted in Poland and descripted in the Section 4.5.2. The pavement is modeled as a linear elastic multi-layer subjected to a static load, thus allowing to calculate stresses and strains in critical points within the pavement. The characteristics of the applied static load (traffic), the pavement structure and the representative stiffness moduli of each course, depending on the season of the year, are the needed input data. One of the most common elastic-based design tools in Italy is KENPAVE software (H. H. Yang, 2004), so used in this research. The methods and results, studied by Lorenzo Paolo Ingrassia, are deeply reported in "*Prediction of the long-term performance of an existing warm recycled motorway pavement*" (Ingrassia et al., 2023).

Analogously to FlexPAVE^{TM} simulations, reported in Table 5.7, the pavement structure was the same, and the case of intact (IS, *E = 1200 MPa*) and cracked (CS, *E = 400 MPa*) subbase were considered.

The temperature dependence of the asphalt courses was considered carrying out four simulations, considering the average temperature of the pavement (T_{AC}, at a depth equal to one third of the overall thickness of the asphalt courses) in the four seasons (winter, spring, summer and autumn). T_{AC} represents the temperature at a depth equal to one third of the overall thickness of the asphalt courses (i.e., about 10 cm) and was calculated based on the average seasonal air temperatures at the field trial location according to Witczak & Shook (1975). The stiffness value of the asphalt courses were obtained from the mastercurve of the laboratory tested materials (Figure 3.12a for OGFC, Figure 5.4a and Figure 5.6a for binder and base asphalt concretes, respectively) determined at a frequency of 15 Hz, which corresponds to the speed of 90 km/h (Brown, 1973).

Table 5.9. Stiffness moduli considered in the KENPAVE simulations.

Course	Winter (T_{AC}=13 °C)	Spring (T_{AC}=18.4 °C)	Summer (T_{AC}=32.4 °C)	Autumn (T_{AC}=22.5 °C)
OGFC	8422 MPa	7025 MPa	3752 MPa	6002 MPa
HMA-BINDER	16252 MPa	13449 MPa	6449 MPa	11313 MPa
HMA-BASE	13370 MPa	10774 MPa	4804 MPa	8871 MPa
WMA-BINDER	15794 MPa	12758 MPa	5611 MPa	10491 MPa
WMA-BASE	16188 MPa	13321 MPa	6414 MPa	11174 MPa
Intact subbase	1200 MPa	1200 MPa	1200 MPa	1200 MPa
Cracked subbase	400 MPa	400 MPa	400 MPa	400 MPa
Subgrade	100 MPa	100 MPa	100 MPa	100 MPa

First, the tensile strains at the bottom of the asphalt courses (29-cm depth) were collected for each season, and in the case of Intact and Cracked Subbase from KENPAVE. Each tensile strain for each scenario was used to calculate the number of 120-kN ESALs needed for the crack initiation (N_0) with the relationship proposed by Verstraeten et al. (1982). Then, the number of 120-kN ESALs needed for the propagation of the crack to the pavement surface (ΔN_0) was calculated with the relationship proposed by Marchionna et al. (1985), which corresponds to a percentage of cracking on the pavement surface of 10%. In this way, the percentage of cracking on the surface was chosen as the common parameter in order to compare FlexPAVE^{TM} and KENPAVE prediction in terms of service life. In this calculation, the contribution of the OGFC against the crack propagation was conservatively neglected, given the relatively low cracking resistance that is typical of open-graded mixtures. The fatigue resistance ($N_{f\_AC\_IS}$ and $N_{f\_AC\_CS}$) was the sum of N_0 (initiation) and ΔN_0 (propagation). The tensile strain at the bottom of the cold recycled course (54-cm depth) was used to calculate the fatigue resistance of the cold-recycled subbase (N_{f_S}) in term of 120-kN ESALs that leads to cracking (i.e., beginning of the granular-like stage), according to Liebenberg & Visser (2004).

For each season (winter, spring, summer and autumn), the actual fatigue resistance of the pavement (N_{tot}) was calculated through the following equation:

$$N_{tot} = N_{f\_S} + N_{f\_AC\_CS} \cdot \frac{N_{f\_AC\_IS} - N_{f\_S}}{N_{f\_AC\_IS}} \tag{5.2}$$

Such equation expresses the actual fatigue resistance of the pavement as the sum of the fatigue resistance of the cold recycled course and the fatigue resistance of the asphalt courses in the case of cracked subbase, the latter multiplied by a correction factor (<1) that quantifies the portion of fatigue resistance still available for the asphalt courses after the subbase cracking (Ingrassia et al., 2023).

Finally, the fatigue resistances related to the different seasons were combined based on the Miner's law on cumulative fatigue damage [(Miner, 1945). The annual traffic was 8.5 million 120-kN ESALs, the same adopted for FlexPAVE^{TM} simulations.

The final results of KENPAVE simulations are reported in Table 5.10. The fatigue resistance of HMA and WMA sections is very similar and only slightly higher for the WMA section with respect to the HMA section, resulting in a fatigue life of about 11 years and 13 years for the HMA section and the WMA section, respectively.

Table 5.10. Outcomes of the KENPAVE simulations.

Section	Fatigue resistance (120-kN ESAL)	Annual traffic (120-kN ESAL)	Fatigue life (years)
HMA	$9.25 \cdot 10^7$	$8.50 \cdot 10^6$	11
WMA	$1.07 \cdot 10^8$	$8.50 \cdot 10^6$	13

Considering that in KENPAVE simulations the pavement is modelled as linear elastic materials and only the asphalt stiffness is taken into account (similar for HMA and WMA, see Table 5.9), the comparable fatigue life was expected. Consequently, KENPAVE is not able to differentiate between two pavements that have similar structure and comparable stiffness moduli, since the actual fatigue behavior is completely neglected.

To carry out a fair comparison between such results with the FlexPAVE^{TM} ones, from FlexPAVE^{TM} a service life that is intermediate between the case of intact subbase and the case of cracked subbase (in the presence of only traffic-induced damage) should be considered, in order to make an analogue of what done with KENPAVE with Equation (5.2). Moreover, since KENPAVE does not take into account thermal stresses and strains, the outcomes of the simulations without thermal damage should be considered.

Under these conditions, according to FlexPAVE^{TM}, WMA ensures a longer service life for the WMA section as compared to the reference HMA section thanks to the better damage properties of the WMA mixtures than those of the HMA mixtures in both the subbase stiffness conditions (see Section 5.4). In fact, from FlexPAVE^{TM}, just considering only the cracked subbase condition, the service life of WMA_CS_F is higher than 30 years and the one of HMA_CS_F is 18 years (Table 5.8), vs. 13 and 11 years, respectively form KENPAVE (Table 5.9). These findings also highlight that the traditional elastic approach on which KENPAVE is based does not allow to catch the actual contribution to the pavement service life provided by high-performance non-standard materials. Therefore, the more advanced design tools such as FlexPAVE^{TM} within the AM-PRS should be used in order to predict the long-term behavior of the pavement more accurately.

5.7 Summary of the findings

The objective of this investigation was to monitor the performance of a full-scale field trial constructed along an Italian motorway, which included a section constructed with WMA mixtures (produced with a WMA chemical additive) and a reference section constructed with conventional HMA mixtures. The WMA and HMA mixtures had the same composition (i.e., amount of RAP and PMB) and differed only for the adopted production and compaction temperatures (40 °C lower for WMA). The characterization was carried out by means of laboratory testing performed on cored samples taken from the binder and base courses of the field trial pavement. In 2022 the VECD characterization was carried out, and such results were compared with the conventional indirect tension tests carried out in 2016 (year of construction) and 2019. Moreover, the VECD results were used as input to predict the performance of the materials in the pavement structure with the software FlexPAVE^{TM}. These results were finally compared with the results obtained with the traditional elastic approach obtained with the software KENPAVE.

Immediately after the construction (2016), WMA showed comparable stiffness properties and improved fatigue resistance with respect to HMA. However, during the in-service life, the stiffness of HMA increased much more than WMA stiffness and it was characterized by a high dispersion of the results. These findings are likely due to a stronger RAP oxidation during the production and construction phases (caused by the high temperatures adopted for HMA) and a higher in-service ageing rate experienced by the HMA section. These factors negatively affected the fatigue performance, leading to a more brittle behavior and a reduced toughness, as demonstrated by lower ε_6 (2019) and S_{app} values (2022).

On the contrary, WMA showed more homogenous properties along the trial section in both binder and base courses. Regarding the fatigue properties, WMA was characterized by a greater tolerance to damage and a slower rate of fatigue resistance loss during the in-service life as compared to HMA. Moreover, for both binder and base courses, the similar shift factor values obtained for HMA and WMA showed that the chemical additive did not alter the thermal susceptibility of the mixture, confirming that the latter depends strictly on the bituminous components (virgin bitumen and bitumen from RAP).

Moreover, it is worth pointing out that the VECD results confirmed the trend of the conventional indirect tensile tests, giving at the same time additional information about the intrinsic properties of the materials and demonstrating the reliability of the VECD model even for WMA mixtures. Further advantages of the VECD characterization are less time-consuming laboratory tests and less cores to be extracted from the pavement thanks to the small specimen geometry.

The pavement performance simulations with FlexPAVE^{TM} indicate warm recycled pavements can have better long-term performance and longer service life than conventional hot recycled pavements, confirming the preliminary results available in the literature. Such promising results add up to the remarkable environmental benefits and energy savings provided by warm recycled pavements, further encouraging their application. The comparison between the conventional elastic-based design method KENPAVE and FlexPAVE^{TM} results highlights the importance to switch from elastic based to viscoelastic based pavement design tools, in order to catch the actual contribution to the pavement service life provided by high-performance non-standard materials.

These findings, gathered during a relatively wide timespan of pavement in-service life, suggest that the WMA section has better long-term performance with respect to the reference HMA section, demonstrating the compatibility between the PMB and the chemical additive throughout in-service ageing as well. Considering also the significant environmental and economic benefits ensured by WMA technologies, warm recycled mixtures produced with WMA chemical additives and PMB represent a reliable and environmentally friendly solution to obtain durable pavements. The existing field trial will be continuously monitored over time, providing further data regarding the evolution of the behavior of these mixtures in the field.

Chapter 6.
S-VECD characterization and application of the viscoplastic shift model on WMAs with high RAP content

6.1 Background and objectives

This research project follows the optimal results obtained from the 7-years study and monitoring of the WMAs in the motorway pavement presented in Chapter 5. In fact, in order to satisfy the always more important sustainability in the infrastructure's framework, WMA technology seems to be one of the most promising solutions for the construction of flexible pavements without penalizing the field performance. WMAs, thanks to the lower production and compaction temperatures of up to 40 °C with respect to the conventional HMAs, allow the reduction of CO_2 in the atmosphere and less energy consumption (Cheraghian et al., 2020). WMAs' technology, such as foaming processes, organic additives and chemical additives (S. D. Capitão et al., 2012; Rubio et al., 2012), have been deeply investigated for decades, and the good performance of the mixtures in both laboratory and field conditions was assessed (Belc et al., 2021; Jattak et al., 2021; Kusam et al., 2017; B. Li et al., 2023; Polo-Mendoza et al., 2022; Spadoni, Ingrassia, Mariani, et al., 2022; Stimilli, Frigio, Cardone, et al., 2017; Yu et al., 2022). Nowadays, the WMAs are usually used all over the world and it is becoming conventional practice for road agencies (Sukhija & Saboo, 2021).
The next challenge regarding the use of WMAs is to incorporate high percentages of RAP. Since the adopted production temperature results in less oxidative hardening of the binder and less re-activation of the RAP binder which has already undergone to oxidative phenomena during the service of the pavement (secondary ageing, Liu et al.2024), RAP can be employed since it works more as aggregate, or the so-called "black aggregate", without penalizing the binder properties (Behnood, 2020; Rathore et al., 2022; Stimilli et al., 2015). This topic represents one of the most beneficial aspects which could further increase the sustainability of these mixtures: reduction of the demand for virgin aggregates which are non-renewable resources, and reduction of the RAP destined to be waste material, thus enhancing the circular economy impact of the pavement. However, the heterogeneity of the RAP treated by a conventional crushing and screening process present a challenge for the variability control of the reclaimed asphalt mixture, especially due to the different bitumen content and its behavior into the mixture, resulting up to date in a low inclusion of RAP content, thus a limited environmental and economic benefit (N. Li et al., 2024; Zaumanis et al., 2022).
Researchers are evaluating the possibility to incorporate up to 60% of RAP in dense-graded asphalt mixtures. It has been found that such WMAs, if polymer modified bitumen is used, can provide good crack propagation resistance, high fatigue resistance, combined with acceptable stiffness which can slightly penalize the rutting resistance (Liu et al., 2024;

Zaumanis et al., 2023). However, the overall performance is usually acceptable for medium/low-traffic pavements (S. Capitão et al., 2023; Keymanesh et al., 2023), whereas studies about high RAP content for motorways sections are not available in the scientific literature. Moreover, it should be underlined that if the research on dense-graded mixtures with high RAP content presents lacks understanding which limit its use by road authorities, the research on open-graded mixtures with RAP content is even much more very restricted. In fact, RAP use in wearing courses is not permitted by many road authorities (Zaumanis et al., 2023).

Given this background, the aim of this research was to investigate the possibility of using WMAs with high RAP content for all the asphalt courses in the Italian motorways, without penalizing the mechanical properties. The WMAs were produced using a chemical additive which allows to decrease the production and compaction temperatures of 40 °C with respect to the conventional HMAs. The RAP content was 25% and 45% for wearing and base courses, respectively, which would mean an increase of 10% and 15%, respectively, with respect to the actually employed HMAs.

6.2 Materials

Two WMAs containing high RAP percentages were investigated: a WMA for wearing course, named OG25W, and a WMA for base course, named DG45W. Both of the mixtures were preliminary studied in laboratory in order to define the optimal total bitumen content and aggregate gradation so that the volumetric and mechanical requirements prescribed by Italian technical specifications (NTC:2022) were satisfied.

These WMAs were compared with the conventional HMAs described in Section 3.2.1. Note that in this Chapter, in order to make the identification of the mixtures as intuitive and clear as possible, the hot mixture OG for wearing course is here named OG15H, and the hot mixture H for base course is here named DG30H.

WMA for wearing course OG25W

OG25W was produced using 25% of RAP deriving from the milling of wearing courses of old motorway pavements and 73% of basaltic virgin aggregate plus 2% of limestone filler. Specifically, the RAP 0/16 was fractioned, and 20% of class 8/16 plus 5% of class 4/8 were used. The use of such classes discarding the class 0/4 (which contains higher amount of bitumen) allows the reduction of the heterogeneity of the material (differently, OG15H was produced with 15% of unfractioned 0/16 RAP)(N. Li et al., 2024).

The two RAP classes and the virgin aggregate were combined in order to obtain the same aggregate gradation usually used for wearing mixtures, as shown in Figure 6.1, characterized by a NMAS of 14 mm. In Table 6.1 the mix design of OG25W indicating the percentages of use of each aggregate class is reported. A dosage equal to 0.3% by aggregate weight of cellulose and glass fiber was added in order to prevent drain-down issues (as for OG15H).

The total binder content (virgin bitumen plus bitumen from RAP) is 5.4% by aggregate weight. The virgin bitumen, produced with SBS polymer-modified bitumen with 3.8% polymer by binder weight, is 4.5% by aggregate weight. It should be noted that the total binder content is 0.3% higher than the reference OG15H, whereas the dosage of the virgin bitumen results in the same (see Section 3.2.1). The same virgin bitumen of the reference HMAs was used characterized by the same properties indicated in Table 3.. The maximum density of mixture OG25W is 2,494 g/cm^3.

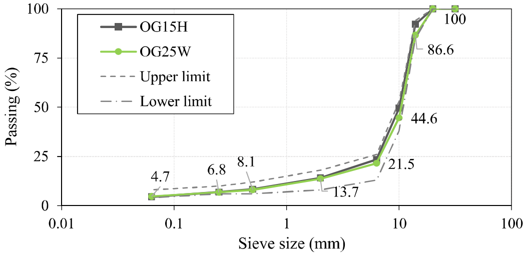

Figure 6.1. Aggregate gradation of OG25W compared with OG15H.

Table 6.1. Mix design of OG25W.

	Virgin aggregate (basaltic)				RAP		Fibers
Class	0/1	0/2	4/8	10/16	4/8	8/16	(by aggr. weight)
% of use	2	10	10	53	5	20	0.3

OG25W was produced with the same amino-type chemical additive employed for the production of the WMA mixture investigate in Chapter 5 (named C1). The dosage was designed in accordance with the recommendations of producer (0.2÷0.5% by total binder weight) and optimized through laboratory trial productions. The dosage was equal to 0.40% by total binder weight. Considering that the mixture contained 25% of RAP and the re-activated bitumen is about 60%, 0.40% by total binder weight corresponds to 0.45% by virgin bitumen weight. Since the chemical additive should not change the binder properties (Ferrotti et al., 2017), the expected PG of the bitumen is PG 76-16.
The production and compaction temperatures of OG25W were 130 °C and 120 °C for the WMA mixtures, so lower of 40°C with respect to OG15H.

WMA for base course DG45W
DG45W was produced using 45% of RAP deriving from the milling of base and wearing courses of old motorway pavements and the remaining 55% of limestone virgin aggregate. Specifically, the RAP 0/20 was fractioned, and divided into the classes 0/8 and 8/20. 15% of 0/8 and 30 30% of 8/16 were used. Such practice has been demonstrated to allow a better control of the mixture properties, reducing the heterogeneity of the material (differently, DG30H was produced with 30% of unfractioned 0/20 RAP). The two RAP classes and the virgin aggregate were combined in order to obtain the same aggregate gradation usually used for base mixtures, as shown in Figure 6.2, characterized by a NMAS of 20 mm. In Table 6.2 the mix design of DG45W with the percentages of use of each aggregate class is reported.
The total binder content (virgin bitumen plus bitumen from RAP) is 4.3% by aggregate weight as for DG30H. As a consequence of the higher RAP content, the added virgin bitumen, produced with SBS polymer-modified bitumen with 3.8% polymer by binder

weight, is 2.7% by aggregate weight, which is lower than the one in DG30H (i.e., 3.0%, see Section 3.2.1). The same virgin bitumen of the reference HMAs was used, and it is modified with SBS dosed at 3.8% bitumen weight, obtaining the same properties indicated in Table 3.. The maximum density of mixture H is 2,505 g/cm^3.

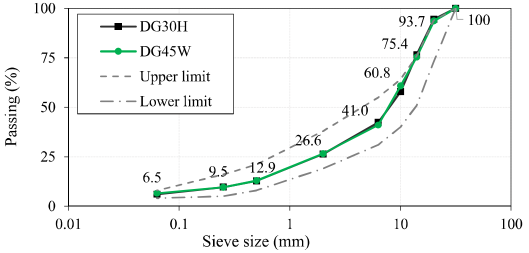

Figure 6.2. Aggregate gradation of DG45W compared with DG30H.

Table 6.2. Mix design of DG45W.

	Virgin aggregate (limestone)			RAP	
Class	0/4	6.3/16	16/22.4	0/8	8/20
% of use	18	12	15	15	30

DG45W was produced with the same amino-type chemical additive employed for the production of the WMA mixture investigate in Chapter 5 (named C1) and OG25W. The adopted dosage was the same as OG25W, equal to 0.40% by total binder weight (always designed in accordance with the recommendations of producer and optimized through laboratory trial productions). Considering that the mixture contained 45% of RAP and the re-activated bitumen is about 60%, 0.40% by total binder weight corresponds to 0.50% by virgin bitumen weight. Since the chemical additive should not change the binder properties (Ferrotti et al., 2017), the expected PG of the bitumen is PG 76-16.

The production and compaction temperatures of DG45W were 130 °C and 120 °C for the WMA mixtures, so lower of 40°C with respect to DG30H.

6.2.1 Field test trial

A 400-m full-scale field test trial was constructed in October 2022 as part of the A1 Italian motorway between the cities of Fiano Romano and Tivoli Terme (near Rome). The construction involved the first lane and consisted of milled and reconstructed asphalt layers. The field test trial is composed of two 200-m sections, i.e., the WMA section and the reference HMA section, each characterized by the same pavement structure adopted for Italian motorways (Figure 6.3):

- An open-graded wearing layer with nominal thickness of 4 cm, constructed with OG25W and OG15H for the WMA and HMA section, respectively.
- A dense-graded layer with a total nominal thickness of 25 cm, whose construction was carried out via the consecutive compaction of two layers: a 15-cm lower layer on the

foundation, called with the suffix *inf*, and a 10-cm upper layer, called with the suffix _*sup*. It was constructed with DG45W and DG30H for the WMA and HMA section, respectively.

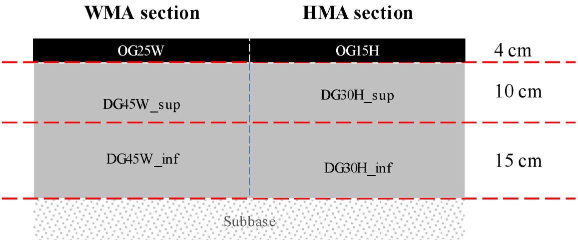

Figure 6.3. Pavement structure of the field test trial.

The existing subbase layer is asphalt-treated and has a nominal thickness of 32 cm (checked by the extraction of cores). An HWD campaign was executed on the subbase, after the milling of the old asphalt layers. The deformations recorded by the 9 geophones were used to construct the deflections bowls and back-calculated with the software BAKFAA to determine the stiffness moduli of the subbase and the subgrade. The average stiffness of the subbase resulted in 12306 MPa and 10623 MPa for the WMA and HMA section, respectively. The average stiffness of the subgrade resulted in 322 MPa and 231 MPa for the WMA and HMA section, respectively. In conclusion, even though the stiffness of such courses in the WMA section is slightly higher, it can be considered comparable to the ones of the HMA section. The average stiffness of the subbase and subgrade were assumed equal to 11400 MPa and 270 MPa, respectively. Moreover, in order to confirm the high stiffness value of the subbase, dynamic modulus tests were carried out on two specimens obtained from the inner part of the cores extracted from the pavement. The tests were carried out following the VECD method described in Section 2.3 for large specimens. Tests were performed at 5, 20, 35 and 40 °C and at the frequencies 0.1, 0.5, 1, 5, 10 and 20 Hz, setting an axial deformation of 30$\mu\varepsilon$ (lower than the values for asphalt mixtures) which ensures a linear behavior of the material. The mastercurve of the average dynamic modulus at 20 °C obtained with the 2S2P1D model long with the experimental data is shown in Figure 6.4. The stiffness obtained at the same testing condition of the HWD, i.e., 20 °C and 30 Hz, was 9109 MPa, that is comparable to the average value of 11400 MPa from HWD analysis, considering the different loading conditions (sinusoidal vs. impulsive).

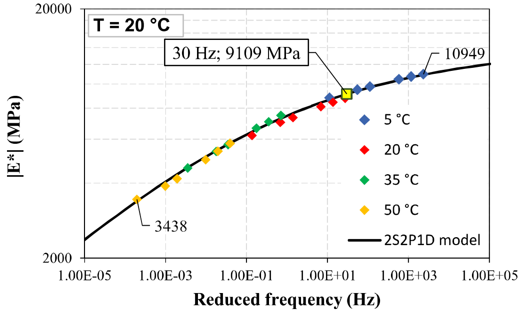

Figure 6.4. Dynamic modulus mastercurve of the asphalt-treated subbase at 20 °C.

6.3 Testing program and procedures

Table 6.3 reports the testing program of this research.

The first stage provided the investigation of laboratory-compacted specimens through the S-VECD characterization of all the mixtures, and the rutting characterization of the DG ones, within the AM-PRS. The rutting characterization of the OG mixtures was not carried out, since it is well-known that the strong skeleton structure given by the high coarse interlocked aggregate, combined with the SBS modified bitumen, ensures a high resistance against permanent deformations. Moreover, OGFC reaches the end of life due to the clogging of the air voids before, so it must be milled and reconstructed every more or less 10 years. In this stage, the reference mixtures DG30H and OG15H were not studied through the S-VECD approach, but the results derived from the research presented in Chapter 3-Section 3.4.2 were used (mixture H and OG, respectively), since they were obtained in the same testing conditions. The WMA mixtures were produced at the asphalt plant at 130 °C, and the gyratory samples were immediately compacted at 120 °C by a gyratory compactor in accordance with EN 12697-31(2019). The gyratory-compacted samples had a diameter of 150 mm and height of 170 mm. The target air void content of the gyratory samples was 8% for DG45W, and 20% for OG25W and OG15H. For the S-VECD characterization, four small test specimens and one large test specimen were vertically extracted from the inner portion of the gyratory-compacted sample of DG45W and OG25W mixtures, respectively. In fact, due to their high air void contents, only the large specimens were considered for the OG mixture. For the rutting characterization, one large test specimen was vertically extracted from each gyratory-compacted sample for both the mixtures. The second stage provided the investigation of the dense-graded cores, both WMA and HMA, extracted from the field test trial to assess the effects of *in situ* compaction. A set of 150-mm diameter cores was extracted from each field test section in February 2023. After cutting the layers at the interface, small specimens destined to the S-VECD characterization were horizontally extracted from the *Base_sup* course (see Figure 5.3a), and large specimens were vertically extracted from *Base_inf* course, as schematized in Figure 6.5. The OGFC was not included in the investigation due to its limited thickness.

Table 6.3. Testing program

	Mixture	S-VECD characterization	Rutting characterization
Laboratory-compacted specimens	DG45W	✓ (small specimens)	✓ (large specimens)
	DG30H	✓* (small specimens)	✓ (large specimens)
	OG25W	✓ (large specimens)	-
	OG15H	✓* (large specimens)	-
Cores from the field test trial	DG45W	✓ (small specimens)	✓ (large specimens)
	DG30H	✓ (small specimens)	✓ (large specimens)

*results from the previous research: Chapter 3, Section 3.4.2.

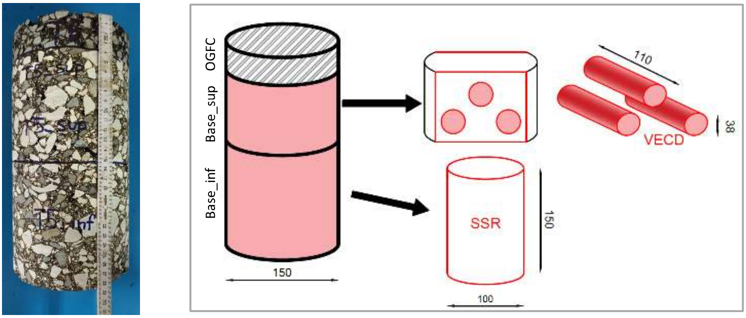

(a) **(b)**

Figure 6.5. (a) Core from the WMA section and (b) scheme of the test specimens obtained from the cores.

For both the set of tests provided in the first (laboratory-compacted specimens) and second (cores from the field test trial) according to Table 6.3, the testing conditions are the same. Regarding the S-VECD characterization, dynamic modulus tests were carried out by means of an AMPT. For both the DG and OG mixtures, the investigated temperatures were 4 °C, 20 °C, and 40 °C (for OG15H: 4 °C, 15 °C, 25 °C and 40 °C, see Section 3.3), based on the bitumen PG 76-16. The frequencies investigated for each temperature were 0.1 Hz, 0.5 Hz, 1 Hz, 5 Hz, and 10 Hz, 20 Hz, plus 0.01 Hz at 40°C. The target axial deformation was 50÷75 με and 85÷125 με for small and large specimens, respectively. The single-operator precision requirements were checked and verified. Then, cyclic fatigue tests were carried out at 21 °C (based on the bitumen PG) for all the mixtures. In order to obtain tests with the proper duration, the peak-to-peak on-specimen amplitude of the sinusoidal strain was selected to be between 180 με and 230 με for DG mixtures, and between 190 με and 290 με for OG mixtures. S_{app} is determined at a specific temperature that is based on the climatic PG of the location where the pavement is constructed. Given that the field test trial is located in a PG 58-10 climatic zone (Giuliani, 2006), the S_{app} reference temperature used in this study was 21°C.

Regarding the rutting characterization on DG45W and DG30H, SSR(AASHTO TP 134, 2019) testing temperatures are based on the climatic conditions of the locations of the field test trial which is in a climatic PG 58-10 (Giuliani, 2006), and on the depth at which the mixture is used in the pavement (Figure 6.3). Therefore, the testing temperature *TH* and *TL* were 43 °C and 29 °C, respectively. In this study, the *RSI* was calculated for each mixture considering the mixture for "intermediate" and the climatic conditions of the field test near Rome.

Finally, fatigue and rutting performance of the mixtures were investigated at the structural level by performing FlexPAVE^{TM} pavement simulations based on the laboratory test results considering the actual Italian motorway pavement.

6.4 Results and analysis

6.4.1 Laboratory specimens

S-VECD fatigue characterization

In Figure 6.6a-b, the experimental data from dynamic modulus tests are represented in Black (norm of the dynamic modulus vs phase angle) and Cole-Cole (dissipation modulus vs. storage modulus) diagrams, respectively. It can be seen that the experimental data obtained at various frequencies and temperatures are aligned in almost continuous curves, confirming the thermo-rheologically simple behavior of all the mixtures. As expected, the OG mixtures are characterized by lower stiffness with respect to the DG ones due to the higher AV content. In Figure 6.6a, it can be observed that DG30H and DG45W are characterized by similar $|E^*|$ and δ values. However, DG30H shows strongly higher values of the dissipation modulus E_2 indicating a more viscous behavior with respect to DG30H (Figure 6.6b). Analogously, OG15H and OG25W present similar $|E^*|$ and δ values (Figure 6.6a), but OG15H is more viscous at low temperatures (Figure 6.6b).

Figure 6.7a reports the shift factors used to construct the storage modulus and phase angle mastercurves in Figure 6.7b-c, respectively. All of them are represented at the reference temperature of 21.1 °C. In Figure 6.7b, the average AV content of the tested specimens are reported. Table 6.4 reports the parameters of the 2S2P1D models.

Shift factor values basically overlap for all the testing temperatures, confirming that the thermo-susceptibility is broadly the same for both WMAs and HMAs due to the same SBS modified bitumen. Moreover, it is not influenced by the presence of the chemical additive. The storage modulus mastercurves (Figure 6.7b) confirm that the DG mixtures present comparable stiffness at similar volumetric properties (2.5% and 2.9% of AV), as also indicated by the similar 2S2P1D parameters of the model (Table 6.4). DG30H is slightly stiffer, likely due to the higher production temperature which causes an higher oxidation of virgin bitumen and to an higher re-activation of the aged bitumen of the RAP. Analogous considerations can be made on the OG mixtures. Despite the lower AV of OG25W (i.e., 4%), the mixtures are characterized by overlapping storage modulus mastercurves with similar parameters of the 2S2P1D model (Table 6.4). It means that the stiffness increment of OG15H is ascribable to the effects of the higher production temperatures on the bitumen, as asserted for the DG mixtures. The phase angle mastercurves (Figure 6.7c) do not highlight significant differences between the mixtures, denoting comparable viscoelastic behavior when the load is applied. OG mixtures show slightly higher phase angle values with respect to DG mixtures, that can be due to the higher total binder content (see Section 6.2).

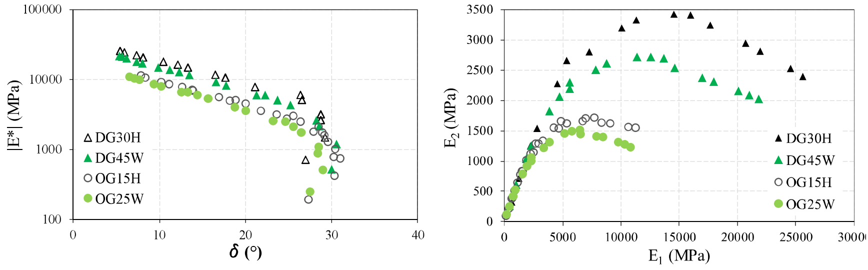

(a) **(b)**

Figure 6.6. Laboratory specimens: (a) Black and (b) Cole-Cole diagrams.

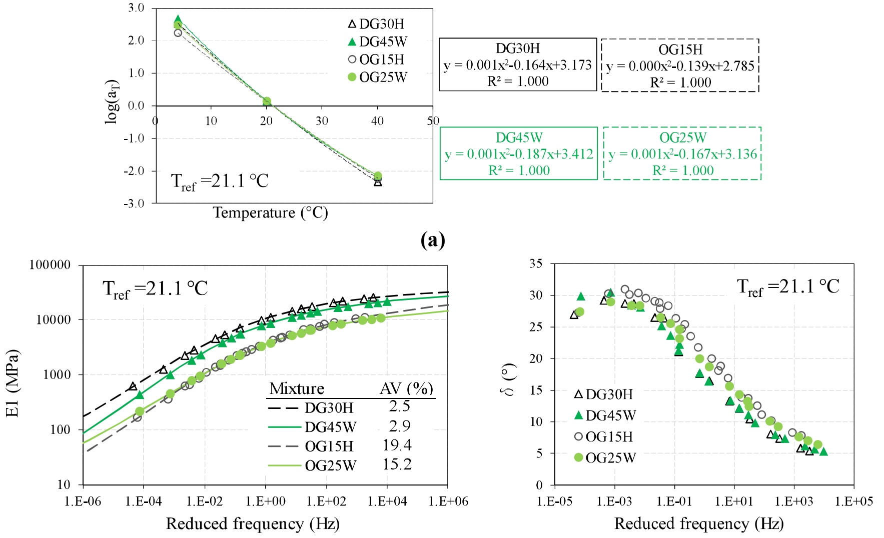

(a)

(b) **(c)**

Figure 6.7. Laboratory specimens: (a) shift factor, (b) storage modulus mastercurves (2S2P1D model) and (c) phase angle mastercurve at 21.1 °C.

Table 6.4. Laboratory specimens: parameters of the 2S2P1D models for the storage modulus.

Mixture	$E_{1,0}$ (MPa)	$E_{1,\infty}$ (MPa)	ξ	k	h	β	$\log\tau$
DG30H	28	40000	1.54	0.14	0.38	1E+12	-0.91
DG45W	5	40000	2.20	0.12	0.41	1E+12	-1.11
OG15H	4	40000	3.74	0.11	0.40	1E+12	-2.23
OG25W	12	40000	3.46	0.08	0.36	1E+12	-2.71

Figure 6.8a shows the replicates overlapping damage characteristic curves obtained from different specimens for each WMAs, then used to construct the fits. Figure 6.8b shows the fit of them for each mixture, including the reference ones (Table 6.3), whose regression coefficients are reported in Table 6.5. Figure 6.8b also reports the average AV of the specimens investigated in the fatigue tests, which are close to those of the specimens used in the dynamic modulus tests (see Figure 6.7b), as required.

It can be noted that the damage characteristic curves overlap but they have different failure points. It is likely due to the heterogeneity given by the RAP, representing surfaces with lower fatigue resistance, that could especially emerge in a specimen with a diameter of 38 mm.

Comparing the *C vs. S* curves of the DG mixtures (Figure 6.8b), it can be seen that the curve of DG45W is in significant lower position with respect to DG30H, as also expressed by the different regression coefficients in Table 6.5, even though such mixtures are characterized by similar stiffness (Figure 6.7b, so similar initial pseudostiffness). This outcome indicates that DG45W undergoes a faster decrease in pseudostiffness during the application of the cyclic loading. Moreover, the lower *S* value at failure (i.e., 270000 of DG45W vs. 360000 of DG30H) indicates a lower capacity to withstand the damage. However, DG45W is capable of resisting at pseudostiffness values *C* lower than DG30H, which should express higher toughness.

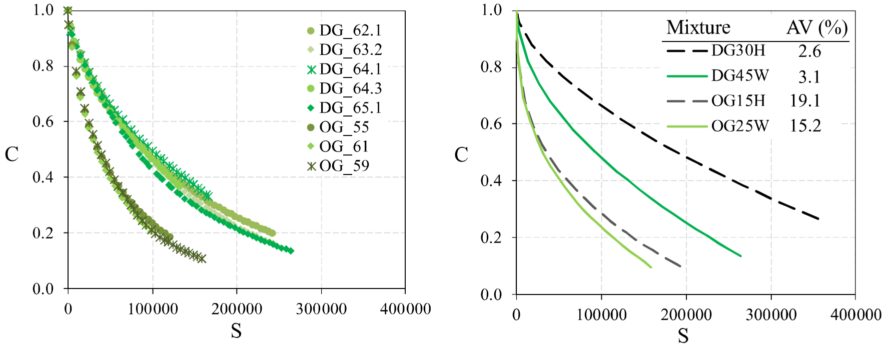

(a) **(b)**

Figure 6.8. Laboratory specimens: (a) experimental damage characteristic curves of the WMAs and (b) fits of the damage characteristic curves of WMAs and HMAs.

Table 6.5. Laboratory specimens: parameters of the damage characteristic curves.

Mixture	C11	C12
DG30H	3.05E-04	6.09E-01
DG45W	1.21E-03	5.27E-01
OG15H	1.29E-02	3.49E-01
OG25W	1.21E-02	3.60E-01

The *C vs. S* curves of the OG mixtures (Figure 6.8b) are characterized by similar shape, as indicated by the C_{11} and C_{12} parameters (Table 6.5), and comparable length, denoting a comparable behavior. Specifically, the only difference is a slightly lower *S* value at failure recorder for DG45W, indicating a lower amount of dissipated energy.

The failure envelopes, whose slope is the parameter D^R are shown in Figure 6.9a. First, it should be underlined that the D^R values of the OG mixtures are higher than the ones of the DG mixtures, meaning higher toughness, and such results cannot be reliable due to their high AV content. Such results can be attributable to the rubbery behavior of the high amount of SBS modified bitumen, not properly taken into account by the D^R. Further research is needed to assess the reliability of this parameter for OG mixtures.

WMAs present slightly lower D^R values with respect to HMAs, but overall comparable. This means that the toughness of the mixtures is not penalized by the higher RAP content thanks to the chemical additive and to the lower production temperature.

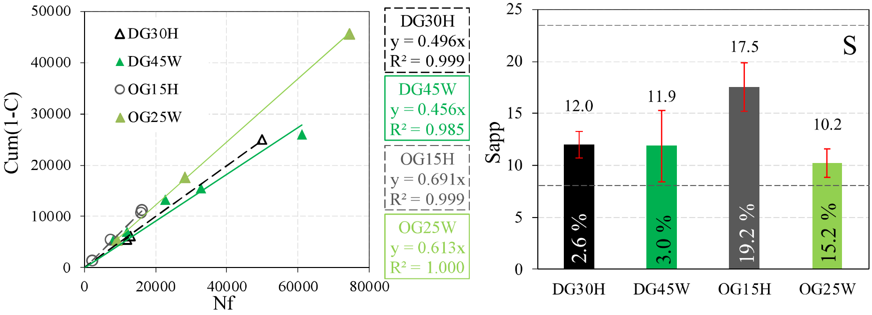

(a) **(b)**

Figure 6.9. Laboratory specimens: (a) D^R failure criterion and (b) S_{app} values (error bars represent the standard deviation).

The fatigue resistance of the mixture must be always evaluated through the damage characteristic curve (which mainly depends on the mixture's stiffness) and the failure criterion D^R which quantifies the mixture's toughness. S_{app} parameter combines these properties, allowing the prediction of the fatigue performance of the mixture within the pavement. The values of this synthetic index are reported in Figure 6.9b, together with the average AV obtained from the dynamic modulus and fatigue tests. It can be noted that DG mixtures provide comparable fatigue performance, and they could withstand a "Standard" level of traffic according to the classification proposed by FHWA. The greater dispersion of the S_{app} values of DG45W is attributable to the local presence of recycled aggregates in the 38 mm specimen, as already observed from the *C vs. S* curves of the specimens (Figure 6.8a). In particular, the analysis of this index shows that the DG30H mixture accumulates more damage at failure (*S* at failure), has higher toughness (D^R), but is stiffer (master curve, *C* values). Otherwise, DG45W takes advantage from a lower stiffness (master curve, *C* values) which makes the mixture potentially less prone to cracking, despite it seems to accumulate a lower level of damage to failure (*S* to failure). The analysis of the pavement with the

FlexPAVE™ software allows to obtain more significant information on the fatigue behavior of the two mixtures from a solely mechanical point of view.

Regarding the OG mixtures, the analysis of the S_{app} index shows that both mixtures satisfy the conditions of a tolerable "Standard" traffic level. However, it highlights that although the mixtures are characterized by similar stiffness (Figure 6.7a), the OG25W mixture shows a lower fatigue performance in line with the results obtained from the fatigue tests, i.e. lower capacity to absorb damage (S at failure) and lower toughness (D^R). As in the case of the D^R parameter, the poor reliability of the S_{app} for open mixtures must be underlined, as this parameter has been calibrated mainly for closed mixtures(Y. D. Wang et al., 2022).

Rutting characterization

Figure 6.10a-b shows the experimental curves representing the evolution of the viscoplastic deformation (ε_{vp}) during the application of the loading cycles at the two testing temperatures (i.e., 43 °C and 29 °C, T_H and T_L respectively) for DG45W and DG30H, respectively. The overlapping of the two replicates for each condition as well as the low difference between them at the end of the test not higher than 11% demonstrate the good quality and reliability of the data to be used within the shift model.

Figure 6.10c shows the comparison of the evolution of the average viscoplastic deformation (ε_{vp}) during the 600 cycles between the two investigated DG mixtures. In the same figure, the average AV of the test specimens is reported. It can be observed that at the high temperature T_H DG45W is less susceptible to permanent deformation at the same volumetric properties. However, at the low temperature T_L the WMA results more susceptible, may due slightly higher AV content (1%) or to the intrinsic behavior. The results from the field specimens will give more information to carry out valuable considerations.

The prediction of the average permanent strain of the mixtures during service in a standard pavement subjected to the climatic of the location of the field test trial and to standard traffic conditions is reported in Figure 6.11. The average AV of the specimens tested at both temperatures are reported in the same figure. The final value at 20 years represents the *RSI*, derived from the application of the shift model in standard conditions, and useful only to compare mixtures between them and not for the actual behavior in the field test trial (as specified in Section 2.5). Based on the *RSI*, DG30H would ensure an higher resistance against rutting, falling in the “Extremely Heavy” class according to the classification suggested by FHWA. On the other hand, DG45W would show an higher susceptibility to rutting, but it would guarantee a satisfying level traffic of the “Very Heavy” class. It can be concluded that both the mixtures are characterized by high and broadly comparable resistance to rutting. The slightly higher susceptibility of DG45W could be ascribable in minor measure to the higher AV and could be related to the stiffness properties of the mixtures. In fact, the dynamic moduli of DG45W were lower at all the temperatures and frequencies than the ones of DG30H (Figure 6.7b) mainly due to lower content of oxidized bitumen from the RAP due to the production temperature of 130 °C instead of 170 °C.

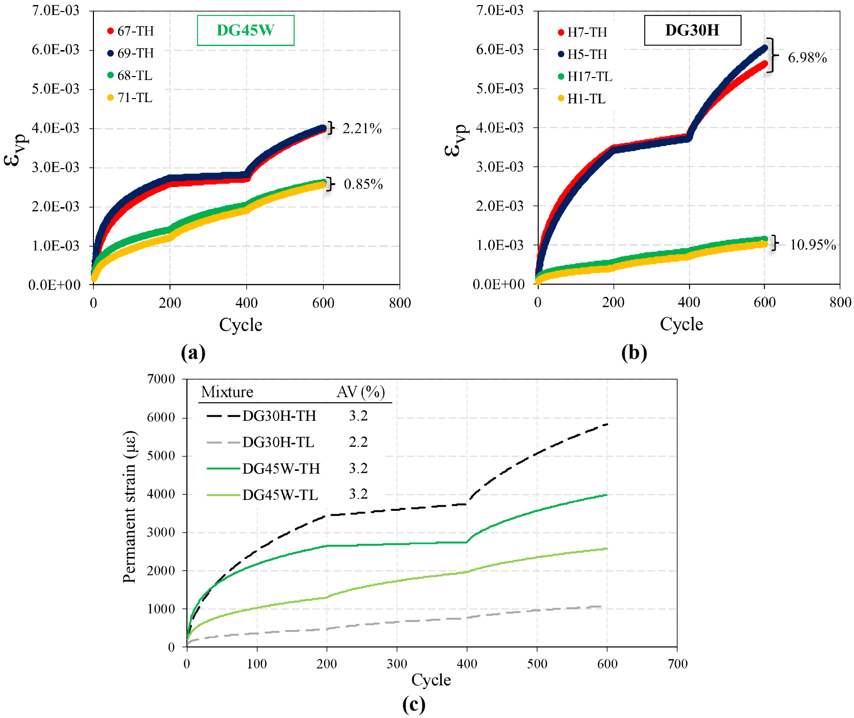

Figure 6.10. Laboratory specimens: experimental permanent strain growth of (a) DG45W and (b) DG30H, and (c) comparison between them.

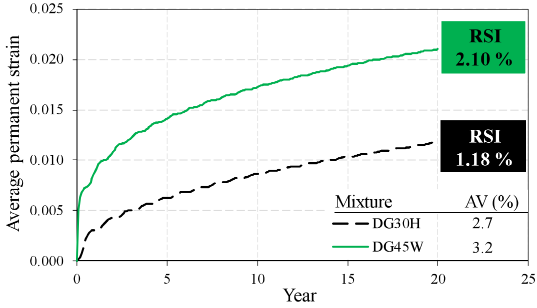

Figure 6.11. Laboratory specimens: prediction of the average permanent strain and RSI.

6.4.2 Field specimens

S-VECD fatigue characterization

In Figure 6.12a-b, the experimental data from dynamic modulus tests are represented in Black (norm of the dynamic modulus vs. phase angle) and Cole-Cole (dissipation modulus vs. storage modulus) diagrams, respectively. The thermo-rheologically simple behavior observed for the laboratory specimens is confirmed for all the mixtures, since the experimental data obtained at various frequencies and temperatures are aligned following continuous curves. From both the figures, it can be noted that and DG45W are characterized by similar stiffness properties and viscoelastic behavior, due to the overlapping of the experimental data.

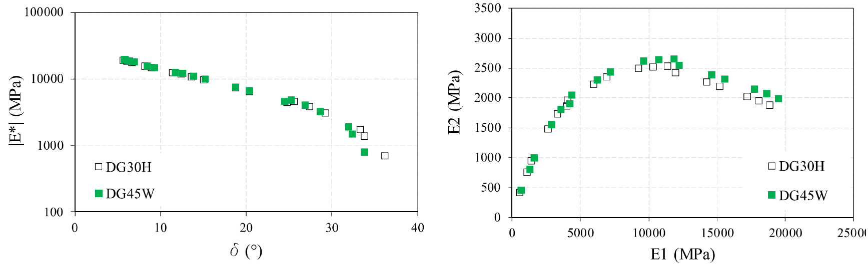

(a) **(b)**

Figure 6.12. Field specimens: (a) Black and (b) Cole-Cole diagrams.

Figure 6.13a reports the shift factors for the construction of the storage modulus and phase angle mastercurves, respectively shown in Figure 6.13b-c. All of them were constructed at the reference temperature of 21.1 °C. In Figure 6.13b, the average AV content of the tested specimens are reported. Table 6.6 reports the fitting parameters of the 2S2P1D models for the storage modulus.

As expected, shift factor values overlap for all the testing temperatures, as expressed by the polynomial fitting regression equations in Figure 6.13a, confirming that the mixtures are characterized by the same thermo-susceptibility, which is influenced by only the SBS modified bitumen and not by the chemical additive. The AV of the DG mixtures under the actual compaction of the field test trial was different. Specifically, as indicated in Figure 6.13b, DG45W was more compactable resulting in AV content lower for 1%. In such volumetric properties, the mixtures present comparable stiffness properties in terms of storage modulus at all the investigate frequencies and temperatures (Figure 6.13b), as also expressed by the similar 2S2P1D parameters of the model (Table 6.6). This outcome confirms that the high RAP included in DG45W does not negatively affect the stiffness of the mixtures thanks to a lower re-activation of its aged bitumen due to the production process at lower temperature with respect to DG30H. Even the phase angle mastercurves (Figure 6.13c) are basically overlapping, suggesting comparable viscoelastic response under the application of the vehicular loads.

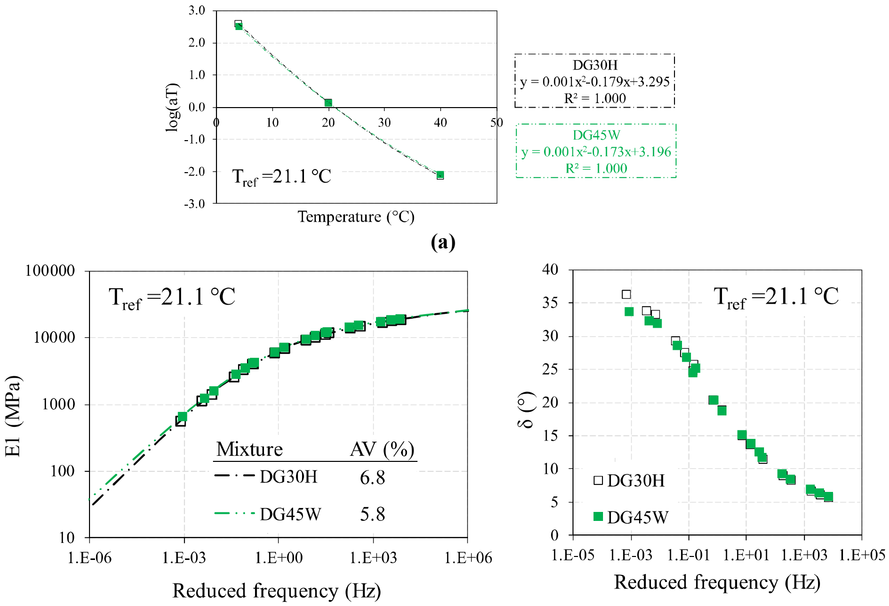

(a)

(b) (c)

Figure 6.13. Field specimens: (a) shift factor, (b) storage modulus mastercurves (2S2P1D model) and (c) phase angle mastercurve at 21.1 °C.

Table 6.6. Field specimens: parameters of the 2S2P1D models for the storage modulus.

Mixture	$E_{1,0}$ (MPa)	$E_{1,\infty}$ (MPa)	ξ	k	h	β	$log\ \tau$
DG30H	0.1	40000	2.84	0.13	0.46	1E+12	-1.33
DG45W	1.9	40000	2.45	0.12	0.44	1E+12	-1.45

Figure 6.14a-b show all the replicates damage characteristic curves for DG45W and DG30H, respectively, for whom middle failures were obtained and the requirements on the *DMR* and test durations were met. It can be observed that, especially for the hot reference mixture (Figure 6.14b), it was not possible to identify three *C vs. S* curves with both trend and final failure points overlapping, even maybe due to the limited number of specimens. This is probably due to the presence of recycled aggregates, which can locally penalize the toughness of the single small specimen, depending on the where they are randomly positioned. The greater dispersion of the characteristic curves for the DG30H specimens is probably attributable to the high production temperatures which re-activate a greater content of aged bitumen in the RAP.

Therefore, for the fitting of the *C vs. S* curves of DG30H, the two *C vs. S* curves in the lowest position (C3_5 and C3_6) were discarded, since they reached a quantity of damage accumulation *S* and/or pseudo-stiffness *C* at failure particularly low and were considered, therefore, not representative.

Differently, for the DG45W mixture (Figure 6.14a), it was possible to identify a group of overlapping *C vs. S* curves, but with different final failure points. Since the same trend was recorded for the laboratory specimens (Figure 6.8a), the fitting was carried out considering these curves.

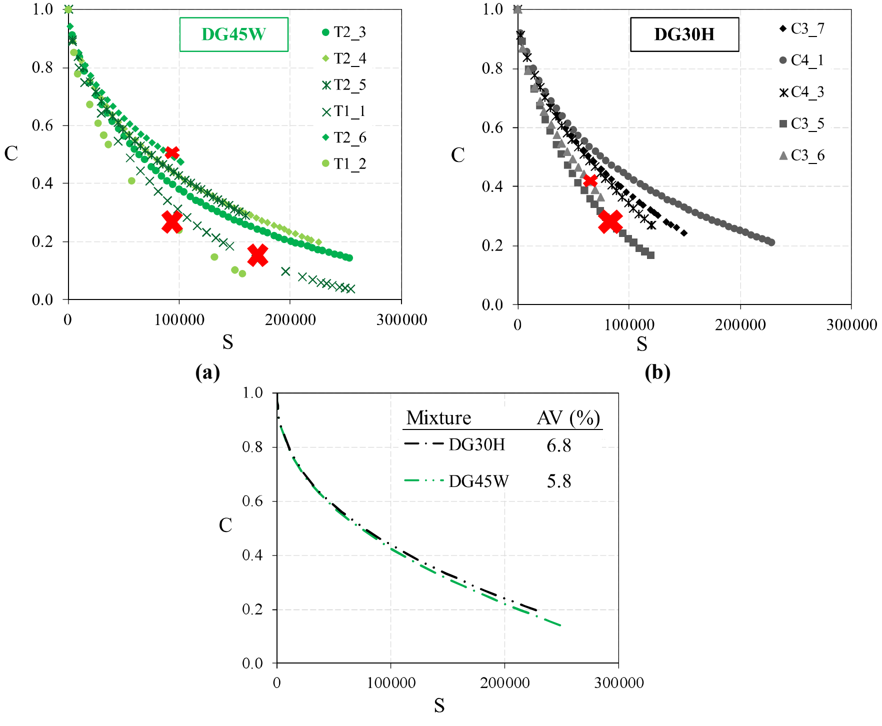

(a)

(b)

(c)

Figure 6.14. Field specimens: experimental damage characteristic curves of (a) DG45W and (b) DG30H (red crosses indicate the discarded ones), and (c) fits of the damage characteristic curves.

Table 6.7. Field specimens: parameters of the damage characteristic curves.

Mixture	C11	C12
DG30H	3.71E-03	4.36E-01
DG45W	3.61E-03	4.41E-01

So, Figure 6.14c shows the fits, whose regression coefficients are reported in Table 6.7. Figure 6.14c also reports the average AV of the specimens investigated in the fatigue tests, equal to the AV of the specimens subjected to the dynamic modulus tests (see Figure 6.13b). It can be noted that the damage characteristic curves overlap but they have different failure points. It is likely due to the heterogeneity given by the RAP, representing surfaces with lower fatigue resistance, that could especially emerge in a specimen with a diameter of 38 mm.

From Figure 6.14c, it can be observed that the curves of the two mixtures basically overlap, as also confirmed by the values of the regression coefficients C_{11} and C_{12} (Table 6.7). This demonstrates that, with the same stiffness properties (Figure 6.13b), the mixtures are characterized by a similar damage evolution during the application of the cyclic load. Furthermore, by analyzing the failure, i.e. the final points of the *C vs. S* curves, it can be noted that the DG45W mixture is capable to resist until lower pseudostiffness *C*, implying greater toughness, accumulating higher damage *S*.

The results in term of the failure criterion D^R are shown in Figure 6.15a. As a consequence of the similar stiffness (Figure 6.13b) and damage characteristic curves (Figure 6.14c), the ability to absorb energy before failure of the WMA is comparable to that of the corresponding hot reference mixture, too. This result corroborates the analysis conducted on the laboratory specimens, and confirms how the lower production temperature and the presence of the WMA additive allow the inclusion of high RAP content without penalizing the performance of mixtures.

The values of the synthetic index S_{app}, summarizing the fatigue resistance of the mixture, of DG30H and DG45W mixtures are shown in Figure 6.15b. For each mixture, the average AV of the tested specimens is reported. From the analysis of S_{app} values, it is possible to note that both mixtures are characterized by a fatigue behavior capable of satisfying the "Standard" traffic level according to the classification proposed by the FHWA.

However, Figure 6.15b highlights that, although the mixtures are characterized by similar stiffness, the DG45W mixture seems to ensure a slightly better fatigue performance likely related to the results obtained from the fatigue tests, i.e. greater capacity to absorb damage (*S* at failure) and greater toughness (D^R). The dispersion of the S_{app} values can be led back to the local presence of RAP in the 38 mm specimens, similarly to what was observed for the *C vs. S* curves of the specimens (Figure 6.14a-b).

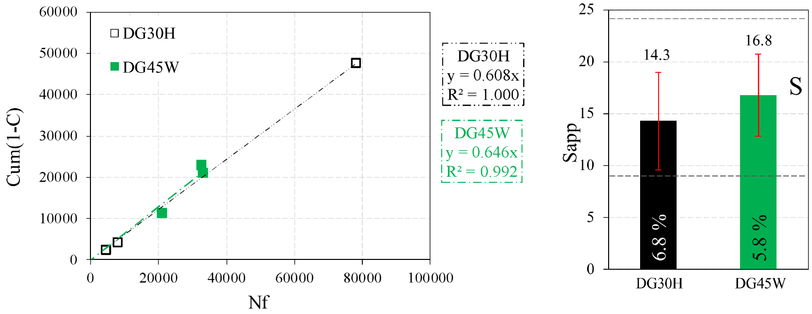

(a) **(b)**

Figure 6.15. Field specimens: (a) D^R failure criterion and (b) S_{app} values.

Rutting characterization

Figure 6.16a-b shows the experimental curves of the evolution viscoplastic deformation (ε_{vp}) during the application of the loading cycles at the two testing temperatures (i.e., 43 °C and 29 °C, T_H and T_L respectively) for DG45W and DG30H, respectively. According to the reference standard, the average difference of the strain at the end of the test should not exceed 25%. This requirement is satisfied for all the mixtures' replicates, asserting the good quality of the data, except for DG45W tested at T_L (Figure 6.16a). For this latter one, due to the limited number of available cores from the field test trial, it was not possible to carry out another replicate.

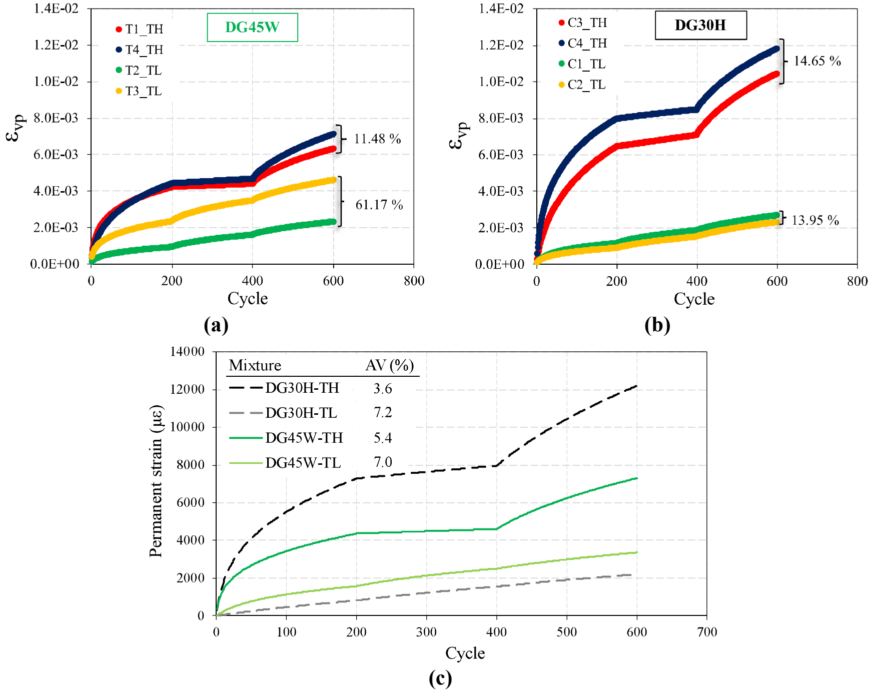

(a) **(b)**

(c)

Figure 6.16. Field specimens: experimental permanent strain growth of (a) DG45W and (b) DG30H, and (c) comparison between them.

Figure 6.16c shows the evolution of the average viscoplastic deformation (ε_{vp}) of the mixtures during the 600 cycles in the same graph. In this figure, the average AV of the test specimens is reported as well. According to the reference standard, the standard deviation of the AV of all the specimens of a mixture should not exceed 0.5%. This limit could not be satisfied, especially for DG30H, and it was taken into account during the analysis of the results. Such variability is almost unavoidable in the field conditions but could be also intrinsic of the mixture due to the heterogeneity given by the RAP penalizing the compactability.

It can be observed that DG45W is more susceptible to permanent deformation than DG30H at T_L (29 °C), whereas it seems to be less deformable at the maximum T_H temperature (43 °C) despite its higher AV (5.4% for DG45W vs. 3.6% for DG30H). It is interesting to notice that such trend in terms of permanent deformations is analogous to the one observed from the laboratory specimens (Figure 6.10c), confirming the overall good data despite the requirements in the AV and repeatability not satisfied, since the environment is much less controlled than the laboratory one.

The prediction of the average permanent strain of the mixtures during service in standard condition (structure of the pavement and traffic) and under the climatic of the location of the field test trial is shown in Figure 6.17. The average AV of the specimens tested at both temperatures are reported in the same figure. The *RSI* values, corresponding to the percentage of the permanent strain of the mixture course at 20 years, are reported.

Based on the *RSI*, which can merely be used for comparison purpose between mixtures, DG30H should exhibit an higher resistance against rutting, falling in the “Very Heavy” traffic level according to the classification suggested by FHWA. DG45W should ensure a high rutting resistance but slightly lower than DG30H, falling in the “Heavy” traffic level. The greater propension to accumulate viscoplastic deformation of DG45W, in line with the rutting results obtained on laboratory-compacted specimens (Figure 6.11), can be ascribable to the higher AV content with respect to DG30H (Figure 6.16c). Specifically, considering that the warm mixture showed the same behavior at both T_L and T_H of the hot reference mixture (see Figure 6.10c and Figure 6.16c), it can be hypothesized that the lower performance of DG45W is due to the higher susceptibility to permanent deformations that the mixture exhibits at medium temperatures (data at T_L).

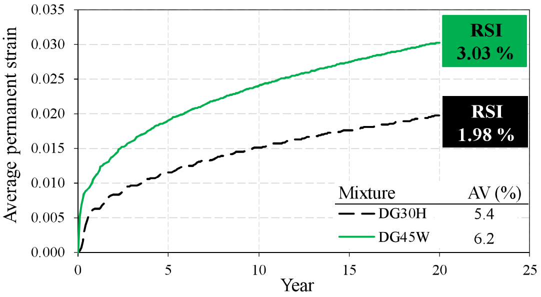

Figure 6.17. Field specimens: prediction of the average permanent strain and RSI.

6.5 Pavement performance simulations

6.5.1 Input data

In this study, FlexPAVE^{TM} analysis was performed for a 30-year pavement service life under both thermal effects and traffic loading, in order to evaluate both fatigue and rutting damage. Two scenarios were considered: *LAB* with the materials' properties of the laboratory-compacted specimens (Figure 6.18a), *FIELD* with the materials' properties of the field specimens (Figure 6.18a).

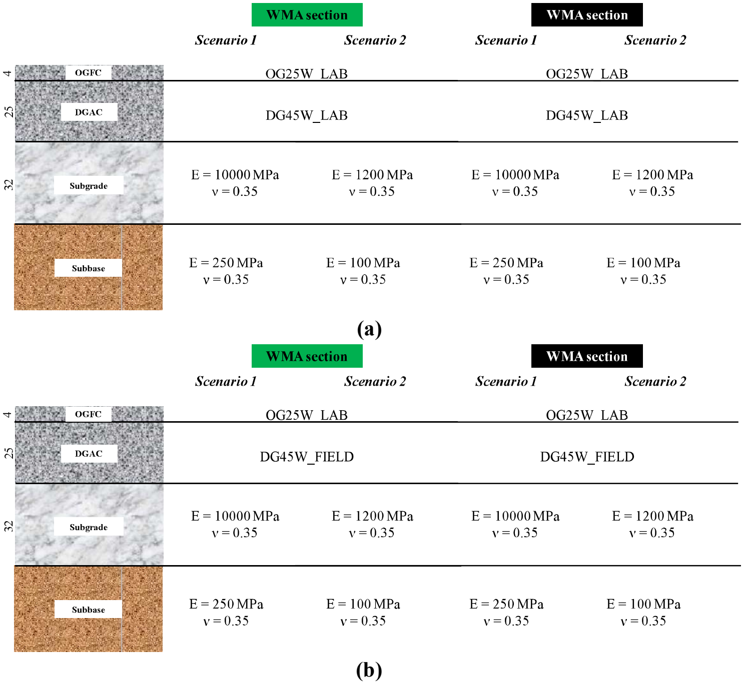

Figure 6.18. Pavement performance simulations: material properties considered for scenario (a) *LAB* and (b) *FIELD*.

The structure of the pavement is the same as the constructed field test track (Figure 6.3), i.e., the WMA section and the HMA section:

- 4-cm open-graded wearing layer. The S-VECD results of the laboratory specimens OG25W and OG15H were used for the WMA and HMA sections, respectively, for both the scenarios. In absence of SSR rutting tests on the OG mixtures, the rut depth was set as 0.

- 25-cm dense-graded asphalt layer, made of the 15 cm (*inf*) and 10 cm (*sup*) courses whose compaction was carried out consecutively, presenting perfect bonding at the interface. The S-VECD and SSR rutting results of DG45W and DG30H were used for the WMA and HMA sections, respectively;
- 32-cm asphalt-treated subbase, modeled as linear elastic material since there were no S-VECD results to model it with viscoelastic behavior. Two scenarios were considered. *Scenario 1* represents the actual field test conditions, i.e., with stiffness modulus equal to 10000 MPa, average between the stiffness modulus from HWD analysis of 11400 MPa (confirmed by $|E^*|$ mastercurve, see Section 6.2.1), and the stiffness modulus from the $|E^*|$ mastercurve (Figure 6.4) at the frequency of 10 Hz (representative of the vehicular load) of 8593 MPa. *Scenario 2* represents the more usual condition of granular subbase in motorways, with stiffness of 1200 MPa (see Section 5.6.1). Poisson's modulus is assumed to be 0.35 in both scenarios.
- Subgrade, modeled as linear elastic material. In *Scenario 1* its stiffness modulus was equal to 250 MPa, i.e. conservatively slightly lower than the average value of 270 MPa derived from the HWD analysis (Section 6.2.1). In *Scenario 2*, the stiffness modulus was assumed of 100 MPa (see Section 5.6.1). Poisson's modulus is assumed to be 0.35 in both scenarios.

The location of the field test trial between the cities of Fiano Romano and Tivoli Terme is very near to Fiumicino, i.e., the field test trial of the research presented in Chapter 5 (Section 5.2.1), and they are in the same A1 motorway. So, as for the climatic conditions, based on a comparison of the annual temperatures and precipitation (Figure 5.12), the city of San Jose (California) was chosen. (whose climatic data are present in the FlexPAVE^{TM} database). Regarding the loading conditions, the traffic is the same of A1 motorway described in Section 5.2.1 from traffic data studies. 8.5 million 120-kN ESALs (single axle, dual wheels) per year were considered. The speed traffic of 90 km/h of the heavy load was considered. The tire inflation pressure was 800 kPa and the contact area was set as circular. No traffic growth was considered.

6.5.2 FlexPAVE^{TM} results

Laboratory conditions_LAB

Figure 6.19 shows the damage contours of the investigated scenarios for HMA and WMA sections after 30 years. Figure 6.20 present the prediction of the corresponding *%damage* after 30 years of service.

In Figure 6.19a-b of *Scenario* 1, it must be underlined that the colors range of the damage factor goes from 0.0 to 0.1. Indeed, the dark red is associated with a damage factor equals to 0.1, meaning the element has been subjected to 10% of the number of cycles to failure. Therefore, it can be immediately observed that the damage is minimal and exclusively involves the upper part of the pavement, whereas the damage at the bottom of the asphalt concrete courses (bottom-up cracking) is absent for both sections.

In particular, in the upper part of the pavement the damage is concentrated for HMA and WMA sections in the OGFC and below the interface between OGFC and base course, and it is probably attributable to thermal effects (Spadoni, Ingrassia, Mocelin, et al., 2022). This result is due to the significant gap of stiffness that occurs between such mixtures' courses (Figure 6.7b), which leads to the onset of tensile stresses under the cyclic thermal variations.

*Scenario 1*_E$_{subbase}$ = 10000 MPa

HMA section WMA section

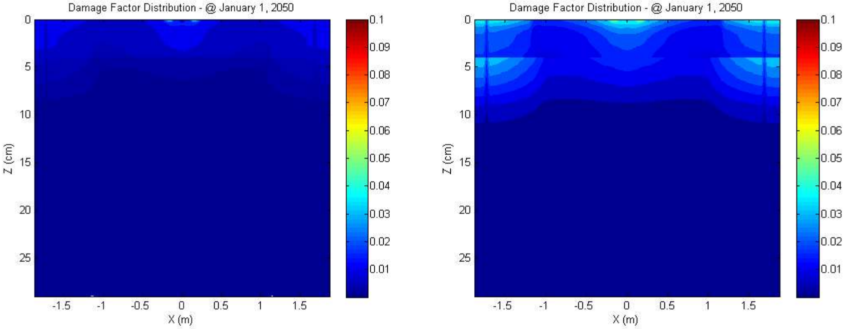

(a) **(b)**

*Scenario 2*_E$_{subbase}$ = 1200 MPa

HMA section WMA section

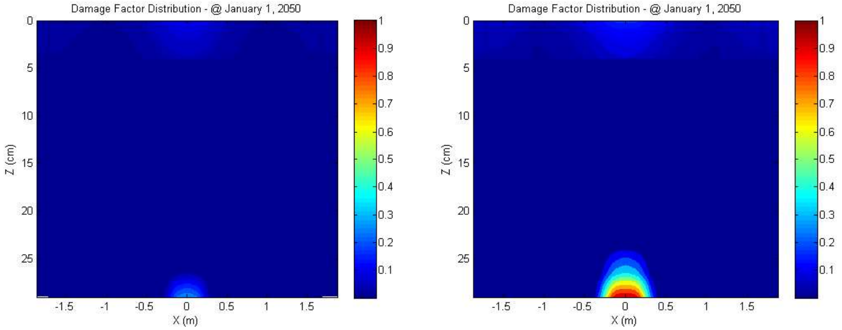

(c) **(d)**

Figure 6.19. Laboratory conditions: damage contours after 30 years of (a,c) HMA and (b,d) WMA sections for (a,b) Scenario 1 and (c,d) Scenario 2.

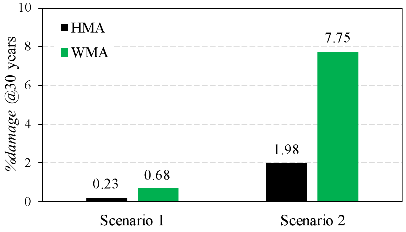

Figure 6.20. Laboratory conditions: *%damage* after 30 years.

The absence of damage to the bottom of the asphalt courses is attributable to the asphalt-treated subbase characterized by high stiffness modulus (i.e., 10000 MPa). In fact, the subbase can distribute and absorb the tensile stresses induced by the vehicle load, thus relieving the stresses in the base course.
The percent of damage in the cross-section area does not reach neither 1% (Figure 6.20). However, it is slightly higher for the WMA section, due to the slightly higher damage due to top-down cracking (Figure 6.19). The *%cracking*, whose calculation is based on the *%damage*, resulted equal to 0.00%.

Regarding Figure 6.19c-d for *Scenario 2*, in which the subbase was considered with a stiffness modulus of 1200 MPa, the colors range of the damage factor goes from 0.0 to 1.0, as usual. It can be noted that the damage is present in the upper part of the pavement, as well as concentrated at the bottom of the asphalt courses (bottom-up cracking), differently from *Scenario 1*. As observed for *Scenario 1*, the damage involving the OGFC is probably due to thermal effects, which mostly affect the superficial courses of the pavement. Moreover, the presence of bottom-up cracking indicates that vehicular loads induce critical tensile strain at the bottom of the base course, attributable to the lower stiffness of the subbase with respect to the one considered in *Scenario 1*. The level of damage reached in the WMA section is higher than the one in the HMA section, as indicated in Figure 6.20 and visible in Figure 6.19d. In the latter one, it can be seen that the damage factor reaches the 0.9 value at the bottom, meaning an almost completely cracked element.
However, in both the cases the amount of damaged after 30 years is very low (Figure 6.20), to which a *%cracking* on the pavement surface less than 1.0% is associated. The high performance is ascribable to the stiffness of the mixture compacted in the laboratory and the 25 cm thickness of the base course adopted in the motorways, which determine very low values of tensile deformation at bottom of the bound materials as well as a longer service during the propagation of the crack up to the surface.

Figure 6.21 shows the predicted rut depth evolution for each pavement course of the investigated scenarios for HMA and WMA sections for 30 years.
It can be observed that in *Scenario 1* (Figure 6.21a-b)*,* the rut depth on subbase and subgrade are almost negligible, due to their deep position within the pavement structure and to the high stiffness properties considered (Figure 6.18a). As expected, in both sections the base course (i.e., DG30H and DG45W) is predominantly subjected to rutting, contributing about 80% to the total accumulation.
Specifically, the curves present a first stage, including the first 5 years of service life, in which the rut depth evolves faster, and then stabilizes in almost linear trend. The expected thickness of the rut at 30 years is equal to 0.95 cm and 1.35 cm for HMA and WMA section, respectively. The slightly higher rutting resistance of DG30H with respect to DG45W confirms the classification given by *RSI* values (Figure 6.11). This outcome can be justified with the higher stiffness of DG30 H (Figure 6.7b), likely due to the higher production temperature which stiffens the virgin bitumen and re-activates the aged RAP bitumen. In order to have a maximum limit of the acceptable rut depth for comparison purpose, the Mechanical-Empirical Pavement Design Guide prescribed by AASHTO (2008) was

considered. According to this MEPD Guide, a limit of 12.7 mm (0.5 inches) in motorways (primary arterials) is set, in order to avoid the hydroplaning phenomenon in wet conditions considering the vehicle speed of 90 km/h (typical of heavy traffic, and used as input in the simulations, see Section 6.6.1). Therefore, the WMA section is expected to meet this 12.7 mm limit for all the design service life of 20 years, whereas HMA section should guarantee more than 30 years of service.

*Scenario 1*_$E_{subbase}$ = 10000 MPa

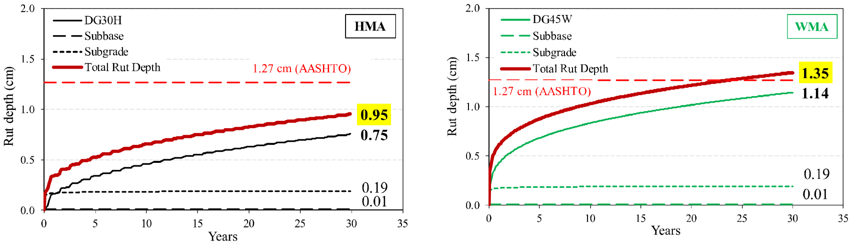

(a) (b)

*Scenario 2*_$E_{subbase}$ = 1200 MPa

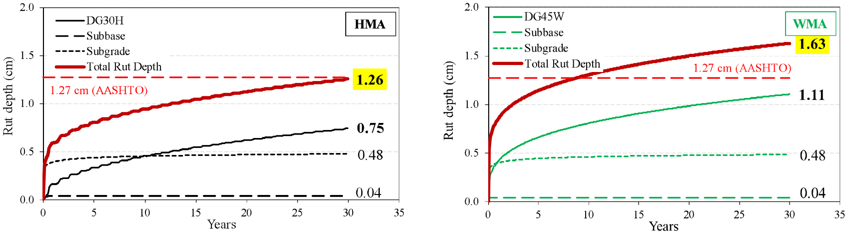

(c) (d)

Figure 6.21. Laboratory conditions: evolution of the rut depth of (a,c) HMA and (b,d) WMA sections for (a,b) Scenario 1 and (c,d) Scenario 2.

Regarding the rutting prediction in the case of subbase with lower stiffness (Figure 6.21c-d), the rut depth of the subbase is the same in both sections (i.e., 0.48 cm) and remains constant during service. As expected, such permanent structural deformation is more than double of the one in *Scenario 1*, and its contribution is about 40% and 30% to the total rut depth in HMA (Figure 6.21c) and WMA section (Figure 6.21d), respectively. The rut depth in the base course is almost the same as the ones experienced in *Scenario 1*. Specifically, the trend of the curves is similar to the ones shown in Figure 6.21a-b, i.e. with the rut evolving more rapidly in the first 5 years, and then stabilizing (almost linear). The rut depth expected at 30 years is equal to 1.26 cm and 1.63 cm, for HMA and WMA sections, respectively. Considering the reference limit value of 12.7 mm, HMA section would ensure the design service life of 20 years, whereas rehabilitation operations would be needed after approximately 7 years of service in WMA section. However, considering that the OGFC is milled and reconstructed every approximately 7-10 years, carrying out this maintenance intervention would make it possible to compensate the rut depth of the courses below.

In conclusion, it can be stated that the long-term performance of the warm mixtures, deduced from the FlexPAVE^{TM} simulations, considering the mechanical properties of samples compacted in the laboratory, seem to be more than adequate both in terms of fatigue and permanent deformations. The accumulation of permanent deformation is modest, while fatigue damage is basically zero when it is possible to rely on a subbase course with a high stiffness modulus. However, even in the case of a subbase with conventional stiffness properties, DG45W would ensure a minimal amount of damage, especially due to fatigue.

Field conditions

Figure 6.22 shows the damage contours of the investigated scenario for HMA and WMA sections after 30 years. Figure 6.23 presents the prediction of the corresponding *%damage* after 30 years of service.

Regarding *Scenario 1* (Figure 6.22a-b), it must be noticed that the colors range of the damage factor goes from 0.0 to 0.1, where 0.1 means that 10% of the number of cycles to failure has been consumed. Indeed, it can be seen that the damage only involves the upper part of the pavement, and it is very limited, as for the *LAB conditions* (Figure 6.19a-b). The damage is concentrated in the OGFC and below the interface between OGFC and base course, and it is probably attributable to thermal effects (Spadoni, Ingrassia, Mocelin, et al., 2022) due to the significant gap of stiffness. This latter one should be similar for both HMA and WMA, since OG mixtures and DG base mixtures are characterized by similar stiffness (Figure 6.7c and Figure 6.12a, respectively). For this reason, the higher top-down cracking in the WMA section can be attributable to the lower fatigue performance of OG25W (Figure 6.9b), too. Bottom-up cracking due to fatigue is absent for both sections, confirming the subbase with high stiffness modulus ensures negligible strain at the bottom of the base course.

The percent of damage in the cross-section area does not reach neither 0.5% (Figure 6.23). However, it is slightly higher for the WMA section, due to the higher quantity of top-down cracking (Figure 6.22a-b). The subsequent *%cracking* resulted equal to 0.00%.

Regarding Figure 6.22c-d for *Scenario 2*, where the subbase has a stiffness modulus of 1200 MPa, the colors range of the damage factor goes from 0.0 to 1.0, as usual. As registered for *Scenario 1*, the damage in the OGFC is probably due to thermal effects, which usually affect the most superficial area of the pavement, and to a lesser extent to fatigue damage. In addition, the presence of potential bottom-up cracking at the base of the bound courses indicates that the tensile stresses induced by the cyclic loads are higher due to the lower stiffness of the subbase compared to *Scenario 1*. The tensile strain is however lower than the critical values for both the sections, so that after 30 years the damage factor is not higher than 0.6. The damaged area at the bottom of the base course after 30 years is similar for HMA and WMA sections and includes the deepest 7 cm thick area. This outcome was expected, since DG30H and DG45W are characterized by similar stiffness (Figure 6.12a) and fatigue (Figure 6.15b) properties. The level of damage reached in the WMA section is higher than the one in the HMA section, as indicated in Figure 6.23, due only to the thermal effects (Figure 6.22c-d). The *%damage* is about 6% after 30 years, to which corresponds a negligible *%cracking*, corroborating the excellent fatigue performance for both the mixtures.

Figure 6.24 shows the predicted rut depth evolution for each pavement course of the investigated scenarios for HMA and WMA sections for 30 years. In all cases, during the first 5 years of service the rut depth rapidly increases, and then stabilizes with a constant slope. Moreover, the influence of the annual temperature range on the accumulation of deformation, which can be assessed by the oscillations of the curve, is more evident for DG30H (Figure 6.24a).

For *Scenario 1* (Figure 6.24a-b), the rut depth on subbase and subgrade are almost negligible, due to their deep position within the pavement structure and to the high stiffness properties considered (Figure 6.18b). Moreover, such values are similar to the ones in *LAB conditions* (Figure 6.21a-b). As expected, in both sections the mixtures DG30H and DG45W are predominantly subjected to rutting, contributing about 80%-90% to the total rut depth. The slightly higher rutting resistance of DG30H with respect to DG45W confirms the classification given by *RSI* values (Figure 6.17). Since the mixtures are characterized by similar stiffness, this outcome confirms the importance of a good rutting resistance at the intermediate temperatures (T_L of SSR tests). In fact, from the experimental data of SSR tests, DG45W is more susceptible to permanent deformation at intermediate temperature but less susceptible at high temperature with respect to DG30H (Figure 6.16). The total rut depth at 30 years is equal to 1.30 cm and 2.14 cm for HMA and WMA section, respectively. Furthermore, the prediction of the rutting of the WMA section evaluated using the data from the specimens extracted from the field (2.14 cm, Figure 6.24b) is approximately 60% higher than the corresponding prediction made with the data from the specimens compacted in the laboratory (1.35 cm, Figure 6.21b), probably due to the higher content of AV in the field specimens. Finally, it should be noted that, while the HMA section satisfies the limit of the maximum rut depth of 12.7 mm specified by MPEDG Guide for almost 30 years, WMA section would require rehabilitation operations after 5 years, in order to avoid possible hydroplaning phenomena. However, it must be always kept in mind that the OGFC must be reconstructed every approximately 7-10 years due to clogging. In such reconstruction, it can be possible to compensate for the occurred rut depth.

In *Scenario 2,* it can be noted that DG45W undergoes a permanent deformation similar to *Scenario 1* (1.94 cm – *Scenario 1* vs. 1.86 cm - *Scenario 2*). Analogously, it is found that the DG30H mixture experiences a permanent deformation of 1.09 in *Scenario 1* similar to that of *Scenario 2* equal to 1.07 cm. This result demonstrates that the stiffness of the unbound layers (subbase and subgrade) below the asphalt courses negligibly influences the extent of the rutting of the asphalt courses, in the hypothesis of the pavement thicknesses considered (Figure 6.18).

However, it is important to note that the maximum rut depth equal to 1.27 cm is reached after approximately 2 and 11 years, respectively for the WMA and HMA section, times after which a maintenance and rehabilitation intervention would be necessary to repristinate the safety and comfort conditions for the users. These result, if compared with the results of *Scenario 1* (actual subbase and subgrade conditions) highlights the importance of the load-bearing capacity offered by the high modulus subbase in delaying the onset of permanent deformations, which are not compatible with the functionality of the motorway pavement.

Ultimately, it can be stated that the long-term performance of the warm mixture, deduced from the FlexPAVE^{TM} simulations, considering the mechanical properties of samples taken on the field test trial, are more than adequate in terms of fatigue and good in terms of permanent deformations, and comparable with the performance of hot mixture typically used in the motorway.

*Scenario 1*_E$_{subbase}$ = 10000 MPa

HMA section WMA section

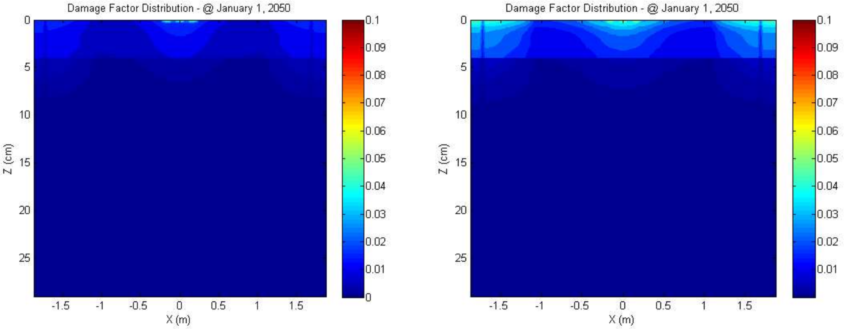

(a) **(b)**

*Scenario 2*_E$_{subbase}$ = 1200 MPa

HMA section WMA section

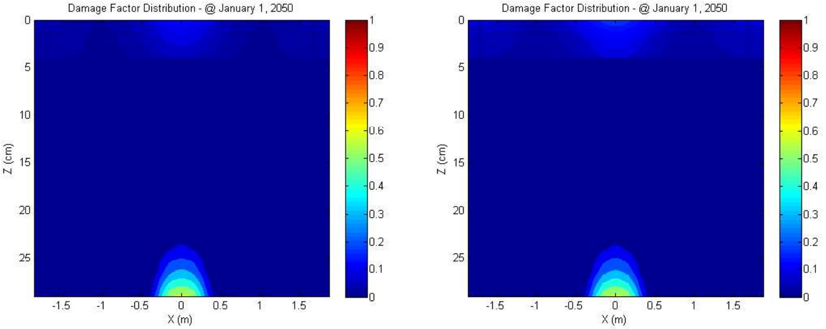

(c) **(d)**

Figure 6.22. Field conditions: damage contours after 30 years of (a,c) HMA and (b,d) WMA sections for (a) Scenario 1 and (b) Scenario 2.

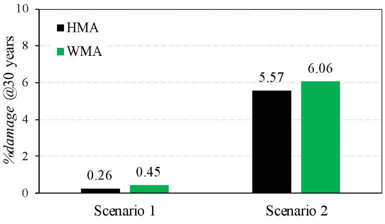

Figure 6.23. Field conditions: *%damage* after 30 years.

*Scenario 1*_E$_{subbase}$ = 10000 MPa

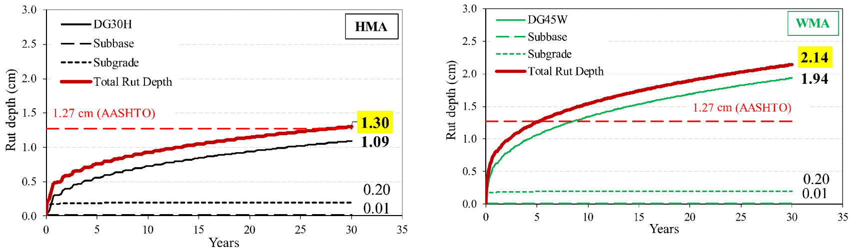

(a) **(b)**

*Scenario 2*_E$_{subbase}$ = 1200 MPa

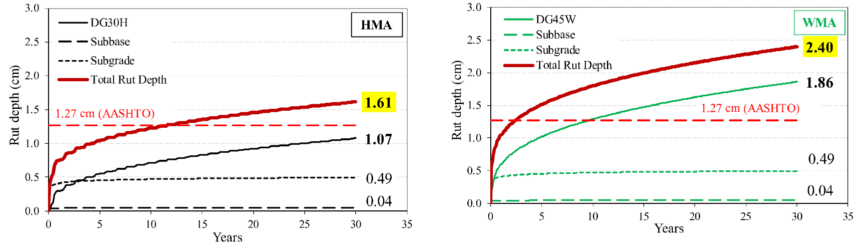

(c) **(d)**

Figure 6.24. Field conditions: evolution of the rut depth of (a,c) HMA and (b,d) WMA sections for (a,b) Scenario 1 and (c,d) Scenario 2.

6.6 Summary of the findings

The objective of this research was to evaluate the fatigue and rutting performance of WMAs for wearing and base courses containing high RAP content. Specifically, the WMA for base course, named DG45W, contained 45% of RAP, and the WMA for wearing course, named OG25%, contained 25% of RAP. Both the mixtures were produced at the asphalt plant at 130°C thanks to the use of a chemical additive. A field test trial was constructed along the A1 Italian motorway, and laboratory-compacted specimens were produced with the same mixtures. The corresponding HMAs actually used in motorways have been investigated for comparison purposes, too.

From the characterization following the AM-PRS specifications of the mixtures in laboratory conditions, it was observed that DG45W should ensure comparable performance to the reference mixture. In particular, the analysis of the synthetic index S_{app} regarding the fatigue performance shows that the reference mixture accumulates more damage at failure has higher toughness, but it is stiffer. Otherwise, DG45W is characterized by lower stiffness which makes the mixture potentially less prone to cracking, despite the fact that it seems to accumulate a lower level of damage to failure. Such lower stiffness despite the 15% increase of RAP is due to the chemical additive which allows a lower production temperature. This latter one has positive effects on the mixtures, since the virgin bitumen is less aged, as well as the RAP bitumen (already oxidated during the service of milled pavement) is much less re-activated. However, the lower stiffness seems to slightly penalize the rutting performance of DG45W. In fact, this latter seems to be more susceptible to permanent deformation at the intermediate temperature of service, whereas it is less susceptible to the high temperatures with respect to the reference hot mixture.

The OG mixture OG25W, whose only fatigue behavior on laboratory specimens was investigated, showed similar stiffness and viscoelastic properties of the reference hot mixture with a lower AV content. This outcome confirms that the WMAs are less subjected to aging and oxidizing phenomena during the production stages. Moreover, DG45W showed slightly lower capacity to absorb damage and lower toughness with respect to the reference hot mixture, due to the 10% increase of RAP. It should be underlined that the D^R and S_{app} values for the OG seems to be not totally reliable, likely due to the rubbery behavior of such mixtures containing about 5% of SBS modified bitumen.

The fatigue and rutting resistance of the DG mixtures evaluated on the field cores corroborates the results obtained from the laboratory specimens.

The material properties were used in FlexPAVETM pavement performance simulations, considering the scenario of subbase with high stiffness modulus present in the field test trial (asphalt-treated base, 10000 MPa) and conventional stiffness typical of a granular subbase in the motorway (1200 MPa). From the results, it can be stated that the long-term performance of the warm mixtures considering the mechanical properties of samples compacted in the laboratory, seem to be more than adequate both in terms of fatigue and permanent deformations. The accumulation of permanent deformation is modest, while fatigue damage is basically zero when it is possible to rely on a subbase course with a high stiffness modulus. However, even in the case of a subbase with conventional stiffness properties, DG45W would ensure a minimal amount of damage, especially due to fatigue. Examining the long-term performance prediction with the materials' properties under the field compaction, the beneficial role of a high bearing capacity of the subbase emerged in the rutting performance. In fact, the rut depth is approximately 2 cm after 30 years, and negligible fatigue damage is expected with a stiffness modulus of 10000 MPa of the subbase. However, the simulations carried out considering the subbase with conventional stiffness properties, highlighted that WMAs do not suffer fatigue damage, whereas DG45W would show high permanent deformation accumulation for which rehabilitation operations would be frequently required to restore the functionality of the pavement. Considering that the OGFC is milled and reconstructed every approximately 7-10 years due to clogging, carrying out this maintenance intervention would make it possible to compensate the rut depth of the courses below.

As future work, the field test track will be continuously monitored through non-destructive testing as well as laboratory tests on cored samples to evaluate the mixtures' performance during service.

Chapter 7
Evaluation of the applicability of the S-VECD approach on Cold Recycled Materials

7.1 Background and objectives

Nowadays, the reuse of construction materials at the end of their service life leads to several beneficial effects for the environment, such as waste reduction and preservation of natural resources. In pavement engineering, cold recycled materials (CRM) could implement the circular economy of a pavement, since the main objective of CRM is to maximize the reuse of the RAP up to 100% replacing the virgin aggregate, and the production is without heating. In fact, the whole recycling process of CRM can be performed at ambient temperature employing bituminous emulsions, indeed significantly limiting the carbon footprint, energy consumption and greenhouse emissions (Cross et al., 2011; Giani et al., 2015; Thives & Ghisi, 2017; Wiesmeth, 2020).

Pavement structures containing base courses built with CRM mixtures are characterized by excellent long-term performance, as demonstrated by several in-field observations (Dolzycki et al., 2017; Dołżycki & Jaskuła, 2019; Godenzoni et al., 2018; Kuchiishi et al., 2019; Vaitkus et al., 2021). However, at the current state of the knowledge, the structural design of cold recycled pavements, is carried out using empirical methods. Therefore, in order to promote a wider use of CRM mixtures based on solid theorical background instead of only in-field experiences which require long-term observations, it is essential to adopt or implement mechanistic-empirical design methods. To this regard, the S-VECD approach could represent a valid solution. However, this approach has been developed for hot mix asphalts, as specified by the reference AASHTOs. In the scientific literature, only a couple of studies have characterized the fatigue behavior of CRM mixtures through uniaxial tests which could be used for the S-VECD analysis (Nemati et al., 2019; Tavassoti et al., 2022). Indeed, very limited data is available in the literature, and few CRMs have been investigated.

Among CRM mixtures, different families can be identified, depending on the type and amount of employed binding agents (Figure 7.1). Cement treated material (CTM) mixtures are produced if recycling is carried out by adding only Portland cement with dosage higher than 1.5%. Their load-related failure is normally due to fatigue (Fedrigo et al., 2020, 2021). If recycling is carried out with a low dosage of cement and adding a small amount of bitumen (normally between 1.0% and 2.5%) bitumen stabilized materials (BSM) are produced. BSM are considered as improved granular materials due to the inclusion up to 1% of Portland cement or other active fillers, like hydrated lime. The load-related failure of BSM is primarily due to permanent deformation (Orosa et al., 2022). Cement bitumen treated materials (CBTM) are produced with similar bitumen dosages but with higher dosages of Portland cement (normally between 1.5 and 4.0%). Load-related failure of CBTM is primarily due to fatigue (Bocci et al., 2011; Buczyński & Iwański, 2017; Dolzycki et al., 2020). CRMs with higher bitumen dosage with respect to BSM are called Cold Recycled Asphalt (CRA).

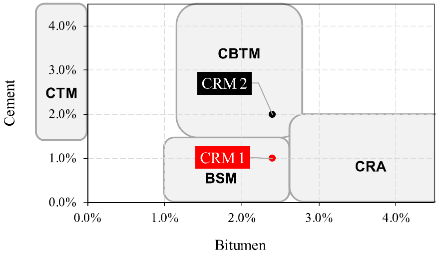

Figure 7.1. Composition of the CRM families and identification of the investigated CRMs.

Within this general context, the present PhD work provides a large research project that has the final aim of evaluating the applicability of the viscoelastic continuum damage (VECD) theoretical-experimental framework to CRM mixtures. Two CRM mixtures produced with bitumen emulsion and different dosages of Portland cement were investigated (Figure 7.1). As a first necessary step, the objective is to provide new insights for understanding the fatigue failure of CRM mixtures. The results of this first step have been published in Graziani et al. (2024). Empirical and energy-based failure criteria, originally developed for AC mixtures, are used to define fatigue failure. A fatigue failure mechanism that highlights the role of cement and a specific failure criterion is finally proposed. As second step, the experimental data obtained from S-VECD fatigue tests are used to obtain the damage characteristic curves and the D^R failure criterion values. Finally, pavement performance simulations are carried out in order to evaluate the possibility to use CRMs as replacement of aggregate base course or as replacement of the lowest asphalt concrete course in thick pavements. The S-VECD characterization has been supervised by the contribution of Dr. Youngsoo Kim of NCSU. For this reason, a 2-weeks research period in NCSU was included, in order to repeat some S-VECD fatigue tests on CRMs.

7.2 Materials and methods

Two CRM mixtures, identified as CRM1 and CRM2, were investigated. Figure 7.2 shows their target aggregate gradation that was obtained by mixing 90% of RA aggregate (RA 0/16) and 10 % of limestone filler (EN 13043, 2002). The bitumen emulsion was a commercial cationic slow-setting type, modified with styrene-butadiene-rubber latex and designated C60BP10 according to EN 13808 (2013). For both mixtures, the dosage (by dry aggregate mass) of bitumen emulsion was 4.0 % (residual bitumen 2.4 %) and the total water content was 4.5 % (1.6 % bitumen emulsion water plus 2.9 % pre-wetting water).

The Portland cement was a type II/A LL, strength class 42.5 according to EN 197-1 (2011). Its dosages were 1.0 % and 2.0 % (by dry aggregate mass) for CRM1 and CRM2, respectively. CRM2 is a CBTM mixture typically produced in Europe for base and binder courses (Mignini et al., 2022; Winter et al., 2020). CRM1 may be considered a BSM and thus, in the field, its failure is expected to be caused by permanent deformation accumulation rather than fatigue. Nonetheless, it was included in the present experiment to verify if its fatigue failure characterization is possible.

The fatigue behavior of the two CRM mixtures is compared to that of two typical AC mixtures for binder courses tested in the research about the S-VECD characterization of typical Polish asphalt mixtures (Chapter 4)(Spadoni et al., 2023). One mixture (AC1) was produced with neat bitumen (PG 70-22), i.e., AC 16_35/50 in Chapter 4, and the other (AC2) with styrene-butadiene-styrene (SBS) polymer modified bitumen (PG 82-16), i.e., AC 16_PmB in Chapter 4. The AC mixtures had similar aggregate gradations (dense graded, only virgin aggregates) and bitumen dosage of 4.5 % by mixture mass (Section 4.2).

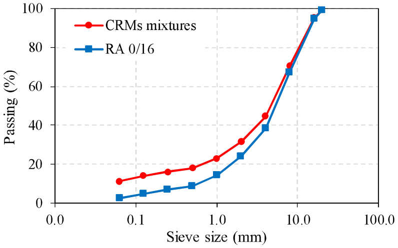

Figure 7.2. Aggregate gradations of the CRM mixtures.

The production stages of the CRMs are in detail described in Appendix C. A part of the pre-wetting water equal to the water absorption was added at the dry aggregate blend. The wet samples were then sealed in plastic bags for 12 h at room temperature in order to allow a uniform moisture distribution and reach the SSD condition. Then, the cement, the remaining pre-wetting water and the bitumen emulsion were gradually added and mixed to the SSD aggregate blend, alternating manual and mechanical mixing, with the aim to obtain a homogeneous mixture (Graziani et al., 2020). One sample from one batch was prepared using a gyratory compactor, which applied a constant pressure of 600 kPa, a speed of 30 rpm and an external angle of inclination of 1.25 ° (EN 12697-31, 2019). Each sample with a diameter of 150 mm and final height of 180 mm was compacted at the target void content (including the volume of air and intergranular water) of 14.0 %. The mass loss during compaction was less than 0.1 %, ensuring that negligible leakage of water or fines occurred.

The volumetric composition of the freshly compacted CRM gyratory specimens was characterized through the measure of the void content V_m (Equation (7.1)) including air and water volumes, and the voids filled with liquid VFL (Equation (7.2)):

$$V_m = \frac{v_A+v_W}{v} = \frac{v-(v_S+v_B)}{v} \tag{7.1}$$

$$VFL = \frac{v_B+v_W}{v_A+v_W+v_B} = \frac{v_B+v_W}{v-v_S} \tag{7.2}$$

where v is the total volume of the specimen whose height varied during compaction, v_A is the volume of the air voids, v_W is the volume of the intergranular water, v_S is the volume of the solids (bulk volume of the aggregates including the absorbed water, filler and un-hydrated cement) and v_B is the volume of the residual bitumen from emulsion (Graziani et al., 2020).

The results in terms of V_m and VFL are shown in Figure 7.3. For both the mixtures, the target void content of 14.0 % was reached. Moreover, VFL reached a maximum value of 57 % for both CRM1 and CRM2, indicating that the mixtures were away from the saturation condition.

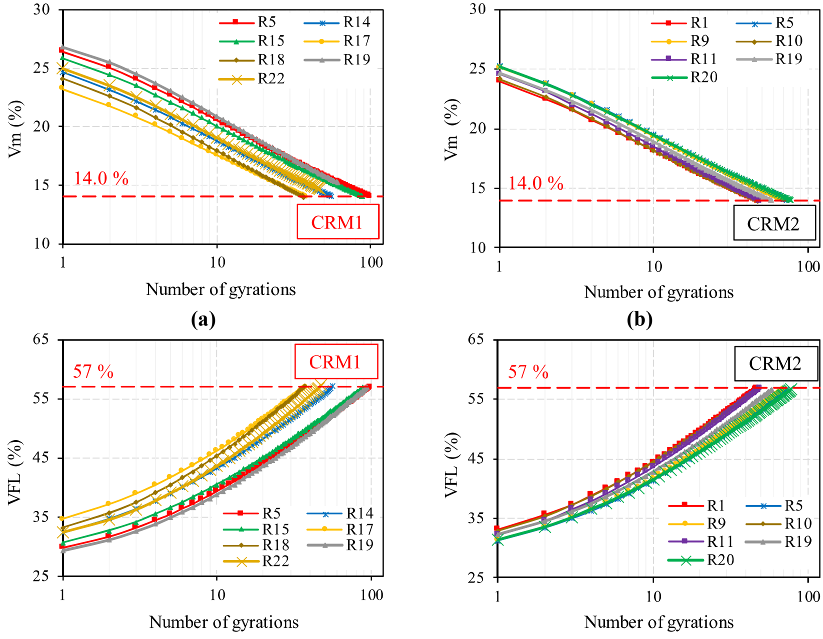

(a) (b)

(c) (d)

Figure 7.3. Volumetric composition during compaction: void content (V_m) in (a) CRM1 and (b) CRM2, and voids filled with liquid (VFL) in (c) CRM1 and (d) CRM2.

A two-stages curing procedure was adopted. The samples were cured for 1 day in oven at 40 °C (dry environment), and then closed in plastic bags and cured for 28 days in a climatic chamber at 40 °C (high humidity). In the first stage, curing of bituminous binder is facilitated due to the moisture loss by evaporation, whereas in the second stage the hydration of the cementitious binder is favored using the non-evaporable water present in the mixture (Cardone et al., 2015). This procedure was adopted because is somewhat similar to what happens in the field, where free evaporation from the surface of the CRM layer is allowed for some hours or days, until the upper layer is constructed.

After the 28 curing days, one test specimen with diameter of 100 mm and height of 130 mm was cored and cut from the inner part of each gyratory sample. The bulk density of the cored specimens was obtained with the hydrostatic method (EN 12697-6, 2020) and then the air void content was calculated according to EN 12697-8 (2018). The average (standard deviation) value of air void content was 12.7 % (0.6 %) for CRM1 and 12.6 % (0.6 %) for CRM2.

It is recalled that the AC mixtures were produced in an asphalt plant, reheated and compacted in the laboratory using a gyratory compactor. The compacted samples had diameter of 150 mm, height of 170 mm and target air void content of 5.0 % for the inner portion of the sample. Afterwards, four small test specimens with diameter of 38 mm and height of 110 mm were cored and cut from each gyratory sample, in accordance with AASHTO PP 99 (2023). The average (standard deviation) value of air void content was 5.3 % (0.4 %) for AC1 test specimens and 5.2 % (0.1 %) for AC2 test specimens.

It is worth underlining that, since this was one of the first experiences ever concerning axial fatigue testing of CRM mixtures, the adoption of the small geometry (38 mm diameter, 110 mm height) was deemed premature. Therefore, the large specimen geometry suggested by AASHTO T 400 (2023) (100 mm diameter, 130 mm height) was considered as a first step.

Dynamic modulus and cyclic fatigue tests were carried out following the same AASHTOs developed for hot mix asphalt (large specimens), with few differences hereafter specified.

Dynamic modulus tests were carried out on large specimens according to AASHTO T 378 (2017). The viscoelastic properties of the test specimens, i.e., dynamic modulus $|E^*|$ and phase angle δ, were determined at various testing temperatures because the thermal susceptibility of CRMs is very low compared to asphalt mixture. Specifically, the testing temperatures were 5 °C, 15 °C, 25 °C, 35 °C, 45 °C and 55 °C, and the tests at 25 °C were repeated before and after all the temperatures from 5 °C to 55 °C in order to check the integrity of the material.

For each temperature, the frequencies investigated were 0.1 Hz, 0.5 Hz, 1 Hz, 5 Hz, 10 Hz and 20 Hz. Four replicate specimens were tested for each mixture, ensuring that the single-operator precision requirements were met.

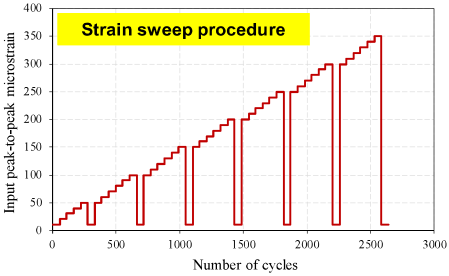

Figure 7.4. Strain sweep tests: loading history (Graziani, Grilli, et al., 2024).

The challenge of carrying out valid S-VECD fatigue tests on CRMs was to identify the proper deformation level, due to the totally unconventional material. In order to understand the proper values, strain sweep tests were conducted, based on the studies of Graziani, Grilli, et al. (2024). Strain sweep tests consisted of repeated dynamic modulus tests in tension-compression mode of loading, at increased target peak-to-peak microstrain (Graziani, Grilli, et al., 2024; Grilli et al., 2024). The fingerprint of the S-VECD fatigue test software (UTS032) was used.

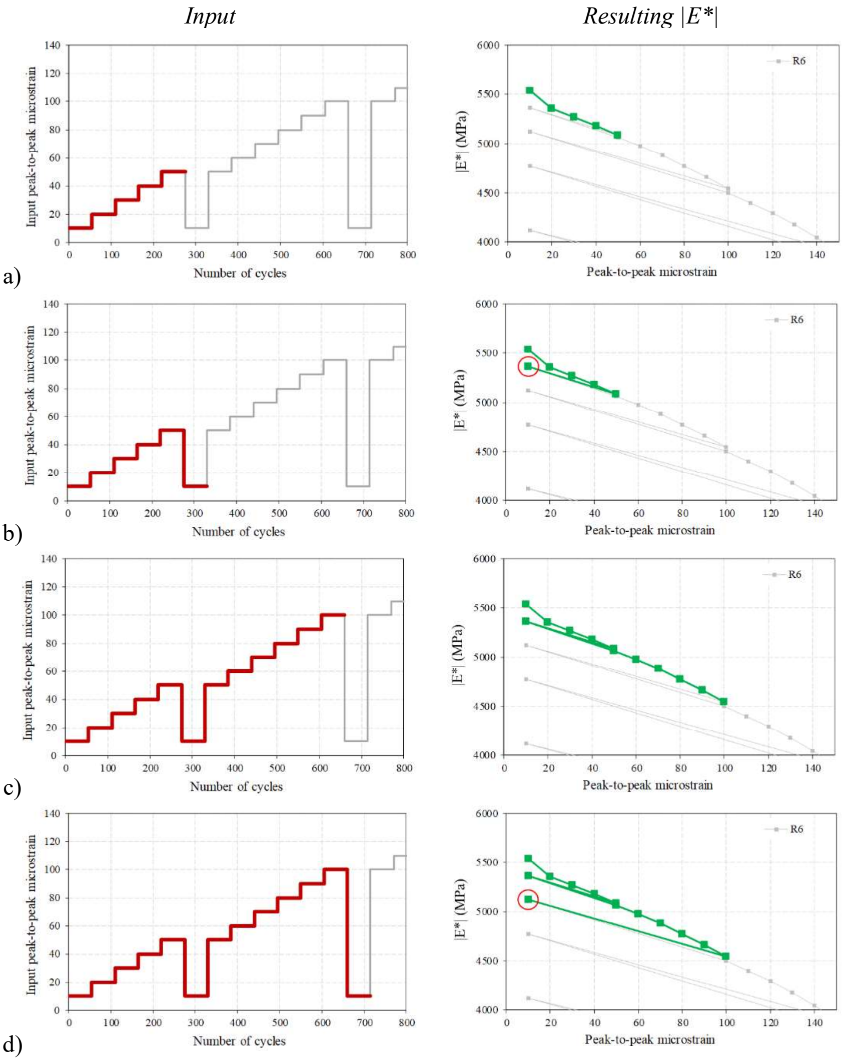

Figure 7.5. Strain sweep tests: explanation of the construction of the strain sweep curve.

The specimens had the same geometry for the fatigue tests. Even the testing conditions were the same, i.e. testing temperature of 20 °C and frequency of 10 Hz. Three replicate specimens were tested for each mixture, with middle failure at the end of the test. The loading history is represented in Figure 7.4. It consisted in increasing the peak-to-peak microstrain form 10 με to 350 με with step of 10 με, plus unload to 10 με after each five blocks of cycles. As fixed by the fingerprint software, fifty-five cycles were performed for each input peak-to-peak microstrain. A rest period of two minutes was set after each block of cycles.

Figure 7.5 shows a graphical explanation to construct the strain sweep curve in terms of the stiffness $|E^*|$. For each block of cycles at a target peak-to-peak microstrain, one $|E^*|$ value is associated. As the peak-to-peak microstrain increases, the stiffness decreases plotting a descending curve (a). Then, to the peak-to-peak of 10 με, the material usually shows a higher $|E^*|$ values (b). Such stiffness values are then used to construct the so-called "small strain curve" (Graziani, Grilli, et al., 2024; Grilli et al., 2024). Then the peak-to-peak microstrain increases for five blocks plotting stiffness decreases (c) and then the block at 10 με is repeated (d). and so on.
Figure 7.6 shows a graphical explanation of the construction of the small strain curve. The small strain curve is constructed using the stiffness moduli $|E^*|$ values measured at 10 με associated to the maximum peak-to-peak microstrain to which the specimen was subjected. Indeed, such curve represents the level of damage to which the specimen has been subjected.

The fingerprint test in tension-compression mode of loading prior to the fatigue test was performed at 20 °C and 10 Hz to evaluate the linear viscoelastic properties of each specimen. The target peak-to-peak on-specimen strain amplitude was set between 25 and 35 microstrain, which is a typical strain value to observe a linear behavior (Jaczewski et al., 2022, 2023). The testing temperature for cyclic fatigue tests was chosen as 20 °C, that is the typical testing temperature for CRMs, considering also the low thermal susceptibility and brittleness at low temperatures. After a rest period of 5 minutes, the cyclic fatigue test was performed at the same temperature and frequency. The initial peak-to-peak on-specimen tensile strain amplitude ($\varepsilon_{0,initial}$) was selected between 70 and 80 microstrain, which led to test durations between 2000 and 60000 cycles. In Figure 7.7a-b the set-up of cyclic fatigue test for CRMs and a specimen after failure are shown, respectively.

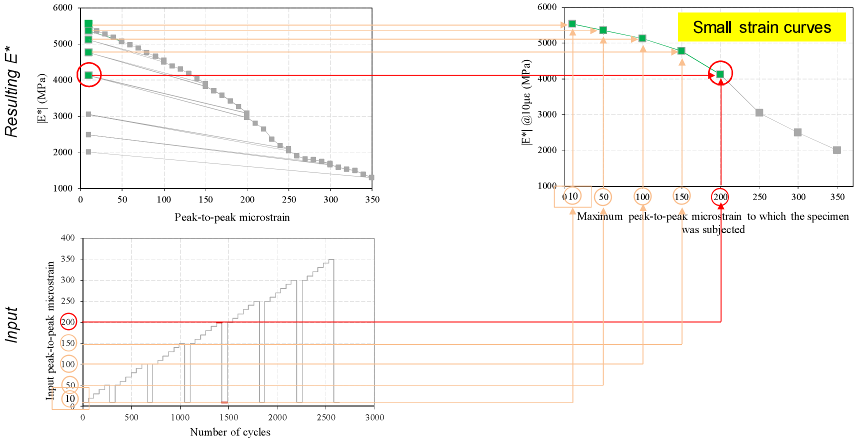

Figure 7.6. Strain sweep tests: explanation of the construction of the small strain curve.

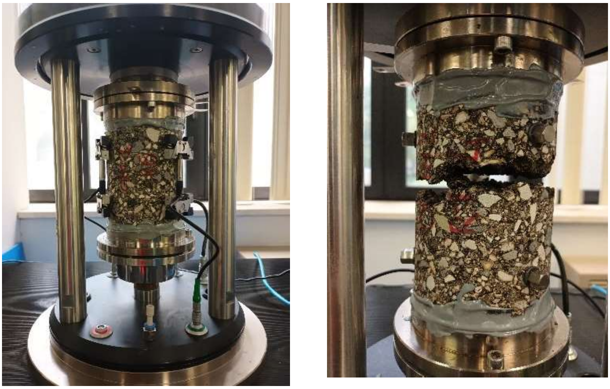

(a) **(b)**

Figure 7.7. S-VECD fatigue tests in the AMPT for CRMs: (a) set-up and (b) broken specimen at the end of the test.

7.3 Results and analysis

7.3.1 Dynamic Modulus

In Figure 7.8a-b, the experimental data from dynamic modulus tests are represented in Black (norm of the dynamic modulus vs phase angle) and Cole-Cole (dissipation modulus vs. storage modulus) diagrams, respectively. It can be seen that the experimental data obtained at various frequencies and temperatures are aligned in continuous curves, stating that the investigated CRMs are characterized by a thermo-rheologically simple behavior. Moreover, as shown is Figure 7.8a by the higher phase angle values of CRM2, CRM2 has a more viscous behavior likely due to the lower cement dosage. Analogously, as shown in Figure 7.8b by the slightly higher E_1 valued of CRM1, CRM1 has a more elastic behavior, attributable to the predominancy of the cementitious binder.

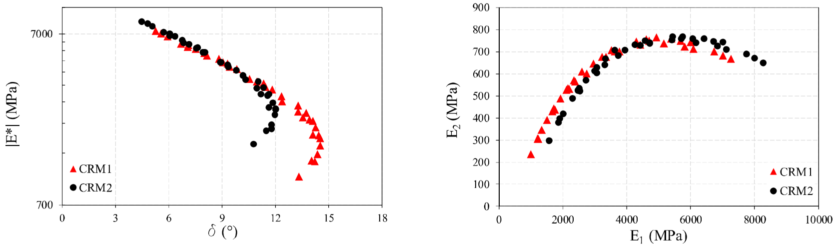

(a) **(b)**

Figure 7.8. Dynamic modulus results: (a) Black and (b) Cole-Cole diagrams.

Figure 7.9a shows the time-temperature shift factors and the equations of the related polynomial regressions. The broadly overlapping of the curves, as well as the similar regression coefficients values indicate that the mixtures have broadly the same thermal susceptibility. This outcome confirms that the thermal susceptibility of mixtures is mainly influenced by the used type of bitumen, which is the same for both the CRMs.

Figure 7.9b shows the experimental phase angle mastercurves at 21.1 °C. The mastercurve of CRM1 is in higher position with respect to the one of CRM2, indicating that the viscoelastic behavior is more pronounced. This is likely due to the lower cement dosage which makes the bitumen component more evident. The lower position of the mastercurve of CRM2 indicates a predominancy of the elastic component, attributable to the cement.

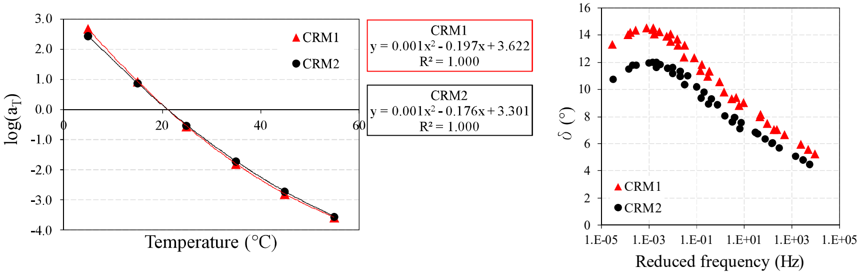

(a) **(b)**

Figure 7.9. Dynamic modulus results: (a) time-temperature shift factors and (b) phase angle mastercurves at 21.1 °C.

Figure 7.10 shows the storage modulus mastercurves (experimental data and related 2S2P1D model) at 21.1 °C for the CRMs. The average AV of the tested specimens (‘%AV’), measured using the saturated surface dry method in accordance with EN 12697-6 (2020), is reported in the same figure. Table 7.1 reports the parameters of the 2S2P1D models. First of all, it can be stated that the 2S2P1D model properly fits the experimental data. As expected, CRM2 is slightly stiffer than CRM1 in all the range of reduced frequency due to its higher cement content (i.e., cement dosed at 2% for CRM2, vs 1% for CRM1). In Table 7.1 it can be seen that the parameters of the CMRs are very similar except for $E_{1,0}$, indicating that the shape of the storage modulus mastercurves are characterized by similar shape but the curve of CRM2 is vertically translated. It can be also noted that the coefficient of the two parabolic elements (i.e., k and h) are very low with respect to the conventional values for asphalt mixtures.

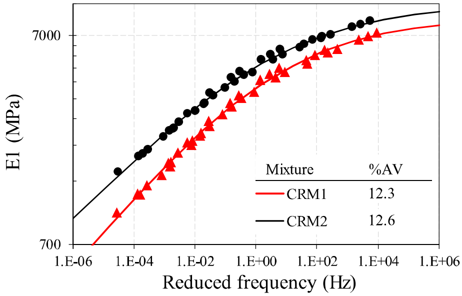

Figure 7.10. Dynamic modulus results: storage modulus mastercurves (experimental data and 2S2P1D model) at 21.1 °C.

Table 7.1. Dynamic modulus results: parameters of the 2S2P1D models for the storage modulus.

Mixture	$E_{1,0}$ (MPa)	$E_{1,\infty}$ (MPa)	ξ	k	h	β	$log\ \tau$
CRM1	53	40000	3.73	0.00069	0.187	1E+12	-4.76
CRM2	84	40000	2.99	0.00033	0.167	1E+12	-4.49

7.3.2 Strain sweep test

Figure 7.11a-b show the strain sweep curves of the dynamic modulus for CRM1 and CRM2, respectively. Analogously, Figure 7.11c-d show the strain sweep curves of the phase angle for CRM1 and CRM2, respectively. Such results are shown for only one specimen per mixture, since similar results were obtained from the others replicates (see Appendix D).

It can be noted that the trend of the dynamic modulus $|E^*|$ is similar for both the CRMs. Specifically, the stiffness slowly decreases until the application of 150 με for CRM1 and 110 με for CRM2. After this first stage, the decrease of $|E^*|$ is higher (i.e., higher slope), and it can be ascribable to the damage of cementitious bonds. Finally, from the application of 250 με, the stiffness stabilizes, likely due to the residual resistance of bituminous bonds.

The trends of the phase angle led to not reliable or clearly understandable results. For both CRMs, the phase angle increases, as expected, due to the decrease for the dynamic modulus. However, high instability was observed for CRM1, may be due to error in the LVDTs records. The phase angle values of CRM2 are most stable and similar between the replicates, but any changes ascribable to damage are visible.

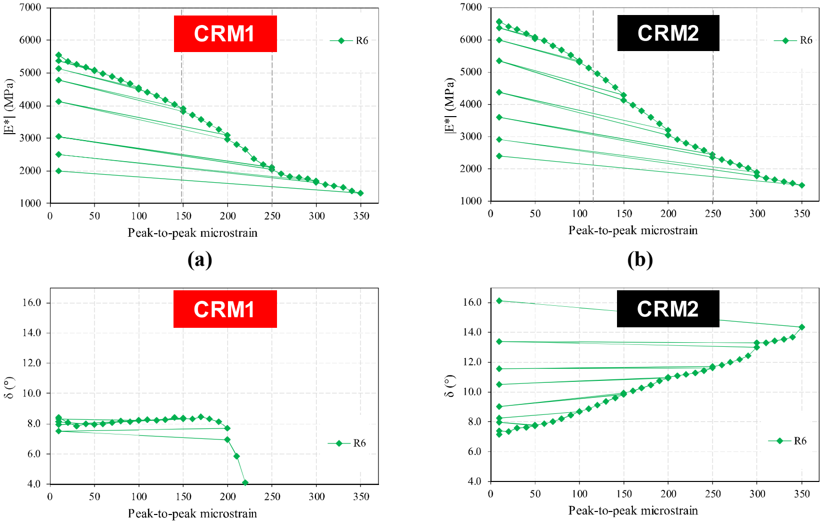

(a) (b)

(c) (d)

Figure 7.11. Strain sweep test results: strain sweep curves of (a-b) dynamic modulus and (c-d) phase angle for CRM1 and CRM2.

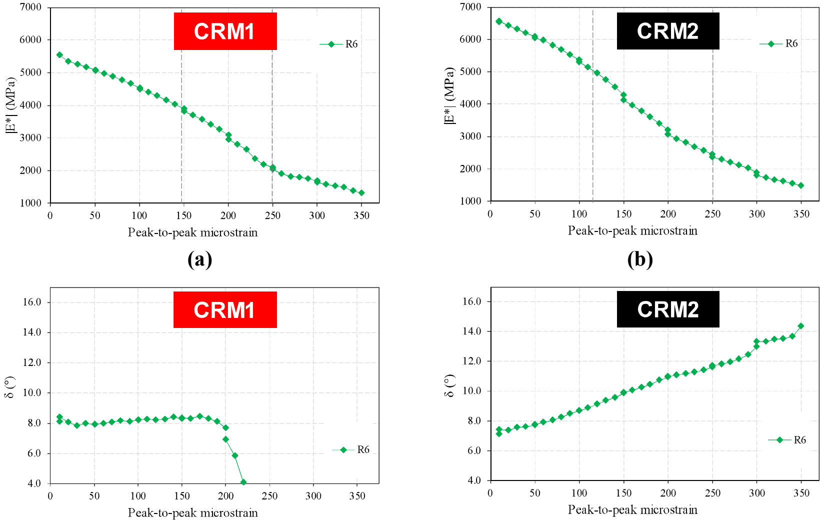

(a) (b)

(c) (d)

Figure 7.12. Strain sweep test results: small strain curves of (a-b) dynamic modulus and (c-d) phase angle for CRM1 and CRM2.

Figure 7.12a-b show the corresponding small strain curves of the dynamic modulus for CRM1 and CRM2, respectively. Analogously, Figure 7.12c-d show the strain sweep curves of the phase angle for CRM1 and CRM2, respectively. It is recalled that the small strain curve can represent the level of damage to which the material was subjected. Indeed, the outcomes form the strain sweep curve are confirmed. The lowest decrease of dynamic moduli, likely due to the damage, is within the range between 100 με and 250 με. No clear outcomes can be deduced from the phase angles.

Thus, it can be concluded that CRM1 and CRM2 start to be damaged when around 140 με are applied. Considering that the strain sweep tests are conducted in tension-compression mode of loading and that the material is damaged mainly due to tension and not compression, an input deformation level of 70 με is a proper value to conduct cyclic fatigue tests in direct tension mode of loading.

7.3.3 Identification of the proper failure criteria

Fatigue failure criteria that have been developed for AC mixtures can be grouped into two main categories: empirical and energy-based (Bhasin et al., 2009; Gajewski et al., 2020; Shen & Lu, 2011; Sudarsanan & Kim, 2022).

The most common empirical criterion consists in arbitrarily defining the specimen failure based on the 50 % reduction of the initial stiffness modulus (AASHTO T 321, 2022; EN 12697-24, 2018). Another common empirical criterion is based on the observation of the phase angle evolution that typically shows an increase followed by a sharp drop. It is assumed that the maximum phase angle corresponds to the formation of macrocracks, and thus to the specimen failure (Reese, 1997).

Energy-based failure criteria rely on the calculation of the dissipated energy per unit volume per cycle (W), i.e., the area of the stress-strain hysteresis loop, using the following linear approximation:

$$W = \pi \cdot \sigma \cdot \varepsilon \cdot \sin\delta = \pi \cdot \varepsilon^2 \cdot E \cdot \sin\delta \tag{7.1}$$

where σ is the stress amplitude, ε is the strain amplitude, E is the stiffness modulus and δ is the phase angle at a given cycle.

Pronk & Hopman (1991) introduced the dissipated energy ratio (*DER*) parameter to identify the fatigue failure, based on the previous work by Van Dijk (1975) and Van Dijk & Visser (1977). *DER* is defined as the ratio between the total cumulated dissipated energy up to cycle n and the dissipated energy at cycle n:

$$DER = \frac{\sum_{i=1}^{n} W_i}{W_n} \tag{7.2}$$

The relationship between *DER* and number of load cycles follows the line of equality (slope equal to 1) when the specimen is undamaged. As damage develops, the *DER* curve progressively bends upwards (strain-controlled tests) or downwards (stress-controlled tests).

It is recalled that the criterion currently adopted by the reference standard AASHTO T 400 (2023) for asphalt mixtures is the stress degradation ratio criterion, which is a simplification of the *DER* criterion. Fatigue failure is identified by the peak value of the product of stress amplitude and cycle number (σN). The main advantage of this criterion is that phase angle measurement is not needed.

The abovementioned criteria, typically adopted for traditional AC mixtures, were applied to the investigated CRM mixtures.

Preliminary observations of stress and strain evolutions during the test

Figure 7.13a shows the evolution of stress and on-specimen strain during the fatigue test for representative specimens of CRM1 (specimen R15, $\varepsilon_{0,initial}$ = 75 microstrain) and CRM2 (specimen R1, $\varepsilon_{0,initial}$ = 80 microstrain). For comparison purposes, Figure 7.13b shows the same data for representative specimens of AC1 (specimen #3, $\varepsilon_{0,initial}$ = 380 microstrain) and AC2 (specimen #3, $\varepsilon_{0,initial}$ = 450 microstrain). In these figures, both stress and strain are normalized with respect to their initial value.

Figure 7.13a shows the different behavior of mixtures CRM1 and CRM2. All CRM1 specimens (plus one CRM2 specimen) exhibited a progressive stress decrease and strain increase until reaching a sub-horizontal asymptote. Instead, for most CRM2 specimens (4 out of 5), both stress and strain followed an S-shape evolution during the test. For the AC mixtures (Figure 7.13ab), the stress reduced rapidly while the strain increased rapidly in the very first phase of the test, then the stress decreased while the strain increased in a steady quasi-linear manner in the second phase, and finally the stress rapidly decreased and the strain rapidly increased in the third phase.

Moreover, it was found out that for the CRM mixtures, the strain variation was predominant over the stress variation and the test was almost in stress control mode, especially for CRM2 specimens with higher cement content (Graziani, Spadoni, et al., 2024). Thus, it can be concluded that the test was more severe for CRM mixtures than for conventional AC mixtures. Moreover, the common fatigue failure criteria that are employed in the case of constant stress or constant strain may not be applicable, especially for CRM mixtures.

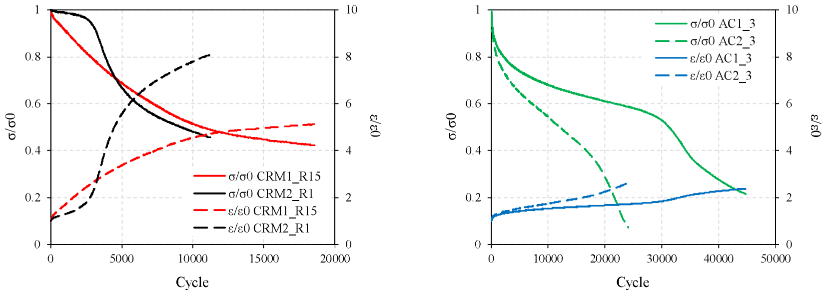

(a) **(b)**

Figure 7.13. Identification of the proper failure criteria: evolution of stress and strain for (a) CRM1 and CRM2, and (b) AC1 and AC2.

Empirical fatigue failure criteria

For the AC mixtures (Figure 7.14b), the three typical stages can be identified. In the initial loading cycles (adaptation phase) the stiffness reduces rapidly while the phase angle increases rapidly due to the combined effect of fatigue damage, heat development and thixotropy. In the second phase (quasi-stationary phase) the stiffness keeps decreasing while the phase angle keeps increasing, both with a steady quasi-linear trend. This behavior is normally associated with the development of damage due to the formation of microcracks. This second phase ends with an inflection point that denotes the beginning of the transition towards the third phase (failure phase), which is characterized by a fast decrease in stiffness and phase angle and is associated with the formation and propagation of macrocracks leading to the specimen physical failure.

The evolution of stiffness modulus and phase angle was similar between CRM1 and CRM2 mixtures, but different from the one described above (Figure 7.14a). Specifically: a) in both the stiffness and phase angle curves the quasi-stationary phase was not present; b) the phase angle evolution showed a sharper maximum value (the maximum δ/δ_0 value was around 1.5 for the AC specimens, higher than 2.0 for the CRM2 specimens and intermediate for the CRM1 specimens); c) the stiffness modulus curves were characterized by a relatively long and almost flat final part (without the inflection point that typically denotes the transition between the second and third phases for AC mixtures). This behavior suggests different fatigue damage mechanisms for CRM mixtures, as compared to traditional AC mixtures.

Figure 7.14 also shows the fatigue failure points identified using the two most common empirical criteria: 50 % reduction in the stiffness modulus ($N_{f,E}$) and maximum phase angle ($N_{f,\delta}$). For all specimens, $N_{f,\delta}$ is higher than $N_{f,E}$. However, the $N_{f,\delta}$ / $N_{f,E}$ ratio is generally lower for CRM mixtures (especially CRM2) as compared to AC mixtures, indicating that $N_{f,\delta}$ is closer to $N_{f,E}$ for CRM mixtures.

The $N_{f,E}$ and $N_{f,\delta}$ values are plotted in Figure 7.15. In particular, the data related to the two ACs are plotted together as a single data set, because AC1 and AC2 exhibited the same macroscopic behavior. Figure 7.15 clearly highlights that the maximum phase angle criterion leads to higher N_f values with respect to the 50 % modulus reduction criterion.

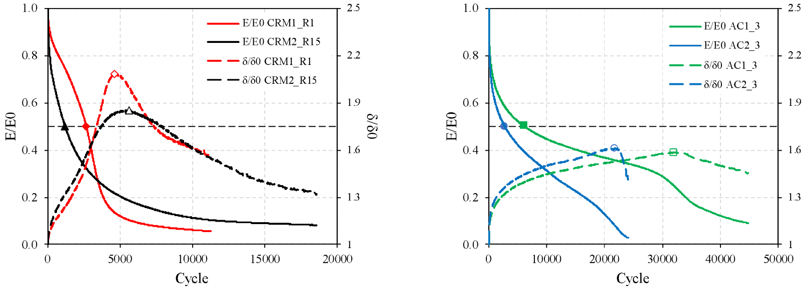

(a) **(b)**

Figure 7.14. Identification of the proper failure criteria: evolution of stiffness modulus and phase angle for (a) CRM1 and CRM2, (b) AC1 and AC2

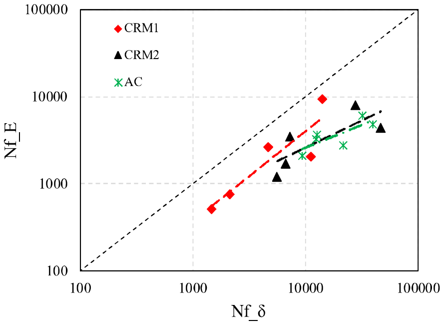

Figure 7.15. Identification of the proper failure criteria: $N_{f,E}$ vs $N_{f,\delta}$.

Energy-based fatigue failure criteria

Figure 7.16a-b show the evolution of the stress degradation ratio parameter ($\sigma{\cdot}N$) for the same four representative specimens shown above. The fatigue failure points corresponding to the maximum $\sigma{\cdot}N$ value ($N_{f,\sigma\cdot N}$) and to the maximum phase angle ($N_{f,\delta}$) are also reported in the figure. Note that, in the two subfigures, the scale on the y-axis is different (the AC specimens showed significantly higher values).

The AC behavior is as expected, with the parameter σ·N increasing during the test until reaching its peak value and then dropping rapidly before specimen collapse. It's noteworthy that $N_{f,\sigma\cdot N}$ slightly preceded $N_{f,\delta}$, consistently with literature findings. Conversely, for the CRM specimens, σ·N steadily increased until specimen collapse, confirming different fatigue damage mechanisms compared to AC mixtures. Specifically, σ·N increased at a higher rate in the first part of the test and at a slower rate in the second part, suggesting a change in the physical mechanism leading to energy dissipation as damage increased during the test. The absence of a peak value in the σ·N curve was expected because the test was almost in pure stress control mode for the CRM mixtures. $N_{f,\delta}$ broadly corresponded to the beginning of the second phase, characterized by a slower increase in the parameter σ·N.

Since the point of maximum for $\sigma{\cdot}N$ cannot be used to define fatigue failure, it is necessary to take a step back and examine first the evolution of the dissipated energy per unit volume per cycle (Equation (7.1), Figure 7.16c-d) during the test. . It should be noted that W was one order of magnitude higher for the AC mixtures, which was expected, given the higher applied strain level and phase angle with respect to CRM mixtures. The fatigue failure point corresponding to the maximum phase angle ($N_{f,\delta}$) is also highlighted in the figure.

For AC specimens, the dissipated energy initially slightly increases, then there is a plateau before a sharp decrease towards the end of the test. The typical phases observed in the evolution of modulus and phase angle (Figure 7.14b) are clearly visible. Moreover, $N_{f,\delta}$ aligns with the conclusion of the constant phase for specimen AC1_3, while it falls within the descending segment of the curve for specimen AC2_3.

Conversely, CRM specimens displayed an initial energy increase, followed by a slower decline, particularly pronounced in CRM2. Unlike AC, there was no clear quasi-stationary phase, indicating a shifting energy dissipation mechanism during the test. Both CRM1 and

CRM2 showed the maximum phase angle closely corresponding to peak W, with CRM2 exhibiting two distinct inflection points in its curve.

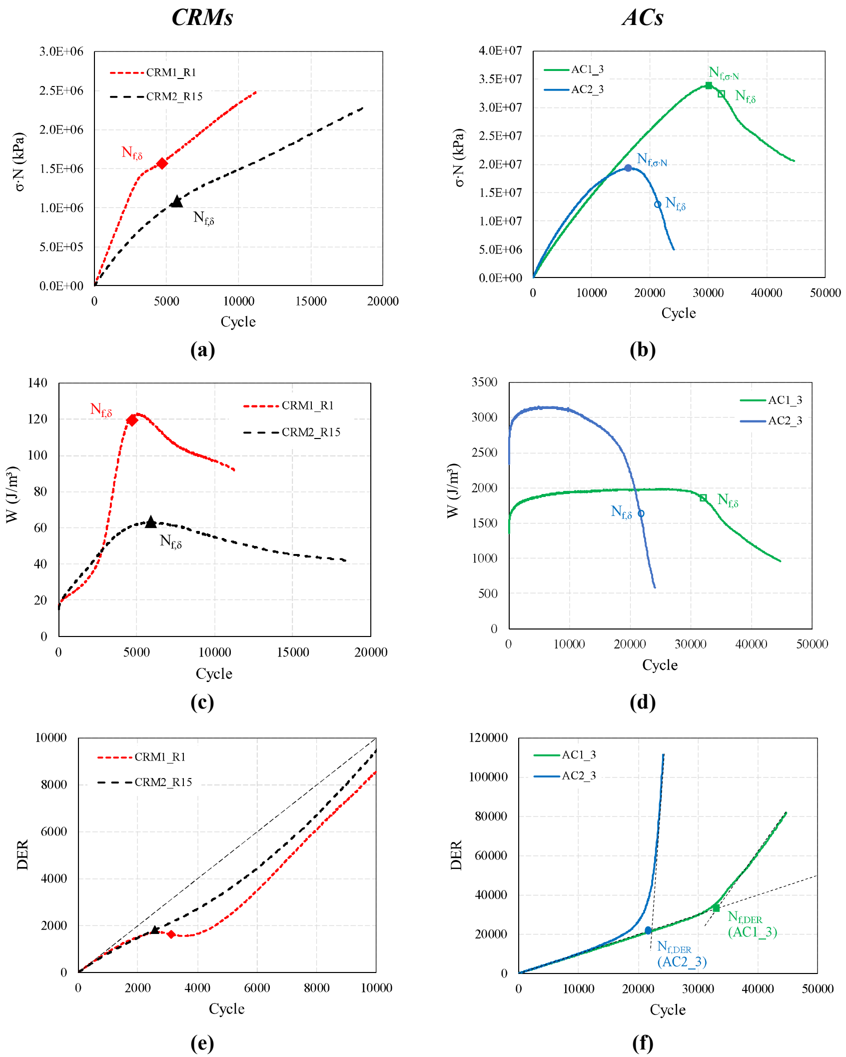

(a) **(b)**

(c) **(d)**

(e) **(f)**

Figure 7.16. Identification of the proper failure criteria: evolution of (a,b) the parameter σ·N, (c,d) dissipated energy per unit volume and (e,f) DER.

The differences in the dissipated energy per cycle led to a different evolution of the *DER* (Figure 7.16e-f). For the CRM specimens, a zoom of the initial part of the test is presented in Figure 7.16e, as these are the data of greatest interest.

In AC, in undamaged specimens, the *DER* curve aligns with the line of equality, then gradually diverges, approaching an oblique irrecoverable fatigue asymptote. Determining the cycles to failure based on the DER curve involves identifying the intersection between the no damage line and this asymptote, as depicted in Figure 7.16f.

Figure 7.16e illustrates a different behavior in CRM mixtures. Initially, DER values are located below the line of equality from the very early testing cycles, which is typically observed in stress-controlled tests. Notably, CRM2 specimens exhibit an interesting sequence: a local maximum, an inflection point, and a subsequent local minimum within a relatively short cycle interval. After the local minimum, *DER* values steadily rise until specimen failure. Though less pronounced in CRM1, a similar inflection point is identifiable.

Interpretation of the results

The experimental results indicated a different behavior in the fatigue damage evolution between CRM and AC specimens. Evidently, this difference lays on the presence of cementitious bonds, and the behavior between CRM1 and CRM2 mixtures further underlines the critical role of cement dosage.

A potential interpretation of the fatigue failure in CRM specimens is depicted in Figure 7.17. Initially, during the fatigue test, the cementitious bonds absorbed the applied tensile load due to their greater stiffness compared to the bituminous bonds. However, their brittleness caused them to a quick failure as the tensile strain amplitude increased in the test's initial stage. This mechanics could justify the local maximum, inflection point, and local minimum characterizing the initial *DER* evolution in CRM2 specimens.

The localized failure of cementitious bonds can be construed as microcracks diminishing the effective area of the specimen, potentially originating from the fracture of cement hydrates or detachment at the interface between hydrates and aggregate particles, primarily composed of RA particles. The stress is then progressively transferred to the bituminous binder. This could lead to the observed sharp rise in dissipated energy per cycle, subsequently causing a decline in *DER*. With an increase in loading cycles, bituminous bonds gradually assumed all the load, thus experiencing increasing damage. A declining trend in dissipated energy per cycle occurred, and the *DER* curve exhibited an increasing trend (slope greater than 1), as for conventional AC mixtures in strain-controlled tests, culminating in macrocrack development and eventual specimen collapse.

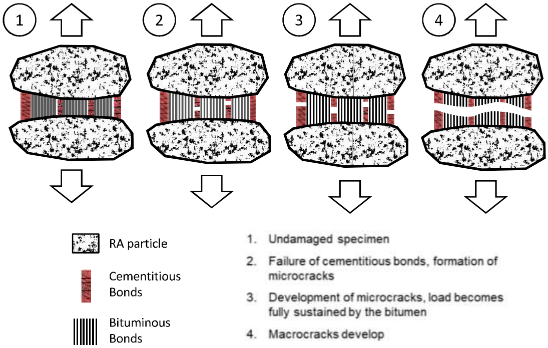

Figure 7.17. Identification of the proper failure criteria: interpretation of fatigue failure of CRM specimens (Graziani, Spadoni, et al., 2024).

The inflection point of the DER curve was proposed to identify the failure of the cementitious bonds whereas, analogously to typical AC mixtures, the subsequent failure of the bituminous bonds was identified through the maximum phase angle value. Based on both criteria, a longer fatigue service life was observed for CRM specimens with lower cement content.

7.3.4 Cyclic fatigue

The S-VECD characterization was carried out on the valid tests included in the identification of the proper failure criteria (Section 7.3.3), plus four valid tests performed in NCSU (two of CRM1: R19-R22 plus two of CRM2:R19-R20), for a total of seven specimens for each mixture.

The two failure criterions which seem to efficiently indicate the failure of the cementitious and bituminous bonds (i.e., the inflection of DER curve and maximum of δ, respectively) were applied. Table 7.2 reports the number of cycles to failure for both the CRMs.

For the analysis with FlexMAT$^{\text{TM}}$, the input .csv files needed to be manually modified, since FlexMAT$^{\text{TM}}$ uses the maximum of the product between the applied stress and the number of cycle (σ·N) as failure criterion, as prescribed by the AASHTOs (Section 2.4). Indeed, only the rows of the input files until the target number of cycles given by $N_{f,DER}$ and $N_{f,\delta}$ were maintained, whereas the remaining rows were cut. $N_{f,DER}$ calculated as the inflection point of DER was approximated to the closest number of cycles recorded by the software during the test.

Figure 7.18 shows the resulting damage characteristic curves for each specimen of CRM1 and CRM2 considering both the failure criteria.

The fits of the C-S curves were manually calibrated varying the $C11$ and $C12$ coefficients, and considering the average value of S, instead of the maximum value. The resulting fits are shown in Figure 7.19a. The C *vs.* S curves of CRM2 are in upper position due to the higher stiffness (Figure 7.10). For both CRMs, curves are longer considering $N_{f,\delta}$ than considering $N_{f,DER}$ likely due to the higher amount of dissipating damage due to the bituminous bonds ($N_{f,\delta}$ usually higher than $N_{f,DER}$). Considering the same failure criterion, CRM1 and CRM2 reach similar pseudostiffness C at failure, whereas CRM2 is characterized by a higher amount of damage S at failure. Figure 7.19b shows the envelopes of the failure criterion D^R and the values are also reported. For both CRMs, D^R values are lower considering $N_{f,DER}$ since only the cementitious bonds, which are the first to break, are considered. Considering the same failure criterion, CRM1 is characterized by higher toughness than CRM2. This outcome is may attributable to the predominancy of the viscoelastic behavior to the bituminous bonds in CRM1 instead of the cementitious ones.

The values of the synthetic index *Sapp* for CRMs are not reliable and have no sense, because *Sapp* has been calibrated on the field performance of asphalt concrete and it can be considered as an empirical formulation.

Table 7.2. Cyclic fatigue results: number of cycles at failure according to the two identified failure criteria.

Mixture	Specimen	$N_{f,DER}$ *(calculated)*	$N_{f,\delta}$ *(approximated)*	$N_{f,\delta}$
CRM1	R5	5178	5180	7280
	R14	17466	17470	46900
	R15	2578	2580	5630
	R17	4290	4290	6720
	R18	29562	29590	28040
	R19	2046	2050	2540
	R22	13537	13530	27690
CRM2	R1	3108	3110	4630
	R5	1573	1570	2130
	R9	1246	1250	1460
	R10	3712	3710	11140
	R11	11776	11780	14170
	R19	2055	2060	4070
	R20	6778	6780	13560

In conclusion, it is not possible to state which of CRMs should provide better fatigue performance. CRM1 is characterized by higher toughness (Figure 7.19b), however CRM1 is characterized by higher stiffness. Only FlexPAVE™ pavement performance simulations can give an answer.

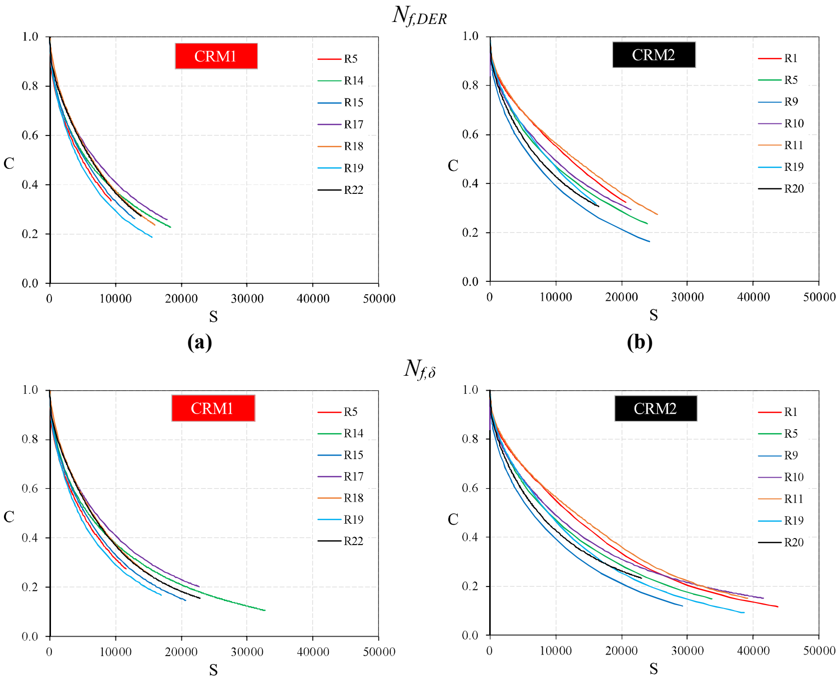

(a) (b)

(c) (d)

Figure 7.18. Cyclic fatigue results: damage characteristic curve for each specimens considering the two failure criteria.

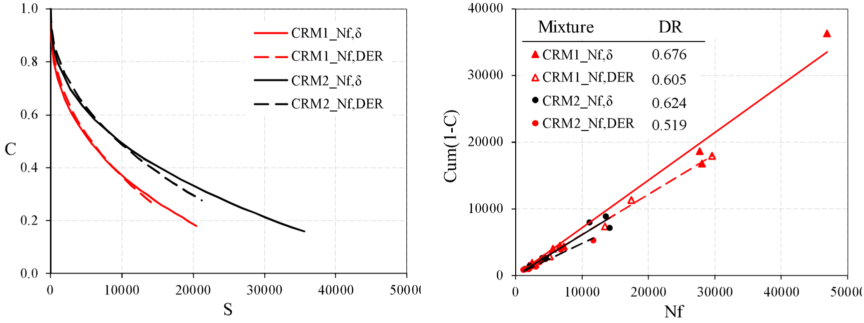

(a) (b)

Figure 7.19. Cyclic fatigue results: (a) fits of the damage characteristic curves for each CRM and D^R failure envelopes considering the two failure criteria.

7.4 Pavement performance simulations

7.4.1 Input data

The evaluation of the fatigue behavior at structural level of the investigated CRMs was performed with FlexPAVE^{TM} software. It should be noted that FlexPAVE^{TM}, as well as the S-VECD approach, has been developed for asphalt mixtures (Y. D. Wang et al., 2018). Indeed, the aim is to evaluate the reliability of the results even for CRMs.

Design structures

Three typical pavement structure (i.e., thin, intermediate and thick pavements), usually adopted in U.S., were considered. The structures are shown in Figure 7.20, together with the traffic range level for a design life 20 years. All the structures are characterized by the same 20-cm thick Aggregate Base Course (ABC) with stiffness of 206 MPa, that is above the subgrade with stiffness of 124 MPa. The thickness of the Asphalt Concrete (AC) course increases as the design traffic level increases.

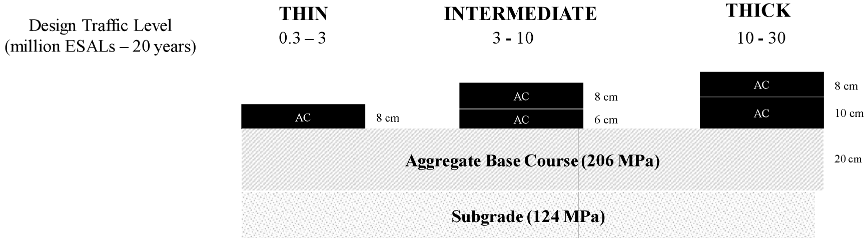

Figure 7.20. Pavement performance simulations: structures of the pavement and design life.

Materials

For the AC course (Figure 7.20), an asphalt concrete with 50/70 neat bitumen for binder courses was used. This mixture was previously studied through the application of the S-VECD approach by Gaudenzi et al. (2023). Figure 7.21a-b show the shift factors and the storage modulus mastercurves (2S2P1D models together with the average experimental data) at the reference temperature of 21.1 °C, respectively, of the AC and the CRMs. From the shift factors (Figure 7.21a), it can be noted that all the mixtures present similar thermo-susceptibility, confirming that it is mainly influenced only by the bitumen. From the storage modulus mastercurves (Figure 7.21b), it is clear that the CRMs are characterized by strongly lower thermos-susceptibility, due to the presence of cement. In the same Figure 7.21b, the reduced frequencies range which influences the fatigue results (i.e., C-S curve) is indicated with a green box.

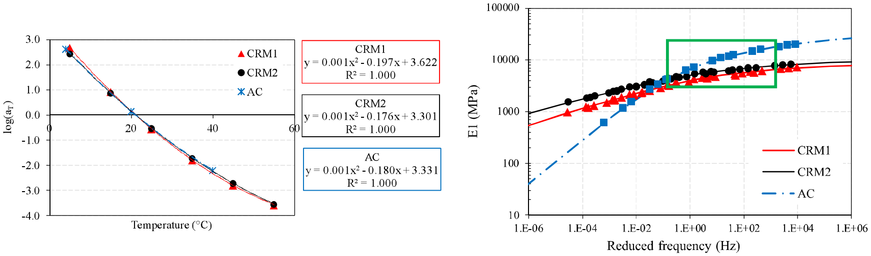

(a) **(b)**

Figure 7.21. Pavement performance simulations, materials: (a) shift factors and (b) storage modulus mastercurves (2S2P1D model) at 21.1 °C.

Figure 7.22a-b show the fits of the damage characteristic curves and the D^R failure criterion values of the AC and the CRMs. It should be recalled that for the AC, the number of cycles to failure corresponds to the cycle in which the product of the applied stress and the number of cycle has a maximum during the test, as prescribed by the reference AASHTO T 411 (2023). For the CRMs, two failure criteria were identified (Graziani, Spadoni, et al., 2024). One failure criterion was the inflection of the DER evolution curve ($N_{f,DER}$) during the test, to which the end of the cement-dominated dissipation behavior is associated. The other failure criterion is the maximum of the phase angle ($N_{f,\delta}$) during the test, representative of the end of the bitumen-dominated dissipation behavior. Since the failure of the cementitious bonds usually precedes the failure of the bituminous bonds ($N_{f,DER} < N_{f,\delta}$), only the failure criterion of the maximum of the phase angle ($N_{f,\delta}$) was considered for FlexPAVE™ simulations.

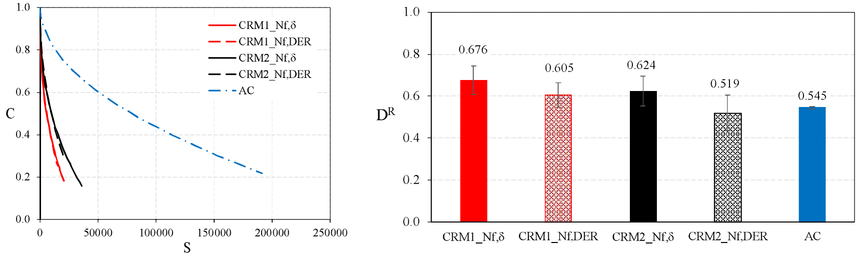

(a) **(b)**

Figure 7.22. Pavement performance simulations, materials: (a) fits of the damage characteristic curves and (b) D^R failure criterion values (the error bars represent the standard deviation).

Traffic conditions

The reference U.S. 80-kN ESAL was considered, i.e., single wheel with dual tires. The tire pressure of 700 kPa and a circular contact area were set. The speed was equal to 70 km/h, representative of heavy load in low/medium traffic level pavements. The average million ESALs values within the design traffic level were chosen. Specifically, 2 million, 7 million

and 20 million in 20 years were considered for thin, intermediate and thick pavements (Figure 7.), respectively. No growth rate of traffic was considered.
For each simulation, the maximum service life of 30 years was investigated. The year of construction was set as 2020.

Climatic conditions
As for the climatic conditions, the city of Raleigh (North Carolina) was considered. The climatic PG of Raleigh is PG 64-22.

7.4.2 The 2-stages procedure adopted for CRMs

Preliminary performance simulations of pavement with a CRM course were carried out in order to check FlexPAVE^{TM} could catch the actual and reliable behavior of CRM even though CRM is an unconventional viscoelastic material.
Many pavement structures were considered, and in this section only one of them is reported as an example, since the same results were obtained for all of them. Specifically, the reported example concerns about the typical thick pavement structure (Figure 7.), where CRM1 was used as replacing of the lower 10-cm thick AC course. Both fatigue and thermal effects were considered, and 10 million 80-kN ESALs in 20 years were set.
Figure 7.23a-b present the damage contour and pseudostiffness contour after 6 months of service. About 3 cm of CRM at the bottom of the course is completely cracked ($DF = 1$, Figure 7.23a), and the upper 8-cm thick AC course has no damage, since the pseudostiffness is the initial value set by FlexPAVE^{TM} (i.e., 0.8) in all the cross-section area (Figure 7.23b). Analogously, Figure 7.23b-c present the damage contour and pseudostiffness contour after 30 years of service. The CRM course is almost all completely cracked (Figure 7.23c), whereas the AC course still experienced an almost negligible level of damage. In fact, the cross-section area of the AC course is characterized by the initial pseudostiffness value of 0.8, expect for a very poor onset of top-down cracking. Finally, Figure 7.23e shows the *%damage* and the corresponding *%cracking* evolution during service. The pavement results completely cracked after about 5 years of service (both *%damage* and *%cracking* reach the asymptote), but the AC course is not damaged. In our opinion, this outcome highlighted that FlexPAVE^{TM} simulations with CRM cannot be treated like the conventional ones.

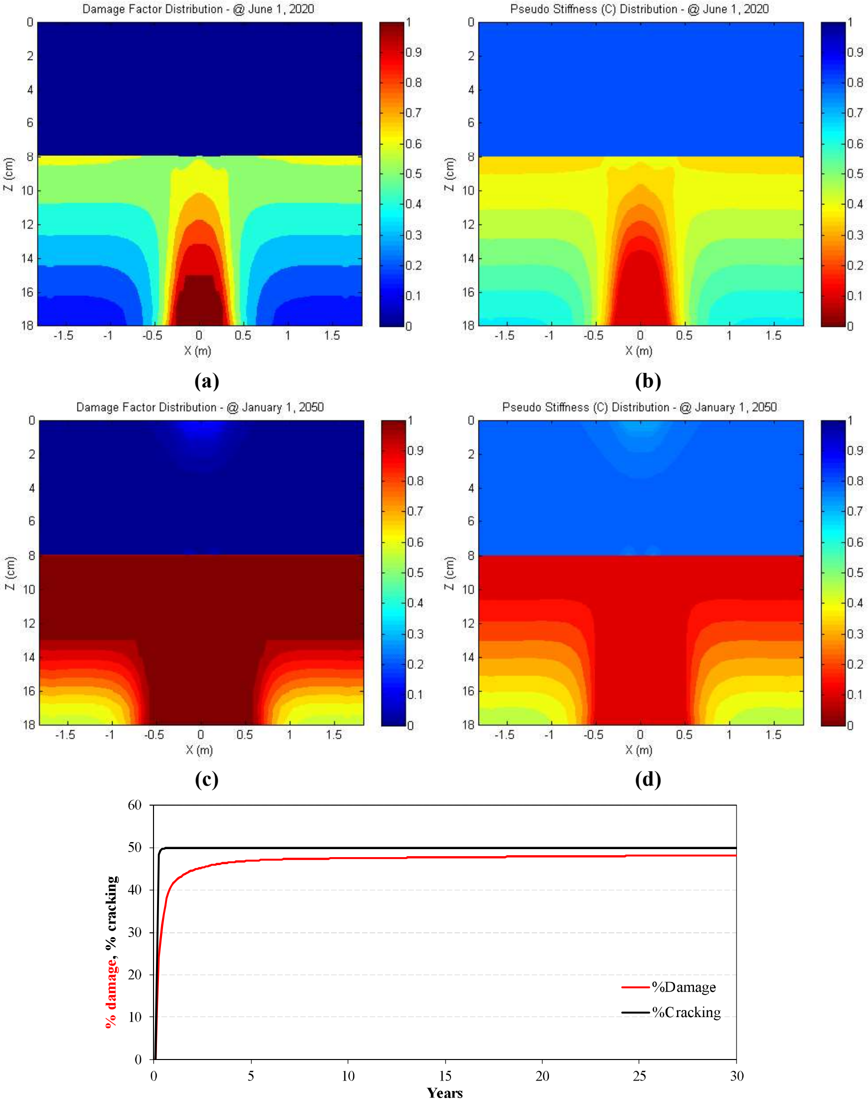

(a) (b)

(c) (d)

(e)

Figure 7.23. Pavement performance simulations, 2-stages procedure for CRMs: (a) damage contour and (b) pseudostiffness contour after 6 months of service, (c) damage contour and (d) pseudostiffness contour after 30 years of service, and (e) *%damage* and *%cracking* evolution during service.

For this reason, the behavior of the CRM was modeled as a 2-stages behavior, as recommended by the South Africa Manual of CRM course design. The 2 stages are the following:

Stage 1. The CRM is modeled as a viscoelastic material. The duration of stage 1 corresponds to the number of 80-kN ESALs *N1* which causes a 2-cm thick area completely cracked at the bottom of the CRM course (i.e., *DM = 1*). The choice of the thickness equal 2-cm is an assumption, and it is the minimum thick for which FlexPAVE^{TM} gives the *DM* values. An example of the damage contour corresponding to N1 is reported in Figure 7.24a, where CRM was used as replacement of the lower AC course in a thick pavement. At *N1*, the average pseudostiffness value weighted on the thickness of the AC course was determined at the center of the dual wheel (coordinate x = 0), representative of the level of damage on AC. However, this value is always not lower than 0.799. For this reason, the *%damage* in stage 1 is assumed equal to 0.

Stage 2. After *N1*, the bottom crack propagates upward, so the CRM is considered completely cracked. Indeed, a new FlexPAVE^{TM} simulation starts, where the CRM course is no longer modeled as viscoelastic, but as a linear elastic material. The input stiffness value is the dynamic modulus value corresponding to $N_{f,\delta}$ during the laboratory S-VECD fatigue tests (Figure 7.24b). The average value for CRM1 and CRM2 resulted of 850 MPa and 950 MPa, respectively. For the AC course, the average pseudostiffness value calculated at *NI* (stage 1) was put as initial *C* value.

The resulting *%damage* is equal to 0 for *N1*, then corresponds to the *%damage* resulting from stage 2. Analogously for the *%cracking* with the transfer function proposed by Wang et al. (2021).

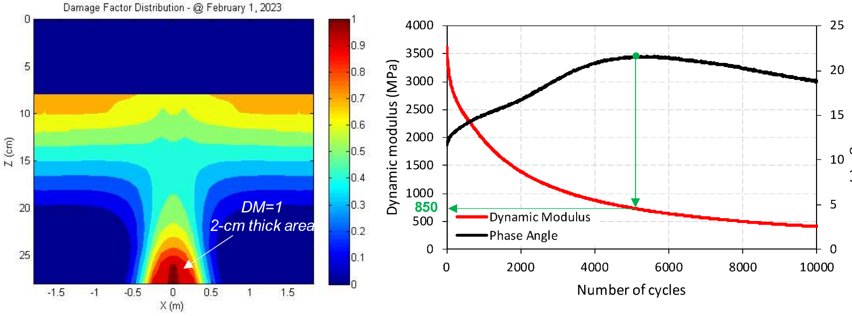

(a) **(b)**

Figure 7.24. Pavement performance simulations, 2-stages procedure for CRMs: (a) example of damage contour at *N1*, and (b) graphical explanation of the determination of the stiffness of CRM at failure.

7.4.3 Use of CRMs as replacement of aggregate base course

The level of damage of the pavement using CRMs as replacement of the ABC course was investigated for all the pavement structures shown in Figure 7.. The damage with both fatigue and thermal effects or with only fatigue effects was evaluated and are shown in the following sections. However, it should be underlined that, as these are the first experiences with FlexPAVE^{TM} simulations with CRMs, it is better to take into account only the results considering only the fatigue damage. In fact, in the case of thermal effects, many assumptions are made, e.g. full bonding between AC and CRM, or the same dilatancy coefficient for both the different materials (nevertheless the presence of cement in CRM).

Thin pavements

Figure 7.25a-d show the damage contours at *N1* (stage 1) for pavements with CRM1(Figure 7.25a-b) and CRM2 (Figure 7.25c-d). It can be seen that CRMs suffer thermal stresses at the interface with AC, especially CRM2 (higher gap of stiffness with AC and low thermo-susceptibility, see Figure 7.21b). Moreover, such thermal stresses cause the failure for CRM2 even at the top of the course (Figure 7.25c). Considering only the fatigue damage, CRM2 shows a slightly higher performance, in according to the damage characteristic curves (Figure 7.22a).

Figure 7.25e reports the *N1* values and Figure 7.25f reports the corresponding years of service of stage 1. The influence of the thermal stresses on the years of service is low and broadly comparable between the pavement with CRMs. The base course with CRM2 is capable of providing more years of service working as a viscoelastic material (i.e., 6 years) with respect to CRM1 (i.e., 2 years).

Figure 7.26a-c show the damage contours of the AC course in the case of pavements with CRMs and ABC as base courses after 30 years of service (for CRMs, stage 1 + stage2) considering both fatigue and thermal effects, whereas Figure 7.26d-f show the same ones considering only the fatigue damage. Figure 7.26g shows the *%damage* evolution with fatigue and thermal effects (continuous lines) and with only fatigue damage (dashed lines). It can be noted that the base course with CRM2 ensures a slightly higher performance than CRM1 due to its higher stiffness. Comparing the effects of CRMs and ABC, the strongly better pavement performance in presence of CRMs is highlighted likely due to higher stiffness. Moreover, pavement with ABC experiences top-down cracking, too. Observing the *%damage* evolutions (Figure 7.26g), it is visible that thermal effects have a negligible influence on the performance, especially for the pavement with ABC and CRM1.

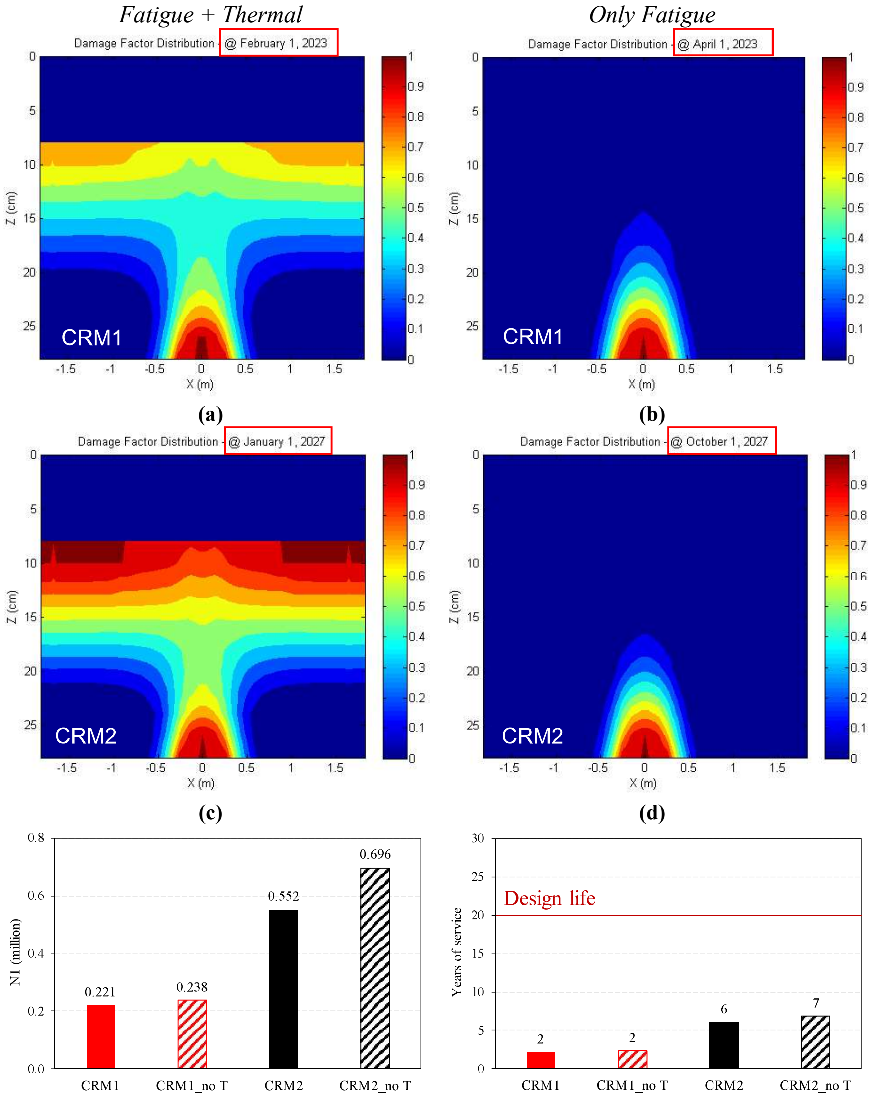

(a) (b) (c) (d) (e) (f)

Figure 7.25. Pavement performance simulations, CRMs as replacement of aggregate base course, thin pavements: (a-d) damage contours at *N1* (stage 1), (e) *N1* values and (f) corresponding years of service.

Fatigue + Thermal

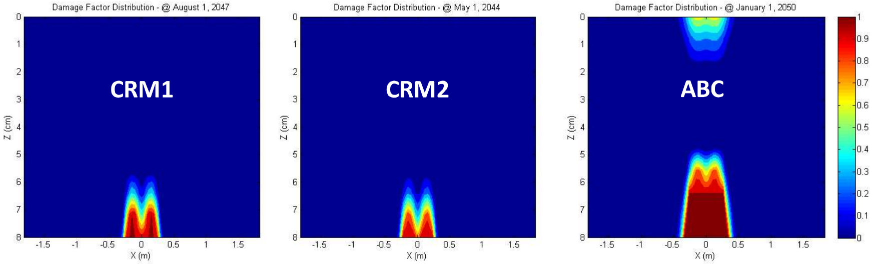

(a) **(b)** **(c)**

Only Fatigue

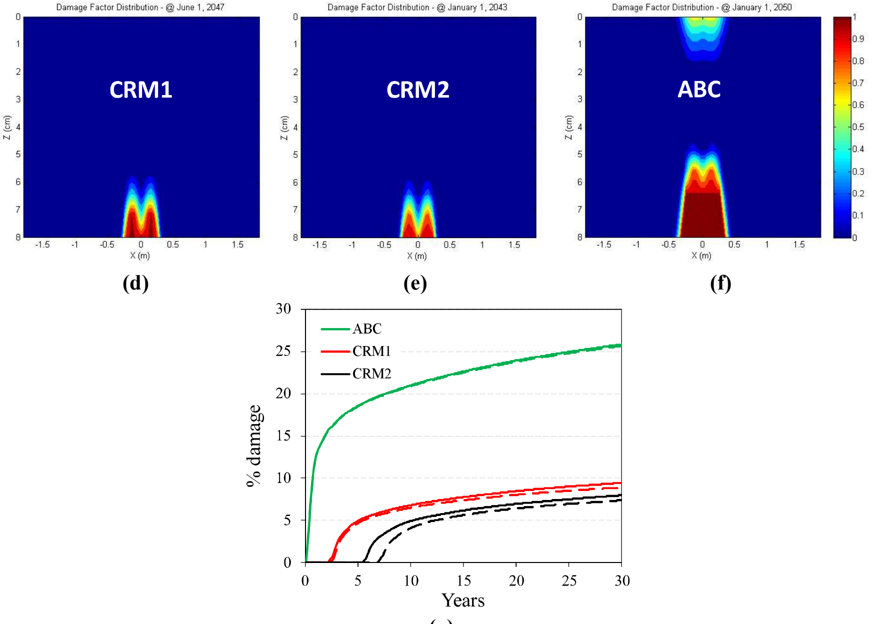

(d) **(e)** **(f)**

(g)

Figure 7.26. Pavement performance simulations, CRMs as replacement of aggregate base course, thin pavements: damage contours after 30 years of service considering (a-c) fatigue and thermal effects or (d-f) fatigue damage, and (g) *%damage* evolution with fatigue and thermal effects (continuous lines) and with only fatigue damage (dashed lines).

Intermediate pavements

Figure 7.27a-d show the damage contours at *N1* (stage 1) for pavements with CRM1(Figure 7.27a-b) and CRM2 (Figure 7.27c-d). Similar considerations to thin pavements can be conducted. CRMs suffer thermal stresses at the interface with AC, especially CRM2 (higher gap of stiffness with AC and low thermo-susceptibility, see Figure 7.21b). Considering only the fatigue damage, CRM2 shows a slightly higher performance, in according to the damage characteristic curves (Figure 7.22a).

Figure 7.27e reports the *N1* values and Figure 7.27f reports the corresponding years of service of stage 1. The influence of the thermal stresses on the years of service is low and slightly higher for the pavement with CRM2. The base course with CRM2 is capable of providing more years of service working as a viscoelastic material with respect to CRM1. The years of service are in both cases higher than the ones for thin pavements (Figure 7.25f).

Figure 7.28a-c show the damage contours of the AC course in the case of pavements with CRMs and ABC as base courses after 30 years of service (for CRMs, stage 1 + stage2) considering both fatigue and thermal effects, whereas Figure 7.28d-f show the same ones considering only the fatigue damage. Figure 7.28g shows the *%damage* evolution with fatigue and thermal effects (continuous lines) and with only fatigue damage (dashed lines).
Similar considerations to thin pavements can be conducted. The base course with CRM2 ensures a slightly higher performance than CRM1 due to its higher stiffness. Comparing the effects of CRMs and ABC, the strongly better pavement performance in presence of CRMs is highlighted likely due to higher stiffness. Moreover, pavement with ABC experiences the onset of top-down cracking (much lower than in thin pavement, see Figure 7.26c,f), too. Observing the *%damage* evolutions (Figure 7.28g), it is visible that thermal effects have a negligible influence on the performance, especially for the pavement with ABC.

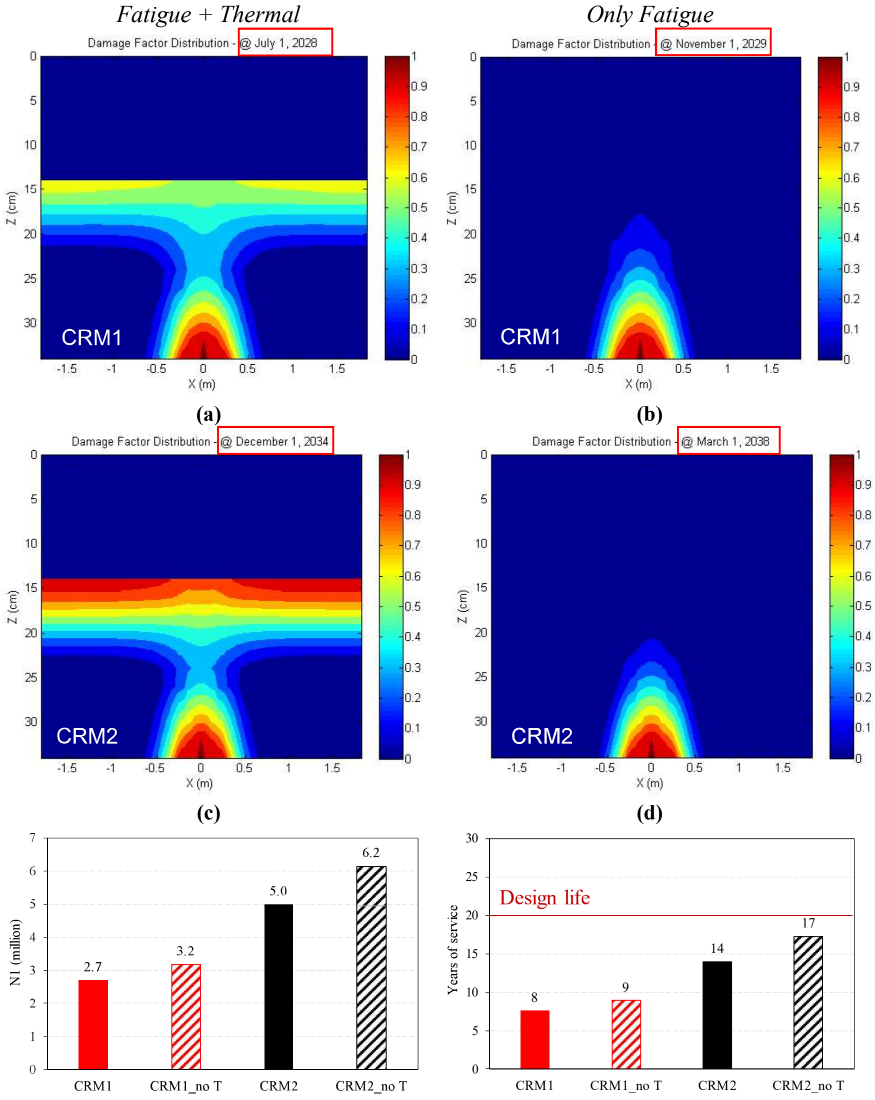

(a) (b) (c) (d) (e) (f)

Figure 7.27. Pavement performance simulations, CRMs as replacement of aggregate base course, intermediate pavements: (a-d) damage contours at *NI* (stage 1), (e) *N1* values and (f) corresponding years of service.

Fatigue + Thermal

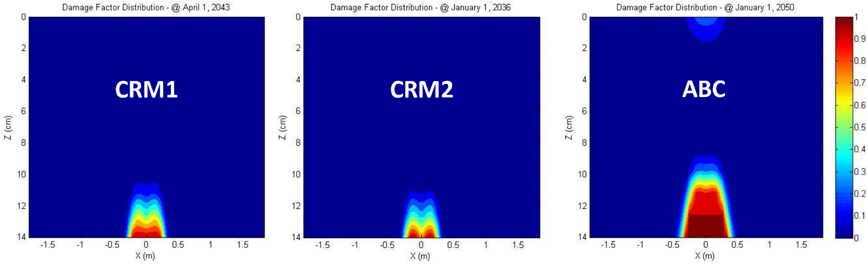

(a) **(b)** **(c)**

Only Fatigue

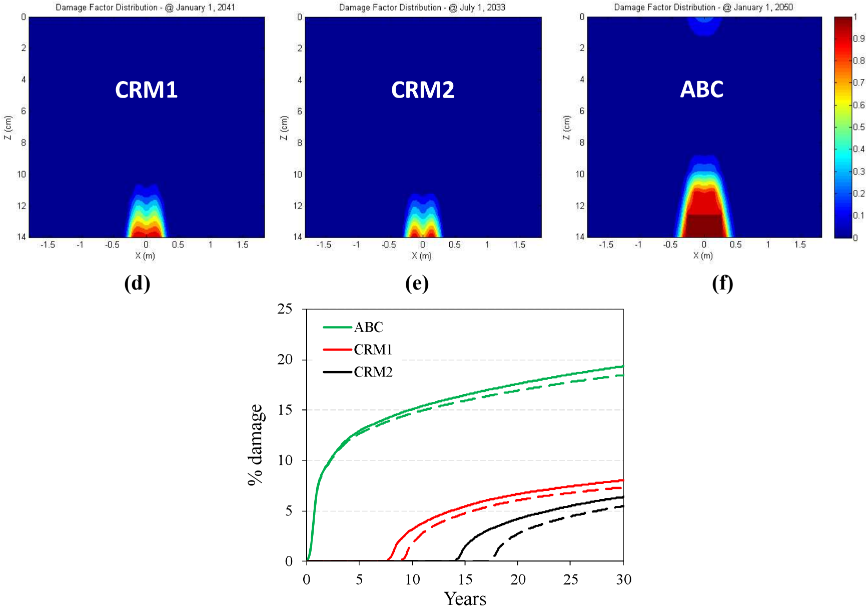

(g)

Figure 7.28. Pavement performance simulations, CRMs as replacement of aggregate base course, intermediate pavements: damage contours after 30 years of service considering (a-c) fatigue and thermal effects or (d-f) fatigue damage, and (g) *%damage* evolution with fatigue and thermal effects (continuous lines) and with only fatigue damage (dashed lines).

Thick pavements

Figure 7.29a-d show the damage contours at *N1* (stage 1) for pavements with CRM1(Figure 7.29a-b) and CRM2 (Figure 7.29c-d). Similar considerations to thin and intermediate pavements can be conducted. CRMs suffer thermal stresses at the interface with AC, especially CRM2 (higher gap of stiffness with AC and low thermo-susceptibility, see Figure 7.21b). However, such damage is considerably lower than in thin and intermediate pavements (Figure 7.25a,c, Figure 7.27a,c, respectively), likely due to the higher depth of the CRM course. Considering only the fatigue damage, the CRMs show comparable resistance.

Figure 7.29e reports the *N1* values and Figure 7.29f reports the corresponding years of service of stage 1. The influence of the thermal stresses on the years of service is comparable for both the pavements. Without considering thermal effects, the years of service in stage 1 increase by about 30%. Differently from the cases of thin and intermediate pavements, the base course with CRM2 provides similar years of service working as a viscoelastic material with respect to CRM1. The years of service are close to the design value of 20 years, and they are in both cases higher than the ones for thin and intermediate pavements (Figure 7.25f, Figure 7.27f).

Figure 7.30a-c show the damage contours of the AC course in the case of pavements with CRMs and ABC as base courses after 30 years of service (for CRMs, stage 1 + stage2) considering both fatigue and thermal effects, whereas Figure 7.30d-f show the same ones considering only the fatigue damage. Figure 7.30g shows the *%damage* evolution with fatigue and thermal effects (continuous lines) and with only fatigue damage (dashed lines).

The base courses with CRM1 and CRM2 ensure broadly comparable performance. Differently from thin and intermediate pavements, a slightly higher performance is observed for the pavement with CRM1 than CRM2. Comparing the effects of CRMs and ABC, the strongly better pavement performance in presence of CRMs is highlighted likely due to higher stiffness. Moreover, pavement with ABC experiences the onset of damage at the top of surface when thermal effects are considered (Figure 7.30c), too. Observing the *%damage* evolutions (Figure 7.28g), it is visible that thermal effects have a negligible influence on the long-term performance of all the pavements.

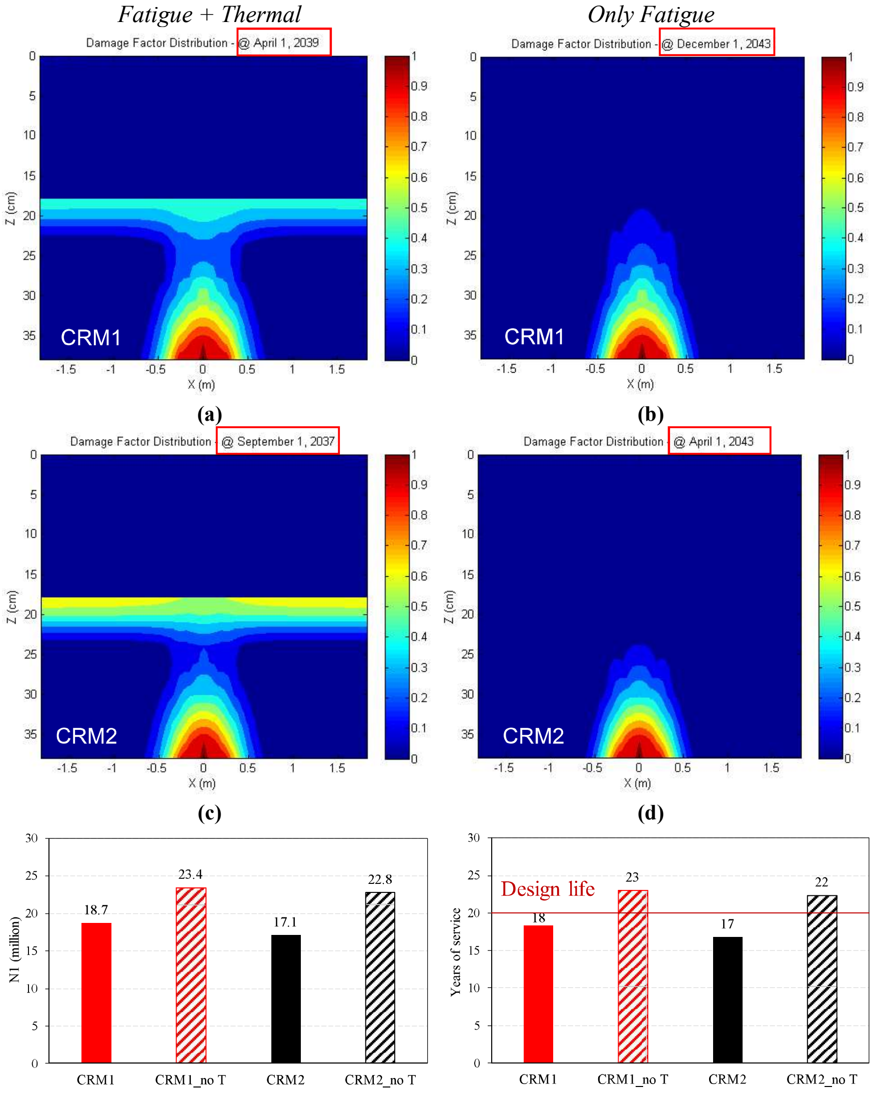

(a) (b) (c) (d) (e) (f)

Figure 7.29. Pavement performance simulations, CRMs as replacement of aggregate base course, thick pavements: (a-d) damage contours at *NI* (stage 1), (e) *N1* values and (f) corresponding years of service.

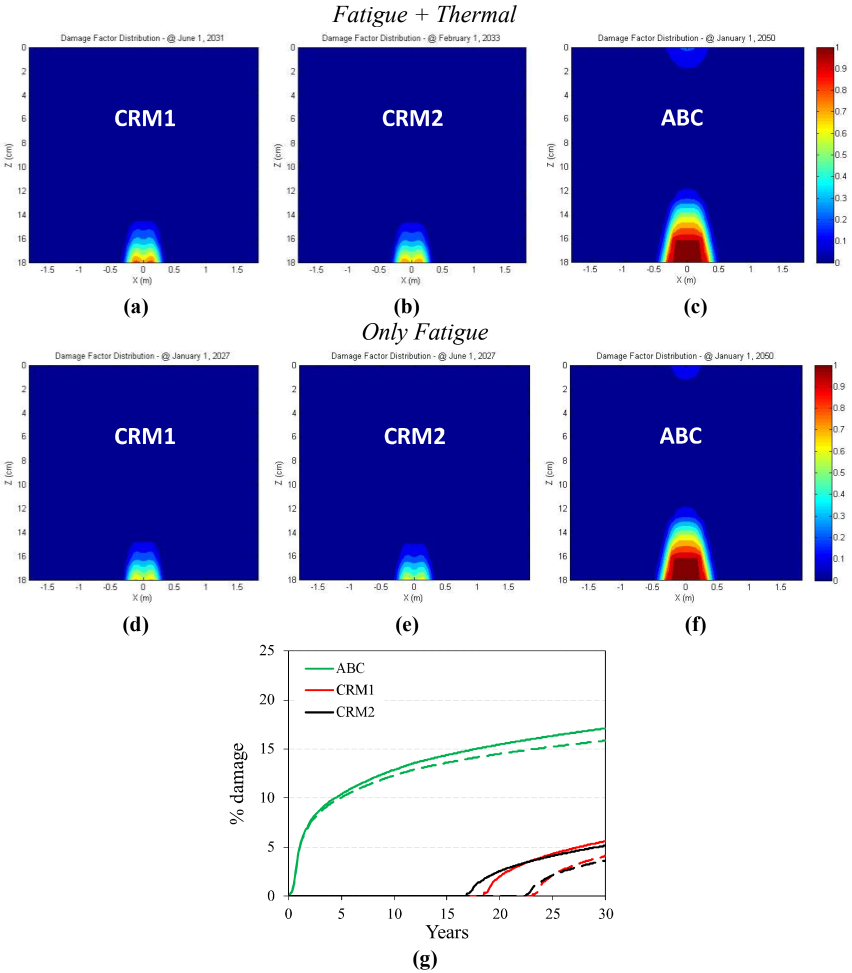

Figure 7.30. Pavement performance simulations, CRMs as replacement of aggregate base course, thick pavements: damage contours after 30 years of service considering (a-c) fatigue and thermal effects or (d-f) fatigue damage, and (g) *%damage* evolution with fatigue and thermal effects (continuous lines) and with only fatigue damage (dashed lines).

7.4.3.1 Effect of CRMs on the vertical and tensile strain

The vertical and horizontal strains in critical points have been evaluated. The strain values are extracted in the FlexPAVE^{TM} simulations where only fatigue damage was considered. It

is recalled that in FlexPAVE^{TM} X, Y, Z indicate the transversal, longitudinal of the traffic and depth, respectively (Figure 2.36).
The strain values which lead to permanent deformation of the subgrade, bottom-up cracking and top-down cracking have been investigated. Due to temperature variations, the strain values change during the day (three periods of time are given: 5:00 AM to Noon, Noon to 7:00 PM, 7:00 PM to 5:00 AM) and during the year (twelve months). As expected, based on the climatic conditions of Raleigh (NC); it was observed that the maximum strain values correspond to the time period Noon to 7:00 PM of August. Indeed, all the following strain values are extracted at this period. It is recalled that FlexPAVE^{TM} pavement response analysis provides the strains in all the directions during the passage of the wheel on the investigated cross-section.

Permanent deformation of the subgrade
The vertical strain ε_{zz} in the middle of the dual-tire wheel (X = 0 m) is evaluated. The maximum of ε_{zz} corresponds to the time T = 0.057021 s, i.e. when the wheel is exactly on the investigated cross-section area. Figure 7.31a,b,c show the trend of the ε_{zz} for thin, intermediate and thick pavements, respectively. The trends in the pavement with ABC, CRM1 and CRM2 for the two stages are reported.

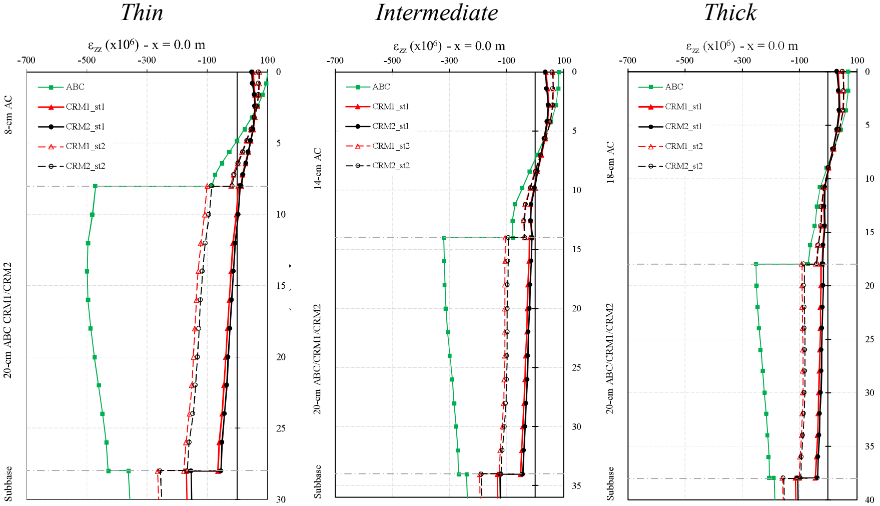

(a) **(b)** **(c)**

Figure 7.31. CRMs as replacement of aggregate base course: trends of ε_{zz} for (a) thin, (b) intermediate and (c) thick pavements (positive values = tension; negative values = compression).

Figure 7.32a shows an example of spatial distribution of ε_{zz} in thin pavement. The evaluation point for the critical ε_{zz}, i.e. at the top of the subgrade, is indicated.

Furthermore, Figure 7.32b,c,d show the critical ε_{zz}, for thin, intermediate and thick pavements, respectively. It can be seen that in all the scenarios the ε_{zz} values are lower in presence of CRM with respect to ABC, especially if stage 1 (CRM modeled as viscoelastic material) is considered. This outcome highlights the beneficial contribution of the CRM in protecting the subgrade from permanent vertical deformation, thus ensuring structural integrity.

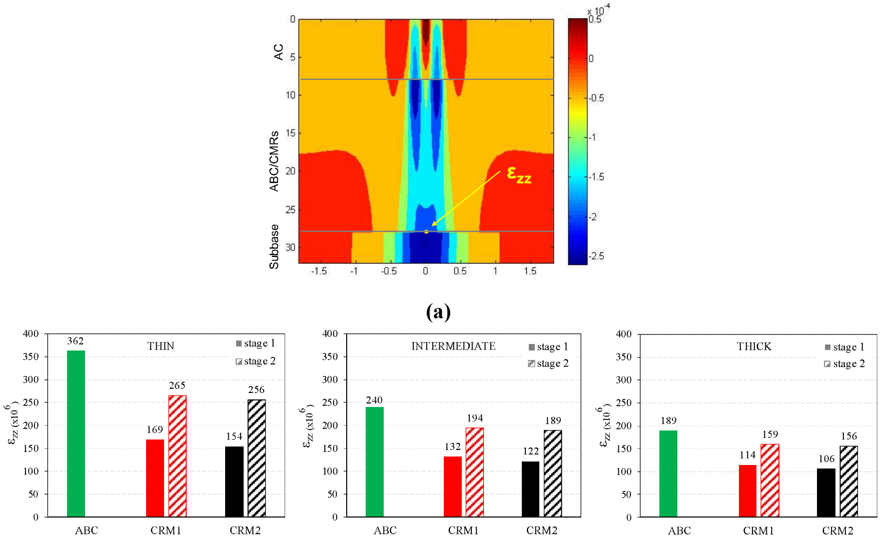

(a)

(b) **(c)** **(d)**

Figure 7.32. CRMs as replacement of aggregate base course: (a) evaluation point for the critical ε_{zz}, and critical ε_{zz} values at the top of subgrade in (a) thin, (b) intermediate and (c) thick pavements.

Bottom-up cracking

Due to the dual tire spacing of 0.30 m, the maximum horizontal tensile strain values at the bottom of the asphalt concrete layer are at x = 0.146 m. The tensile strain which leads to bottom-up cracking is the maximum between the tensile strain in the transversal direction ε_{xx} and in the traffic direction ε_{yy}. In both cases, the maximum of ε_{xx} and ε_{yy} corresponds to the time T = 0.057021 s, i.e. when the wheel is exactly on the investigated cross-section area. Figure 7.33a,b,c show the trend of the ε_{xx} for thin, intermediate and thick pavements, respectively. Analogously, Figure 7.33d,e,f show the trend of the ε_{yy} for thin, intermediate and thick pavements, respectively. The trends in the pavement with ABC, CRM1 and CRM2 for the two stages are reported.

Figure 7.34a,b show an example of spatial distribution of ε_{xx} and ε_{yy} in thin pavement, respectively. The evaluation point for the critical ε_{xx} and ε_{yy}, i.e. at the bottom of the AC layer, is indicated.

Furthermore, Figure 7.34c,d,e show the critical ε_{xx} and ε_{yy}, for thin, intermediate and thick pavements, respectively. First, it can be noted that when CRMs are modeled as viscoelastic material (stage 1), ε_{xx} values are negative, meaning that the AC course results all in compression (as also visible in Figure 7.33a,b,c). Moreover, the tensile strain when CRMs are modeled as linear elastic material are very limited, too. This outcome confirms that the viscoelastic properties and bearing capacity offered by CRMs preserve the AC from fatigue damage. Then, it can be seen that in general ε_{yy} is higher than ε_{xx}, meaning the tensile strains are higher in the traffic direction than in the transverse direction. Finally, it can be seen that horizontal tensile strain values are lower in presence of CRM with respect to ABC, especially if stage 1 (CRM modeled as viscoelastic material) is considered. The difference is higher as the AC course's thickness decreases. Indeed, the bottom-up cracking is always lower if the ABC is replaced with CRMs.

Transversal direction ε_{xx}

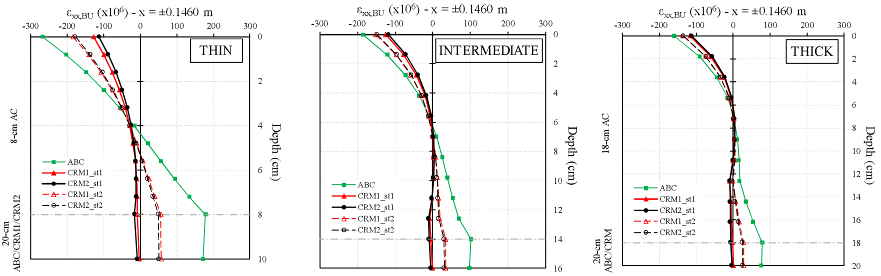

(a) (b) (c)

Traffic direction ε_{yy}

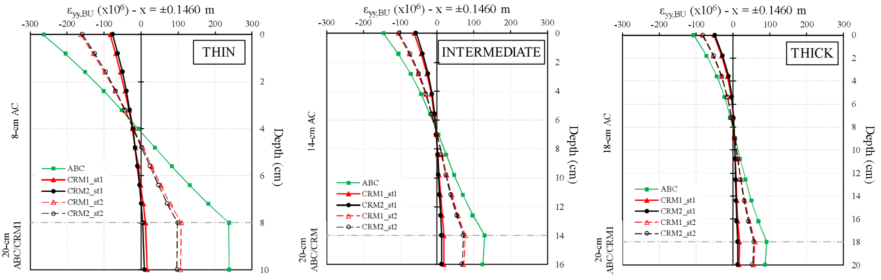

(d) (e) (f)

Figure 7.33. CRMs as replacement of aggregate base course: trends of (a,b,c) ε_{xx} and (d,e,f) ε_{yy} for thin, intermediate and thick pavements, respectively (positive values = tension; negative values = compression).

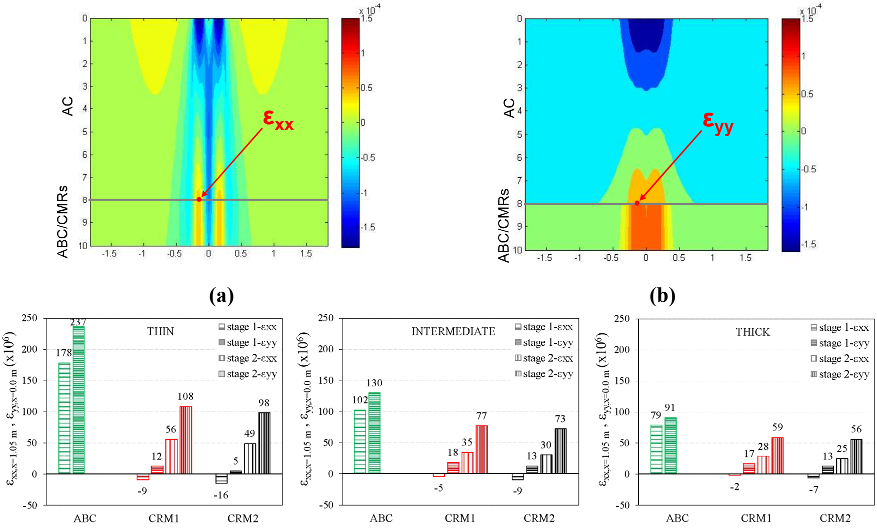

(a) (b)

(c) (d) (e)

Figure 7.34. CRMs as replacement of aggregate base course: evaluation point for the critical (a) ε_{xx} and (b) ε_{yy} values at the bottom of AC course, and critical ε_{xx} and ε_{yy} values in (c) thin, (d) intermediate and (e) thick pavements (positive values = tension; negative values = compression).

Top-down cracking

The tensile strains which lead to top-down cracking on the surface are evaluated in two points with different *x*-coordinate. In the transversal direction *x*, the maximum ε_{xx} value occurs at a distance of x= 1.0585 m (Canestrari & Ingrassia, 2020), and a variable T in the range 0.017-0.053 s. In the traffic direction *y*, the maximum ε_{yy} value occurs at the center of the dual tire wheel (x = 0.0 m), and a variable T in the range 0.017-0.027 s.

Figure 7.35a,b,c show the trend of the ε_{xx} for thin, intermediate and thick pavements, respectively. Analogously, Figure 7.35d,e,f show the trend of the ε_{yy} for thin, intermediate and thick pavements, respectively. The trends in the pavement with ABC, CRM1 and CRM2 for the two stages are reported.

Figure 7.36a,b show an example of spatial distribution of ε_{xx} and ε_{yy} in thin pavement, respectively. The evaluation point for the critical ε_{xx} and ε_{yy}, i.e. on the surface, is indicated. Furthermore, Figure 7.36c,d,e show the critical ε_{xx} and ε_{yy}, for thin, intermediate and thick pavements, respectively. First, it can be noted that ε_{xx} at x = 1.0585 m is always higher than ε_{yy} at x = 0.0 m for the pavements with CRMs, whereas ε_{xx} is lower than ε_{yy} for the pavement with ABC. The performance of the pavements with CRMs modelled as viscoelastic material (stage 1) is broadly comparable to that one where CRMs is considered as linear elastic material (stage 2); only a slightly lower ε_{yy} was observed in stage 2.

Considering the strain in the transversal direction ε_{xx} at x = 1.0585 m, ABC ensures lower top-down cracking. Conversely, considering the strain in the traffic direction ε_{yy} at x = 0.0 m, CRMs ensure lower top-down cracking.

However, the damage contours due to fatigue given by FlexPAVE^{TM} only included the damage right under the wheel (Figure 7.26, Figure 7.28, Figure 7.30), associated to ε_{yy}. The damage associated to ε_{xx} at x = 1.0584 m is not taken into account because this area is excluded from the evaluated area. In fact, the evaluated area is composed by two overlapping triangles (Figure 2.37), whose base on the top has dimension of 1.70 m, i.e., 0.85 m from the center of the wheel (lower than 1.0584 m).

Transversal direction ε_{xx}

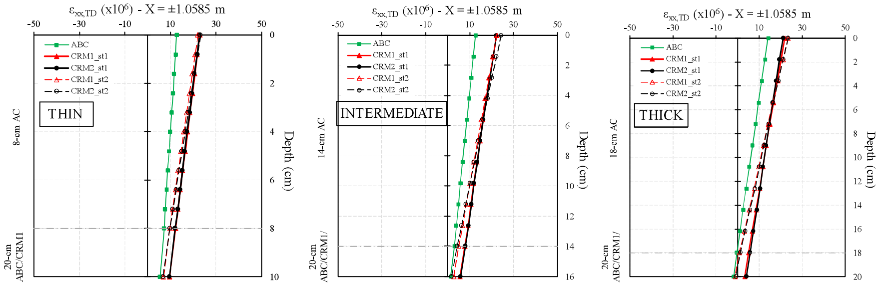

(a) (b) (c)

Traffic direction ε_{yy}

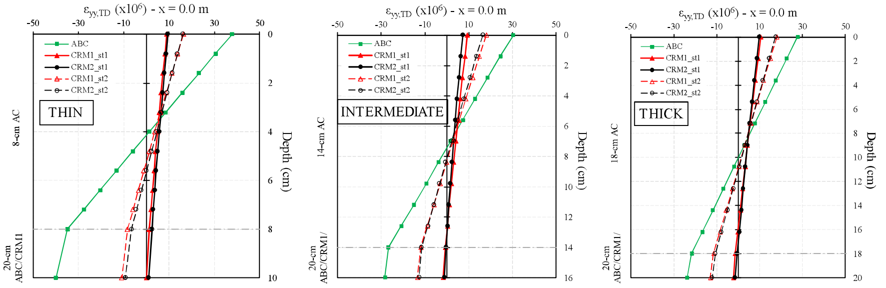

(d) (e) (f)

Figure 7.35. CRMs as replacement of aggregate base course: trends of (a,b,c) ε_{xx} and (d,e,f) ε_{yy} for thin, intermediate and thick pavements, respectively (positive values = tension; negative values = compression).

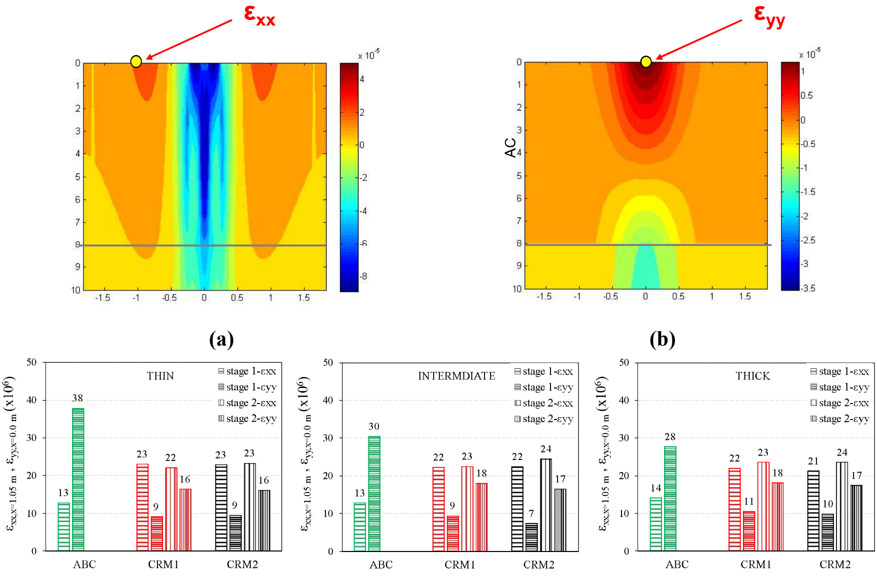

(a)

(b)

(c)

(d)

(e)

Figure 7.36. CRMs as replacement of aggregate base course: evaluation point for the critical (a) ε_{xx} and (b) ε_{yy} values on the surface, and critical ε_{xx} and ε_{yy} values in (c) thin, (d) intermediate and (e) thick pavements.

7.4.4 Use of CRMs as replacement of AC_base course in thick pavement

The level of damage of the pavement using CRMs as replacement of AC course was investigated for thick pavements (Figure 7.20). Specifically, only the lower 10-cm thick AC base course was replaced with CRM, as shown in Figure 7.37. The aim is to determine what is the equivalent thickness of the CRM course in order to obtain the same pavement performance as with the reference 10-cm AC base course.
The fatigue damage, without the thermal effects, was evaluated.
The CRM thickness course was set equal to 12.5 cm and 15 cm, i.e., plus 25% and 50% of the reference 10-cm thick AC course.

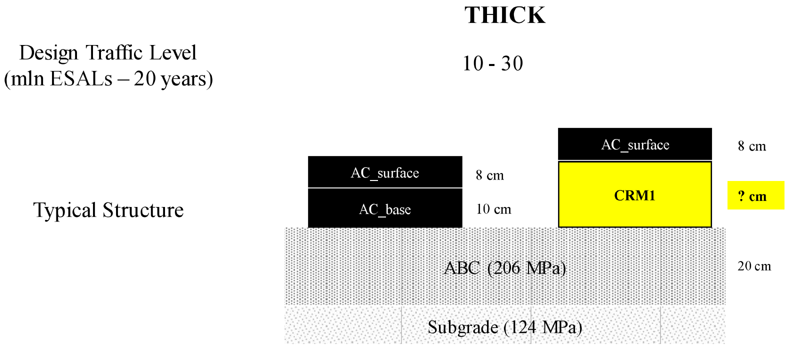

Figure 7.37. Pavement performance simulations, CRMs as replacement of AC_base course: structures of the thick pavement and design life for the study of CRM as replacement of AC course.

Thickness of 12.5 cm of the CRM course
Figure 7.38a,b show the damage contours at *N1* (stage 1) for pavements with CRM1(Figure 7.38a) and CRM2 (Figure 7.38b). The damage due to bottom-up cracking involves almost all the thickness course of CRM1 (i.e., 12.5 cm), and about 11 cm of CRM2.
Figure 7.38c reports the months of service of stage 1. In both the CRMs courses, the bottom-up crack starts very early, after about half a year. CRM2 seems to provide slightly higher performance, likely due to its higher stiffness which ensures a better stress distribution.
Figure 7.38d-e show the damage contours of the upper 8-cm thick AC surface course with the AC-base replaced with CRMs (Figure 7.37) after 30 years of service (for CRMs, stage 1 + stage2) only due to fatigue damage. Figure 7.38f shows the damage contour of the conventional AC course, i.e., total AC-surface plus AC-base (Figure 7.37), in the same conditions. It can be noted that the bottom-up cracking involves broadly the same area in presence of CRMs, as well as the low damage due to top-down cracking. Bottom-up cracking causes the onset of the crack at the bottom of the AC course. Conversely, in the reference pavement with only AC, bottom-up cracking involves the lowest 6 cm, and the AC-surface presents a very low amount of damage due to top-down cracking.

Stage 1 of CRMs

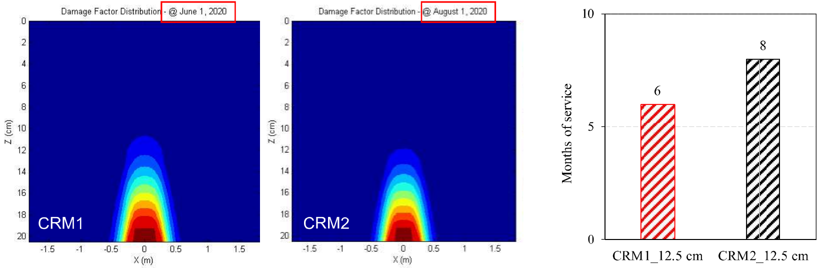

(a) **(b)** **(c)**

After 30 years

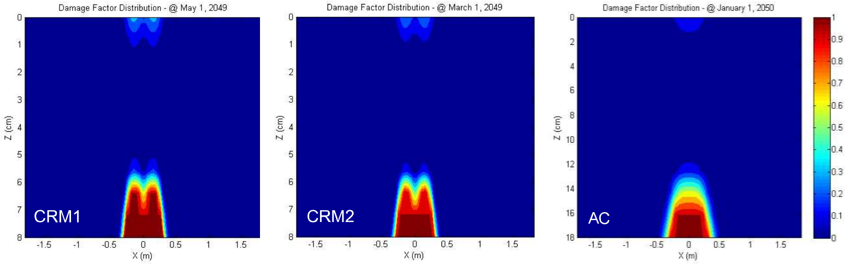

(d) **(e)** **(f)**

Figure 7.38. CRMs as replacement of AC_base course, 12.5-cm thick CRM course: (a-b) damage contours at *NI* (stage 1) and (c) corresponding years of service, (d-f) damage contours after 30 years of service.

Thickness of 15 cm of the CRM course

Figure 7.39a,b show the damage contours at *N1* (stage 1) for pavements with CRM1(Figure 7.39a) and CRM2 (Figure 7.39b). The damage due to bottom-up cracking involves about 10 cm of CRM1, and about 8 cm of CRM2. These values are slightly lower than in the previous scenario with the CRM thickness course of 12.5 cm, as expected.

Figure 7.39c reports the months of service of stage 1. Even in this case, in both the CRMs courses, the bottom-up crack starts very early, after no more than one year. CRM2 seems to provide slightly higher performance, likely due to its higher stiffness.

Figure 7.39d-e show the damage contours of the upper 8-cm thick AC surface course with the AC-base replaced with CRMs (Figure 7.37) after 30 years of service (for CRMs, stage 1 + stage2) only due to fatigue damage. Figure 7.39f shows the damage contour of the conventional AC course, i.e., total AC-surface plus AC-base (Figure 7.37), in the same conditions, and it is the same of Figure 7.38f. It can be noted that the bottom-up cracking involves broadly the same area in presence of CRMs, as well as the low damage due to top-down cracking. Bottom-up cracking causes the onset of the crack at the bottom of the AC course. The thicknesses of both the damage are slightly lower than the ones with 12.5-cm thick CRMs course.

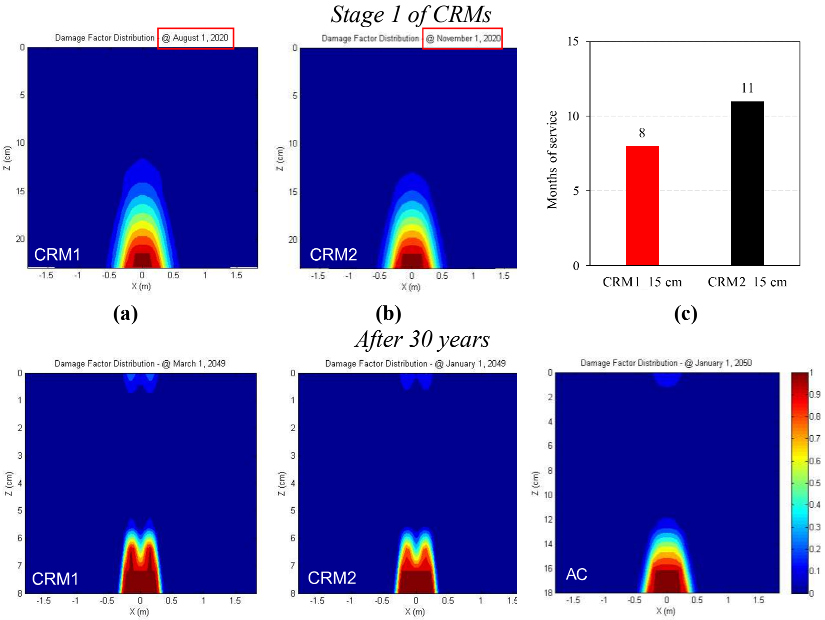

(a) (b) (c)

(d) (e) (f)

Figure 7.39. Pavement performance simulations, CRMs as replacement of AC_base course, 15-cm thick CRM course: (a-b) damage contours at *NI* (stage 1) and (c) corresponding years of service, (d-f) damage contours after 30 years of service.

Finally, to compare the results, Figure 7.40a,b show the *%damage* and *%cracking* evolutions, respectively, of the pavements with CRMs with different thickness and the reference one with only AC. Comparing the results between the CRMs with the same thickness course, it is confirmed that CRM2 shows slightly higher fatigue performance than CRM1 for both the thicknesses investigated. As expected, the pavement performance increases as the CRM thickness course increases.

Finally, comparing the performance of the pavements with CRMs and only AC, it can be concluded that a 15-cm thick CRM1 course can be used as replacement of AC_base, whereas a 12.5 -cm thick CRM2 course can be used as replacement of AC_base.

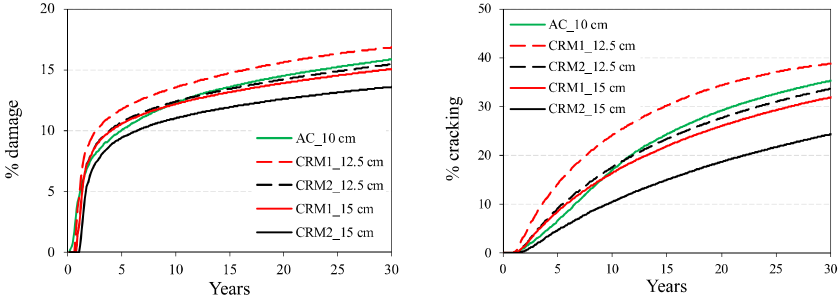

(a) **(b)**

Figure 7.40. Pavement performance simulations, CRMs as replacement of AC_base course: (a) *%damage* and (b) *%cracking* evolutions.

7.5 Summary of the findings

The objective of this research was to check the applicability of the S-VECD approach to CRMs, since this approach has been developed for only asphalt concrete. CRMs are sustainable materials, made of RAP with addition of filler (maximum 20%), cement and bitumen emulsion. Cement ensures high stiffness and low thermal-susceptibility, whereas bitumen gives a viscoelastic behavior. Up to date, the design of pavement including CRMs is empirical, thus the S-VECD model could provide a mechanical-based design.

To this aim, two CRM mixtures characterized by different dosages of Portland cement (1% and 2%) were produced in the laboratory. The typical tests provided by the S-VECD approach were conducted, with the addition of strain sweep tests to understand the proper deformation level to be set as input for the cyclic fatigue tests. The conventional failure criterion adopted for AC (i.e., stress degradation ratio) does not work for CRMs, since the stress evolution during the fatigue test highlighted that the test was almost in pure stress control mode for the CRM mixtures whereas it was in mixed mode for the AC mixtures. Thus, empirical and energy-based failure criteria typically adopted for AC mixtures were applied to analyze the results. It was found out that at the beginning of the fatigue test, the CRM specimens showed a cement-dominated damage behavior, followed by the breaking of the cementitious bonds, which led to the transition towards a bitumen-dominated damage behavior. Afterwards, further damage of the bituminous bonds led to the specimen collapse. The inflection point of the DER curve was proposed to identify the failure of the cementitious bonds whereas, analogously to typical AC mixtures, the subsequent failure of the bituminous bonds was identified through the maximum phase angle value. Based on both criteria, a longer fatigue service life was observed for CRM specimens with lower cement content.

Since the maximum of the phase angle usually occurs after the inflection of the *DER* value in terms of number of cycles, the S-VECD characterization was carried out considering as failure of the specimen the maximum of the phase angle. From the comparison of the results obtained in terms of damage characteristics curve and D^R failure criterion, it was highlighted

CRM1 is characterized by higher toughness, however CRM1 is characterized by higher stiffness. Thus, FlexPAVETM performance simulations were conducted, considering the typical pavement structure (i.e., thin, intermediate and thick pavements). An innovative 2-stages procedure was adopted, in which the CRM course is modeled as viscoelastic until the onset of the crack. After that, CRM is modeled as a linear elastic material, with its stiffness modulus at failure.

Using CRM as replacement of the ABC; it was obtained that the performance of the CRM course increases as the thickness of the AC course above it increases. The fatigue performance of CRM2 is slightly higher than CRM1, in accordance with the damage characteristic curves. Considering the CRMs as replacement of ABC after failure, pavement with CRMs shows better performance than pavement with conventional ABC thanks to the high stiffness due to the presence of cement and 100% RAP. Moreover, CRMs provide lower vertical strain than ABC, protecting the subbase from the onset of permanent deformations, as well as lower tensile strain at the bottom of the AC course than ABC, especially if their viscoelastic properties are considered.

Finally, even the possibility to use CRMs as replacement of the lower AC course in thick pavements was investigated. Analyzing the evolution of the *%damage*, it was concluded that 15-cm thick CRM1 course or 12-cm thick CRM2 course can be used as replacement of 10-cm AC course.

8. Conclusions

In recent decades, the increased demand for heavy transport in Europe has highlighted the crucial role of road infrastructure, especially motorways and expressways, in providing adequate service and safety to users. Fatigue cracking, resulting from cyclic load application and temperature variations, is the most common distress affecting pavement durability. Current research focuses on improving material properties and developing reliable pavement design tools to consider such improved properties. New materials aim to enhance resistance to fatigue, rutting, and thermal cracking, while also promoting sustainability and circular economy principles. However, conventional pavement design methods in Europe often fail to account for these improved material properties. A promising solution is the adoption of Asphalt Mixture Performance-Related Specifications (AM-PRS), which utilize mechanistic-based approaches for fatigue and rutting characterization. This thesis evaluated the reliability of AM-PRS for both conventional and innovative asphalt mixtures used in Italian and Polish motorways, as well as their applicability to Cold Recycled Mixtures.

The thesis included a comprehensive analysis of various aspects related to the S-VECD characterization of asphalt mixtures. Many in-plant produced asphalt mixtures were investigated, in both the conditions of laboratory and in field compaction (i.e., cores from field trials). In comparison with the reference SBS modified asphalt mixture currently employed in Italian motorway pavements for binder and base courses, the following mixtures were studied: asphalt mixtures containing polymeric compounds added with the dry method, three typical Polish asphalt mixtures with neat or SBS modified bitumen, warm mix asphalt containing 30% of RAP extracted after six years of service and warm mix asphalt with up to 45% of RAP produced with chemical additive. Furthermore, three mixtures for wearing course were included: an open-graded hot mix asphalt with 15% of RAP (typically used in 80% of Italian motorways), an open-graded warm mix asphalt with 25% of RAP and an SMA mixture. Finally, the applicability of the S-VECD approach to characterize the fatigue behavior of Cold Recycled Materials was evaluated.

The main conclusion is that the obtained intrinsic viscoelastic and fatigue properties of the mixtures were consistent with their composition, demonstrating the reliability and applicability of the approach developed in U.S. even for conventional Europeans mixtures and innovative ones. Moreover, the method requires few laboratory tests in comparison with the traditional ones to characterize the fatigue and rutting behavior of a mixture. The analysis, too, is user-friendly, since ad-hoc Excel spreadsheets are given. However, there are particular mixtures for which further studies on the meaning of parameters are needed, e.g. the D^R failure criterion parameter for OG (low stiffness identified as rubbery behavior) and the reliability of the SSR results for SMA. FlexPAVE™ simulations allow a reliable prediction of the materials' performance in the pavement under various loading and climatic conditions, and an optimization of the course thickness with respect to conventional methods. It can be concluded that the VECD approach could represent a valid mechanical-based design method even for CRMs. However, some adjustments are needed. As an example, in order to actually take into account the particular failure mechanism of CRMs, a 2-stages procedure was proposed to predict the failure performance with FlexPAVE™ software.

Overall, this work contributes to advancing pavement design practices and lays the basis for future research in this field in Europe. Once the reliability of the method will be totally assessed for our mixtures studying a huge amount of different materials and comparing the results with the behavior in the field, such approach can be adopted by road agencies laboratories in order to optimize in few days the design of a mixture.

References

Abed, A., Thom, N., & Grenfell, J. (2019). A novel approach for rational determination of warm mix asphalt production temperatures. *Construction and Building Materials*, *200*. https://doi.org/10.1016/j.conbuildmat.2018.12.082

Ahmad Nazki, M., Chopra, T., & Chandrappa, A. K. (2020). Rheological properties and thermal conductivity of bitumen binders modified with graphene. *Construction and Building Materials*, *238*. https://doi.org/10.1016/j.conbuildmat.2019.117693

Airey, G. D. (2003). Rheological properties of styrene butadiene styrene polymer modified road bitumens. *Fuel*, *82*(14). https://doi.org/10.1016/S0016-2361(03)00146-7

Airey, G. D. (2004). Styrene butadiene styrene polymer modification of road bitumens. *Journal of Materials Science*, *39*(3). https://doi.org/10.1023/B:JMSC.0000012927.00747.83

Almeida-Costa, A., & Benta, A. (2016). Economic and environmental impact study of warm mix asphalt compared to hot mix asphalt. *Journal of Cleaner Production*, *112*. https://doi.org/10.1016/j.jclepro.2015.10.077

Almusawi, A., Sengoz, B., Ozdemir, D. K., & Topal, A. (2022). Economic and environmental impacts of utilizing lower production temperatures for different bitumen samples in a batch plant. *Case Studies in Construction Materials*, *16*. https://doi.org/10.1016/j.cscm.2022.e00987

Angelone, S., Cauhapé Casaux, M., Borghi, M., & Martinez, F. O. (2016). Green pavements: reuse of plastic waste in asphalt mixtures. *Materials and Structures/Materiaux et Constructions*, *49*(5). https://doi.org/10.1617/s11527-015-0602-x

Antunes, V., Freire, A. C., & Neves, J. (2019). A review on the effect of RAP recycling on bituminous mixtures properties and the viability of multi-recycling. In *Construction and Building Materials* (Vol. 211). https://doi.org/10.1016/j.conbuildmat.2019.03.258

Awoyera, P. O., & Adesina, A. (2020). Plastic wastes to construction products: Status, limitations and future perspective. *Case Studies in Construction Materials*, *12*. https://doi.org/10.1016/j.cscm.2020.e00330

Batioja-Alvarez, D., Myung, J., Tian, Y., Lee, J., & Haddock, J. E. (2020). A comparative study of SMA and dense graded HMA mixtures using a laboratory rutting test and accelerated pavement testing. *Advances in Materials and Pavement Performance Prediction II - Contributions to the 2nd International Conference on Advances in Materials and Pavement Performance Prediction, AM3P 2020*. https://doi.org/10.1201/9781003027362-59

Behnood, A. (2020). A review of the warm mix asphalt (WMA) technologies: Effects on thermo-mechanical and rheological properties. In *Journal of Cleaner Production* (Vol. 259). https://doi.org/10.1016/j.jclepro.2020.120817

Behnood, A., & Modiri Gharehveran, M. (2019). Morphology, rheology, and physical properties of polymer-modified asphalt binders. In *European Polymer Journal* (Vol. 112). https://doi.org/10.1016/j.eurpolymj.2018.10.049

Belc, A. L., Ciutina, A., Buzatu, R., Belc, F., & Costescu, C. (2021). Environmental impact assessment of different warm mix asphalts. *Sustainability (Switzerland)*, *13*(21). https://doi.org/10.3390/su132111869

Bhasin, A., Castelo Branco, V. T., Masad, E., & Little, D. N. (2009). Quantitative Comparison of Energy Methods to Characterize Fatigue in Asphalt Materials. *Journal of Materials in Civil Engineering*, *21*(2). https://doi.org/10.1061/(asce)0899-1561(2009)21:2(83)

Błazejowski, K. (2016). Stone matrix asphalt: Theory and practice. In *Stone Matrix Asphalt: Theory and Practice*.

Błażejowski, K., Ostrowski, P., Wójcik-Wiśniewska, M., & Baranowska, W. (2020). *Mieszanki i nawierzchnie z ORBITON HiMA*.

Bocci, M., Grilli, A., Cardone, F., & Graziani, A. (2011). A study on the mechanical behaviour of cement-bitumen treated materials. *Construction and Building Materials*, *25*(2). https://doi.org/10.1016/j.conbuildmat.2010.07.007

Brown, S. F. (1973). Determination of Young's modulus for bituminous materials in pavement design. *Highway Research Records*, *431*.

Buczyński, P., & Iwański, M. (2017). Fatigue Life Comparison of Recycled Cold Mixes with Foamed Bitumen and with Bitumen Emulsion. *Procedia Engineering*, *172*. https://doi.org/10.1016/j.proeng.2017.02.035

Canestrari, F., & Ingrassia, L. P. (2020). A review of top-down cracking in asphalt pavements: Causes, models, experimental tools and future challenges. In *Journal of Traffic and Transportation Engineering (English Edition)* (Vol. 7, Issue 5). https://doi.org/10.1016/j.jtte.2020.08.002

Capitão, S. D., Picado-Santos, L. G., & Martinho, F. (2012). Pavement engineering materials: Review on the use of warm-mix asphalt. In *Construction and Building Materials* (Vol. 36). https://doi.org/10.1016/j.conbuildmat.2012.06.038

Capitão, S., Picado-Santos, L., Almeida, A., & Mendes, F. (2023). Assessment of aged and unaged hot and warm asphalt concrete containing high reclaimed asphalt pavement rate rejuvenated with waste cooking oil. *Construction and Building Materials*, *400*. https://doi.org/10.1016/j.conbuildmat.2023.132801

Cardone, F., Grilli, A., Bocci, M., & Graziani, A. (2015). Curing and temperature sensitivity of cement-bitumen treated materials. *International Journal of Pavement Engineering*, *16*(10). https://doi.org/10.1080/10298436.2014.966710

Cardone, F., Spadoni, S., Ferrotti, G., & Canestrari, F. (2022). Asphalt mixture modification with a plastomeric compound containing recycled plastic: laboratory and field investigation. *Materials and Structures/Materiaux et Constructions*, *55*(3). https://doi.org/10.1617/s11527-022-01954-4

Castorena, C., Kim, Y. R., Pape, S., & Lee, K. (2017). *Development of Small Specimen Geometry for Asphalt Mixture Performance Testing IDEA Program Final Report NCHRP IDEA Project N-181*.

Chavez, F., Marcobal, J., & Gallego, J. (2019). Laboratory evaluation of the mechanical properties of asphalt mixtures with rubber incorporated by the wet, dry, and semi-wet process. *Construction and Building Materials*, *205*. https://doi.org/10.1016/j.conbuildmat.2019.01.159

Chehab, G. R., Kim, Y. R., Schapery, R. A., Witczak, M. W., & Bonaquist, R. (2002). Time-temperature superposition principle for asphalt concrete with growing damage in tension state. *Asphalt Paving Technology: Association of Asphalt Paving Technologists-Proceedings of the Technical Sessions*, *71*.

Chehab, G. R., Kim, Y. R., Schapery, R. A., Witczak, M. W., & Bonquist, R. (2003). Characterization of asphalt concrete in uniaxial tension using a viscoelastoplastic continuum damage model. *Asphalt Paving Technology: Association of Asphalt Paving Technologists-Proceedings of the Technical Sessions*, *72*.

Cheraghian, G., Cannone Falchetto, A., You, Z., Chen, S., Kim, Y. S., Westerhoff, J., Moon, K. H., & Wistuba, M. P. (2020). Warm mix asphalt technology: An up to date review. In *Journal of Cleaner Production* (Vol. 268). https://doi.org/10.1016/j.jclepro.2020.122128

Choi, Y. T., & Kim, Y. R. (2014). Implementation and verification of a mechanistic permanent deformation model (Shift model) to predict rut depths of asphalt pavement. *Asphalt Paving Technology: Association of Asphalt Paving Technologists-Proceedings of the Technical Sessions*, *83*(January). https://doi.org/10.1080/14680629.2014.927085

Christensen, D. W., & Anderson, D. A. (1992). Interpretation of dynamic mechanical test data for paving grade asphalt. *Asphalt Paving Technology: Association of Asphalt Paving Technologists-Proceedings of the Technical Sessions*, *61*.

Cross, S., Chesner, W., Justus, H., & Kearney, E. (2011). Life-cycle environmental analysis for evaluation of pavement rehabilitation options. *Transportation Research Record*, *2227*. https://doi.org/10.3141/2227-05

D'Angelo, S., Ferrotti, G., Cardone, F., & Canestrari, F. (2022). Asphalt Binder Modification with Plastomeric Compounds Containing Recycled Plastics and Graphene. *Materials*, *15*(2). https://doi.org/10.3390/ma15020516

Daniel, J. S., Kim, Y. R., Brown, S., Rowe, G., Chehab, G., & Reinke, G. (2002). Development of a simplified fatigue test and analysis procedure using a viscoelastic, continuum damage model. *Asphalt Paving Technology: Association of Asphalt Paving Technologists-Proceedings of the Technical Sessions*, *71*.

Dolzycki, B., Jaczewski, M., & Szydlowski, C. (2017). The long-term properties of mineral-cement-emulsion mixtures. *Construction and Building Materials*, *156*. https://doi.org/10.1016/j.conbuildmat.2017.09.032

Dołżycki, B., & Jaskuła, P. (2019). Review and evaluation of cold recycling with bitumen emulsion and cement for rehabilitation of old pavements. In *Journal of Traffic and Transportation Engineering (English Edition)* (Vol. 6, Issue 4). https://doi.org/10.1016/j.jtte.2019.02.002

Dolzycki, B., Szydlowski, C., & Jaczewski, M. (2020). The influence of combination of binding agents on fatigue properties of deep cold in-place recycled mixtures in Indirect Tensile Fatigue Test (ITFT). *Construction and Building Materials*, *239*. https://doi.org/10.1016/j.conbuildmat.2019.117825

Eslaminia, M., & Guddati, M. N. (2016). Fourier-finite element analysis of pavements under moving vehicular loading. *International Journal of Pavement Engineering*, *17*(7), 602–614. https://doi.org/10.1080/10298436.2015.1007237

Fedrigo, W., Núñez, W. P., Schreinert, G. G., Kleinert, T. R., Matuella, M. F., Castañeda López, M. A., & Ceratti, J. A. P. (2021). Flexural strength, stiffness and fatigue of cement-treated mixtures of reclaimed asphalt pavement and lateritic soil. *Road Materials and Pavement Design*, *22*(5). https://doi.org/10.1080/14680629.2019.1660207

Fedrigo, W., Núñez, W. P., & Visser, A. T. (2020). A review of full-depth reclamation of pavements with Portland cement: Brazil and abroad. In *Construction and Building Materials* (Vol. 262). https://doi.org/10.1016/j.conbuildmat.2020.120540

Ferrotti, G., Ragni, D., Lu, X., & Canestrari, F. (2017). Effect of warm mix asphalt chemical additives on the mechanical performance of asphalt binders. *Materials and Structures/Materiaux et Constructions*, *50*(5). https://doi.org/10.1617/s11527-017-1096-5

FHWA. (2019). *FHWA-HIF-19-091: TechBrief: Cyclic Fatigue Index Parameter (Sapp) for Asphalt Performance Engineered Mixture Design*.

FHWA. (2021). *FHWA-HRT-21-044: TechBrief: Rutting Strain Index (RSI) Parameter for Asphalt Performance Engineered Mixture Design*. https://highways.dot.gov/research

Frigio, F., Stimilli, A., Virgili, A., & Canestrari, F. (2017). Performance assessment of plant-produced warm recycled mixtures for open-graded wearing courses. *Transportation Research Record*, *2633*. https://doi.org/10.3141/2633-04

Gajewski, M., Bańkowski, W., & Pronk, A. C. (2020). Evaluation of fatigue life of high modulus asphalt concrete with use of three different definitions. *International Journal of Pavement Engineering*, *21*(14). https://doi.org/10.1080/10298436.2018.1564302

Gaudenzi, E., Ingrassia, L. P., Cardone, F., Lu, X., & Canestrari, F. (2023). Investigation of unaged and long-term aged bio-based asphalt mixtures containing lignin according to the VECD theory. *Materials and Structures/Materiaux et Constructions*, *56*(4). https://doi.org/10.1617/s11527-023-02160-6

Ghanbari, A., Underwood, B. S., & Kim, Y. R. (2022). Development of a rutting index parameter based on the stress sweep rutting test and permanent deformation shift model. *International Journal of Pavement Engineering*, *23*(2). https://doi.org/10.1080/10298436.2020.1748190

Giani, M. I., Dotelli, G., Brandini, N., & Zampori, L. (2015). Comparative life cycle assessment of asphalt pavements using reclaimed asphalt, warm mix technology and cold in-place recycling. *Resources, Conservation and Recycling*, *104*. https://doi.org/10.1016/j.resconrec.2015.08.006

Giuliani, F. (2006). Come individuare l'intervallo delle "temperature di progetto" del bitume secondo la metodologia SHRP. *Quarry & Construction*, 1–12.

Godenzoni, C., Graziani, A., Bocci, E., & Bocci, M. (2018). The evolution of the mechanical behaviour of cold recycled mixtures stabilised with cement and bitumen: field and laboratory study. *Road Materials and Pavement Design*, *19*(4). https://doi.org/10.1080/14680629.2017.1279073

Graziani, A., Grilli, V., Virgili, A., & Jaczewsky, M. (2024). A deformation sweep testing procedure to evaluate damage in cold recycled material mixtures. *14th International Society for Asphalt Pavements (ISAP)*.

Graziani, A., Raschia, S., Mignini, C., Carter, A., & Perraton, D. (2020). Use of fine aggregate matrix to analyze the rheological behavior of cold recycled materials.

Materials and Structures/Materiaux et Constructions, *53*(4). https://doi.org/10.1617/s11527-020-01515-7

Graziani, A., Spadoni, S., Ingrassia, L. P., Virgili, A., & Canestrari, F. (2024). Composite fatigue failure of cold recycled material mixtures: new insights into the role of bitumen and cement. *Materials and Structures*, *57*(1). https://doi.org/10.1617/s11527-023-02285-8

Grilli, V., Grilli, A., Graziani, A., & Jaczewsky, M. (2024). Effect of strain level on the stiffness of cold recycled bituminous mixtures. *8th International Conference Bituminous Mixtures and Pavements*.

Guo, M., Liu, H., Jiao, Y., Mo, L., Tan, Y., Wang, D., & Liang, M. (2020). Effect of WMA-RAP technology on pavement performance of asphalt mixture: A state-of-the-art review. In *Journal of Cleaner Production* (Vol. 266). https://doi.org/10.1016/j.jclepro.2020.121704

Habbouche, J., Boz, I., Diefenderfer, B. K., & Kim, S. (2022). Multi-Level Laboratory Performance Evaluation of Conventional and High Polymer-Modified Asphalt Mixtures. In *Transportation Research Record* (Vol. 2676, Issue 5). https://doi.org/10.1177/03611981211056642

Hettiarachchi, C., Hou, X., Wang, J., & Xiao, F. (2019). A comprehensive review on the utilization of reclaimed asphalt material with warm mix asphalt technology. In *Construction and Building Materials* (Vol. 227). https://doi.org/10.1016/j.conbuildmat.2019.117096

Hou, T., Underwood, B. S., & Kim, Y. R. (2010). Fatigue performance prediction of North Carolina mixtures using the simplified viscoelastic continuum damage model. *Asphalt Paving Technology: Association of Asphalt Paving Technologists-Proceedings of the Technical Sessions*, *79*.

Huet, C. (1963). Etude par une méthode d'impédance du comportement viscoélastique des matériaux hydrocarbonés. *Thèse de Doctorat d'ingénieur, Faculté Des Sciences de l'université de Paris*.

Ingrassia, L. P., Cardone, F., Ferrotti, G., & Canestrari, F. (2021). Monitoring the evolution of the structural properties of warm recycled pavements with Falling Weight Deflectometer and laboratory tests. *Road Materials and Pavement Design*, *22*(S1). https://doi.org/10.1080/14680629.2021.1906302

Ingrassia, L. P., Lu, X., Canestrari, F., & Ferrotti, G. (2018). Tribological characterization of bituminous binders with Warm Mix Asphalt additives. *Construction and Building Materials*, *172*. https://doi.org/10.1016/j.conbuildmat.2018.03.275

Ingrassia, L. P., Spadoni, S., Ferrotti, G., Virgili, A., & Canestrari, F. (2023). Prediction of the Long-Term Performance of an Existing Warm Recycled Motorway Pavement. *Materials*, *16*(3). https://doi.org/10.3390/ma16031005

Jaczewski, M., Szydlowski, C., & Dolzycki, B. (2022). Preliminary study of linear viscoelasticity limits of cold recycled mixtures determined in Simple Performance Tester (SPT). *Construction and Building Materials*, *357*. https://doi.org/10.1016/j.conbuildmat.2022.129432

Jaczewski, M., Szydłowski, C., & Dołżycki, B. (2023). Stiffness of cold-recycled mixtures under variable deformation conditions in the IT-CY test. *Case Studies in Construction Materials*, *18*. https://doi.org/10.1016/j.cscm.2023.e02066

Jattak, Z. A., Hassan, N. A., & Mohd Satar, M. K. I. (2021). Moisture susceptibility and environmental impact of warm mix asphalt containing bottom ash. *Case Studies in Construction Materials*, *15*. https://doi.org/10.1016/j.cscm.2021.e00636

Judycki, J., Jaskula, P., Pszczoła, M., Ryś, D., Jaczewski, M., Alenowicz, J., & Dolzycki, B. (2014). *Analizy i projektowanie konstrukcji nawierzchni podatnych i półsztywnych // Analysis and design of flexible and semi-rigid pavement structures*. https://www.researchgate.net/publication/262733126

Judycki, J., Jaskuła, P., Pszczoła, M., Ryś, D., Jaczewski, M., Alenowicz, J., Dołzycki, B., & Stienss, M. (2017). New polish catalogue of typical flexible and semi-rigid pavements. *MATEC Web of Conferences*, *122*. https://doi.org/10.1051/matecconf/201712204002

Kataware, A. V., & Singh, D. (2020). Effect of short-term ageing on high-temperature performance of SBS modified binder containing warm mix asphalt additives. *Road Materials and Pavement Design*, *21*(3). https://doi.org/10.1080/14680629.2018.1509804

Keymanesh, M. R., Amani, S., Omran, A. T., & Karimi, M. M. (2023). Evaluation of the impact of long-term aging on fracture properties of warm mix asphalt (WMA) with high RAP contents. *Construction and Building Materials*, *400*. https://doi.org/10.1016/j.conbuildmat.2023.132671

Kim, D., & Kim, Y. R. (2017). Development of Stress Sweep Rutting (SSR) test for permanent deformation characterization of asphalt mixture. *Construction and Building Materials*, *154*. https://doi.org/10.1016/j.conbuildmat.2017.07.172

Kim, D., Norouzi, A., Kass, S., Liske, T., & Kim, Y. R. (2017). Mechanistic performance evaluation of pavement sections containing RAP and WMA additives in Manitoba. *Construction and Building Materials*, *133*. https://doi.org/10.1016/j.conbuildmat.2016.12.035

Kim, R. Y., Guddati, M. N., Choi, Y.-T., Kim, D., Norouzi, A., Wang, Y. D., Keshavarzi, Ashouri, M., Ghanbari, A., Wargo, A. D., & Underwood, B. S. (2022). *FHWA-HRT-21-093: Hot-Mix Asphalt Performance Related Specification Based on Viscoelastoplastic Continuum Damage (VEPCD) Models*. https://doi.org/10.21949/1521679

Kim, Y. R. (2018). Asphalt mixture performance-related specifications. *Advances in Materials and Pavement Performance Prediction - Proceedings of the International AM3P Conference, 2018*. https://doi.org/10.1201/9780429457791-32

Kim, Y. R., & Little, D. N. (1990). One-Dimensional Constitutive Modeling of Asphalt Concrete. *Journal of Engineering Mechanics*, *116*(4). https://doi.org/10.1061/(asce)0733-9399(1990)116:4(751)

Kluttz, R. Q., Kim, Y. R., & Dongré, R. (2018). Performance modeling of a highly modified asphalt pavement. *Advances in Materials and Pavement Performance Prediction - Proceedings of the International AM3P Conference, 2018*. https://doi.org/10.1201/9780429457791-16

Kuchiishi, A. K., Santos Antão, C. C. dos, Vasconcelos, K., & Bernucci, L. L. B. (2019). Influence of viscoelastic properties of cold recycled asphalt mixtures on pavement response by means of temperature instrumentation. *Road Materials and Pavement Design*, *20*(sup2). https://doi.org/10.1080/14680629.2019.1633781

Kusam, A., Malladi, H., Tayebali, A. A., & Khosla, N. P. (2017). Laboratory Evaluation of Workability and Moisture Susceptibility of Warm-Mix Asphalt Mixtures Containing Recycled Asphalt Pavements. *Journal of Materials in Civil Engineering*, *29*(5). https://doi.org/10.1061/(asce)mt.1943-5533.0001825

Lastra-González, P., Calzada-Pérez, M. A., Castro-Fresno, D., Vega-Zamanillo, Á., & Indacoechea-Vega, I. (2016). Comparative analysis of the performance of asphalt concretes modified by dry way with polymeric waste. *Construction and Building Materials*, *112*. https://doi.org/10.1016/j.conbuildmat.2016.02.156

Lee, K., Pape, S., Castorena, C., & Richard Kim, Y. (2017). Evaluation of small specimen geometries for asphalt mixture performance testing and pavement performance prediction. *Transportation Research Record*, *2631*. https://doi.org/10.3141/2631-09

Li, B., Li, N., Yu, X., Xie, J., Zhan, H., Ding, J., & Ma, H. (2023). Evaluation of the field-aged performance of foamed warm mix asphalt: Comparisons with hot mix asphalt. *Case Studies in Construction Materials*, *18*. https://doi.org/10.1016/j.cscm.2022.e01750

Li, N., Zhan, H., Li, H., Yu, X., Tang, W., Wang, Z., & Zhang, Y. (2024). Investigation of Recycled Asphalt Pavement Materials Treated by Refined Crushing and Screening Process: Comparison with Conventional Methods. *Journal of Materials in Civil Engineering*, *36*(2). https://doi.org/10.1061/jmcee7.mteng-16734

Liebenberg, J. J. E., & Visser, A. T. (2004). Towards a mechanistic structural design procedure for emulsion-treated base layers. In *Journal of the South African Institution of Civil Engineering* (Vol. 46, Issue 3).

Lin, P., Yan, C., Huang, W., Li, Y., Zhou, L., Tang, N., Xiao, F., Zhang, Y., & Lv, Q. (2019). Rheological, chemical and aging characteristics of high content polymer modified asphalt. *Construction and Building Materials*, *207*. https://doi.org/10.1016/j.conbuildmat.2019.02.086

Liu, L., Sun, L., Xu, J., Li, M., Xing, C., & Zhang, Y. (2024). Effect of RAP's preheating temperature on the secondary aging and performance of recycled asphalt mixtures containing high RAP content. *Construction and Building Materials*, *411*, 134719. https://doi.org/10.1016/j.conbuildmat.2023.134719

Lu, D. X., Saleh, M., & Nguyen, N. H. T. (2019). Effect of rejuvenator and mixing methods on behaviour of warm mix asphalt containing high RAP content. *Construction and Building Materials*, *197*. https://doi.org/10.1016/j.conbuildmat.2018.11.205

Marchionna, A., Cesarini, M., Fornaci, M., & Malgarini, M. (1985). Modello di degradazione strutturale delle pavimentazioni. *Autostrade*, *27*, 44–62.

Mignini, C., Cardone, F., & Graziani, A. (2022). Complex modulus of cement-bitumen treated materials produced with different reclaimed asphalt gradations. *Materials and Structures/Materiaux et Constructions*, *55*(7). https://doi.org/10.1617/s11527-022-02009-4

Miner, M. A. (1945). Cumulative Damage in Fatigue. *Journal of Applied Mechanics, Transactions ASME*, *12*(3). https://doi.org/10.1115/1.4009458

Morea, F., Marcozzi, R., & Castaño, G. (2012). Rheological properties of asphalt binders with chemical tensoactive additives used in Warm Mix Asphalts (WMAs). *Construction and Building Materials*, *29*. https://doi.org/10.1016/j.conbuildmat.2011.10.010

Nemati, R., Dave, E. V., Sias, J. E., Thibodeau, E. S., & Worsman, R. K. (2019). Evaluation of Laboratory Performance and Structural Contribution of Cold Recycled Versus Hot Mixed Intermediate and Base Course Asphalt Layers in New Hampshire. *Transportation Research Record*, *2673*(6). https://doi.org/10.1177/0361198119844761

Olard, F., & Di Benedetto, H. (2003). General "2S2P1D" Model and Relation Between the Linear Viscoelastic Behaviours of Bituminous Binders and Mixes. *Road Materials and Pavement Design*, *4*(2). https://doi.org/10.1080/14680629.2003.9689946

Orosa, P., Pérez, I., & Pasandín, A. R. (2022). Evaluation of the shear and permanent deformation properties of cold in-place recycled mixtures with bitumen emulsion using triaxial tests. *Construction and Building Materials*, *328*. https://doi.org/10.1016/j.conbuildmat.2022.127054

Ouis, D. (2003). Effect of structural defects on the strength and damping properties of a solid material. *European Journal of Mechanics, A/Solids*, *22*(1). https://doi.org/10.1016/S0997-7538(02)01256-1

Padula, F. R. G., Nicodemos, S., Mendes, J. C., Willis, R., & Taylor, A. (2019). Evaluation of fatigue performance of high RAP-WMA mixtures. *International Journal of Pavement Research and Technology*, *12*(4). https://doi.org/10.1007/s42947-019-0051-y

Pereira, R., Almeida-Costa, A., Duarte, C., & Benta, A. (2018). Warm mix asphalt: Chemical additives' effects on bitumen properties and limestone aggregates mixture compactibility. *International Journal of Pavement Research and Technology*, *11*(3). https://doi.org/10.1016/j.ijprt.2017.10.005

Perez-Martinez, M., Marsac, P., Gabet, T., Hammoum, F., de Mesquita Lopes, M., & Pouget, S. (2016). Effects of ageing on warm mix asphalts with high rates of reclaimed asphalt pavement. *RILEM Bookseries*, *13*. https://doi.org/10.1007/978-94-024-0867-6_16

Polo-Mendoza, R., Peñabaena-Niebles, R., Giustozzi, F., & Martinez-Arguelles, G. (2022). Eco-friendly design of Warm mix asphalt (WMA) with recycled concrete aggregate (RCA): A case study from a developing country. *Construction and Building Materials*, *326*. https://doi.org/10.1016/j.conbuildmat.2022.126890

Pronk, A. C. (2003). Revival of the Huet-Sayegh response model. *DWW-2003-29*.

Pronk, A. C. (2005). *The Huet-Sayegh Model: A Simple and Excellent Rheological Model for Master Curves of Asphaltic Mixes*. https://doi.org/10.1061/40825(185)8

Pronk, A. C., & Hopman, P. C. (1991). Energy dissipation: The leading factor of fatigue. In *Highway Research: Sharing the Benefits. The United States Strategic Highway Research Program*.

Pszczola, M. (2019). Equivalent temperature for design of asphalt pavements in Poland. *MATEC Web of Conferences*, *262*. https://doi.org/10.1051/matecconf/201926205010

Pszczoła, M., Ryś, D., & Jaskuła, P. (2017). Analysis of climatic zones in Poland with regard to asphalt performance grading. *Roads and Bridges - Drogi i Mosty*, *16*(4). https://doi.org/10.7409/rabdim.017.016

Ragni, D., Ferrotti, G., Lu, X., & Canestrari, F. (2018). Effect of temperature and chemical additives on the short-term ageing of polymer modified bitumen for WMA. *Materials and Design*, *160*. https://doi.org/10.1016/j.matdes.2018.09.042

Ranieri, M., Costa, L., M. Oliveira, J. R., R. D. Silva, H. M., & Celauro, C. (2017). Asphalt Surface Mixtures with Improved Performance Using Waste Polymers via Dry and Wet Processes. *Journal of Materials in Civil Engineering*, *29*(10). https://doi.org/10.1061/(asce)mt.1943-5533.0002022

Rathore, M., Haritonovs, V., Merijs Meri, R., & Zaumanis, M. (2022). Rheological and chemical evaluation of aging in 100% reclaimed asphalt mixtures containing rejuvenators. *Construction and Building Materials*, *318*. https://doi.org/10.1016/j.conbuildmat.2021.126026

Reese, R. (1997). Properties of aged asphalt binder related to asphalt concrete fatigue life. *Journal of the Association of Asphalt Paving Technologists*, *66*, 604–632.

Rubio, M. C., Martínez, G., Baena, L., & Moreno, F. (2012). Warm Mix Asphalt: An overview. *Journal of Cleaner Production*, *24*. https://doi.org/10.1016/j.jclepro.2011.11.053

Ryś, D., Jaskuła, P., Jaczewski, M., & Pszczoła, M. (2019). Application and evaluation of M-EPDG for performance analysis of Polish typical flexible and rigid pavements. *Roads and Bridges - Drogi i Mosty*, *18*(4). https://doi.org/10.7409/rabdim.019.019

Sabouri, M., Choi, Y. T., Wang, Y., Hwang, S., Baek, C., & Kim, R. Y. (2016). Effect of rejuvenator on performance properties of WMA mixtures with high RAP content. *RILEM Bookseries*, *11*. https://doi.org/10.1007/978-94-017-7342-3_38

Saleh, N. F., Keshavarzi, B., Yousefi Rad, F., Mocelin, D., Elwardany, M., Castorena, C., Underwood, B. S., & Kim, Y. R. (2020). Effects of aging on asphalt mixture and pavement performance. *Construction and Building Materials*, *258*. https://doi.org/10.1016/j.conbuildmat.2020.120309

Sangita, Khan, T. A., Sabina, & Sharma, D. K. (2011). Effect of waste polymer modifier on the properties of bituminous concrete mixes. *Construction and Building Materials*, *25*(10). https://doi.org/10.1016/j.conbuildmat.2011.04.003

Schapery, R. A. (1984). Correspondence principles and a generalized J integral for large deformation and fracture analysis of viscoelastic media. In *International Journal of Fracture* (Vol. 25).

Schapery, R. A. (1987). *Deformation and Fracture Characterization of Inelastic Composite Materials Using Potentials*.

Sengoz, B., & Isikyakar, G. (2008). Evaluation of the properties and microstructure of SBS and EVA polymer modified bitumen. *Construction and Building Materials*, *22*(9). https://doi.org/10.1016/j.conbuildmat.2007.07.013

Shen, S., & Lu, X. (2011). Energy based laboratory fatigue failure criteria for asphalt materials. *Journal of Testing and Evaluation*, *39*(3). https://doi.org/10.1520/JTE103088

Singh, D., Chitragar, S. F., & Ashish, P. K. (2017). Comparison of moisture and fracture damage resistance of hot and warm asphalt mixes containing reclaimed pavement materials. *Construction and Building Materials*, *157*. https://doi.org/10.1016/j.conbuildmat.2017.09.176

Spadoni, S., Ingrassia, L. P., Jaskuła, P., & Canestrari, F. (2023). Advanced fatigue and rutting characterisation of Polish asphalt mixtures based on the VECD model and viscoplastic shift model. *Road Materials and Pavement Design*, *24*(S1). https://doi.org/10.1080/14680629.2023.2180296

Spadoni, S., Ingrassia, L. P., Mariani, E., Cardone, F., & Canestrari, F. (2022). Long-term performance assessment of a warm recycled motorway pavement. *Case Studies in Construction Materials*, *17*. https://doi.org/10.1016/j.cscm.2022.e01451

Spadoni, S., Ingrassia, L. P., Mocelin, D., Richard Kim, Y., & Canestrari, F. (2022). Comparison of asphalt mixtures containing polymeric compounds and polymer-modified bitumen based on the VECD theory. *Construction and Building Materials*, *349*. https://doi.org/10.1016/j.conbuildmat.2022.128725

Stimilli, A., Frigio, F., Canestrari, F., & Sciolette, S. (2017). In-plant production of warm recycled mixtures produced with sbs modified bitumen: A case study. *Transport Infrastructure and Systems - Proceedings of the AIIT International Congress on Transport Infrastructure and Systems, TIS 2017*. https://doi.org/10.1201/9781315281896-21

Stimilli, A., Frigio, F., Cardone, F., & Canestrari, F. (2017). Performance of warm recycled mixtures in field trial sections. *Bearing Capacity of Roads, Railways and Airfields - Proceedings of the 10th International Conference on the Bearing Capacity of Roads, Railways and Airfields, BCRRA 2017*. https://doi.org/10.1201/9781315100333-183

Stimilli, A., Virgili, A., & Canestrari, F. (2015). New method to estimate the “re-activated” binder amount in recycled hot-mix asphalt. *Road Materials and Pavement Design*, *16*. https://doi.org/10.1080/14680629.2015.1029678

Stimilli, A., Virgili, A., & Canestrari, F. (2017). Warm recycling of flexible pavements: Effectiveness of Warm Mix Asphalt additives on modified bitumen and mixture performance. *Journal of Cleaner Production*, *156*. https://doi.org/10.1016/j.jclepro.2017.03.235

Sudarsanan, N., & Kim, Y. R. (2022). A critical review of the fatigue life prediction of asphalt mixtures and pavements. In *Journal of Traffic and Transportation Engineering (English Edition)* (Vol. 9, Issue 5). https://doi.org/10.1016/j.jtte.2022.05.003

Sukhija, M., & Saboo, N. (2021). A comprehensive review of warm mix asphalt mixtures-laboratory to field. In *Construction and Building Materials* (Vol. 274). https://doi.org/10.1016/j.conbuildmat.2020.121781

Tavassoti, P., Solaimanian, M., & Chen, X. (2022). Characterization of fatigue performance of cold mix recycled asphalt mixtures through uniaxial tension–compression testing. *Construction and Building Materials*, *329*. https://doi.org/10.1016/j.conbuildmat.2022.127155

Thives, L. P., & Ghisi, E. (2017). Asphalt mixtures emission and energy consumption: A review. In *Renewable and Sustainable Energy Reviews* (Vol. 72). https://doi.org/10.1016/j.rser.2017.01.087

Underwood, B., Baek, C., & Kim, Y. (2012). Simplified viscoelastic continuum damage model as platform for asphalt concrete fatigue analysis. *Transportation Research Record*, *2296*. https://doi.org/10.3141/2296-04

Underwood, B. S. (2006). *Experimental investigation and constitutive modeling of asphalt concrete mixtures in uniaxial tension*. North Carolina State Uniersity.

Underwood, B. S., Kim, Y. R., & Guddati, M. N. (2010). Improved calculation method of damage parameter in viscoelastic continuum damage model. *International Journal of Pavement Engineering*, *11*(6). https://doi.org/10.1080/10298430903398088

Vaitkus, A., Čygas, D., Laurinavičius, A., Vorobjovas, V., & Perveneckas, Z. (2016). Influence of warm mix asphalt technology on asphalt physical and mechanical properties. *Construction and Building Materials*, *112*. https://doi.org/10.1016/j.conbuildmat.2016.02.212

Vaitkus, A., Gražulytė, J., Baltrušaitis, A., Židanavičiūtė, J., & Čygas, D. (2021). Long-term performance of pavement structures with cold in-place recycled base course. *Baltic Journal of Road and Bridge Engineering*, *16*(2). https://doi.org/10.7250/bjrbe.2021-16.523

Van Dijk, W. (1975). Practical Fatigue Characterization of Bituminous Mixes. *Association of Asphalt Paving Technologists (AAPT)*, 38–74.

Van Dijk, W., & Visser, W. (1977). The Energy Approach to Fatigue for Pavement Design. *Association of Asphalt Paving Technologists (AAPT)*, 1–40.

Vasudevan, R., Ramalinga Chandra Sekar, A., Sundarakannan, B., & Velkennedy, R. (2012). A technique to dispose waste plastics in an ecofriendly way - Application in construction of flexible pavements. *Construction and Building Materials*, *28*(1). https://doi.org/10.1016/j.conbuildmat.2011.08.031

Verstraeten, J., Veverka, V., & Francken, L. (1982). *RATIONAL AND PRACTICAL DESIGNS OF ASPHALT PAVEMENTS TO AVOID CRACKING AND RUTTING. 1.*

Wang, D., Riccardi, C., Jafari, B., Cannone Falchetto, A., & Wistuba, M. P. (2021). Investigation on the effect of high amount of Re-recycled RAP with Warm mix asphalt (WMA) technology. *Construction and Building Materials*, *312*. https://doi.org/10.1016/j.conbuildmat.2021.125395

Wang, Y. D., Ghanbari, A., Underwood, B. S., & Kim, Y. R. (2021). Development of preliminary transfer functions for performance predictions in FlexPAVE^{TM}. *Construction and Building Materials*, *266*. https://doi.org/10.1016/j.conbuildmat.2020.121182

Wang, Y. D., Keshavarzi, B., & Kim, Y. R. (2018). Fatigue Performance Prediction of Asphalt Pavements with FlexPAVETM, the S-VECD Model, and DR Failure Criterion. *Transportation Research Record*, *2672*(40), 217–227. https://doi.org/10.1177/0361198118756873

Wang, Y. D., Underwood, B. S., & Kim, Y. R. (2022). Development of a fatigue index parameter, Sapp, for asphalt mixes using viscoelastic continuum damage theory. *International Journal of Pavement Engineering*, *23*(2). https://doi.org/10.1080/10298436.2020.1751844

Wang, Y., & Richard Kim, Y. (2019). Development of a pseudo strain energy-based fatigue failure criterion for asphalt mixtures. *International Journal of Pavement Engineering*, *20*(10). https://doi.org/10.1080/10298436.2017.1394100

Wiesmeth, H. (2020). Implementing the Circular Economy for Sustainable Development. In *Implementing the Circular Economy for Sustainable Development*. https://doi.org/10.1016/B978-0-12-821798-6.09993-2

Winter, M., Mollenhauer, K., Graziani, A., Mignini, C., Giancontieri, G., Lo Presti, D., Bjurström, H., Kalman, B., Hornych, P., & Gaudefroy, V. (2020). Design of flexible pavements with cold recycled asphalt bases: comparison of five national approaches. *Proceedings of the 8th Transport Research Arena TRA 2020*.

Witczak, M. W., & Shook, J. F. (1975). FULL-DEPTH ASPHALT AIRFIELD PAVEMENTS. *ASCE Transp Eng J*, *101*(2). https://doi.org/10.1061/tpejan.0000505

Wu, S., & Montalvo, L. (2021). Repurposing waste plastics into cleaner asphalt pavement materials: A critical literature review. In *Journal of Cleaner Production* (Vol. 280). https://doi.org/10.1016/j.jclepro.2020.124355

Xiao, F., Su, N., Yao, S., Amirkhanian, S., & Wang, J. (2019). Performance grades, environmental and economic investigations of reclaimed asphalt pavement materials. *Journal of Cleaner Production*, *211*. https://doi.org/10.1016/j.jclepro.2018.11.126

Yang, H. H. (2004). Pavement Analysis and Design (Second Edition). In *Education*.

Yang, L., Zhou, D., & Kang, Y. (2020). Rheological properties of graphene modified asphalt binders. *Nanomaterials*, *10*(11). https://doi.org/10.3390/nano10112197

Yang, X., You, Z., Perram, D., Hand, D., Ahmed, Z., Wei, W., & Luo, S. (2019). Emission analysis of recycled tire rubber modified asphalt in hot and warm mix conditions. *Journal of Hazardous Materials*, *365*. https://doi.org/10.1016/j.jhazmat.2018.11.080

Yu, X., Liang, X., Chen, C., & Ding, G. (2022). Towards the low-energy usage of high viscosity asphalt in porous asphalt pavements: A case study of warm-mix asphalt additives. *Case Studies in Construction Materials*, *16*. https://doi.org/10.1016/j.cscm.2022.e00914

Zani, L., Giustozzi, F., & Harvey, J. (2017). Effect of storage stability on chemical and rheological properties of polymer-modified asphalt binders for road pavement construction. *Construction and Building Materials*, *145*. https://doi.org/10.1016/j.conbuildmat.2017.04.014

Zaumanis, M., Boesiger, L., Kunz, B., Mazzoni, H., Bruhin, P., Mazor, S., & Poulikakos, L. (2022). Three indexes to characterise crushing and screening of reclaimed asphalt pavement. *International Journal of Pavement Engineering*, *23*(14), 4977–4990. https://doi.org/10.1080/10298436.2021.1990287

Zaumanis, M., Poulikakos, L., Arraigada, M., Kunz, B., Schellenberg, U., & Gassmann, C. (2023). Asphalt recycling in polymer modified pavement: A test section and recommendations. *Construction and Building Materials*, *409*. https://doi.org/10.1016/j.conbuildmat.2023.134005

Zeng, M., Bahia, H. U., Zhai, H., Anderson, M. R., & Turner, P. (2002). Rheological modeling of modified asphalt binders and mixtures. *Asphalt Paving Technology: Association of Asphalt Paving Technologists-Proceedings of the Technical Sessions*, *70*.

Zhang, S., Wang, D., Guo, F., Deng, Y., Feng, F., Wu, Q., Chen, Z., & Li, Y. (2021). Properties investigation of the SBS modified asphalt with a compound warm mix asphalt (WMA) fashion using the chemical additive and foaming procedure. *Journal of Cleaner Production*, *319*. https://doi.org/10.1016/j.jclepro.2021.128789

Zhao, Y., & Kim, Y. R. (2003). Time-Temperature Superposition for Asphalt Mixtures with Growing Damage and Permanent Deformation in Compression. *Transportation Research Record*, *1832*, 03–3903.

Zofka, A., Błażejowski, K., & Ostrowski, P. (2021). Fatigue performance of asphalt pavements with highly polymer-modified asphalt binders. *Road Materials and Pavement Design*, *22*(S1). https://doi.org/10.1080/14680629.2021.1905701

Zulkernain, N. H., Gani, P., Chuck Chuan, N., & Uvarajan, T. (2021). Utilisation of plastic waste as aggregate in construction materials: A review. In *Construction and Building Materials* (Vol. 296). https://doi.org/10.1016/j.conbuildmat.2021.123669

Publications and conference presentations

1) Spadoni S, Ingrassia LP, Mocelin D, Richard Kim Y, Canestrari F. Comparison of asphalt mixtures containing polymeric compounds and polymer-modified bitumen based on the VECD theory. *Construction and Building Materials*. 2022;349:128725. doi:10.1016/j.conbuildmat.2022.128725

2) Spadoni S, Ingrassia LP, Mariani E, Cardone F, Canestrari F. Long-term performance assessment of a warm recycled motorway pavement. *Case Studies in Construction Materials*. 2022;17:e01451. doi:10.1016/j.cscm.2022.e01451

3) Spadoni S, Ingrassia LP, Canestrari F. S-VECD model to investigate the fatigue performance of asphalt mixtures. In: *Proceeding of the 7th SIIV Arena on Sustainable Pavements and Road Materials* (9 September 2022). doi:10.6093/978-88-6887-147-5

4) Ingrassia LP, Spadoni S, Ferrotti G, Virgili A, Canestrari F. Prediction of the Long-Term Performance of an Existing Warm Recycled Motorway Pavement. *Materials*. 2023;16(3):1005. doi:10.3390/ma16031005

5) Spadoni S, Ingrassia LP, Jaskula P, Canestrari F. Advanced fatigue and rutting characterisation of Polish asphalt mixtures based on the VECD model and viscoplastic shift model. *Road Materials and Pavement Design*. 2023; 24(S1): 145-159. doi:10.1080/14680629.2023.2180296

6) Graziani A, Spadoni S, Ingrassia LP, Virgili A, Canestrari F. Composite fatigue failure of cold recycled material: new insights into the role of bitumen and cement. *Materials and Structures*. 2024;57:10. doi:/10.1617/s11527-023-02285-8

Oral presentation to the XVIII International SIIV Summer School: Sustainable Pavement and Road Materials. 5th – 9th September 2022, Naples, Italy. (Paper (3))

Oral presentation to the European Asphalt Technology Association – EATA 2023. 12th -14th June 2023, Gdansk, Poland. (Paper (5))

Appendix A: Proficiency check with NCSU

Dynamic Modulus Test – Mixture H – Italy

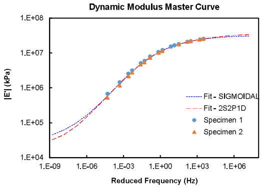

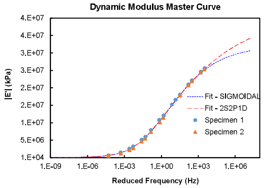

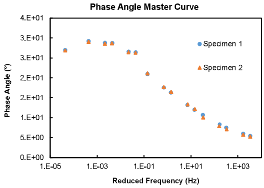

Test Results	Temperature	4°C					20°C					40°C					
	Loading Rate	10 Hz	5 Hz	1 Hz	0.5 Hz	0.1 Hz	10 Hz	5 Hz	1 Hz	0.5 Hz	0.1 Hz	10 Hz	5 Hz	1 Hz	0.5 Hz	0.1 Hz	0.01 Hz
Dynamic Modulus (MPa)	Specimen 1	25717	24735	22288	21127	18314	16923	15571	12489	11228	8401	6590	5665	3577	1896	1650	759.5
	Specimen 2	25489	24526	22105	20964	181222	16294	14928	11876	10628	7862	6082	5178	3133	2479	1334	588
	Repeatability (S_R%)	0.9	0.8	0.8	0.8	1.1	3.8	4.2	5.0	5.5	6.6	8.0	9.0	13.2	15.5	21.2	25.5
	Acceptable Limit (%), n=2	19	19	19	19	19	19	19	19	19	22	22	22	27	32	32	38
	Pass / Fail	Pass	Pass	Pass	Pass	Pass	Pass	Pass	Pass	Pass	Pass	Pass	Pass	Pass	Pass	Pass	Pass
Phase Angle (deg)	Specimen 1	5.31	5.78	6.97	7.69	9.79	11.23	12.26	15.13	16.4	19.7	24.75	25.22	27.73	27.94	28.71	27.03
	Specimen 2	5.45	5.83	7.13	7.86	10	11.97	13.16	16.28	17.6	21.15	25.89	26.47	29.09	29.3	29.89	27.94
	Repeatability (S_R)	0.14	0.11	0.16	0.17	0.21	0.74	0.9	1.15	1.2	1.45	1.14	1.25	1.36	1.36	1.18	0.91
	Acceptable Limit (deg), n=2	2.2	2.2	2.2	2.2	2.2	2.2	2.2	2.2	2.2	2.5	2.5	2.5	3.0	3.7	3.7	4.3
	Pass / Fail	Pass	Pass	Pass	Pass	Pass	Pass	Pass	Pass	Pass	Pass	Pass	Pass	Pass	Pass	Pass	Pass

Data Quality Indicator

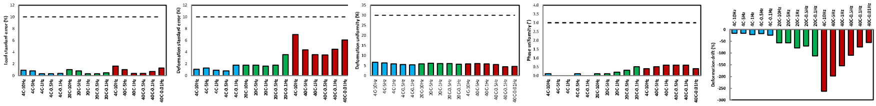

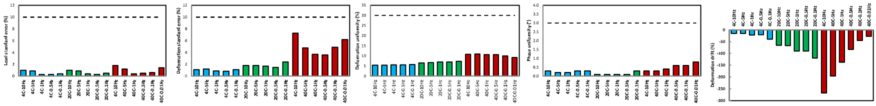

Appendix A
Proficiency check with NCSU

Dynamic Modulus Test – Mixture H - NCSU

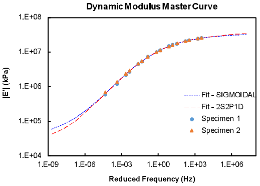

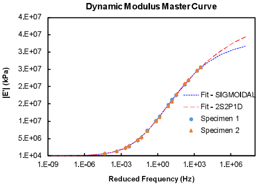

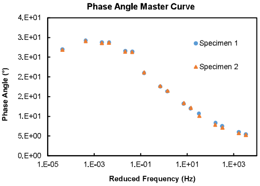

Test Results	Temperature	4°C					20°C					40°C					
	Loading Rate	10 Hz	5 Hz	1 Hz	0.5 Hz	0.1 Hz	10 Hz	5 Hz	1 Hz	0.5 Hz	0.1 Hz	10 Hz	5 Hz	1 Hz	0.5 Hz	0.1 Hz	0.01 Hz
Dynamic Modulus (MPa)	Specimen 1	25749	24658	21996	20778	17799	16557	15116	11918	10628	7841	5894	5001	3072	2449	1359	649.1
	Specimen 2	25767	24767	22233	21034	18159	16108	14768	11693	10490	7797	6084	5243	3350	2748	1593	755.3
	Repeatability (S_R%)	0.1	0.4	1.1	1.2	2.0	2.7	2.3	1.9	1.3	0.6	3.2	4.7	8.7	11.5	15.9	15.1
	Acceptable Limit (%), n=2	19	19	19	19	19	19	19	19	19	22	22	22	27	32	32	38
	Pass / Fail	Pass	Pass	Pass	Pass	Pass	Pass	Pass	Pass	Pass	Pass	Pass	Pass	Pass	Pass	Pass	Pass
Phase Angle (deg)	Specimen 1	5.45	6.02	7.53	8.35	10.69	12.02	13.21	16.34	17.56	20.99	26.40	26.58	28.76	28.8	29.23	27.02
	Specimen 2	5.26	5.73	7.12	7.87	10.09	12.15	13.35	16.49	17.69	21.15	26.28	26.42	28.66	28.59	29.08	26.87
	Repeatability (S_R)	0.19	0.29	0.41	0.48	0.60	0.13	0.14	0.15	0.13	0.16	0.12	0.16	0.10	0.21	0.15	0.15
	Acceptable Limit (deg), n=2	2.2	2.2	2.2	2.2	2.2	2.2	2.2	2.2	2.2	2.5	2.5	2.5	3.0	3.7	3.7	4.3
	Pass / Fail	Pass	Pass	Pass	Pass	Pass	Pass	Pass	Pass	Pass	Pass	Pass	Pass	Pass	Pass	Pass	Pass

Data Quality Indicator

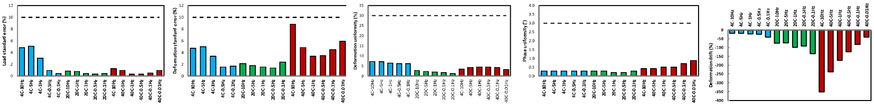

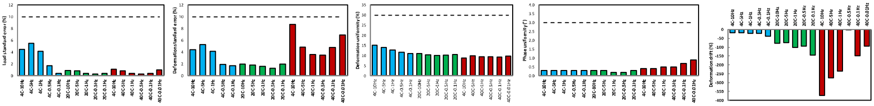

Dynamic Modulus Test – Mixture H – Multilaboratory precision

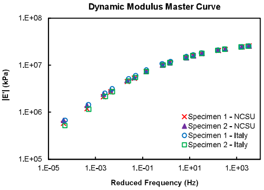

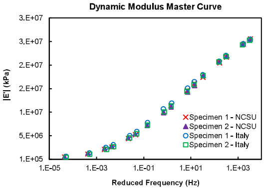

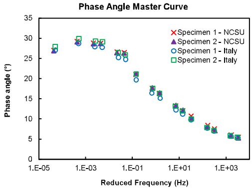

Test Results	Temperature	4°C					20°C					40°C					
	Loading Rate	10 Hz	5 Hz	1 Hz	0.5 Hz	0.1 Hz	10 Hz	5 Hz	1 Hz	0.5 Hz	0.1 Hz	10 Hz	5 Hz	1 Hz	0.5 Hz	0.1 Hz	0.01 Hz
Dynamic Modulus (MPa)	Mixture H - NCSU	25758	24713	22115	20908	17979	16333	14942	11806	10559	7819	5989	5122	3211	2599	1476	702
	Mixture H - Italy	25603	24631	22197	21046	18218	16609	15250	12183	10929	8132	6336	5422	3355	2688	1492	674
	Reproducibility (S_R%)	0.6	0.3	0.4	0.7	1.3	1.7	2.0	3.1	3.4	3.9	5.6	5.7	4.4	3.4	1.1	4.1
	Acceptable Limit (%), n=2	8	8	8	8	8	8	8	8	8	10	10	10	12	12	16	20
	Pass / Fail	Pass	Pass	Pass	Pass	Pass	Pass	Pass	Pass	Pass	Pass	Pass	Pass	Pass	Pass	Pass	Pass
Phase Angle (deg)	Mixture H - NCSU	5.36	5.88	7.33	8.11	10.39	12.09	13.28	16.42	17.63	21.07	26.34	26.50	28.71	28.70	29.16	26.95
	Mixture H - Italy	5.38	5.78	7.05	7.78	9.90	11.60	12.71	15.71	17.00	20.43	25.32	25.85	28.41	28.62	29.30	27.49
	Reproducibility (S_R)	0.02	0.10	0.28	0.33	0.50	0.48	0.57	0.71	0.63	0.65	1.00	0.66	0.30	0.07	0.15	0.54
	Acceptable Limit (deg), n=2	0.8	0.8	0.8	0.8	0.8	0.8	0.8	0.8	0.8	1.0	1.0	1.0	1.3	1.3	1.8	2.2
	Pass / Fail	Pass	Pass	Pass	Pass	Pass	Pass	Pass	Pass	Pass	Pass	Pass	Pass	Pass	Pass	Pass	Pass

Appendix A
Proficiency check with NCSU

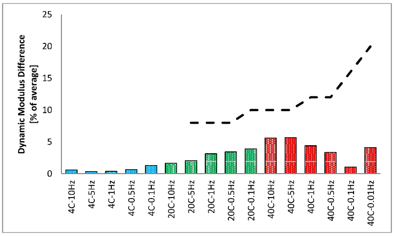

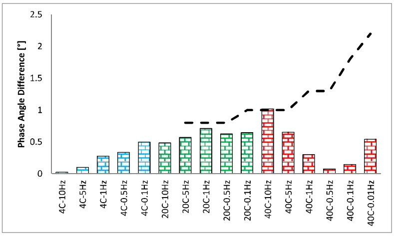

Dynamic Modulus Test – Mixture GC - Italy

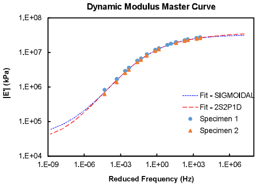

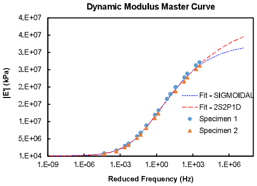

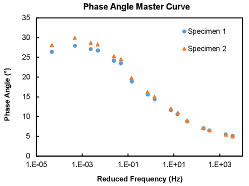

Test Results	Temperature	4°C					20°C					40°C					
	Loading Rate	10 Hz	5 Hz	1 Hz	0.5 Hz	0.1 Hz	10 Hz	5 Hz	1 Hz	0.5 Hz	0.1 Hz	10 Hz	5 Hz	1 Hz	0.5 Hz	0.1 Hz	0.01 Hz
Dynamic Modulus (MPa)	Specimen 1	27284	26398	24071	22963	20239	18529	16903	13697	12388	9373	7346	6316	4036	3284	1910	924.3
	Specimen 2	26245	25274	22877	21749	19032	17215	15847	12747	11457	8601	6741	5765	3590	2876	1592	705.7
	Repeatability (S_R%)	3.9	4.4	5.1	5.4	6.1	7.4	6.4	7.2	7.8	8.6	8.6	9.1	11.7	13.2	18.2	26.8
	Acceptable Limit (%), n=2	19	19	19	19	19	19	19	19	19	22	22	22	27	27	32	38
	Pass / Fail	Pass	Pass	Pass	Pass	Pass	Pass	Pass	Pass	Pass	Pass	Pass	Pass	Pass	Pass	Pass	Pass
Phase Angle (deg)	Specimen 1	5.31	5.72	6.97	7.69	9.79	11.23	12.26	15.13	16.40	19.70	24.75	25.22	27.73	27.94	28.71	27.03
	Specimen 2	5.45	5.83	7.13	7.86	10.00	11.97	13.16	16.28	17.60	21.15	25.89	26.47	29.09	29.30	29.89	27.94
	Repeatability (S_R)	0.08	0.11	0.01	0.09	0.20	0.36	0.41	0.61	0.66	0.89	1.00	1.12	1.55	1.60	2.00	1.63
	Acceptable Limit (deg), n=2	2.2	2.2	2.2	2.2	2.2	2.2	2.2	2.2	2.2	2.5	2.5	2.5	3.0	3.0	3.7	4.3
	Pass / Fail	Pass	Pass	Pass	Pass	Pass	Pass	Pass	Pass	Pass	Pass	Pass	Pass	Pass	Pass	Pass	Pass

Data Quality Indicator

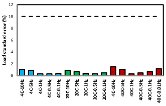

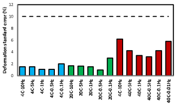

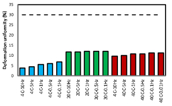

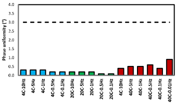

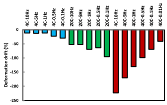

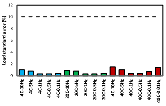

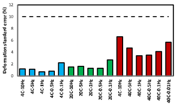

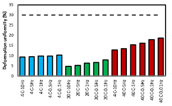

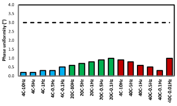

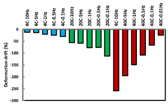

Dynamic Modulus Test – Mixture GC - NCSU

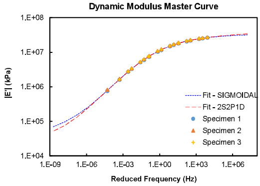

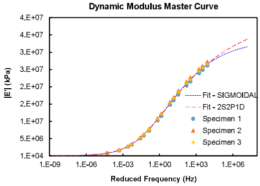

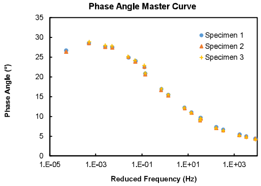

Test Results	Temperature	4°C					20°C					40°C					
	Loading Rate	**10 Hz**	**5 Hz**	**1 Hz**	**0.5 Hz**	**0.1 Hz**	**10 Hz**	**5 Hz**	**1 Hz**	**0.5 Hz**	**0.1 Hz**	**10 Hz**	**5 Hz**	**1 Hz**	**0.5 Hz**	**0.1 Hz**	**0.01 Hz**
Dynamic Modulus (MPa)	**Specimen 1**	25007	24057	21658	20559	18018	16414	15113	11989	10704	7877	6509	5590	3654	3044	1813	843.9
	Specimen 2	26155	25203	22816	21643	19006	17282	15896	12707	11320	8457	6863	5848	3850	3204	1919	917.2
	Specimen 3	25511	24619	22282	21242	18622	16966	15625	12460	11155	8270	6764	5795	3763	3128	1841	880.55
	Repeatability (S_R%)	4.49	4.65	5.20	5.13	5.33	5.14	5.04	5.80	5.57	7.07	5.27	4.49	5.22	5.12	5.71	8.32
	Acceptable Limit (%), n=2	19	19	19	19	19	19	19	19	19	22	22	22	27	27	32	38
	Pass / Fail	Pass	Pass	Pass	Pass	Pass	Pass	Pass	Pass	Pass	Pass	Pass	Pass	Pass	Pass	Pass	Pass
Phase Angle (deg)	**Specimen 1**	5.00	5.42	6.66	7.33	9.17	11.07	12.24	15.49	16.93	20.85	24.02	24.89	27.51	27.65	28.53	26.69
	Specimen 2	4.90	5.27	6.46	7.05	8.98	10.91	12.09	15.33	16.7	20.62	23.88	25.03	27.41	27.57	28.49	26.37
	Specimen 3	4.73	5.16	6.41	7.04	9.04	10.96	12.18	15.51	17.02	20.97	24.2	25.13	27.83	27.98	28.89	26.53
	Repeatability (S_R)	0.27	0.26	0.25	0.29	0.13	0.11	0.06	0.02	0.09	0.12	0.18	0.24	0.32	0.33	0.36	0.16
	Acceptable Limit (deg), n=2	2.2	2.2	2.2	2.2	2.2	2.2	2.2	2.2	2.2	2.5	2.5	2.5	3.0	3.0	3.7	4.3
	Pass / Fail	Pass	Pass	Pass	Pass	Pass	Pass	Pass	Pass	Pass	Pass	Pass	Pass	Pass	Pass	Pass	Pass

Data Quality Indicator

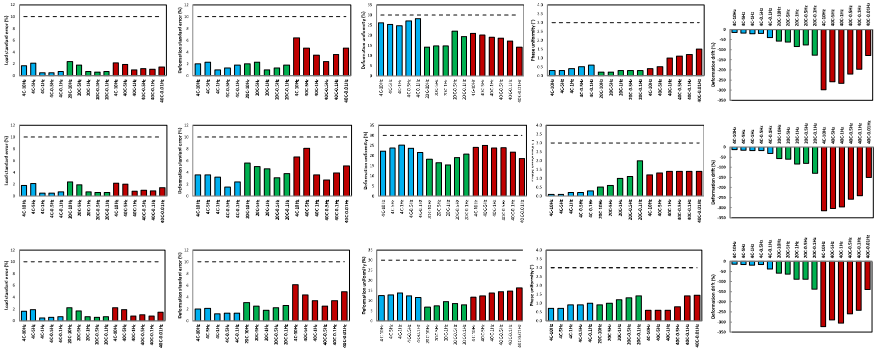

Appendix A
Proficiency check with NCSU

Dynamic Modulus Test – Mixture GC – Multilaboratory precision

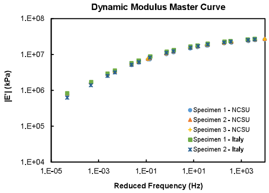

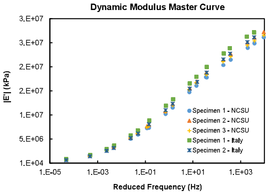

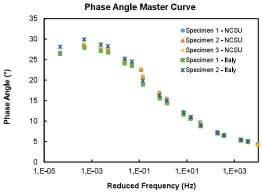

Test Results	Temperature	4°C					20°C					40°C					
	Loading Rate	10 Hz	5 Hz	1 Hz	0.5 Hz	0.1 Hz	10 Hz	5 Hz	1 Hz	0.5 Hz	0.1 Hz	10 Hz	5 Hz	1 Hz	0.5 Hz	0.1 Hz	0.01 Hz
Dynamic Modulus (MPa)	Mixture GC - NCSU	25558	24626	22252	21148	18549	16887	15545	12385	11060	8201	6712	5744	3756	3125	1858	881
	Mixture GC - Italy	26765	25836	23474	22356	19636	17872	16375	13222	11923	8987	7044	6041	3813	3080	1751	815
	Reproducibility (S_R%)	4.6	4.8	5.3	5.6	5.7	5.7	5.2	6.5	7.5	9.1	4.8	5.0	1.5	1.5	5.9	7.7
	Acceptable Limit (%), n=2	8	8	8	8	8	8	8	8	8	10	10	10	12	12	16	20
	Pass / Fail	Pass	Pass	Pass	Pass	Pass	Pass	Pass	Pass	Pass	Pass	Pass	Pass	Pass	Pass	Pass	Pass
Phase Angle (deg)	Mixture GC - NCSU	4.9	5.3	6.5	7.1	9.1	11.0	12.2	15.4	16.9	20.8	24.0	25.0	27.6	27.7	28.6	26.5
	Mixture GC - Italy	5.1	5.4	6.5	7.1	8.9	10.8	11.8	14.7	15.9	19.3	24.0	24.7	27.5	27.9	28.9	27.2
	Reproducibility (S_R)	0.17	0.14	0.03	0.08	0.19	0.22	0.37	0.75	0.97	1.49	0.03	0.32	0.09	0.16	0.28	0.67
	Acceptable Limit (deg), n=2	0.8	0.8	0.8	0.8	0.8	0.8	0.8	0.8	0.8	1.0	1.0	1.0	1.3	1.3	1.8	2.2
	Pass / Fail	Pass	Pass	Pass	Pass	Pass	Pass	Pass	Pass	Failed	Failed	Pass	Pass	Pass	Pass	Pass	Pass

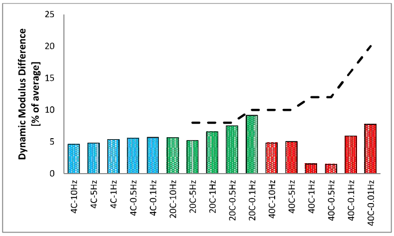

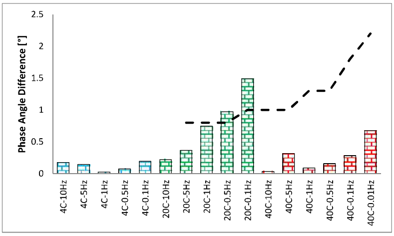

Cyclic fatigue – Mixture H

All Specimens

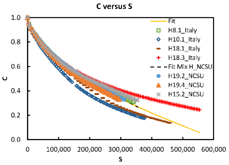

Accepted Specimens

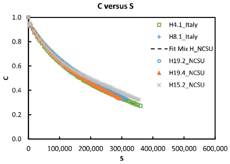

Based on AASHTO TP 133

🟩 Acceptable

🟥 Not acceptable

Specimen	Fingerprint |E*| (MPa)	Test Temperature	DMR, 0.85<DMR<1.15	N_f	Air Voids (%)	Cum. (1-C)	DR	Input Strain (μ)	S_{app}	Actuator Strain Standard Error (<10%)	Reason
H 4.1_Italy	16822	21°C	1.08	20530	2.3	10713	0.522	190	12.9	3.43%	
H 4.2_Italy	15135		0.97	900	2.2	373	0.415	230	8.3	2.88%	Short test, low air voids
H8.1_Italy	15375		0.96	14530	2.7	7128	0.491	210	12.5	3.14%	-
H10.1_Italy	14050		0.90	22330	3.7	12532	0.561	170	11.8	3.77%	High air voids
H18.1_Italy	13717		0.87	4440	1.9	2891	0.651	230	17.2	2.60%	Low air voids
H18.3_Italy	17475		1.12	281840	1.4	165800	0.588	170	20.8	3.68%	Long test, low air voids
H19.2_NCSU	15407		0.98	11840	2.8	5417	0.457	220	11.2	3.73%	-
H19.4_NCSU	16436		1.05	12760	2.7	6084	0.477	200	11.2	4.05%	-
H15.2_NCSU	14923		0.96	49870	2.9	24888	0.499	210	13.5	3.25%	-

Appendix A
Proficiency check with NCSU

Peak to Peak Strain

H19.2 - NCSU

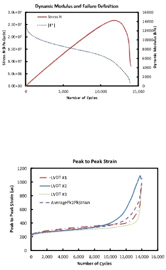

H19.4 - NCSU

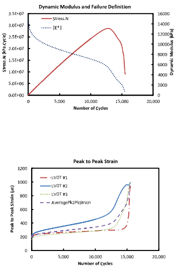

H 15.2 - NCSU

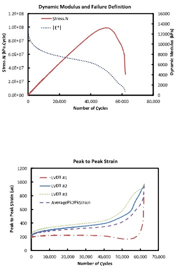

H4.1 - Italy

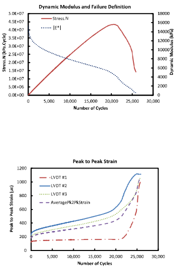

H8.1 - Italy

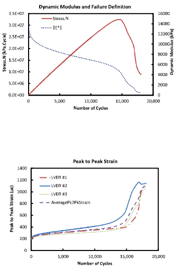

Cyclic fatigue – Mixture GC

All Specimens

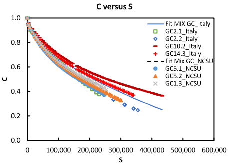

Accepted Specimens

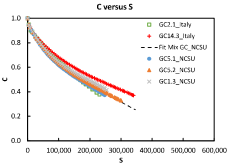

Based on AASHTO TP 133

🟩 Acceptable

🟥 Not acceptable

Specimen	Fingerprint |E*| (MPa)	Test Temperature	DMR, 0.85<DMR<1.15	N_f	Air Voids (%)	Cum. (1-C)	DR	Input Strain (μ)	S_{app}	Actuator Strain Standard Error (<10%)	Reason
GC2.1_Italy	15735	21°C	0.93	2650	2.5	1067	0.403	230	8.1	3.14%	-
GC2.2_Italy	16355		0.96	1280	2.3	624	0.488	230	11.3	3.77%	Short test
GC4.1_Italy	15996		0.93	1210	3.0	713	0.589	230	14.9	4.24%	Short test
GC10.2_Italy	18843		1.10	304330	2.1	150230	0.494	170	17.2	3.26%	Long test, low air voids
GC14.3_Italy	15812		0.93	27690	3.3	12684	0.458	210	12.9	3.68%	-
GC5.1_NCSU	15262		0.95	73570	2.6	32379	0.440	160	7.9	3.09%	-
GC5.2_NCSU	14454		0.90	27410	2.7	12986	0.474	200	9.6	3.22%	-
GC1.3_NCSU	15249		0.95	48360	3.0	21630	0.447	200	9.2	3.47%	-

5.1 - NCSU

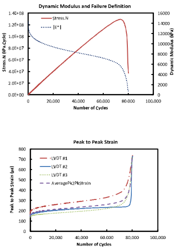

5.2 - NCSU

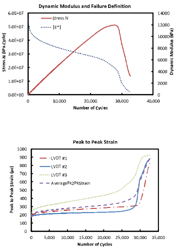

1.3 - NCSU

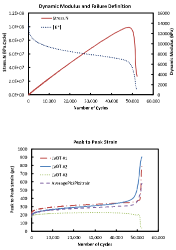

GC2.1 - Italy

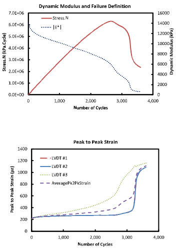

GC14.3 - Italy

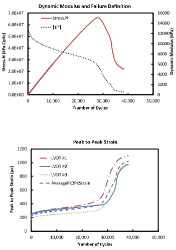

Appendix B: S-VECD fatigue parameters

Chapter 3

Laboratory specimens

H LAB

Specimen No & ID	Fingerprint |E*| [MPa]	DMR 0.85<DMR<1.15	N_f	log (N^f)	Cum. (1-C)	DR_a	Input Strain (μ)	Vuoty SSD [%]	Sapp
H_19.2	15407	0.98	11840	4.07	5417	0.457	220	2.6	11.21
H_19.4	16436	1.05	12760	4.11	6084	0.477	200	2.4	11.24
H_15.2	14923	0.96	49870	4.70	24888	0.499	210	3.0	13.50
Average	*15589*	*1.00*	*24823*	*4.29*	*12129*	*0.478*	*210*	*2.7*	*11.98*

GC LAB

Specimen No & ID	Fingerprint |E*| [MPa]	DMR 0.85<DMR<1.15	N_f	log (N^f)	Cum. (1-C)	DR_a	Input Strain (μ)	Vuoty SSD [%]	Sapp
GC_5.1	15262	0.95	73570	4.87	32379	0.440	160	2.1	7.90
GC_5.2	14454	0.90	27410	4.44	12986	0.474	200	2.5	9.61
GC_1.3	15249	0.95	48360	4.68	21630	0.447	200	2.0	9.25
Average	*14988*	*0.93*	*49780*	*4.66*	*22332*	*0.454*	*187*	*2.2*	*8.92*

PC LAB

Specimen No & ID	Fingerprint |E*| [MPa]	DMR 0.85<DMR<1.15	N_f	log (N^f)	Cum. (1-C)	DR_a	Input Strain (μ)	Vuoty SSD [%]	Sapp
PC_2.3	15455	0.89	19250	4.28	9592	0.498	200	3.4	11.94
PC_3.3	17168	1.00	26990	4.43	12157	0.450	190	2.0	10.43
PC_4.4	16126	0.94	11490	4.06	4830	0.420	190	2.7	8.80
Average	*16250*	*0.94*	*19243*	*4.26*	*8859*	*0.456*	*193*	*2.7*	*10.39*

OG H LAB

Specimen No & ID	Fingerprint |E*| [MPa]	DMR 0.85<DMR<1.15	N_f	log (N^f)	Cum. (1-C)	DR_a	Input Strain (μ)	%AV GEOM. [%]	Sapp
OG_H_3	5974	0.97	7310	3.86	5387	0.737	280	19.9	20.70
OG_H_5	6784	1.09	1960	3.29	1303	0.665	290	18.2	15.49
OG_H_6	5999	0.97	16020	4.20	11157	0.696	260	19.1	17.78
OG_H_7	6814	1.10	15810	4.20	10687	0.676	230	19.3	16.12
Average	*6393*	*1.03*	*10275*	*3.89*	*7134*	*0.694*	*265*	*19.1*	*17.52*

Field specimens

H field sup

Specimen No & ID	Fingerprint |E*| [MPa]	DMR 0.85<DMR<1.15	N_f	log (N^f)	Cum. (1-C)	DR_a	Input Strain (μ)	Vuoty SSD [%]	Sapp
H4_10	6681	0.83	9920	4.00	8174	0.824	250	8.7	15.77
H5_10	8151	1.01	**520**	2.72	333	0.640	370	8.2	15.65
H7_10	8433	1.05	9900	4.00	7633	0.771	200	9.2	15.59
H8_10	8137	1.02	5730	3.76	3562	0.622	250	8.7	12.74
H9_10	9536	**1.19**	2220	3.35	1339	0.603	300	8.8	15.49
Average	*8608*	*1.07*	*2823*	*3.27*	*1744*	*0.62*	*307*	*8.6*	*15*

In red the discarder tests

Appendix B
S-VECD fatigue parameters

GC field sup

Specimen No & ID	**Fingerprint |E*| [MPa]**	**DMR 0.85<DMR<1.15**	**N_f**	**log (N^f)**	**Cum. (1-C)**	**DR_a**	**Input Strain (μ)**	**Vuoty SSD [%]**	**Sapp**
G1_10	7242	1.02	9490	3.98	7362	0.776	220	9.9	12.44
G3_10	6407	0.91	**980**	2.99	767	0.783	210	9.2	12.47
G5_10	7141	1.00	16100	4.21	14675	0.911	200	9.9	13.05
Average	*6930*	*0.98*	*8857*	*3.73*	*7601*	*0.823*	*210*	*9.7*	*12.66*

PC field sup

Specimen No & ID	**Fingerprint |E*| [MPa]**	**DMR 0.85<DMR<1.15**	**N_f**	**log (N^f)**	**Cum. (1-C)**	**DR_a**	**Input Strain (μ)**	**Vuoty SSD [%]**	**Sapp**
P2_10	10310	1.00	2290	3.36	1185	0.518	250	5.8	9.77
P3_10	10198	0.99	32950	4.52	15830	0.480	230	7.3	12.05
P6_10	11029	1.08	13020	4.11	6312	0.485	240	7.4	11.98
Average	*10614*	*1.03*	*22985*	*4.32*	*11071*	*0.48*	*235*	*7.4*	*12.01*

In red the discarder tests

H field inf

Specimen No & ID	**Fingerprint |E*| [MPa]**	**DMR 0.85<DMR<1.15**	**N_f**	**log (N^f)**	**Cum. (1-C)**	**DR_a**	**Input Strain (μ)**	**Vuoty SSD [%]**	**Sapp**
H3_15	15437	1.03	36130	4.56	21830	0.604	220	1.9	22.47
H9_15	13195	0.89	19700	4.29	11081	0.562	230	2.2	22.06
H10_15	13634	0.92	11870	4.07	6771	0.570	250	2.9	22.14
H11_15	13894	0.93	29900	4.48	19313	0.646	240	2.9	22.87
Average	*14040*	*0.94*	*24400*	*4.35*	*14749*	*0.596*	*235*	*2.5*	*22.38*

GC field inf

Specimen No & ID	**Fingerprint |E*| [MPa]**	**DMR 0.85<DMR<1.15**	**N_f**	**log (N^f)**	**Cum. (1-C)**	**DR_a**	**Input Strain (μ)**	**Vuoty SSD [%]**	**Sapp**
G3_15	13906	0.95	9480	3.98	5967	0.629	210	4.6	14.38
G4_15	13496	0.92	10530	4.02	5718	0.543	210	5.4	13.75
G8_15	15582	1.06	49360	4.69	26183	0.530	200	3.2	13.66
G9_15	15395	1.05	**1350**	3.13	689	0.510	210	4.0	13.65
Average	*14266*	*0.97*	*7120*	*3.71*	*4125*	*0.561*	*210*	*4.7*	*13.89*

In red the discarder tests

PC field inf

Specimen No & ID	**Fingerprint |E*| [MPa]**	**DMR 0.85<DMR<1.15**	**N_f**	**log (N^f)**	**Cum. (1-C)**	**DR_a**	**Input Strain (μ)**	**Vuoty SSD [%]**	**Sapp**
P12_15	14576	1.13	35670	4.55	18444	0.517	210	4.3	16.00
P14_15	12655	0.99	280760	5.45	144221	0.514	220	5.5	15.55
P9_15	15024	**1.178269692**	16350	4.21	8181	0.500	210	3.8	14.10
P1_15	10162	0.80	3940	3.60	2559	0.649	250	5.2	14.97
P2_15	12794	1.00	4560	3.66	2466	0.541	240	4.8	13.38
Average	*14085*	*1.10*	*110927*	*4.74*	*56949*	*0.510*	*213*	*4.7*	*15.22*

In red the discarder tests

Appendix B
S-VECD fatigue parameters

Chapter 4

SMA 11_PmB

Specimen ID	Fingerprint |E*| [MPa]	DMR 0.85<DMR<1.15	N_f	log (N^f)	Cum. (1-C)	DR_a	Input Strain (μ)	Vuoty SSD [%]	Sapp
277-F1-3	4035	0.94	12690	4.10	10522	0.829	900	4.3	71.5
277-F2-1	3922	0.92	2600	3.41	1995	0.767	1150	4.2	57.4
277-F2-3	4008	0.94	6990	3.84	5631	0.806	1000	3.8	63.6
277-F3-3	4114	0.97	14060	4.15	11777	0.838	900	4.0	76.6
Average						*0.810*		*4.1*	*67.3*

AC 16_PmB

Specimen ID	Fingerprint |E*| [MPa]	DMR 0.85<DMR<1.15	N_f	log (N^f)	Cum. (1-C)	DR_a	Input Strain (μ)	Vuoty SSD [%]	Sapp
299_F1_3	7121	0.87	50640	4.70	37272	0.736	400	5.3	47.5
299_F2_1	8033	1.00	10320	4.01	6994	0.678	430	5.1	40.3
299_F4_2	7858	0.97	16310	4.21	11888	0.729	450	5.3	48.0
Average						*0.714*		*5.2*	*45.3*

AC 16_35/50

Specimen ID	Fingerprint |E*| [MPa]	DMR 0.85<DMR<1.15	N_f	log (N^f)	Cum. (1-C)	DR_a	Input Strain (μ)	Vuoty SSD [%]	Sapp
267-F1-3	7088	1.03	11490	4.06	7491	0.652	400	5.3	32.9
267-F2-1	6516	0.94	6060	3.78	4001	0.660	430	4.9	30.5
267-F5-1	6660	0.97	30050	4.48	20126	0.670	380	5.6	34.5
Average						*0.661*		*5.2*	*32.6*

AC 22_35/50

Specimen ID	Fingerprint |E*| [MPa]	DMR 0.85<DMR<1.15	N_f	log (N^f)	Cum. (1-C)	DR_a	Input Strain (μ)	Vuoty SSD [%]	Sapp
265-F1-1	9671	1.03	29520	4.47	15167	0.514	230	5.5	18.2
265-F1-4	9525	1.02	17880	4.25	8667	0.485	210	5.8	14.6
265-F2-4	9534	1.02	13020	4.11	6222	0.478	230	5.4	15.5
Average						*0.492*		*5.5*	*16.1*

Chapter 5

HMA 2022_BINDER

Specimen No & ID		Fingerprint |E*| [MPa]	DMR 0.85<DMR<1.15	N_f	log (N^f)	Cum. (1-C)	DR_a	Input Strain (μ)	Vuoty SSD [%]	Sapp
H5_2	Hbinder A1_Rip.1	10343	0.95	6540	3.82	3562	0.545	260	4.3	13
H5_3	Hbinder A1_Rip.2	9932	0.91	100010	5.00	66151	0.661	230	4.9	22
H6_3	Hbinder A1_Rip.3	12179	1.12	24490	4.39	13970	0.570	240	4.8	18
Average							*0.592*		*4.7*	*18*

WMA 2022_BINDER

Specimen No & ID		Fingerprint |E*| [MPa]	DMR 0.85<DMR<1.15	N_f	log (N^f)	Cum. (1-C)	DR_a	Input Strain (μ)	Vuoty SSD [%]	Sapp
W1_1	Wbinder A1_Rip.1	11127	1.13	12430	4.09	8887	0.715	300	3.6	28
W1_3	Wbinder A1_Rip.2	9322	0.95	46420	4.67	35882	0.773	270	4.2	31
W3_2	Wbinder A1_Rip.3	8864	0.91	53430	4.73	37936	0.710	300	4.1	27
Average							*0.733*		*4.0*	*29*

HMA 2022_BASE

Specimen No & ID		Fingerprint |E*| [MPa]	DMR 0.85<DMR<1.15	N_f	log (N^f)	Cum. (1-C)	DR_a	Input Strain (μ)	Vuoty SSD [%]	Sapp
H4.5	Hbase A1_Rip.1	8624	1.05	13190	4.12	10860	0.823	280	6.5	26
H4.6	Hbase A1_Rip.2	8754	1.07	11030	4.04	7763	0.704	280	6.4	19
H4.9	Hbase A1_Rip.3	7821	0.95	37830	4.58	30989	0.819	280	7.3	25
H5.6	Hbase A1_Rip.4	9595	1.16	6900	3.84	5074	0.735	270	4.2	20
Average							*0.770*		*6.1*	*22*

WMA 2022_BASE

Specimen No & ID		Fingerprint |E*| [MPa]	DMR 0.85<DMR<1.15	N_f	log (N^f)	Cum. (1-C)	DR_a	Input Strain (μ)	Vuoty SSD [%]	Sapp
W2.4	Wbase A1_Rip.1	12603	1.24	34410	4.54	23981	0.697	260	3.0	29
W2.7	Wbase A1_Rip.2	12028	1.18	10500	4.02	7381	0.703	270	3.7	27
W2.8	Wbase A1_Rip.3	11594	1.13	55520	4.74	37595	0.677	240	4.4	24
W3.4	Wbase A1_Rip.4	12404	1.22	52220	4.72	38168	0.731	250	2.6	32
Average							*0.702*		*3.4*	*28*

Chapter 6

Laboratory specimens

DG30H

Specimen ID	Fingerprint |E*| [MPa]	DMR 0.85<DMR<1.15	N_f	log (N^f)	Cum. (1-C)	DR_a	Input Strain (μ)	Vuoty SSD [%]	Sapp
1 : H19.2	15407	0.98	11840	4.07	5417	0.457	220	2.8	11.2
2 : H19.4	16436	1.05	12760	4.11	6084	0.477	200	2.7	11.2
3 : H15.2	14923	0.96	49870	4.70	24888	0.499	210	2.9	13.5
Average						*0.478*		*2.8*	*12.0*

DG45W

Specimen ID	Fingerprint |E*| [MPa]	DMR 0.85<DMR<1.15	N_f	log (N^f)	Cum. (1-C)	DR_a	Input Strain (μ)	Vuoty SSD [%]	Sapp
1 : W62.1	13237	1.08	11810	4.07	6975	0.591	190	3.6	13.9
2 : W63.2	12642	1.02	22740	4.36	13242	0.582	180	3.3	12.8
3 : W64.1	12473	1.01	32780	4.52	15397	0.470	180	3.1	9.6
4 : W64.3	13439	1.09	61040	4.79	25980	0.426	150	2.3	7.2
5 : W65.1	11630	0.94	7970	3.90	5316	0.667	210	3.0	15.7
Average						*0.547*		*3.1*	*11.9*

OG15H

Specimen ID	Fingerprint |E*| [MPa]	DMR 0.85<DMR<1.15	N_f	log (N^f)	Cum. (1-C)	DR_a	Input Strain (μ)	Vuoty SSD [%]	Sapp
OG_H_3	5974	0.97	7310	3.86	5387	0.737	280	19.9	20.7
OG_H_5	6784	1.09	1960	3.29	1303	0.665	290	18.2	15.5
OG_H_6	5999	0.97	16020	4.20	11157	0.696	260	19.1	17.8
OG_H_7	6814	1.10	15810	4.20	10687	0.676	230	19.3	16.1
Average						*0.694*		*19.1*	*17.5*

Appendix B
S-VECD fatigue parameters

OG25W									
Specimen ID	**Fingerprint |E*| [MPa]**	**DMR 0.85<DMR<1.15**	**N_f**	**log (N^f)**	**Cum. (1-C)**	**DR_a**	**Input Strain (μ)**	**Vuoty SSD [%]**	**Sapp**
1 : W55	5559	0.97	74520	4.87	45621	0.612	190	15.3	10.6
2 : W61	6426	1.12	8970	3.95	5248	0.585	200	15.4	8.7
3 : W59	6472	1.13	28120	4.45	17468	0.621	190	15.0	11.3
Average						*0.606*		*15.2*	*10.2*

Field specimens

DG30H									
Specimen ID	**Fingerprint |E*| [MPa]**	**DMR 0.85<DMR<1.15**	**N_f**	**log (N^f)**	**Cum. (1-C)**	**DR_a**	**Input Strain (μ)**	**Vuoty SSD [%]**	**Sapp**
1 : C3_7	10384	1.03	4440	3.65	2421	0.545	220	5.7	12.5
2 : C4_1	10466	1.03	78230	4.89	47646	0.609	210	8.0	19.6
3 : C4_3	11309	1.12	8080	3.91	4233	0.524	220	6.7	10.7
4 : C3_5	9090	0.89	9990	4.00	6334	0.634	190	6.3	10.6
5 : C3_6	9399	0.93	5180	3.71	2415	0.466	200	6.7	6.7
Average						*0.559*		*6.8*	*14.3*

In red the discarder tests

DG45W									
Specimen ID	**Fingerprint |E*| [MPa]**	**DMR 0.85<DMR<1.15**	**N_f**	**log (N^f)**	**Cum. (1-C)**	**DR_a**	**Input Strain (μ)**	**Vuoty SSD [%]**	**Sapp**
1 : T2_3	11533	1.10	32700	4.51	22915	0.701	200	6.0	20.0
2 : T2_4	10750	1.02	33030	4.52	20999	0.636	230	5.7	17.9
3 : T2_5	10125	0.95	21110	4.32	11387	0.539	220	5.8	12.3
4 : T1_1	7649	**0.73**	1430	3.16	1308	0.915	400	8.5	26.6
5 : T2_6	11765	1.12	**135940**	5.13	59444	0.437	170	5.0	9.5
6 : T1_2	6757	**0.64**	450	2.65	350	0.779	320	7.7	14.5
Average						*0.625*		*5.8*	*16.8*

In red the discarder tests

Chapter 7

CRM1_Nf,δ							
Specimen No & ID	Fingerprint |E*| (MPa)	DMR, 0.85<DMR<1.15	Nf	log (Nf)	Cum. (1-C)	DR	Input Strain (με)
R5	4111	0.81	7280	3.86	4274	0.587	80
R14	4167	0.82	46900	4.67	36245	0.773	70
R15	4572	0.90	5630	3.75	3998	0.710	75
R17	5465	1.08	6720	3.83	4435	0.660	75
R18	4294	0.85	28040	4.45	16791	0.599	70
R19	4673	0.92	2540	3.40	1853	0.730	75
R22	4642	0.91	27690	4.44	18658	0.674	70
Average	4561	0.90				0.676	

Appendix B
S-VECD fatigue parameters

CRM1_Nf,DER

Specimen No & ID	Fingerprint |E*| (MPa)	DMR, 0.85<DMR<1.15	Nf	log (Nf)	Cum. (1-C)	DR	Input Strain (με)
R5	4111	0.81	5180	3.71	2806	0.542	80
R14	4167	0.82	17470	4.24	11335	0.649	70
R15	4572	0.90	2580	3.41	1535	0.595	75
R17	5465	1.08	4290	3.63	2554	0.595	75
R18	4294	0.85	29590	4.47	17968	0.607	70
R19	4673	0.92	2050	3.31	1450	0.707	75
R22	4642	0.91	13530	4.13	7288	0.539	70
Average	4561	0.90				0.605	

CRM2_Nf,δ

Specimen No & ID	Fingerprint |E*| (MPa)	DMR, 0.85<DMR<1.15	Nf	log (Nf)	Cum. (1-C)	DR	Input Strain (με)
R1	7398	1.20	4630	3.67	2537	0.548	80
R5	7061	1.15	2130	3.33	1362	0.639	80
R9	6291	1.02	1460	3.16	991	0.679	75
R10	7100	1.16	11140	4.05	7906	0.710	75
R11	7399	1.20	14170	4.15	7144	0.504	75
R19	6736	1.09	4070	3.61	2591	0.637	75
R20	6148	1.00	13560	4.13	8846	0.652	70
Average	6876	1.12				0.624	

CRM2_Nf,DER

Specimen No & ID	Fingerprint |E*| (MPa)	DMR, 0.85<DMR<1.15	Nf	log (Nf)	Cum. (1-C)	DR	Input Strain (με)
R1	7398	1.20	3110	3.49	1292	0.415	80
R5	7061	1.15	1570	3.20	905	0.576	80
R9	6291	1.02	1250	3.10	808	0.646	75
R10	7100	1.16	3710	3.57	1987	0.536	75
R11	7399	1.20	11780	4.07	5227	0.444	75
R19	6736	1.09	2060	3.31	928	0.450	75
R20	6148	1.00	6780	3.83	3848	0.568	70
Average	6876	1.12				0.519	

Appendix C: Production of the CRMs

CRM 1

Composition of the gyratory specimen

ID	Name	Dosage with oven-dried aggregates [g]	Density (apparent) [g/cm^3]
RA1	**0/16**	2782	**2.482**
RA2	**0/16**	2782	**2.516**
Filler	**calcareo**	618.3	**2.650**
Cement	**Cem II/A_LL**	123.7	**3.150**
Bitumen		148.4	**1.015**
Water		278.3	**1.000**
Abs Water		89.7	**1.000**

Total weight 6733 g

Mixture to produce
(amount of material slightly higher)

ID	Name	Dosage oven-dried aggregates [g]
RA1	**0/16**	2835
RA2	**0/16**	2835
Filler	**calcareo**	630
Water (abs)		91.4
Cement	**Cem II/A_LL**	126
Emulsion		252
Water (pre-wetting)		91
TOTAL		6861

Prepared the day before

CRM 2

Composition of the gyratory specimen

ID	Name	Dosage with oven-dried aggregates [g]	Density (apparent) [g/cm^3]
RA1	**0/16**	2802	**2.482**
RA2	**0/16**	2802	**2.516**
Filler	**calcareo**	622.8	**2.650**
Cement	**Cem II/A_LL**	62.3	**3.150**
Bitumen		149.5	**1.015**
Water		280.3	**1.000**
Abs Water		90.4	**1.000**

Total weight 6720 g

Mixture to produce
(amount of material slightly higher)

ID	Name	Dosage oven-dried aggregates [g]
RA1	**0/16**	2835
RA2	**0/16**	2835
Filler	**calcareo**	630
Water (abs)		91.4
Cement	**Cem II/A_LL**	63
Emulsion		252
Water (pre-wetting)		91
TOTAL		6798

Prepared the day before

Preparation of the mixture

The day before: the aggregates (RA1 + RA2 + Filler) are mixed with the W_{abs}

Aim: aggregates in ssd condition the day after for the compaction

Mixing
50 % RA1 + 50 % RA2

5670 g of RA are weighted in a bowl

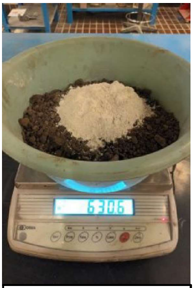

630 g of filler are added

RA and filler are manually mixed

Resulting RA + Filler

W_{abs} = 91.4 g is added

After newly mixing, resulting RA + Filler + W_{abs}

Wrapped in a plastic bag (no water evaporation)

Preparation of the mixture

All the procedure takes about 15 minutes (one gyratory sample from one batch)

The surface of the mixer bin has been moistened

The material is unwrapped and put in the mixer bin

The cement content is the only difference in the mixture's production

The cement is added (CRM1-63 g; CRM2-126 g)

Mixing all the solids – mixer (about 1')

Since smaller particles are spread in the edges of the bin

Mixing all the solids – manual (about 1')

Water pre-wetting = 91 g is added

Mixing all the solids – mixer + manual (about 2')

Half of the emulsion = 126.0 g is added

Appendix C
Production of the CRMs

Mixing all the solids – mixer + manual (about 2')

Half of the emulsion = 126.0 g is added

Mixing all the solids – mixer + manual (about 2')

The mixture is ready

The gyratory samples are moved using plates

Tare of the plate and the 2 disks

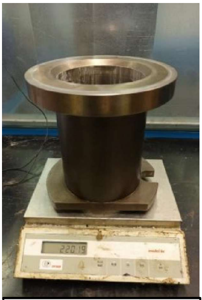

Weight of the mould (tare) – diameter = 150 mm

A disk is put at the bottom. The mixture is put in the mould.

The mixture is slightly compacted with a spatula

Weight of the gyratory sample: CRM1-6733 g, CRM2-6720 g

A disk is put on the mixture

Gyratory compactor Tecnotest

Compaction at fixed heigh = 180 mm

Weight after compaction to check the water loss

Extraction of the gyratory sample

The plate is put at the superior part of the gyratory sample

Gross weight of the gyratory sample with the tare

The net weight is calculated as the difference

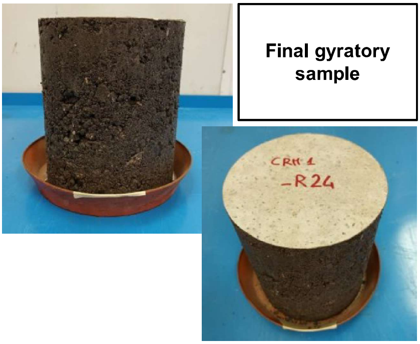

Final gyratory sample

Appendix D: CRMs’ strain sweep test results

Strain sweep curves (3 replicates for each CRM with middle failure)

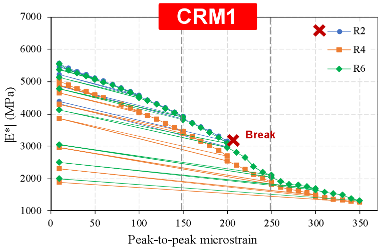

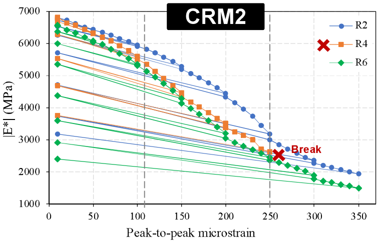

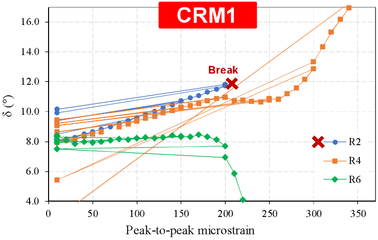

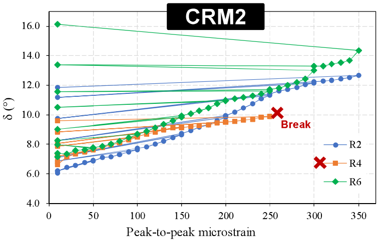

Small strain curves (3 replicates for each CRM with middle failure)

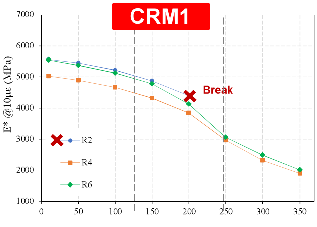

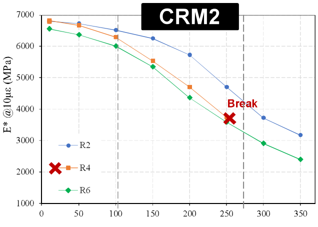

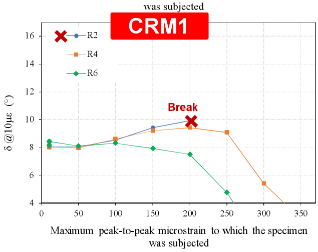

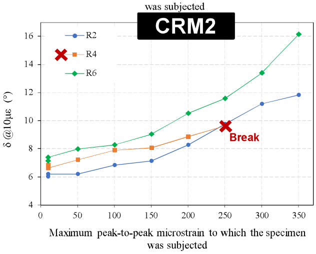

Appendix E: S-VECD fatigue tests considerations gained from experience

1. *Test stopped as it starts*

The test automatically stopped as it starts is usually simply due to the input deformation level too high. So, the next test should be conducted at a lower strain level.
However, sometimes it could happen that, once lowered the actuator to see the failure surface, the failure is actually between the glue and the base plate with the grooves clearly visible, as shown in Figure D1.A. In this case, the problem is in the gluing procedure. The used epoxy may not be properly mixed, or the base plate was not completely cleaned using alcohol. The specimen has not been subjected to damage, and can be newly glued to the base plate. The integrity of the specimen can be checked through the fingerprint dynamic modulus value.
A similar situation is shown in Figure D.1B. In this case, the failure is right after the glue. There is a very thin film of glue and asphalt mixture on the base plate. This can be due to the end surface of the specimen not perfectly cleaned, maybe due to the presence of dust. Even in this case, the specimen should be undamaged. Once cleaned the base plate, the specimen could be newly glued, and its undamaged condition would be confirmed from the fingerprint dynamic modulus value.

D1.A

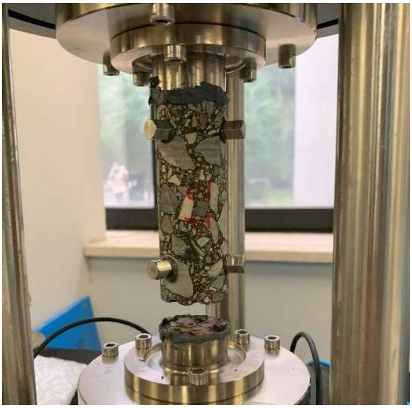

D1.B

2. *LVDT records an abnormal increasing value*

During the cyclic fatigue test, of course the LVDT should record an increasing value (i.e., it expands) due to the opening of the microcracks up to failure. However, it could happen that one LDVT or more than one record an increasing value even while the specimen is conditioning or during fingerprint test. The reason is ascribable to the glue of the gauge points, which may not be properly mixed. Basically, the gauge point is falling down under the weight of the x-men plus transducer. In fact, it usually happens to the lower gauge point (Figure D2). This problem could happen during dynamic modulus tests, too, especially at high temperatures to which the glue becomes softer for the same reason. The test must be stopped, and after that the gauge point problem is fixed, it can be carried out.

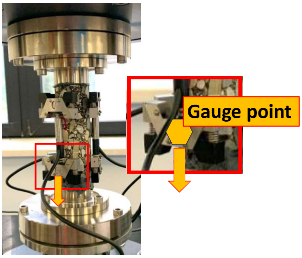

D2

3. *LVDT record a decreasing strain and the test is automatically stopped*

One or more LVDT record a decreasing value of microstrain, as depicted in Figure D3.A. It happens when an end-failure will occur. As explained in Figure D3.B, if the macrocrack develops outside the area recorder by the LVDTs, the LVDT cannot record increasing strains but it is like unloaded. When the LVDT records the 0 value, the software automatically stops the test.

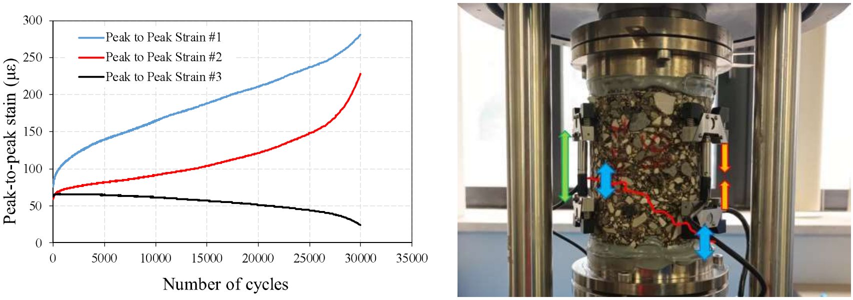

D3.A **D3.B**

4. *End failure*

Once the test has been automatically stopped by the software, the actuator is lowered down in order to see the failure. Figure D4.A-D4.C show typical end-failures obtained in small specimens. End-failure can be ascribable to three causes:

- higher AV in the ends of the specimens, due to a non-optimal compaction;
- end surfaces not parallel or not flatness, due to a wrong cut of the specimens;
- wrong gluing of the specimen to the plates. If the specimen has non-flatness end surfaces (but few field cores are available), during gluing the operator must place the specimen perpendicular to the base plates, and must keep it straight for the

time that the glue gets hard (5-7 minutes). Otherwise, the specimen tends to fall losing the perpendicularity under the weight of the gluing jig. Of course, this procedure cannot be possible for large specimens, for which the glue takes at least 1-2 hours to harden.

- The shims were not properly positioned.

The test with end-failure must be discarded.


D4.A


D4.B


D4.C

5. *Multiple failure surface*

Once the test has been automatically stopped by the software, the actuator is lowered down in order to see the failure. Figure D5.A-D5.B show an open-graded and a CRM large specimen, respectively, where the failure surfaces were multiple. For the OG specimen, this is likely due to the inevitable not homogeneous distribution of the AV. For the CRM, it can be due to the intrinsic variability of the material for the presence of RAP. However, it can happen also to conventional dense-graded mixtures, but in minor measure. The test should be discarded, since weird damage characteristic curves usually occurs, even though the main crack is in the middle.


D5.A


D5.B

6. Failure surface with broken aggregate

Once the test has been automatically stopped by the software, the actuator is lowered down in order to observe the failure surface, too, that should be within the binder. However, as shown in Figure D6.A-D6.D the surface could present different situations:

- Figure D6.A-D6.B: broken or totally crushed virgin aggregate. It is usually due to an over-compaction of the gyratory specimens. Since the compaction is at fixed height (180 mm), the gyratory compactor applies gyrations until this condition. If the material is too much, or the design of the mixture is wrong (e.g., too much coarse aggregate) or the compaction temperature is too low, broken aggregate could occur. The test is in direct tension configuration, so such aggregates are obviously the weaker point of the chain that fails.
- Figure D6.C: broken RAP aggregate (a thin light brown film is visible around the aggregate failure surface). It can be due to the previous justification, i.e., an over-compaction of the mixture which occurs in the break of RAP aggregate. Furthermore, the RAP aggregate could have microcracks derived from the milling, that make the RAP weak and more susceptible due to compaction loading.
- Figure D6.D: uncovered RAP aggregate (the surface is light brown). Low binder content is used in the mixture, or the mixing procedure is not well executed.

In all such cases, if middle-failure occurs, the tests are not automatically discarded. It was observed that overlapping damage characteristic curves can be obtained, depending on the measure of the area with broken aggregate.


D6.A


D6.B


D6.C


D6.D

7. Considerations on resulting damage characteristic curve and failure criterion

7.1. *Limit on DMR.* The *DMR* should be within 0.85 and 1.15 in order to limit the specimen-to-specimen variability. In fact, it was observed that lower *DMR* will cause a damage characteristic curve in lower position, and vice versa (Figure D7.A).

7.2. *End-failure or the presence of broken aggregate on the failure surface*. In both the cases, the damage characteristic curve will result shorter than the right ones (Figure D7.B). This is likely due to the right evolution of the damage within the material during the development of homogenously distributed microcracks. During this stage, the overlapping curve corresponds, i.e., the intrinsic evolution of the damage. However, when the macrocracks initiate outside the gauge length or within an aggregate, the failure quickly occurs, differently from the valid tests where the damage is mostly within the binder phase in the recorded area. Moreover, a shorter damage characteristic curve usually lead to a lower D^R value. Recalling the definition of D^R, the numerator is the *Sum(1-C)*, which represents the area shown in Figure D7.C. Even though at the denominator there is *Nf*, which is usually lower, the resulting D^R value is lower since it is capable of catching the wrong failure not inside the binder or outside the recorded area.

7.3. *Limit on the duration*. The duration of the test should be within 2000 and 80000 cycles. In fact, it was observed that higher durations lead to longer damage characteristic curve and higher D^R value (for the same reason explained in *7.2*), as show in Figure D7.D). Conversely, it was seen that the damage characteristic curve obtained from test last for less than 2000 cycles are slightly shorter with low consequences on the D^R (Figure D7.D).

7.4. *Use of high percentages of RAP*. As explained in Chapter 6, it was found that the damage characteristic curves of specimens with high RAP content (45%) could present different failure points (Figure D7.E). It has an influence on the D^R value, too, but it falls within the prescribed limit. Specifically, to shorter damage characteristic curve corresponds a lower D^R value and vice versa.

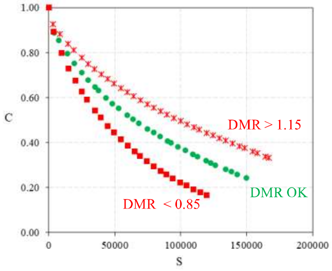

D7.A

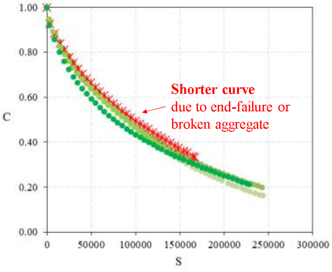

D7.B

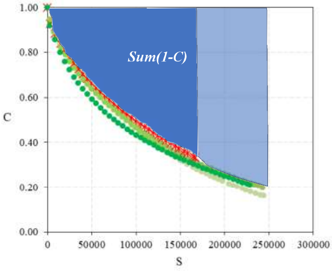

D7.C

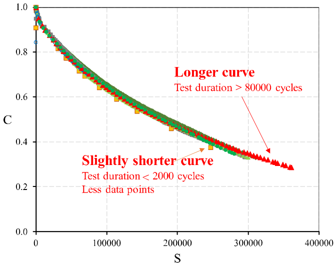
1.0
0.8
0.6
0.4
0.2
0.0
C
0
100000
200000
300000
400000
S
Longer curve
Test duration > 80000 cycles
Slightly shorter curve
Test duration < 2000 cycles
Less data points

D7.D

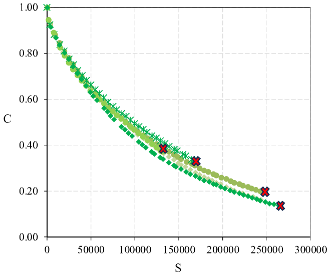
1.00
0.80
0.60
0.40
0.20
0.00
C
0
50000
100000
150000
200000
250000
300000
S

D7.E